A NUMERICAL STUDY OF PLATE ANCHORS EMBEDDED IN SAND

by

ZEIN EDDINE MEROUANI

Ingenieur Civil (Ecole Polytechnique d'Alger)

A Thesis Submitted for the Degree of

Master of Science

Department of Civil Engineering,

University of Glasgow.

February, 1988.

بسم الله الرحمن الرحيم

IN THE NAME OF ALLAH, THE MOST MERCIFUL,

THE MOST GRACIOUS

TO MY PARENTS

ACKNOWLEDGEMENTS

The work described in this thesis was carried out in the Department of Civil Engineering at the Univerity of Glasgow, under the general guidance of Professor D.M. WOOD.

The author would like to express his appreciation to the head of department, Dr. D.R. GREEN, Professor H.B. SUTHERLAND and Professor D.M. WOOD for the provision of facilities in the department.

The author is greatly indebted to Dr. T.G. DAVIES for valuable supervision, encouragement and advice during the course of this study.

My grateful thanks are also due to:

My friends J. Moussa, A. Bouazza, M. Souici, F. Abidi, R. Saadi, E. Osman, S. Murthi and Y.K. To for their useful discussions and comments.

My friends T. Ayoub, Y. Arroum, M. Dib, M. Seddiki, M. Bendahgane, R.Manaa, S. Djellab, M. Benredouane, D. Abderrahmane, R. Seridi, H. Fernane, M. Ben– El– Kadi and T. Boumerfeg for their encouragements.

The C.N.E.R.I.B. and the British Council for their financial support during the period of the research.

The staff of the general direction of C.N.E.R.I.B. for their encouragement and trust.

G. Irving and other members of staff for their assistance.

Finally, my special thanks are reserved for my family for their boundless patience and continual encouragement throughout the years.

CONTENTS

CHAPTER THREE: CONSTITUTIVE LAWS

SUMMARY

The work described in this thesis begins with an elastic analysis of ground anchors in which several assumptions were made. Some of these assumptions limited the applicability of the analysis but some useful insights into the stress distribution around ground anchors were obtained. However, a more realistic non-linear analysis was required before any definitive conclusion could be drawn. Finite element analysis appeared to be the most appropriate method. However, since the behaviour of sand is rather complex (dilatancy, softening,...) an appropriate stress-strain model was then necessary. After a review of several constitutive models for sands, Vermeer's model which has the merit of being relatively simple yet comprehensive, has been studied in detail. However, this model does not describe softening behaviour since this is not a material property of a continuum. For this reason among others, it was decided that little advantage would be gained by implementing the model into the finite element program. Instead, a simple linear elastic-perfectly plastic model based on the Mohr-Coulomb yield criterion was employed in the finite element analyses. The effects of soil properties, embedment depth and initial stress conditions were studied as well as the effects of sand inhomogeneity and test scale. Contours representing the stress distribution around the anchor and yield propagation during the loading history were plotted. This gave an insight into the progressive mechanism of failure occuring in the soil mass. The results from the finite element anlyses were based on the so-called k_4 failure load concept which appeared to give satisfactory results for loose sands.

NOTATION

Major symbols used in the text are listed below. Others are defined as they first appear.

B Strain matrix.

b_j Body force per unit volume

c Cohesion of the material.

D Anchor diameter.

D^e Elastic constitutive matrix.

D^{ep} Elasto_plastic constitutive matrix.

dS_n Area of the n^{th} anchor element.

dw Increment of uniformly distributed load.

E Young's modulus.

f Yield function.

F_{ij} Tensor function for Mindlin solution.

G_s & G_o Shear modulus and reference shear modulus.

H Embedment depth.

H Hardening parameter .

(I_1, I_2, I_3) & (J_1, J_2, J_3) Stress invariants.

J Jacobian matrix.

K Global stiffness matrix.

K_o Coefficient of earth pressure at rest.

k Bulk modulus.

K^e Element stiffness matrix.

M_p Material prameter.

N Number of anchor elements.

N_i Shape function.

P Point load.

p_o Reference pressure in Vermeer's model.

p Mean stress.

P_u Ultimate load.

Q Plastic potential.

q Deviatoric stress.

u_i Displacement vector.

y_n Position vector.

z Depth.

α Vermeer's model parameter, or anchor inclination.

β Vermeer's model parameter.

σ_{ij} Stress tensor.

$\sigma_1, \sigma_2, \sigma_3$ Principal stresses.

σ Stress measure defined by Vermeer's model

δ_{ij} Kronecker delta.

$\underline{\epsilon}$, $\underline{\epsilon^e}$, $\underline{\epsilon^p}$ Total, Elastic & Plastic strain vectors.

ϵ_v, ϵ_d Volume & Deviatoric strains.

ϵ_{ij} Strain tensor.

ν Poisson's ratio.

φ Angle of friction.

γ Unit weight of soil.

ψ Angle of dilatancy.

τ Shear stress on the failure plane.

$\underline{\Psi}$ Vector of residual forces.

λ Plasticity multiplier.

λ, μ Lame's constants.

CHAPTER 1 INTRODUCTION

1.1 BACKGROUND :

Ground anchors are used for anchoring structures that transmit considerable tensile forces to their foundations. Such structures are high–mast transmission towers, suspended or arch bridges, off–shore structures, structures supporting excavations, dams, etc... as shown in Figure 1.1. A detailed description of ground anchors has been given by Hanna[29].

A plate anchor consists of a plate, usually made of metal or concrete, connected to the anchored structure by means of a tie rod or a cable. With respect to Fig 1.2, we consider anchor plates of diameter D buried at depth H in sand. The soil properties are the Young's modulus of elasticity E, Poisson's ratio ν, the angle of internal friction φ, the relative density Dr and the unit weight γ. The anchor plate is loaded by an uplift force.

The main objectives of the present study is to attempt to predict the stress distribution in the soil around anchor plates, the load–displacement relation for anchors up to collapse and their failure mechanisms. This work has of course been preceeded by many experimental and numerical studies which we now briefly summarize before reviewing the literature in detail.

Model and field tests:

For over twenty years, tests have been carried out on in–situ full–scale models and in laboratories on reduced–scale models to predict the behaviour of anchor plates in soils. Balla (1961) was the first to establish a systematic method to design ground anchors in sands based on insitu and laboratory model tests. This work was continued by Matsuo (1968), Meyerhof and Adams (1968), and many others in order to establish a general method for calculating the soil uplift resistance to tensile

forces transmitted to buried plates. However, before such methods can be established, an increased understanding is required of the relative importance of the many variables associated with uplift resistance and of the nature of the failure mechanism.

Semi–empirical theories:

Since the early sixties many authors have attempted to develop a general theory to determine the uplift capacity of anchors based on the shape of the failure surface. Although Balla (1961), Matsuo (1968), and Fadl (1981) carried out tests on circular anchors buried in sand, the shapes of the failure surfaces and the pull–out capacities predicted by the authors differ from each other. More than twenty years have passed by since the work done by Balla (1961) and yet no satisfactory semi–empirical theory has emerged to predict the behaviour of soils loaded by ground anchors. The reason is that semi–empirical theories are necessarily related to the particular test conditions. If tests are performed on one type of soil, it is difficult to propose a general design method although some authors have attempted to do so. For instance many authors, using one type of soil, investigated the effect of the angle of internal friction on the uplift capacity. Such a change in friction angle induces a change in relative density.

Early authors like Balla (1961) and Matsuo (1968) took into account the effect of friction angle φ in their calculations without considering other material parameters. Later, Fadl (1981), considered the effect of the relative density. However since he used only one type of sand in his experiments, it was thus impossible to separate the effect of relative density from that of friction angle. Figures 1.24 and 1.25 representing results obtained by Bouazza (1988) show clearly that different sands having the same friction angle give different responses and different sands having the same relative density give different responses too. These results show that characterisation of sand in terms of φ alone or Dr alone is inadequate.

Numerical studies:

Several linear analytical techniques to study the elastic behaviour of soils under anchor loading have been reported (Fox (1948), Rowe and Booker (1979,1981), Selvadurai (1981)). However, the behaviour of soil in general and that of sand in particular is not elastic and, consequently such methods cannot give reliable results, even at working loads. More powerful methods such as "finite elements" have been used more recently, Rowe and Davis (1982), Ito and Kitahara (1982) , Vermeer and Sutjiadi (1985), Desai et al (1986). The major difficulties in their use arise from the determination of appropriate stress– strain relations for sand.

1.2 LITERATURE REVIEW:

In this section, we discuss significant laboratory and field tests and their associated theories as well as numerical studies.

1.2.1 Experimental Work:

Experimental work has been conducted on both reduced–scale models in laboratories and on full–scale models on field; each part will be discussed separately.

a/ Model tests:

1/ A. Balla (1961):

The sand used in this study was dense with a friction angle in the range of 36° and 38°; the moisture content w varied between 10% and 12%. Balla considered shallow anchors (H/D ranged between 1 and 4) buried at depths of about 100 mm. Balla used so–called mushroom foundations in his tests. Spatial (or whole foundation) models were used to determine the uplift capacity of foundations and semi–spatial models were used to determine the failure surface. The meridional section of the failure surface is a curve which starts out from the upper plane of the anchor with a vertical tangent curving outwardly from the axis, and intersecting the ground level at an angle approximately equal to $\pi/4 + \varphi/2$ (Fig. 1.3). Figure 1.4 shows that the breakout resistance $P_u = f(H^3)$ for a given anchor diameter and Figure 1.5 shows comparison between the pull–out capacity predicted by several authors and his experimental results. Balla based his semi–empirical theory on results obtained from tests on dense sand. However, the shape of the failure surface would be different for loose sand.

2/ W.H. Baker and R.L. Kondner (1966):

Baker and Kondner used in their experiments a dense uniform sand (Ottawa

sand) with a friction angle of 42°. They tested both shallow and deep circular anchors in the H/D range of 1.5 to 21. The diameter of their model anchor was about 50 mm. Figure 1.6 shows the pull–out capacity versus depth of embedment H for shallow anchors. Figure 1.7 shows the test results in terms of pull–out (break_out) factor F_p ($F_p = 4P_u/\pi D^2\gamma H$) versus $[H/D]^2$ and a comparison with Balla's prediction for $\varphi = 42°$. For shallow anchors , a failure surface similar to that proposed by Balla was observed. The appearance of the intersection of the failure surface (circle) on the sand surface observed only for shallow anchors indicates a difference in the mode of failure between deep and shallow anchors. Figure 1.7 shows a linear relation between the break–out factor and $[H/D]^2$ for shallow anchors ($H/D < 6$). The expression of the pull–out factor has the form:

$$\frac{P_u}{H\ D^2\ \gamma} = 3.0 + 0.67\ \frac{H^2}{D^2} \qquad (1.1)$$

For deep anchors ($H/D \geq 6$), the expression for the pull–out force is:

$$P_u = 170\ D^3\ \gamma + C_3\ D^2\ b\ \gamma + C_4\ H\ D\ b\ \gamma \qquad (1.2)$$

where $C_3 = 2800$ and $C_4 = 470$ for the particular laboratory conditions,

and b is the anchor thickness.

3/ M. Matsuo (1968):

Matsuo carried out tests on air–dry and wet sand in a dense state at unit weights between 13.6 kN/m^3 and 15.4 kN/m^3, and loam. The model anchor used was circular with a diameter of about 300 mm. Matsuo considered only shallow anchors for which H/D varied between 0.3 and 5. Fig 1.10 shows a logarithmic relation between P_u and the anchor depth. Table 1.1 summarises his test results and the predictions given by his theory based on the combined logarithmic spiral–straight line sliding surface (Fig 1.9).

The difference between the test results and the predicted values of the uplift capacity reach a value of 47 % which is hardly satisfactory even for a semi–empirical theory. Like Balla, the proposed sliding surface is valid for dense sands only.

Table 1.1 Experimental and Predicted Results of Pull–out Capacity, Matsuo 1968:

Test	Variation (%)	Test Result (ton)	Calculated Value (ton)
A	24	17.0	12.9
	47	32.3	17.1
B	31	34.7	24.1
	26	31.7	23.4
C	11	40.2	35.9

4/ G.G. Meyerhof and J.I. Adams (1968):

Meyerhof and Adams carried out tests on uniformly graded and well graded sands in both loose and dense states. The tests performed in dense sand showed that the uplift capacity increased quadratically with anchor depth and was higher for well graded sand than for uniform sand. For loose sand, the increase in uplift capacity with depth was approximately linear. The behaviour of both dense and loose uniform sands was observed using time exposure photographs. For anchors embedded in dense sand at shallow depths, a distinct slip surface occured which extended in a shallow arc from the anchor edges to the soil surface. At greater embedment depths the failure surface was less distinct being initially curved and then essentially vertical and extending to the surface. In loose sand, at large embedment depths, the failure surface was essentially vertical and limited to the zone directly above the anchor. In loose sand at shallow embedment depths the failure surface was again essentially vertical but extended to the ground surface. This was a very interesting qualitative study which indicated the different shapes of the failure surface associated with different depths of embedment and relative density of sand.

5/ T.H. Hanna et al (1972):

In this work, attention focussed on displacements around the anchor. The tests were performed on anchors embedded to a depth of up to 750 mm and diameter of anchor up to 150 mm. The sand movement was measured in the vicinity of the anchor and the authors observed that the magnitude and direction of the sand

displacements were regulated by the anchor embedment depth and the relative density as well as the applied anchor load level. For shallow depths of anchor embedment the sand movements were nearly vertical but as the embedment depth increased the displacements radiated outwards from the anchor. This was an interesting study but insufficient data were obtained for a complete description of the displacement field.

6/ B.M. Das and G.R. Seeley (1975,1977):

A loose silica sand was used during these experiments with a friction angle and unit weight of 31° and 15 kN/m^3 respectively. Rectangular and strip anchors of aspect ratio L/D = 1, 2, 3 and 5 were analysed. The anchors were about 50 mm wide. Reproduced from their first paper, Fig 1.14 showed that the critical embedment ratio, that is the transitional embedment ratio between shallow and deep anchors, increases with increasing aspect ratio.

In their second paper, the experiments were performed on the same sand but this time the authors tested shallow horizontal and inclined anchors, for a range of H/D ratios between 1 and 6. The angle of inclination varied between 0° and 50°. The authors noticed that the axial pull–out resistance of shallow anchors increases with increase of anchor inclination (Fig–1.13). For a given embedment depth and anchor inclination, the inclination factor α (α is the ratio of the pull–out factor at a given angle of inclination to the pull–out factor of a horizontal anchor at the same depth) is smaller for strip anchors as compared to square ones (Fig 1.15). The inclination factor α for a given anchor plate decreased with increasing embedment ratio. In the case of deep anchors, for anchor inclination from 0° to about 50°, the uplift capacity appears to be approximately the same. This could mean that for deep anchors failure is of a local nature.

The authors considered only a loose sand thus excluding dilatancy effects. They took into consideration uniquely the anchor aspect ratio and anchor inclination at different anchor depths. Tests were performed on one type of sand and no change in the friction angle was made.

7/ M.C. Wang and A.H. Wu (1980):

The variables investigated by the authors were the anchor orientation, the embedment depth, the internal friction angle and the anchor–soil friction angle δ. The material used was an Ottawa sand at two different densities ($\rho = 1.78$ t/m^3 $\varphi = 35°$ and $\rho = 1.62$ t/m^3 $\varphi = 30°$). The size of the vertical and inclined rectangular anchors was about 90 x 40 mm. The anchors were made of perspex ($\delta = 16°$), brass ($\delta = 19°$) and brass covered by sand paper ($\delta = 25°$). Wang and Wu confirmed Das and Seeley's findings, that anchor resistance increases with the angle of inclination. They also noted that anchor capacity increases with increasing internal friction angle and that the effect is more prominent at greater H/D ratios. For given soil conditions, greater anchor–soil friction results in higher anchor resistance. This was the first proper investigation of the effect of anchor roughness on uplift capacity.

8/ M.O. Fadl (1981):

The tests were performed on Leighton Buzzard sand, at three different densities (Dr= 85% $\varphi = 41.5°$; Dr= 50% $\varphi = 36.5°$; Dr= 25% $\varphi = 33.6°$). Both deep and shallow anchors were considered in vertical and inclined positions. The anchors were circular and their diameters varied from 25 mm to 75 mm. For shallow anchors, a conical failure surface was observed to propagate from the edges of the anchor to the ground surface (Fig 1.16). For deep anchors, the failure surface was conical from the edges of the anchor for some distance then became cylindrical up to the ground surface. Although the author found that the uplift capacity depended on the relative density (Fig.1.17), he could not separate this effect from the effect of the angle of friction φ since he worked on only one type of soil.

9/ H. Ito and Y. Kitahara (1982):

These model tests were carried out on loose ($\varphi = 34°$ $\rho = 1.5$t/m^3) and dense ($\varphi = 35.5°$ $\rho = 1.6$t/m^3) sand. The anchors were dentiform shaped as shown in Fig 1.18. The dentiform part of the anchor penetrates an undisturbed zone of the ground to give higher pull–out capacity. Various shapes of anchor plates with

different number of teeth were tested in laboratory and on site and the authors found that the pull–out resistance of footings having the dentiform parts exceeded that of the ones without dentiform parts by 30% to 100%. However, the number of penetrating teeth has practically little effect on the resistance.

10/ R.K. Rowe and E.H. Davis (1982):

The authors performed their tests on anchors in a dry, medium grained quartz Sydney sand at two different unit weights (γ= 14.9 kN/m^3 φ_{peak}= 32° ψ_{peak}= 4° and γ= 15.3 kN/m^3 φ_{peak}= 33° ψ_{peak}= 10°). Experiments were carried out on both shallow and deep anchors with the embedment ratio varying from 1 to 8. The anchors were about 50 mm wide and their aspect ratios varied from 1 to 8.75. Among the variables investigated were anchor embedment depth, friction angle, initial stress state K_o and anchor roughness. Figure 1.21 shows that the anchor capacities obtained by Das and Seeley (1975) were greater than the ones obtained by Rowe and Davis although the friction angle of the sand they used had a smaller value than the one used by Rowe and Davis. The value of the angle of dilatancy (ψ= 10°) is higher than might be expected from a sand of that density.

11/ I.B. Zakaria (1986):

Zakaria carried his tests on Leighton Buzzard sand at three different relative densities; medium (Dr= 49% γ= 15.75 kN/m^3), medium dense (Dr= 70% γ= 16.40 kN/m^3) and dense (Dr= 92% γ= 17.11 kN/m^3). The anchors used were circular and the range of diameters varied from 25mm to 75 mm. Both shallow and deep anchors were tested and the embedment ratio varied from 3 to 15. In Figure 1.22 the author compared his data with the values of pull–out capacity predicted by Fadl's theory. The values obtained by Zakaria are higher than those predicted by Fadl (Fig 1.22). At H/D = 15, the difference is about 30% for Dr= 70%. Figure 1.23 depicts the effect of a disturbed zone of soil around the anchor on the breakout factor in dry sand and shows that the uplift capacity decreases with increased soil disturbance.

12/ A. Bouazza (1988):

Bouazza performed tests on four types of sands;namely Leighton Buzzard, Lochaline, Douglasmuir and Hyndford sands. Tests were carried out on the sands in loose, medium and dense states in which the relative densities varied between 13% to 85%. The author tested both deep and shallow anchors with a range of H/D ratios between 2 and 12. The anchors were circular with diameters of about 30 mm. He studied the effects of both the friction angle and the relative density. Figure 1.24 shows the effect of the friction angle (φ= 38.8° and φ= 38.1°) at constant relative density (Dr= 60%) and Figure 1.25 shows the effect of the relative density (Dr= 65% and Dr= 53%) at constant friction angle (φ= 40°). In this study, the author showed that the effect of friction angle is distinct from the effect of relative density.

b/ Field tests:

1/ H.B. Sutherland (1965):

At Sizewell Nuclear Power Station, eight vertical shafts were constructed upwards from the cooling water tunnels by jacking cylindrical linings vertically from the tunnel to sea bed level. This operation was carried out in cohesionless soil through a depth of six meters, approximately. Shafts 2, 3, 4 and 5 were grouped together in an intake area where the angle of internal friction of the soil was approximately 42° while shafts 6, 7, 8, and 9 were grouped in the outfall area where φ was about 35°. Grouting was carried out on shafts 7 and 9 and its effect on the pull– out capacity is shown in Fig 1.26 . The loads required to raise shafts 2, 3, 4 and 5 were about 50% greater than those given by Balla's theory and lower than those predicted by Sutherland's model tests for the same conditions, as shown in Fig 1.26.

2/ W.H. Baker and R.L. Kondner (1966):

Pull−out tests were performed on two full−scale field earth anchors buried in a relatively uniform sand (dune deposit in Los Angeles). The friction angle was $\varphi = 37°$ and the unit weight was $\gamma = 16.8$ kN/m^3. A 120mm diameter shaft was first drilled and cased to the desired anchor depth, then a chemical grout was placed at the bottom of the grout to stabilize the sand during the reaming operation. The anchor was formed by filling the void at the bottom of the shaft with concrete after a 22 mm diameter high strength steel tie rod had been inserted in the shaft. Results of the two field tests and the dimension of the anchors are shown in Fig 1.28 . Figures 1.27 and 1.29 show the field tests results compared with results obtained from the authors model tests for various anchor diameters and the predictions given by Balla and the authors. Values of anchor capacity determined from field tests were higher than the values predicted by the theory.

3/ M. Matsuo (1968):

Field tests were carried out on sand, sandy loam ($\varphi = 35°$ to $43°$), Kanto loam and clay, all unsaturated. Square concrete slab footings of 1.10m to 1.80m were buried in two types of excavations: the first one was vertical and the second one was inclined. In all tests on vertical anchors, failure occured on the vertical sections along the outsides of the footing. In the other tests the failure surface started from the edge of the slab and expanded outwards towards the ground surface. The author stated that for sandy soils the shape of the failure surface was similar to those obtained during laboratory tests.

1.2.2 Analysis:

a/ Semi– empirical theories:

1/ M. Balla (1961):

Balla's theory is based on laboratory tests carried out by himself and field test results taken from literature. This theory is valid for shallow anchors only. From observations during tests, the author assumed a circular slip surface extending from the anchor edges to the ground surface making an angle of $\pi/4 - \varphi/2$ with the ground surface (Fig 1.3). The radius of the slip surface r is determined as follows:

$$r = \frac{H}{\sin(\frac{\pi}{4} + \frac{\varphi}{2})} \qquad (1.3)$$

The expression of the limit load is given:

$$P_u = H^3 \gamma \left[\frac{c}{\gamma} \frac{1}{H} F_2(\varphi,\gamma) + F_1(\varphi, \frac{H}{D}) + F_3(\varphi,\gamma) \right] \qquad (1.4)$$

where F_1, F_2 and F_3 are given by charts and c is the cohesion of the soil.
Balla stated that his predictions were in good agreement with the results of Mors (in German) and Fielitz (in German). The slip surface considered by Balla is typical of dense sands; loose sands behave differently as described by Meyerhof and Adams[52].

2/ L.G. Mariupol'skii (1965):

Mariupol'skii based his theory on results given by A.S. Kananyan[47]. The author assumed a curved slip failure surface and assumed that failure occured, not only by shearing, but in tension, a wedge of soil lifting away from the soil below at the limiting value of shear stress of the soil (Fig 1.30). For deep anchors, the author presented a solution based on the assumption that the work done by the anchor during vertical displacement should equal the work needed to expand a vertical cylindrical cavity to the radius of the anchor (Fig 1.31). Expressions for the

ultimate load are given for both deep and shallow anchors.

Shallow anchors:

$$P_u = W_0 + (R^2 - R_0^2) \frac{\gamma H \left[1 - \left[\frac{R_0}{R}\right]^2 + K \tan \varphi \frac{H}{R} \right] + 2 c \frac{H}{R}}{1 - \left[\frac{R_0}{R}\right]^2 - n \frac{H}{R}} \quad (1.5)$$

where n is function of the friction angle and is given in charts,

W_0 is the anchor weight,

K is the coefficient of lateral earth pressure,

R_0 and R are the shaft and anchor plate radii, respectively,

c is the soil cohesion.

Deep anchors:

$$P_u = W_0 + N \gamma H \pi (R^2 - R_0^2) \quad (1.6)$$

N is given from charts.

The author stated that these formulae are restricted to moist but unsaturated soil.

3/ M. Matsuo (1968):

This method of design for shallow anchors is based on laboratory and field test results carried out by the author as described earlier. In this method, the sliding surface is assumed to be composed of a combined curve consisting of a logarithmic spiral 'cd' and its tangential straight line 'de' as shown in Fig 1.9. The straight line intersects the ground surface at an angle of $\pi/4 - \varphi/2$ Matsuo's expression for the pull–out capacity of anchors is:

$$P_u = W + \gamma (D_2^3 K_1 - V_3) + D_2^2 K_2 \quad (1.7)$$

where K_1 and K_2 are function of φ and θ_0.

D_2 and θ_0 are defined in Fig 1.9.

V_3 is the volume of anchor and shaft.

Here again the failure surface is particular to dense sand; for loose sand the failure surface is different, as shown by Meyerhof and Adams[52]. Another point to notice is that the relation between embedment ratio and breakout factor is not logarithmic as determined by the author (Fig 1.10), although over the practical range

of parameters equations (1.7) does yield a reasonable approximation.

4/ G.G. Meyerhof and J.I. Adams (1968):

This theory is derived for strip footings and then modified for circular and rectangular footings for use in sand and in clay. For anchors at shallow depth, at the ultimate uplift load P_u a soil mass having a truncated conical shape is lifted up and the failure surface reaches the ground surface (Fig 1.11). Accordingly, a state of general shear failure exists along the failure surface on which a cohesive force C_f and a friction force F are mobilized. The expression for the ultimate uplift load is:

$$P_u = \tfrac{1}{2}\, s\, \pi\, \gamma\, D\, H^2\, K_u \tan\varphi + W \qquad (1.8)$$

where W is the weight of the soil mass and plate

K_u is the nominal uplift capacity of earth pressure on vertical plane

$s = 1 + m.H/D$ is the shape factor

m is given in Table 1.2.

Table 1.2 Coefficient m for various values of φ:

φ (deg.)	20	25	30	35	40	45
m	0.05	0.1	0.15	0.25	0.35	0.5

The authors reported that with increasing embedment depth, the compressibility and deformation of the soil mass above the plate prevent the failure surface from reaching the ground surface (Fig 1.11). The extent of this local shear failure is included in the analysis by limiting the vertical extent H_c of the failure surface and utilizing the surcharge pressure above the level of the failure surface $P_0 = \gamma (H - H_c)$.

The expression for the ultimate uplift force for greater embedment depths is:

$$P_u = \tfrac{1}{2}\, s\, \pi\, \gamma\, D\, (2H - H_c)\, H_c\, K_u \tan\varphi + W \qquad (1.9)$$

Table 1.3 gives H_c/D as function of φ.

The theoretical predictions are compared with results obtained by the authors and other investigators as shown in Figure 1.12. The authors' predictions rather

underestimate anchor capacities.

Table 1.3 Values of critical hight H_c:

φ (deg.)	20	25	30	35	40	45	48
H_c/D	2.5	3	4	5	7	9	11

5/ A.S. Vesic (1971,1972):

Vesic treated the breakout resistance of objects embedded in a soil mass in a similar way to the expansion of cavities in an infinite soil mass. The extent of the cavity formed depends on whether the anchor is buried at great or shallow depth. The cavity is formed as the pressure increases until equilibrium is achieved when the cavity radius R_u is sustained by an internal pressure p as shown in Figure 1.32 . The ultimate value p_u is:

$$p_u = \gamma H F_q \qquad (1.10)$$

where F_q is a dimensionless spherical cavity expansion factor given by charts or tables. Figure 1.33 depicts the predicted results compared with field test data reported by Balla[1], Sutherland[80] and Baker and Kondner[2]. This plot shows that a wide variation of φ (from 40° to 50°) has little effect on the breakout capacity predicted by Vesic, which is in contradiction to practical experience.

6/ M.C. Wang and A.H. Wu (1980):

A theoretical analysis was carried out by the authors using upper bound limit analysis (W.F. Chen 1975, Drucker, Prager and Greenberg 1952). The problem was treated as a plane strain problem. The failure mechanism for shallow anchors is shown in Figure 1.34a in which the slip line ABCD is approximated by two straight lines and one segment of a logarithmic spiral. By equating the rate of work done by external forces to the rate of internal energy dissipation the authors obtain:

$$\frac{P_u}{\gamma B D^2} = \frac{\cos \delta}{2 \cos^2 \left[\cos(\xi+\delta) - \sin\xi \tan\delta \right]} (A + B + C)$$

A, B and C are function of α, φ, δ, ξ, θ, and H/D

where

α is the anchor inclination,

φ is the angle of internal friction, and

δ is the friction angle between anchor plate and soil,

ζ and θ are defined in Fig 1.34.

Figure 1.34b shows the local shear failure mechanism adopted in this analysis for deep anchors: the slip line comprises a straight line AB and a segment of a logarithmic spiral BC. From consideration of the work done by the passive earth pressure developed along OC, the limit load P_u has an expression similar to that for shallow anchors. The pull–out capacities predicted by the authors were compared with results obtained by other investigators, namely Meyerhof and Adams[52] and Vesic[91,92], as shown in Fig 1.35.
There are some discrepancies between the authors results and these test data especially at higher friction angles.

7/ M.O. Fadl (1981):

This theory is based on the laboratory tests described previously. The shape of the failure surface for shallow anchors is a truncated cone with an apex angle α from the edges of the anchor to the ground surface (Fig 1.16b). For deep anchors, it is a truncated cone up to a certain height H_c then cylindrical up to the soil surface (Fig 1.16c).

In general the pull–out force consists of four components (Fig 1.16a):

$$P_u = P_1 + P_2 + P_3 + P_4 \qquad (1.11)$$

where

P_1 is the weight of soil in the truncated cone FGIJ,

P_2 is the weight of soil in the elliptical prism GIVW,

P_3 is the shear resistance along the surface of the oblique truncated cone FGIJ, and

P_4 is the partial shear resistance along the surface of the elliptical prism GIVW.

The expressions for the pull–out force are,

For shallow vertical anchors:

$$P_u = \tfrac{1}{2}\,\pi\gamma\, H\,(8\,H^2\tan^2\alpha + 12\,H\,D\tan\alpha + 3D^2) \qquad (1.12)$$

For deep vertical anchors:

$$P_u = f(H,\ H_c,\ D,\ \alpha,\ \varphi) \qquad (1.13)$$

The predictions of the author are in good agreement with Bemben and Kupferman[5] and his own laboratory tests (Fig 1.17b and 1.17c). However, the author included the effect of relative density in his theory based on rather scant data. Also of some concern is that the slip surface adopted by the author for deep anchors does not indicate failure of a local nature.

8/ P.A. Vermeer and W. Sutjiadi (1985):

This theory is intended for the design of shallow rectangular and strip plates buried in cohesionless soils. The data on which the method was tested was taken from the literature (Das and Seeley[14,15], Rowe and Davis[72]). The typical feature of shallow anchors is the formation of trumpet–shaped (often assumed straight) shear bands from the edges of the anchor plate to the soil surface. The authors found that the angle of dilatancy affected the shape of the failure surface. The angle of dilatancy, which can be described as the change in volume associated with the shear distortion of an element of granular material, varies from 0° for loose sand to about 20° for dense sand. Figure 1.36 shows the assumed failure mechanism: a truncated wedge inclined at the angle of dilatancy ψ. Figure 1.37 depicts the load–displacement curves for different initial stress conditions. The limit load is calculated from the expression:

$$P_u = P_1 + P_2 + P_3 \qquad (1.14)$$

where

P_1 is the weight of soil above the anchor,

P_2 is the weight of truncated wedge, and

P_3 is the shearing resistance along the shear band.

The break–out factor is;

$$\frac{P_u}{\gamma\ B\ L\ H} = 1 + \left[\frac{H}{B} + \frac{H}{L}\right] \tan\varphi \cos\varphi_{cv} \qquad (1.15)$$

where φ_{cv} is the friction angle at the critical density.

Figure 1.38 shows good agreement between the results given by the authors and those published by Rowe and Davis[72]. It would be interesting to see what would be the correlation between the predictions based on this theory and some experimental results for dense sand, because the sand used by Rowe and Davis is rather loose and in that case $\psi \simeq 0$.

b Linear (working load) studies:

The following theories consider the soil as an elastic medium. Although anchor displacements predicted by elastic theory cannot be reliable, an elastic stress distribution in the soil may be quite accurate as a first approximation at working load levels.

1/ E.N. Fox (1948):

Fox was among the first researchers to give a solution for a rectangular footing at depth H beneath the surface of a semi-infinite elastic mass of Young's modulus E and Poisson's ration ν. He used the solution given by Mindlin for a point load and integrated it over the surface of the footing. The area is considered to be uniformly loaded which presumes the footing to be flexible. Figure 1.39 shows the ratio of mean settlement of a footing at depth H to that of a surface footing (both flexible) versus $H/(ab)^{\frac{1}{2}}$ for particular values of ratio a/b, where a and b are the footing dimensions. Despite the fact that anchors are rigid and not flexible as supposed by the author this study shed light on the importance of the major geometrical variables.

2/ R.K. Rowe and J.R. Booker (1979):

Rowe and Booker used an analytical technique for the analysis of anchors of

general shape buried at depth H below the surface of an isotropic elastic soil layer (characterised by E and ν) which extended a further distance H' below the anchor as shown in Fig 1.40.

The stiffness $P/(D\,\delta E)$ of rigid circular anchors can be expressed as:

$$\frac{P}{D\ \delta\ E} = \frac{I_d\ (H/D = \infty)\ I_H}{1 - \nu^2} \qquad (1.17)$$

where P is the applied load, δ is the displacement of the anchor and I_d and I_H are given by Figures 1.41 and 1.42. Figure 1.41 shows that for $\nu = 0.3$ in a semi-infinite mass $I_d = 2.2$ and therefore $P/(D\,\delta E) \simeq 2.4\ I_H$. Figure 1.42 gives I_H as a function of depth ratio H/D and for different values of d/D and $\nu = 0.3$.

3/ A.P.S. Selvadurai (1981):

Selvadurai presented an analytical solution for the displacement of a rigid disk embedded in an elastic semi-infinite space using Betti's reciprocal theorem. The analysis of the bonded disk inclusion problem was restricted to a single half space ($z \geqslant 0$) in which the plane $z = 0$ is subjected to the mixed boundary conditions

$$\begin{aligned} u_r(r,0) &= 0 && r \geqslant 0 \\ u_z(r,0) &= w && 0 \leqslant r \leqslant \tfrac{1}{2} D \\ \sigma_{zz}(r,0) &= 0 && \tfrac{1}{2} D < r < \infty \end{aligned} \qquad (1.18)$$

The expression for the axial displacement u_z along the z-axis is:

$$u_z(0,z) = \frac{P}{8\ \pi\ G\ D\ (1-\nu)} \left[(3-4\nu)\ \tan^{-1}\left(\frac{D}{2z}\right) + \frac{D\ z}{2(D^2/4 + z^2)} \right] \qquad (1.19)$$

where G is the shear modulus.

The methodology adopted to illustrate the applicability of Betti's reciprocal theorem to the embedded disk is heuristic rather than rigorous. A rigorous treatment "requires proof of the applicability of Betti's reciprocal theorem for both exterior domains and concentrated loads" (Selvadurai).

4/ R.K. Rowe and J.R. Booker (1981):

A finite layer technique was used for the analysis of buried circular footings in

non− homogeneous, anisotropic elastic soils. The anchors were considered to be rigid and fully bonded to the soil and the soil was assumed to be either isotropic, or cross− anisotropic with a plane of isotropy parallel to the soil surface. Particular attention was paid to anchors in soils whose modulus increases linearly with depth ($E = E_0 + \mu z$), where μ is a constant (Fig 1.43). The behaviour of both isolated and multiple anchors was examined. In this method it was assumed that the deposit may be divided into a number of distinct layers $z_k \leqslant z \leqslant z_{k+1}$ in which the Poisson's ratio ν_k is assumed to be constant and the elastic modulus is assumed to vary exponentially with depth as:

$$E = E_k \exp \left[2 \mu_k (z - z_k) \right] \qquad (1.20)$$

where E_k is the elastic modulus at $z = z_k$

and μ_k is the variation of E with depth.

The analysis of a rigid anchor was achieved by subdividing the anchor into four uniformly loaded ring elements on which the pressure distribution was specified to be:

$$\begin{aligned} \sigma_z(r) &= \frac{1}{\pi D \left[\tfrac{1}{2} D^2 - r^2 \right]^{\frac{1}{2}}} && 0 \leqslant r \leqslant \tfrac{1}{2} D \\ \sigma_z(r) &= 0 && \text{elsewhere.} \end{aligned} \qquad (1.21)$$

The displacement δ of the anchor was written as:

$$\delta = \frac{P (1+\nu) (3-4\nu) M_{HD} R_N R_a}{8 (1-\nu) D E_a} \qquad (1.22)$$

where

E_a is the vertical Young's modulus in the anchor vicinity,

M_{HD} is an influence factor for the effect of embedment,

R_N is a correction factor for the effect of non− homogeneity,

R_a is a correction factor for the effect of anisotropy.

The coefficients M_{HD}, R_N and R_a are given in charts by the authors. For a homogeneous isotropic soil, the previous expression becomes:

$$\delta = \frac{P (1+\nu) (3-4\nu) M_{HD}}{8 (1-\nu) D E_a} \qquad (1.23)$$

and Figure 1.44 gives M_{HD} versus H/D for different values of H'/D and $\nu = 0.3$

where H' is the height of soil below the anchor.

Although this analysis should be commended for its rigour and comprehensiveness, it is unclear how the results of an elastic analysis would be applied in practice.

c Nonlinear (ultimate load) studies:

1/ J.R. Davie and H.B. Sutherland (1977):

Davie and Sutherland were the first to carry out a finite element analysis of ground anchors. Their data were based on experiments they had performed in the laboratory on "glyben" , a test clay composed of sodium bentonite and glycerine, and also a silty clay. Both shallow and deep circular anchors were studied by the authors. An axisymmetric finite element program using 200 constant strain rectangular elements was utilized. The behaviour of clay was assumed to be linear elastic– perfectly plastic. No cracking was assumed to occur under tensile stresses, but a gap was assumed between the anchor and the soil below. The yield stress in compression and the yield stress in tension were assumed to be equal, and undrained loading conditions were assumed. Contours representing the stress distribution obtained from a finite element analysis at both elastic and ultimate states were plotted (Fig 1.45). The values of ultimate uplift force obtained from shallow anchor tests in glyben were reported to range from 50% to 65% of the predicted values. In the contour plots, a singularity appears near the edges of the anchor due to the loading discontinuity. Some criticisms of this work are that the tensile yield stress should be different from the compressive yield stress and the boundaries are probably not distant enough. However, the difference in the stress distribution between elastic and ultimate states is particularly interesting.

2/ H. Ito and Y. Kitahara (1982):

The numerical analyses performed by Ito and Kitahara were compared with laboratory and in-situ tests carried out by the authors on cohesionless and clayey soils. A three dimensional finite element analysis of a "dentiform" footing was carried out by the authors. The stress-strain relations used in the finite element analysis were based on triaxial tests carried out on the material. The numerical results appear to be in good agreement with both laboratory and field test data (Fig 1.18). For simplicity, a formula of Matsuo's type was proposed for use with dentiform anchors.

3/ R.K. Rowe and E.H. Davis (1982):

This numerical analysis was based on the experimental work described previously. A "k_4 failure load" was adopted for deep anchors. This so-called k_4 failure load is the load which produces four times the displacement that would have occured if the soil had remained elastic. The analysis was performed for plane strain as well as axisymmetric conditions. The Mohr-Coulomb failure criterion was assumed. The finite element mesh consisted of 670 to 1200 constant strain elements under the boundary conditions shown in Figure 1.20. The authors concluded that soil dilatancy and anchor roughness affect significantly the anchor capacity and the effect of in-situ stresses is significant only for soils with small dilatancy. An expression for the anchor capacity was proposed:

$$p_u = \gamma H F_\gamma R_\psi R_r R_k \qquad (1.26)$$

where F_γ, R_ψ, R_r and R_k are correction factors for friction angle, dilatancy, anchor roughness, and initial stress state respectively. The authors predictions were compared with those of Das and Seeley[14,15]. Since the authors and Das & Seeley performed their tests on loose sands, their predictions should be closer for $\psi = 0$ than for than for $\psi > 10°$, but this is not the case.

4/ P.A. Vermeer and W. Sutjiadi (1985):

These elasto-plastic finite element computations were performed to check the assumptions made by the authors in the semi-empirical theory based on the failure

mechanism represented in Figure 1.36. The material has a shear modulus G, a Poisson's ratio ν, angle of internal friction φ and angle of dilatancy ψ and the computer program simulates the localisation of deformation in shear bands. The anchor problem is schematized to a passive trap door problem. First, stresses due to the weight of the soil are computed and then the trap door is lifted in a number of displacement increments. The two curves in Figure 1.37 represent the load–displacement relation for a shallow anchor (H/D = 3.33) for two different Poisson's ratios (ν= 0.33 and ν= 0.49) and thus two different values of initial horizontal stress. High initial horizontal stresses apparently give rise to softening behaviour associated with a high peak load.

5/ C.S. Desai et al (1986):

A mesh of 352 eight–noded isoparametric hexahedral elements was used in this finite element analysis. A thin layer interface element was also used to simulate the interaction behaviour between anchor and soil. The computed tensile stresses in the interface and in the soil around the anchor were evaluated at every incremental load, converted into equivalent nodal loads and redistributed to the surrounding medium. A constitutive model that allowed for plastic hardening, volume change, and stress path dependency was used for soil. The yield function was given by:

$$f = J_2 + \alpha I_1^2 - \beta I_1 (I_3)^{1/3} - \gamma I_1 = 0 \qquad (1.27)$$

where

J_2 is the second invariant of the deviatoric stress tensor,

I_1, I_3 are the first and third invariants of the total stress tensor,

α, β, γ are material response functions.

The constitutive matrix for the interface consisted of normal and shear components within a nonlinear elastic model. The moduli E and ν for the normal behaviour were identical to those of the sand, and a Mohr–Coulomb failure criterion was assumed. The coefficient of earth pressure at rest K_0 was taken as:

$$K_0 = \nu / (1 - \nu) \qquad (1.28)$$

Three finite element analyses were performed by assuming the sand behaviour to be

linearly elastic, elasto–plastic without interface and elasto–plastic with interface. Figures 1.28 and 1.29 represent the load–displacement curves at fixed and free anchor heads, respectively. They show that larger values of displacements are predicted by the finite element analysis than those observed on field.

6/ Cragg et al (1986):

This is an analysis of another type, a probability–based method for designing foundations. Hypothetical variations in weather induced load and strength of a tower foundation is represented in Figure 1.46. The shaded area in the region where these two distributions overlap, an area where load on the foundation may exceed its strength, represents the probability of foundation failure. Three modes of loading were considered in the design. Wind, ice and wind–on–ice load distributions were expressed by the Gumbal type–1 equation:

$$F(P_u) = \exp\left[- \exp \frac{B - P_u}{C} \right] \qquad (1.29)$$

where

$F(P_u)$ is the cumulative probability of failure,

P_u is the extreme weather induced load,

B, C are location and scale parameters.

The foundation uplift strength was assumed to follow the normal distribution which is expressed by:

$$F(S) = \frac{1}{\chi\ (2\pi)^{\frac{1}{2}}} \exp\left[- \frac{1}{2} \left(\frac{S - \nu}{\chi} \right) \right] \qquad (1.30)$$

where

F(S) is the probability that strength will not exceed S,

S is the foundation uplift strength,

μ is the mean value of S, and

χ is the standard deviation of S.

A data base consisting of 160 test results was assembled. The ultimate uplift capacity P_u was computed from Meyerhof and Adams's expression:[52]

$$P_u = \tfrac{1}{2}\ \gamma\ \pi\ D\ H^2\ K_u\ \tan\varphi + W \qquad (1.31)$$

A normal distribution for foundation strength can be constructed by using:

$$\underline{P}_u = \tfrac{1}{4} \left(P_{u++} + P_{u+-} + P_{u-+} + P_{u--} \right) \qquad (1.32)$$

and the standard deviation of ultimate uplift capacity is :

$$\chi_{pu} = \left[\tfrac{1}{4} \left(P_{u++}^{\,2} + P_{u+-}^{\,2} + P_{u-+}^{\,2} + P_{u--}^{\,2}\right) - \underline{P}_u^{\,2} \right]^{\frac{1}{2}} \qquad (1.33)$$

where $P_{u\pm\pm} = \tfrac{1}{2} \gamma \pi D H^2 (K_u \pm \chi) \tan(\varphi \pm \chi_\varphi) + W.$ (1.34)

The authors concluded through an example that tower foundations are over-dimensioned in the Ontario region. However, more investigations need to be made with other types of probability distribution and other theories than that due to Meyerhof and Adams[52].

1.3 CONCLUSIONS:

a. Experimental work and semi-empirical theories:

Many authors have considered very specific conditions and attempted to derive general theories for pull-out capacities of anchors. Some authors even considered one type of soil in a certain state (dense or loose) and have given general formulae for the shape of the failure surface and anchor capacity. For instance Balla[1], Mariupol'skii[47], and Matsuo[49] carried out tests on dense sand and proposed theories for general use. Fadl[26] pointed out the important effect of the relative density but did not separate it from the effect of friction angle. A wider range of types of sand need to be tested and a wider range of parameters need to be examined in laboratory studies. Field tests are in general costly and laborious but these data are essential since scale effects seem to have some influence on pull-out capacity .

Table 1.4 summarises the present situation of anchor design through the predictions made by some authors since 1961.It shows the large differences in the calculated anchor uplift capacities and therefore the uncertainties in current design practice.

Table 1.4 Predicted anchor uplift capacities:

Theory	$\frac{p_u}{\gamma H}$ for $\frac{H}{D} = 3$	
	$\varphi = 25°$	$\varphi = 45°$
Balla	8.0	10.3
Mariupol'skii	3.3	9.2
Matsuo	9.2	15.0
Meyerhof and Adams	3.3	14.4
Vesic	4.3	7.0
Fadl	2.0	20.0
Rowe and Davis	2.4	6.2
Vermeer and Sutjiadi	1.8	2.6

Note: p_u is the mean anchor pressure.

b. Linear analysis:

The behaviour of sand is not elastic. Although several sophisticated elastic analyses of anchors have been reported the major difficulty is that elastic analysis is based on small deformations of a loaded body and therefore such analyses are restricted at best to working load behaviour of anchors.

c. Finite element analysis:

Few finite element analyses have been carried out. Some of these analyses were performed on very fine meshes using constant strain elements, eg Rowe and Davis[72], which makes them rather costly. These finite element analyses appear to be improving. The reported difference between the observed and the calculated ultimate values were about 50% in 1977 by Davie and Sutherland, and were reported to be less than 10% in 1986 by Desai and co-writers. Whether true predictions, as opposed to interpretation of available test data, can be made to this level of accuracy remains problematic. The major difficulty in the finite element analysis arises in the modelling of the constitutive relations.

d. Probability–based analysis:

Probabilistic methods such as the one proposed by Cragg et al[13] have value in identifying the likely range of uncertainty in predictions of anchor capacity. However it has not yet been established whether deterministic analyses (on which the probability method is based) provide accurate solutions.

1.4 OBJECTIVES:

The primary objective of this thesis is to identify and resolve the major difficulties in the numerical analysis of the pull–out capacity of anchors.

At the outset, a study of the elastic stress distribution around anchors, incorporating the influence of embedment depth, anchor shape and soil parameters, will be conducted to develop some insight into the mechanics of soil–anchor interaction. Thereafter, constitutive models for sand are examined and their behaviour under various loading conditions simulated by computer.

The final stage is the finite element analysis of the pull–out resistance of deep and shallow circular anchors. In this analysis , the influence of the soil properties on the uplift capacity of the anchor will be studied and the progressive mechanism of failure occuring in the soil mass, for both shallow and deep anchors, will be followed during the loading history.

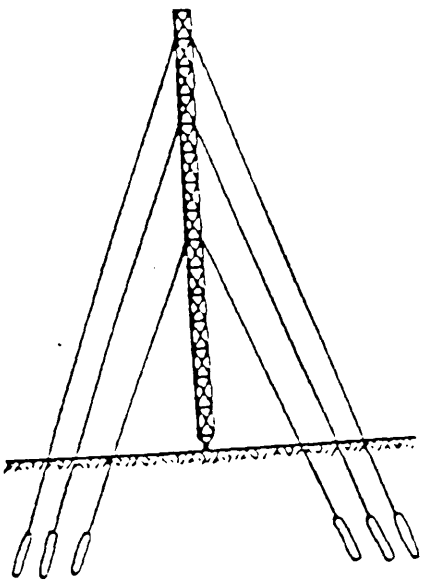

Radio transmission mast

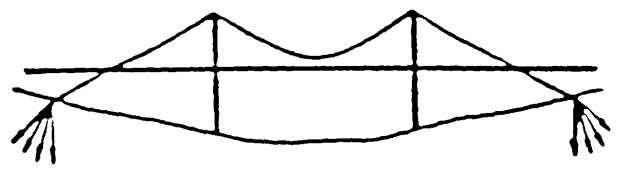

Cable suspension

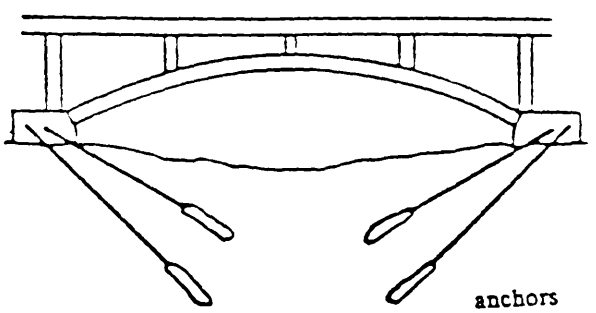

Arch bridge

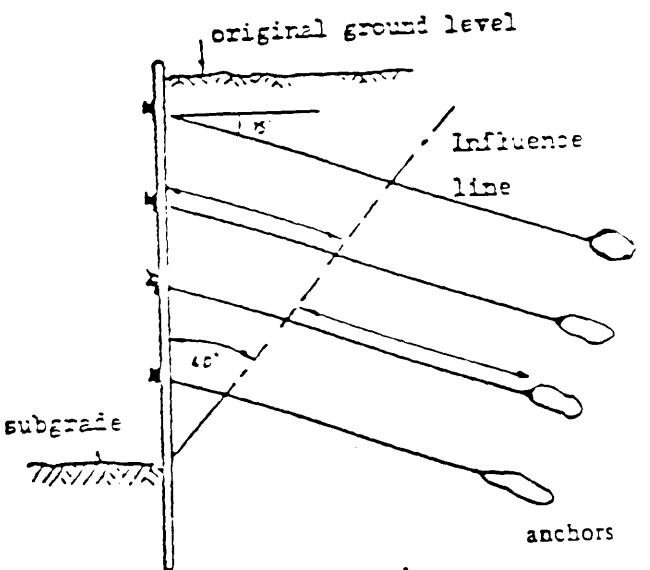

Supporting deep excavation

Fig 1.1 Some uses of ground anchors.

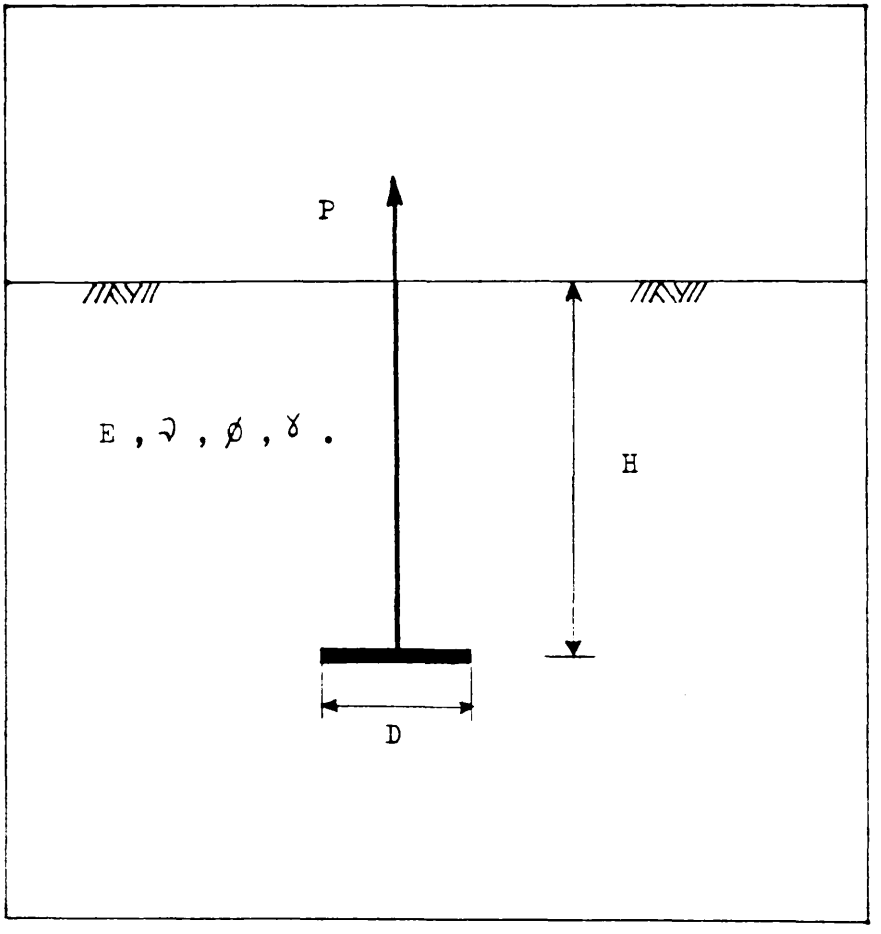

Fig 1.2 Soil-anchor system.

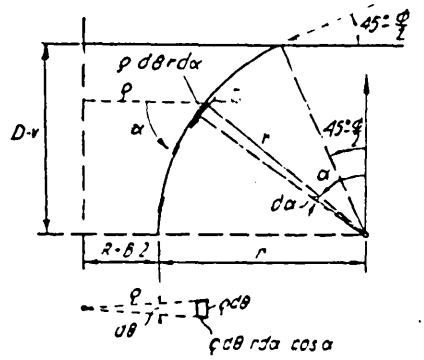

Fig 1.3 Proposed slip surface, Balla 1961.

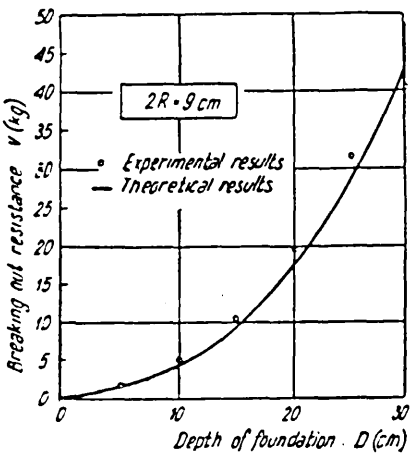

Fig 1.4 Comparison of theoretical and model test results, Balla 1961.

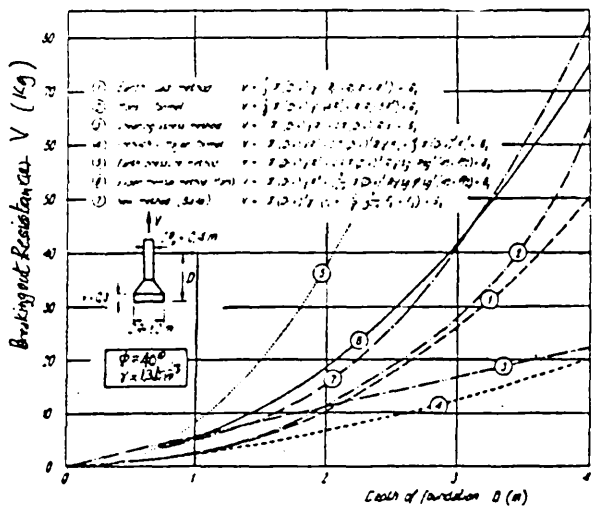

Fig 1.5 Comparison of methods of calculation, Balla 1961.

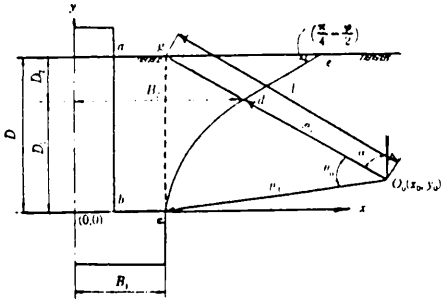

Fig 1.9 Proposed slip surface, Matsuo 1968.

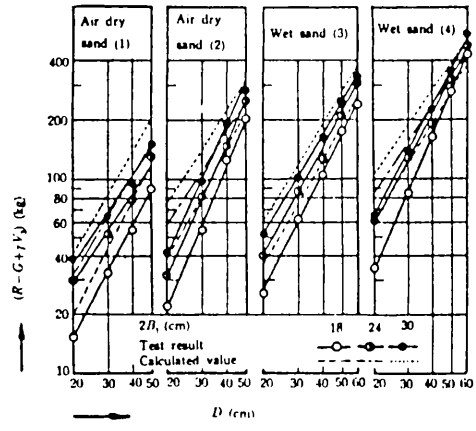

Fig 1.10 Pull out resistance versus anchor depth, Matsuo 1968.

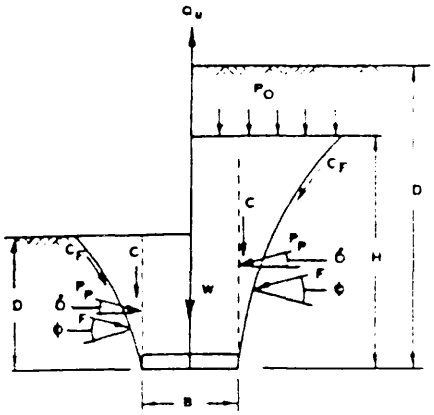

Fig 1.11 Proposed failure surface for deep and shallow strip anchors, Meyerhof & Adams 1968.

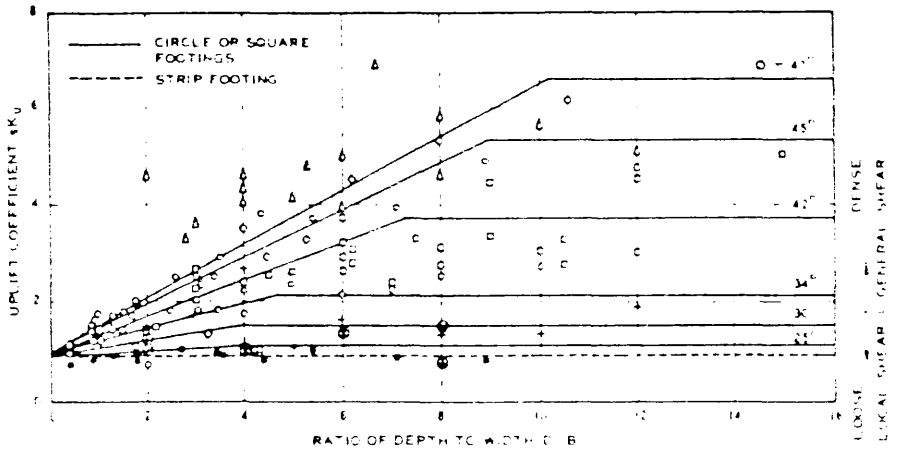

RECENT DATA - RECTANGULAR FOOTINGS SLENDER SHAFTS - MEYERHOF

⊗ DENSE
⊕ LOOSE

PUBLISHED DATA - CIRCULAR FOOTINGS SLENDER SHAFTS

- o DENSE SILICA SAND ADAMS AND HAYES 1967
- ◇ DENSE CONCRETE SAND ADAMS AND HAYES 1967
- □ DENSE SILICA SAND BAKER AND KONDER 1966
- △ DENSE SAND MACDONALD 1963
- • LOOSE SILICA SAND ADAMS AND HAYES 1967
- + LOOSE SAND MACDONALD 1963

1" TO 4" DIAMETER

Fig 1.12 Comparison of theory and model tests in sand, Meyerhof & Adams 1968.

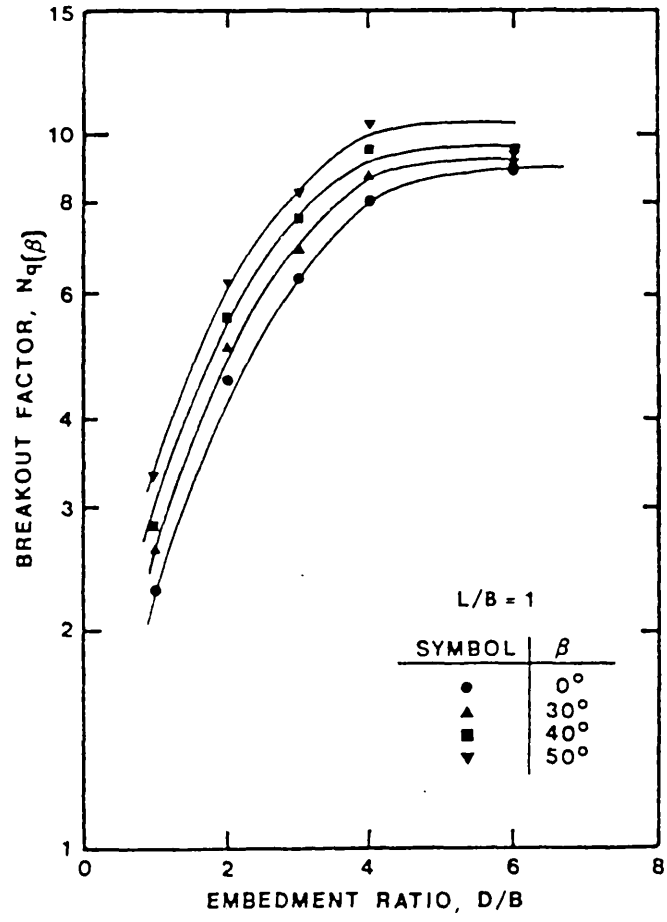

Fig 1.13 Breakout factor for square anchor, Das & Seeley 1977.

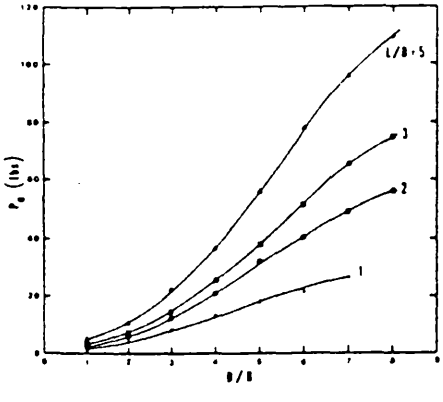

Fig 1.14 Breakout load of shallow rectangular anchors, Das & Seeley 1975.

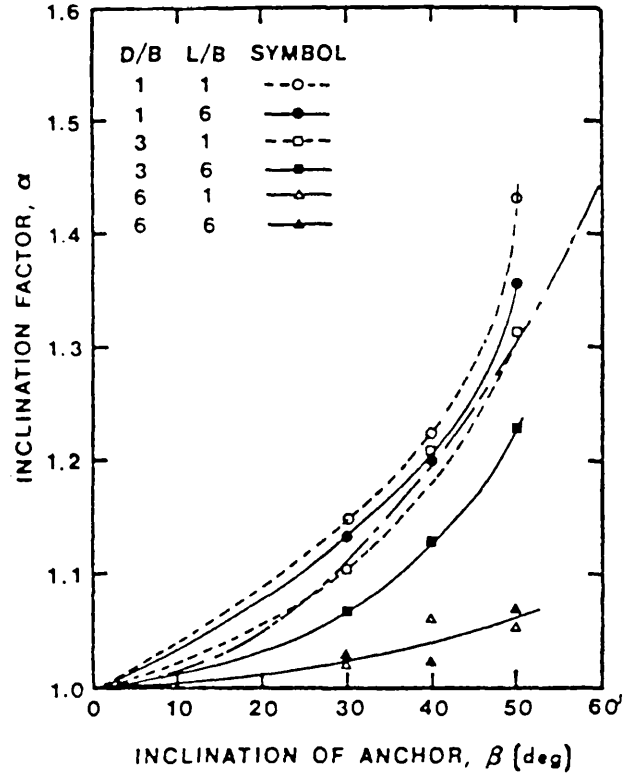

Fig 1.15 Variation of inclination factor with anchor inclination, Das & Seeley 1977.

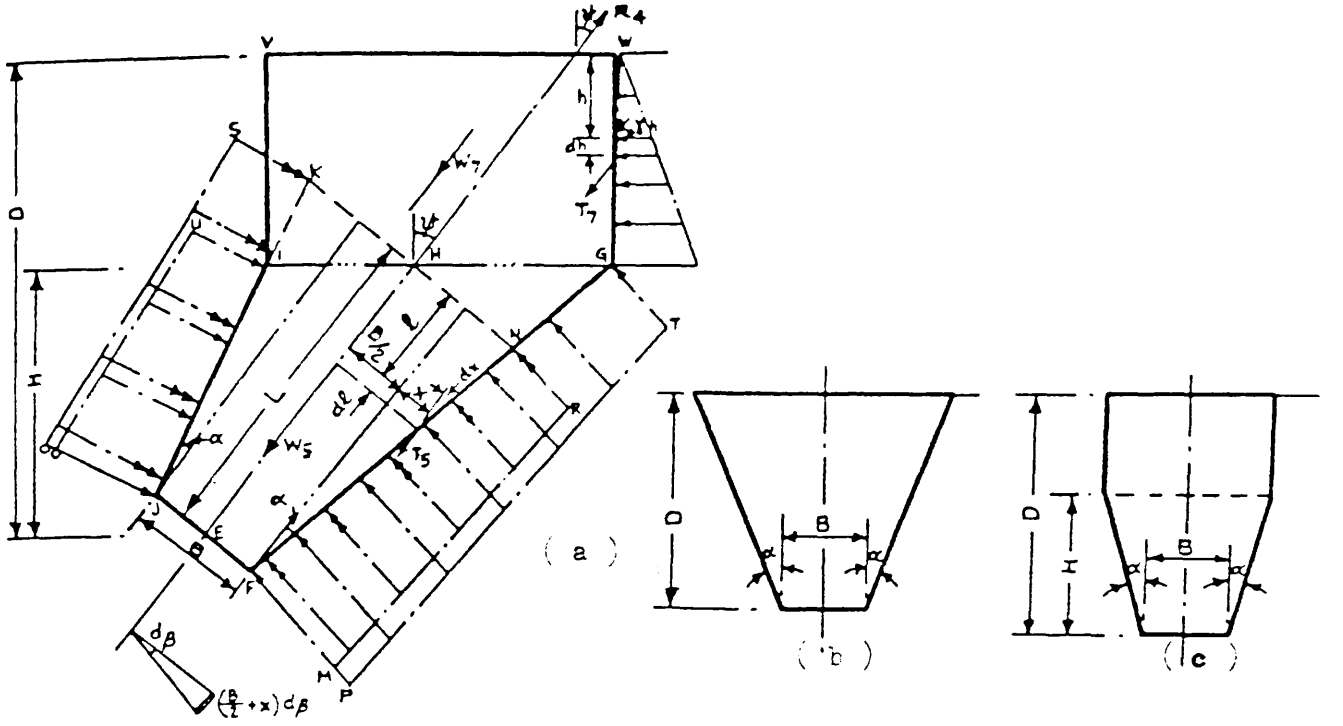

Fig 1.16 Proposed failure surface for deep and shallow circular anchors, Fadl 1981.

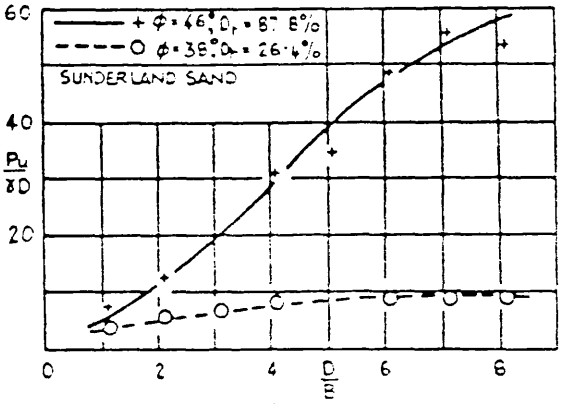

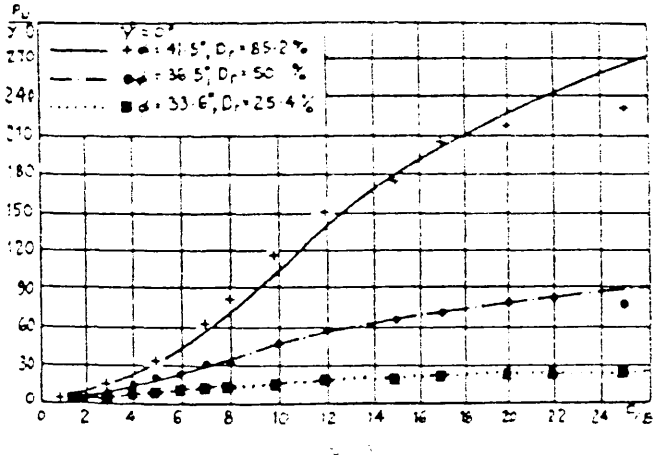

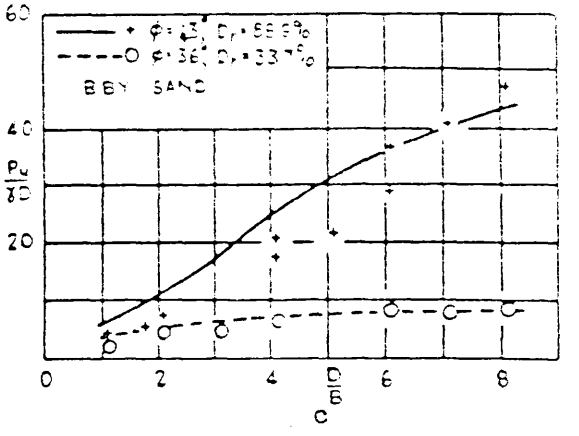

Fig 1.17 Dimensionless [illegible] anchors in dense sand, Fadl 1981.

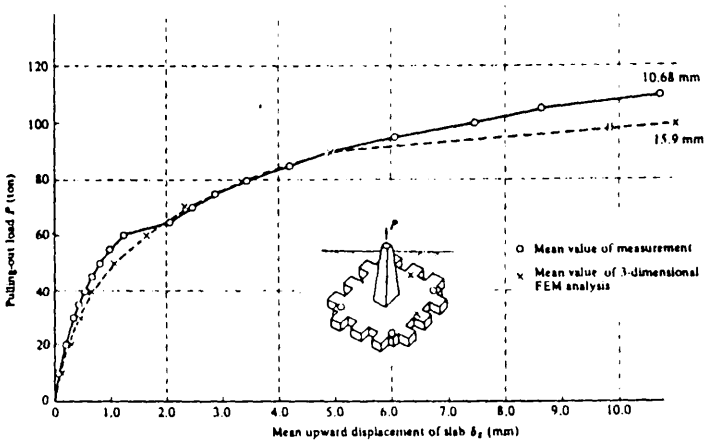

Fig 1.18 Comparison of F.E.M. and experimental results, Ito & Kitahara 1982.

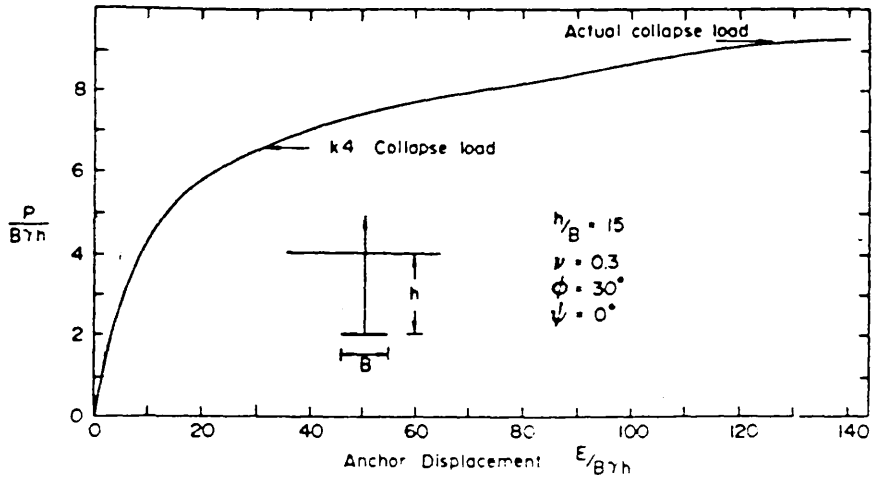

Fig 1.19 Load-displacement curve by F.E.M. , Rowe & Davis 1982.

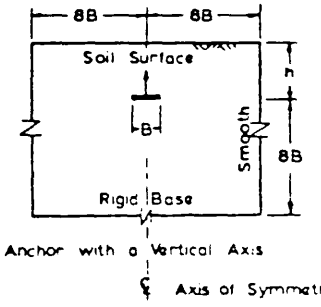

Fig 1.20 Boundary conditions for F.E.M. analysis, Rowe & Davis 1982.

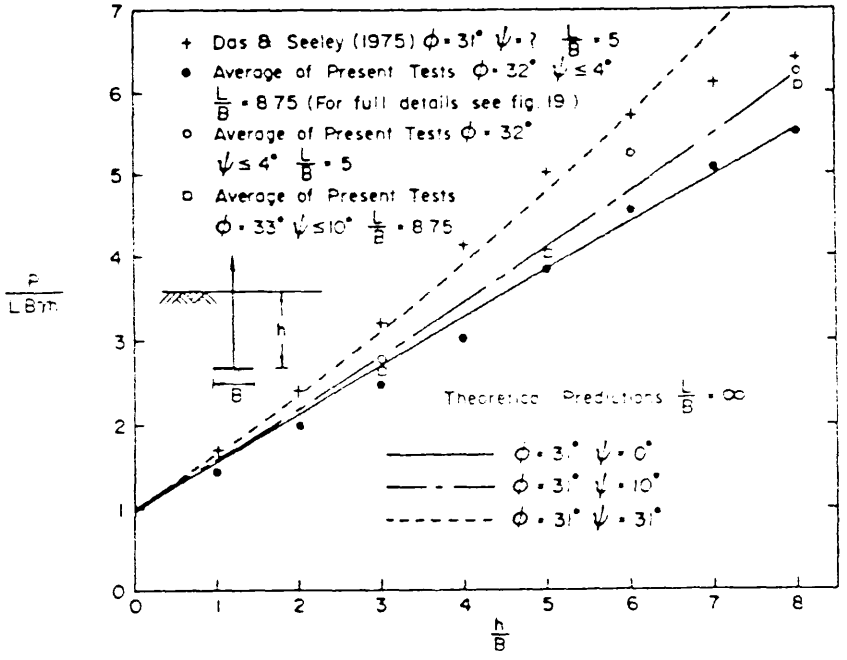

Fig 1.21 Comparison of experimental and theoretical collapse loads, Rowe & Davis 1982.

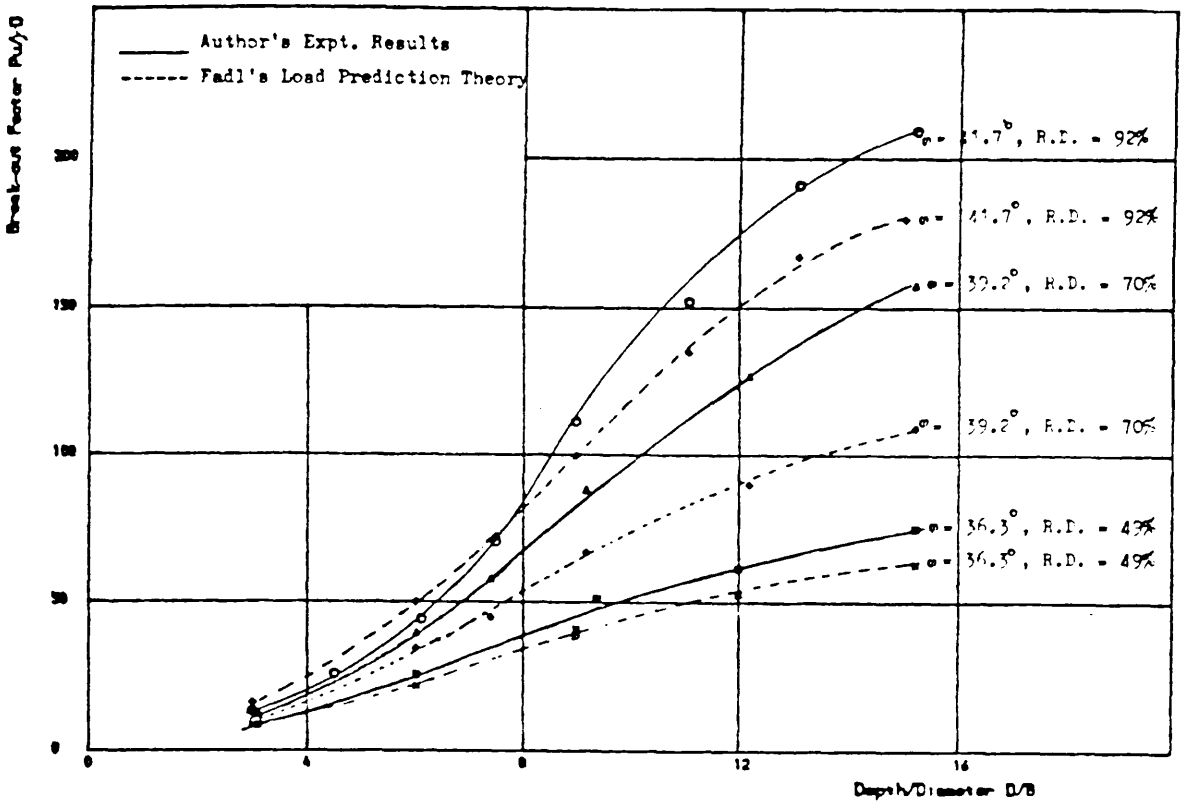

Fig 1.22 Comparison of test results with Fadl's predictions, Dakaria, 1986.

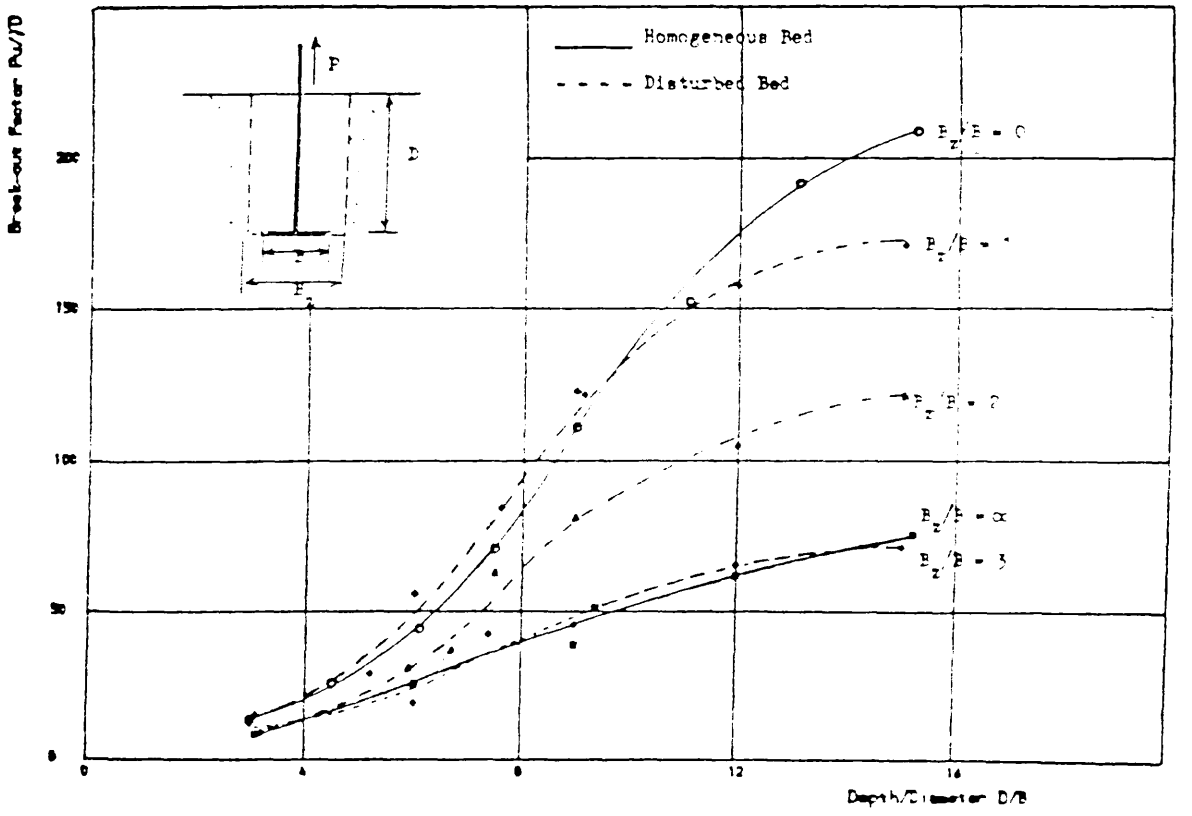

Fig 1.23 Effect of disturbed sand bed on uplift capacity, Dakaria, 1986.

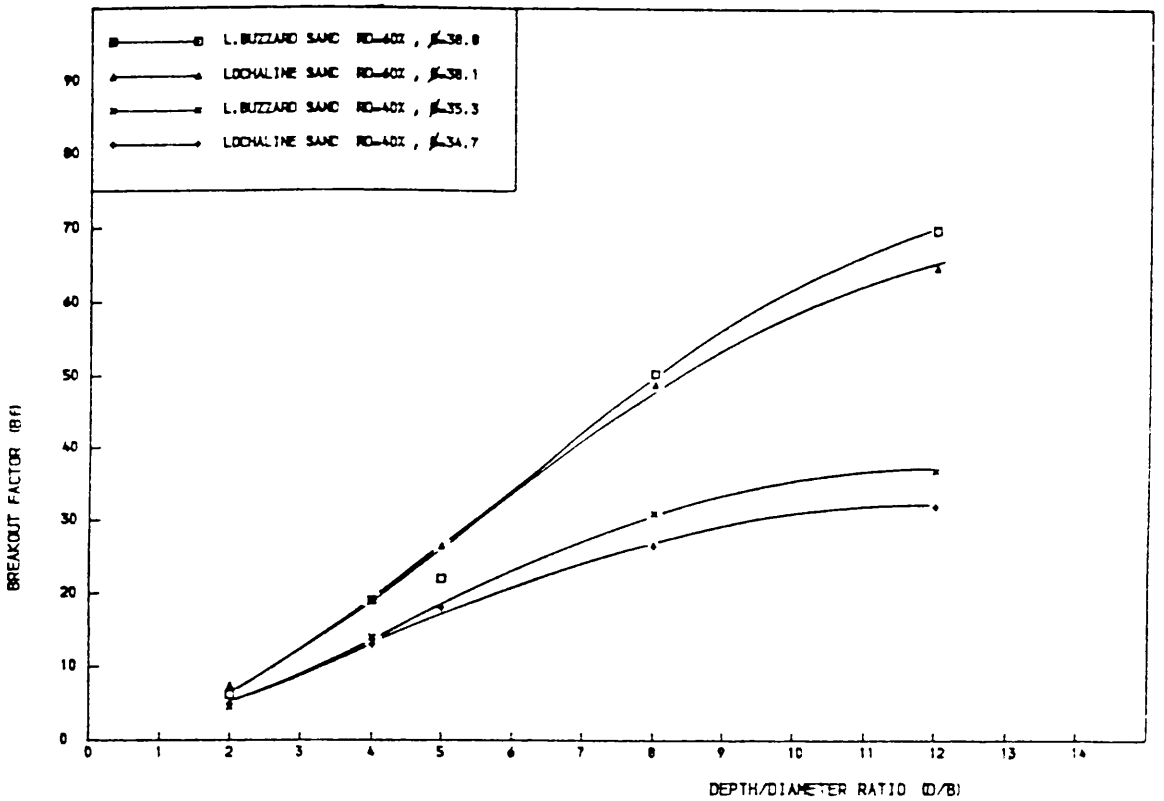

Fig 1.24 Effect of friction angle on anchor capacity, Bouazza 1988.

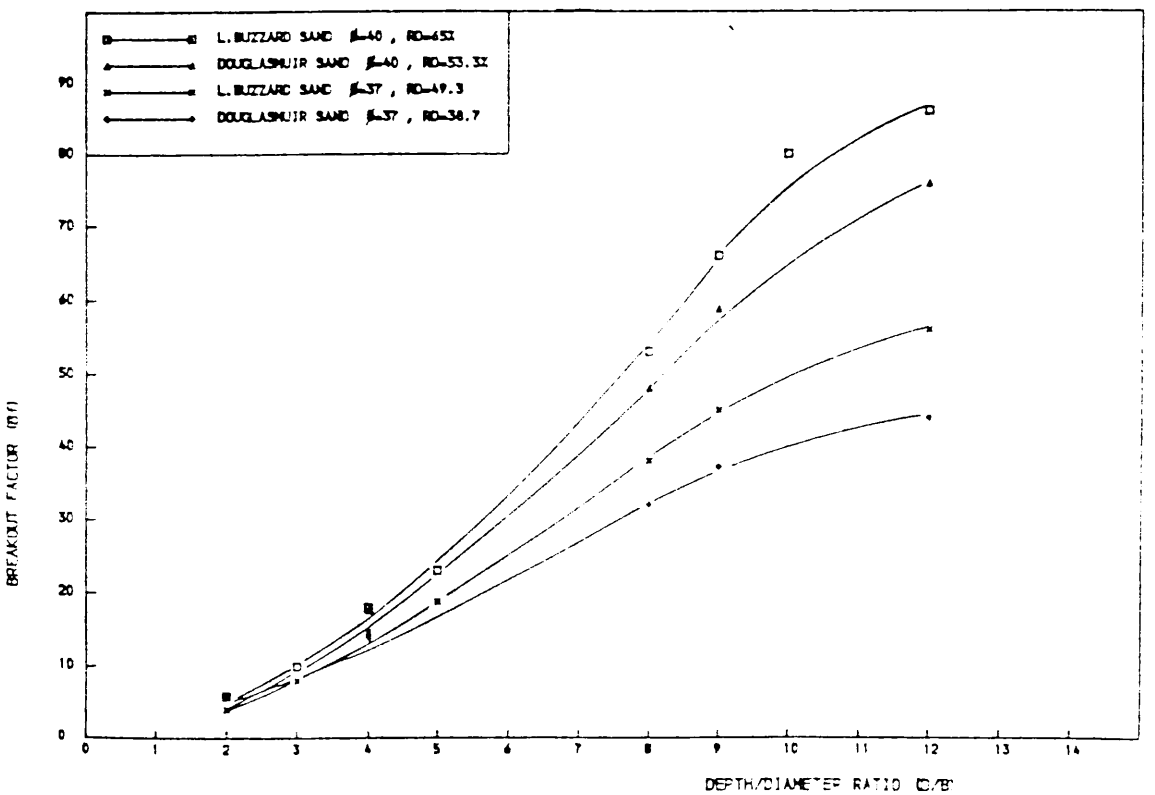

Fig 1.25 Effect of relative density on anchor capacity, Bouazza 1988.

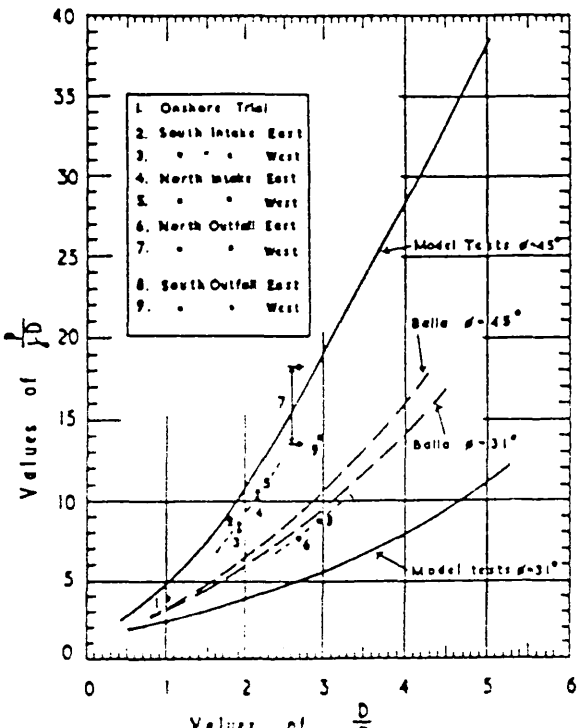

Fig. 1. Comparison of Silvester's results with Balla's theory, Silvester (1964).

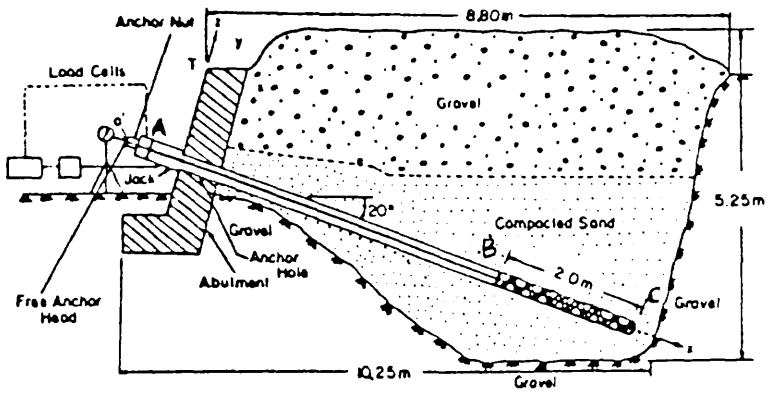

Fig 1.27 Elevation of anchor-soil system, Desai et al1984.

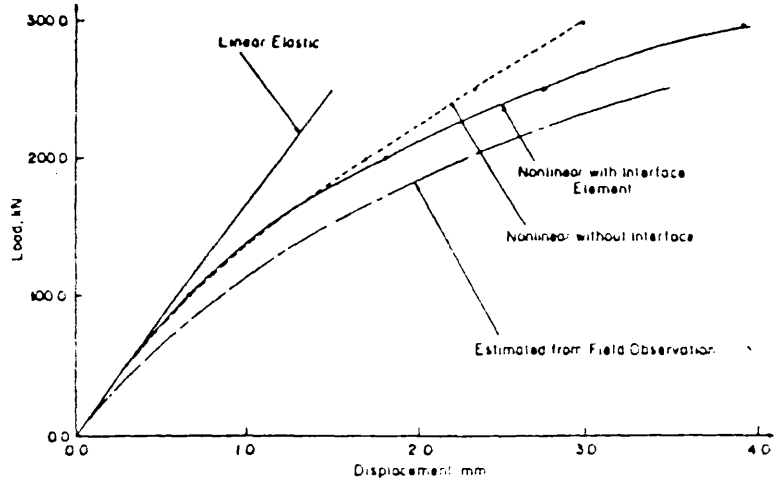

Fig 1.28 Load-displacement for fixed anchor head (point B in Fig 1.27, Desai et al 1986.

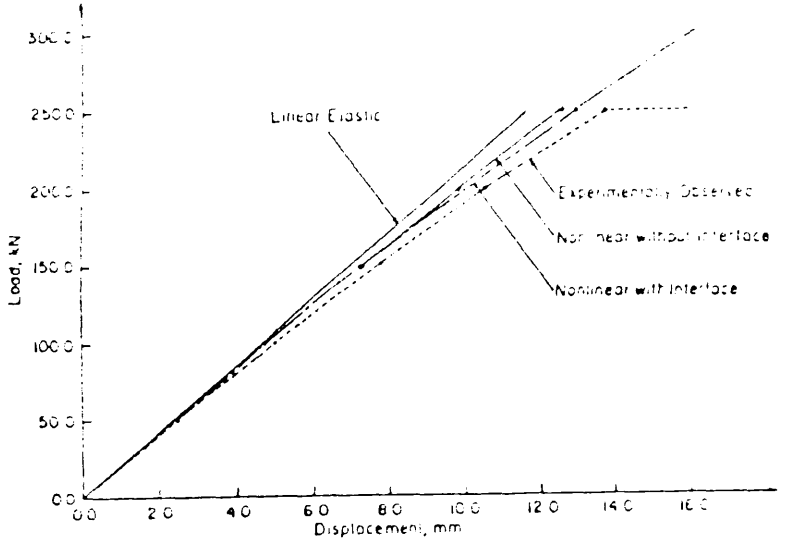

Fig 1.29 Load-displacement [illegible] Desai et al 1984.

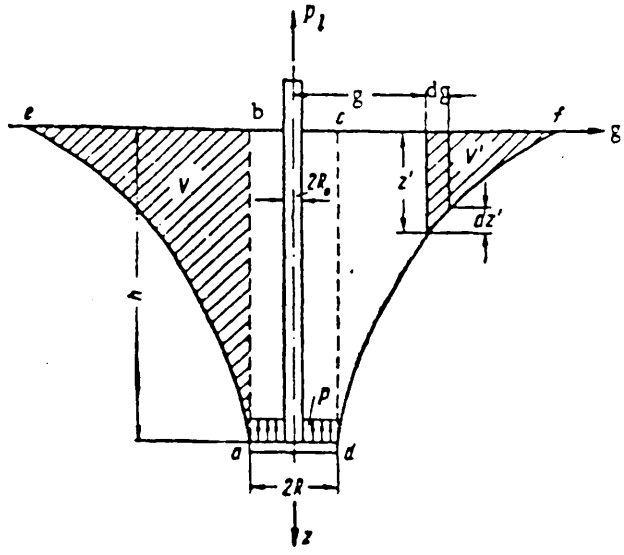

Fig 1.30 Proposed failure surface for shallow anchor, Mariupol'skii 1965.

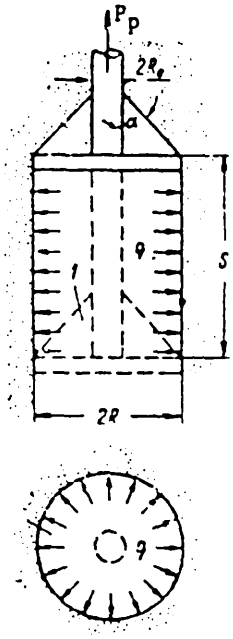

Fig 1.31 Design diagram for deep anchor, Mariupol'skii 1965.

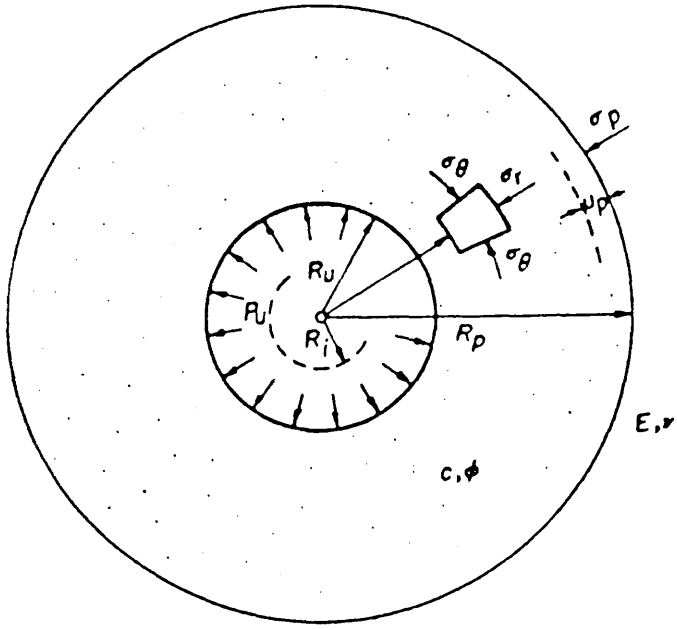

Fig 1.[illegible] Expansion of cavity, Vesic 1972.

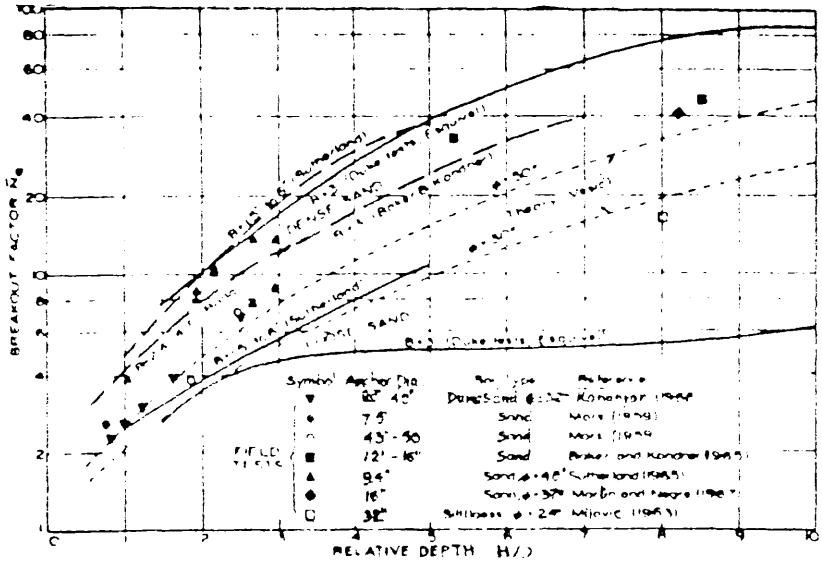

Fig 1.[illegible] [illegible] Breakout Factor [illegible] Vesic 1971.

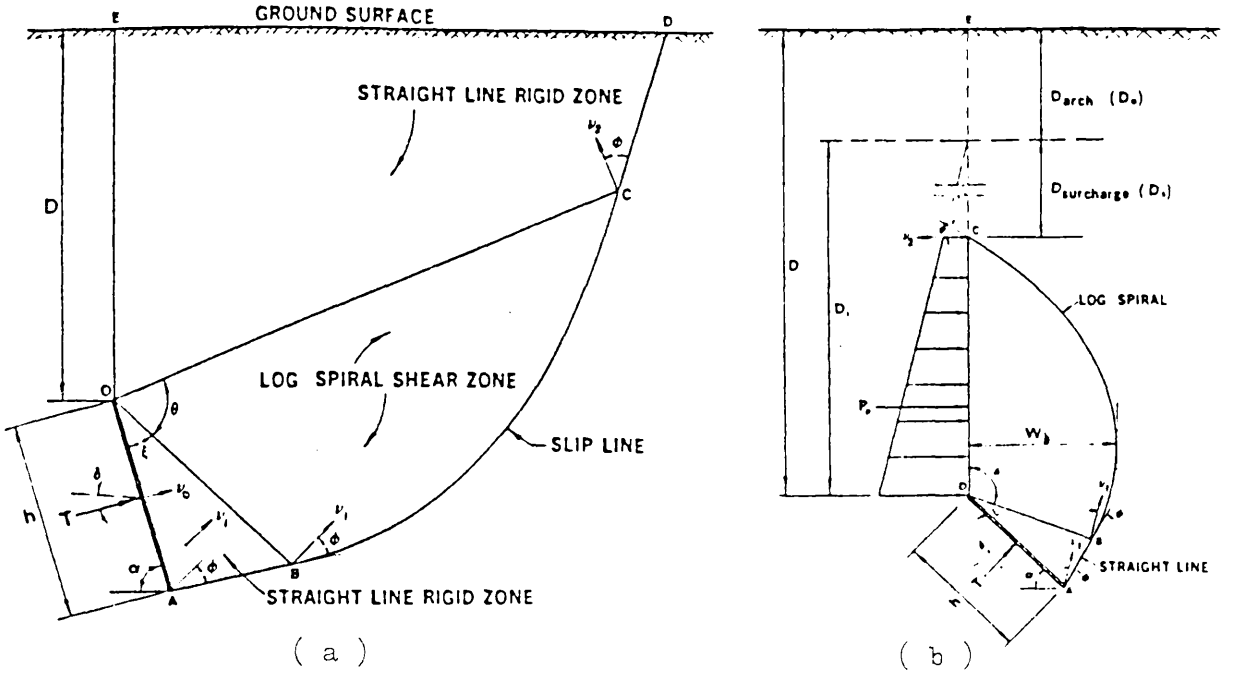

Fig 1.34 Proposed failure surface for shallow (a) and deep anchor (b), Wang & Wu 1982.

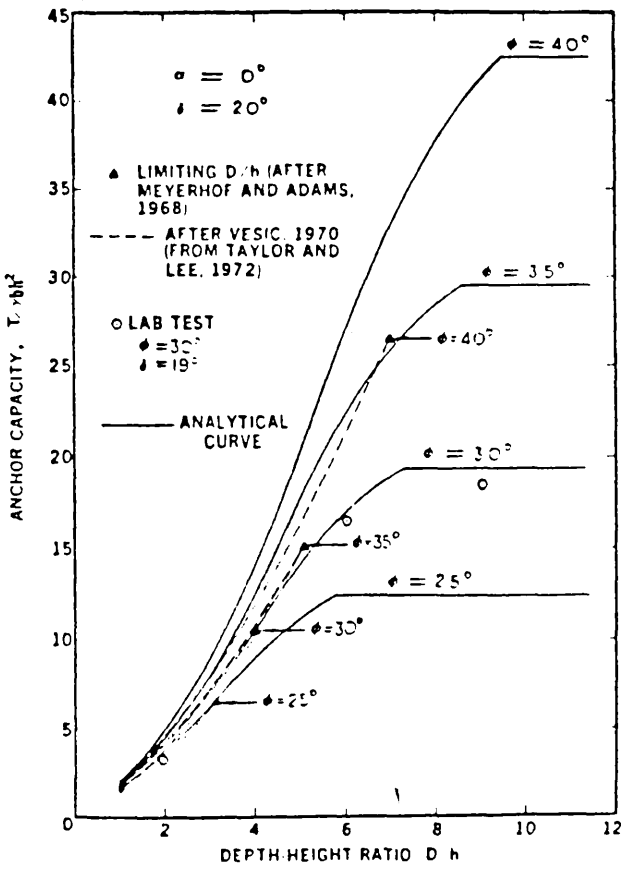

Fig 1.35 Theoretical and experimental anchor capacity, Wang and Wu 1982.

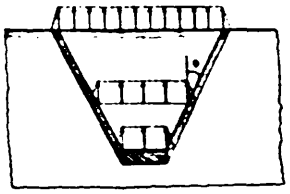

Fig 1.36 Proposed failure mechanism for shallow rectangular anchors, Vermeer & Sutjiadi 1985.

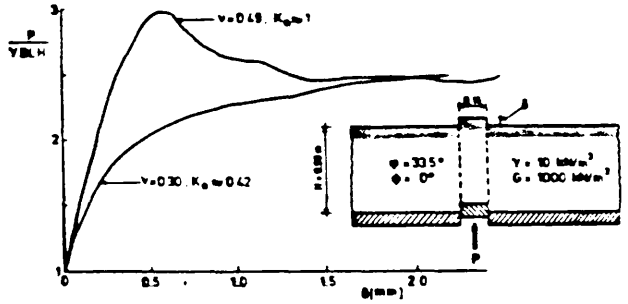

Fig 1.37 Computed load deflection curves, Vermeer & Sutjiadi 1985.

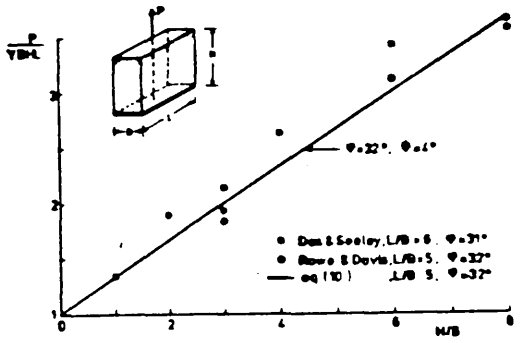

Fig 1.38 Comparison of experimental and theoretical limit loads, Vermeer & Sutjiadi 1985.

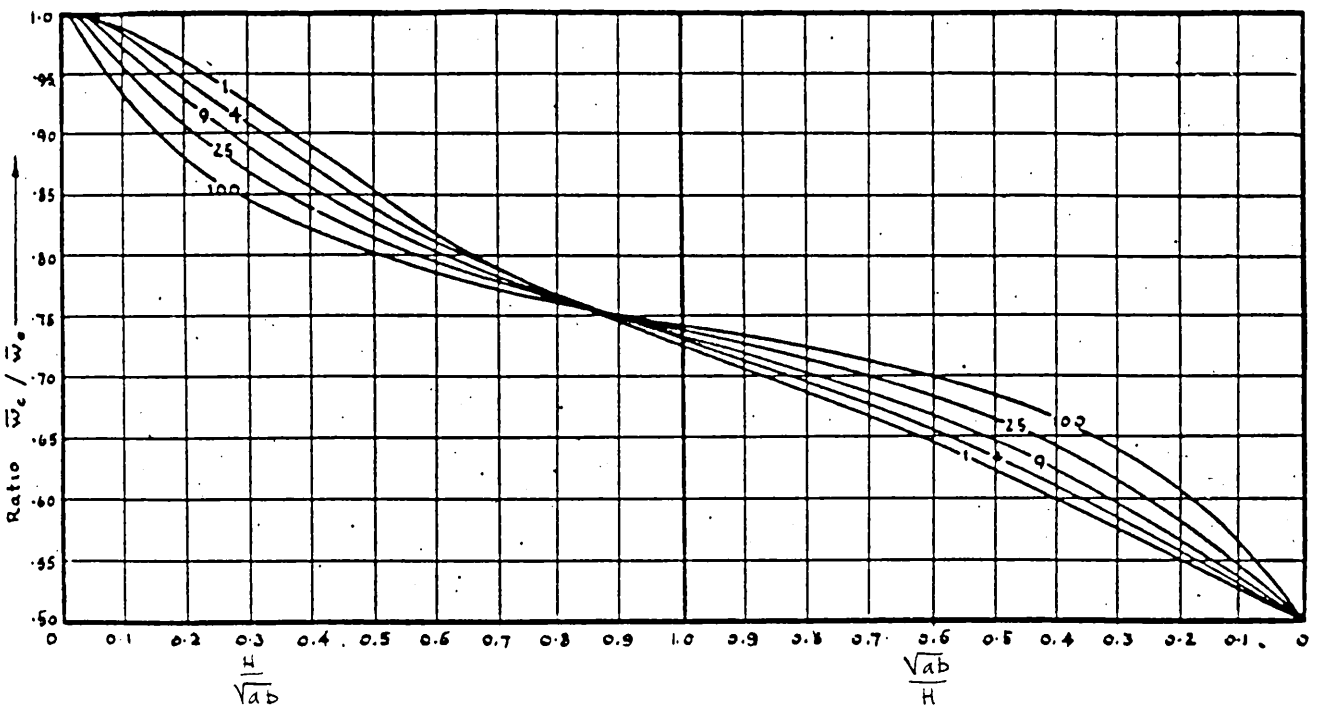

Fig 1.39 Mean settlement versus depth ratio, Fox 1948.

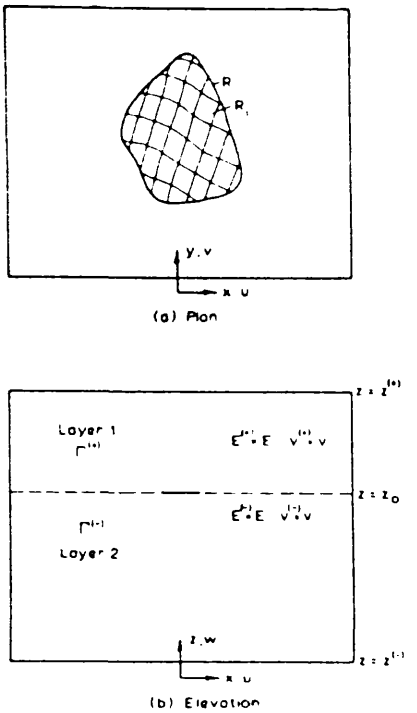

Fig 1.40 Problem configuration of ground anchor, Rowe & Booker 1979.

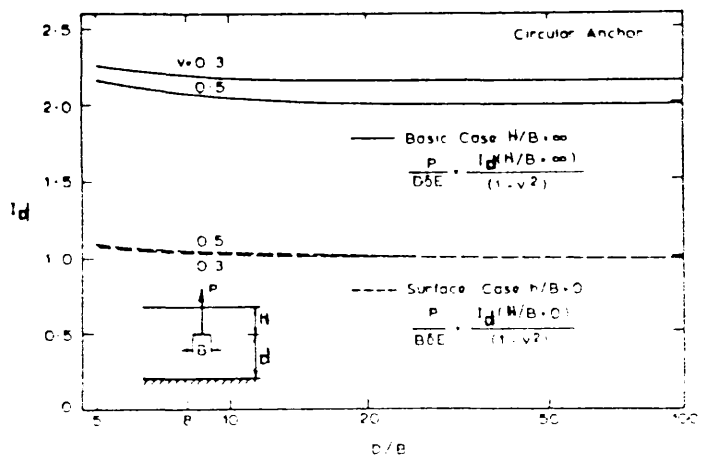

Fig 1.41 Effect of base condition on stiffness, Rowe & Booker 1979.

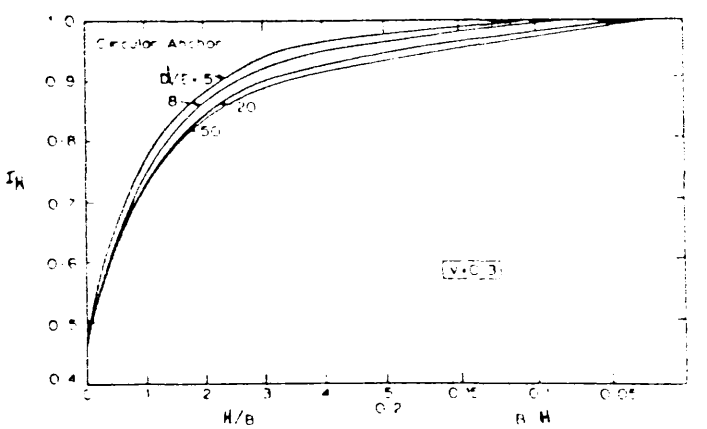

Fig 1.42 Effect of embedment ratio, Rowe & Booker 1979.

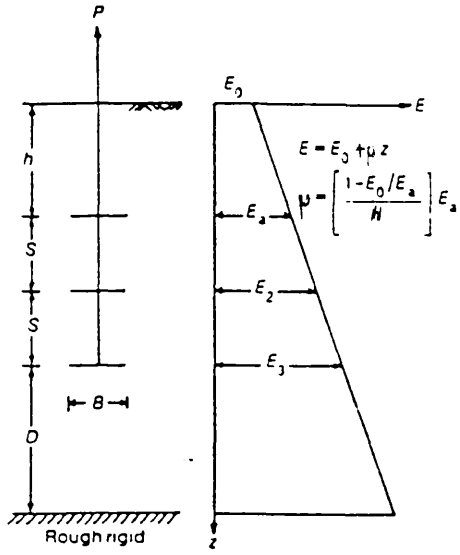

Fig 1.43 Approximation function for Young's modulus, Rowe & Booker 1981.

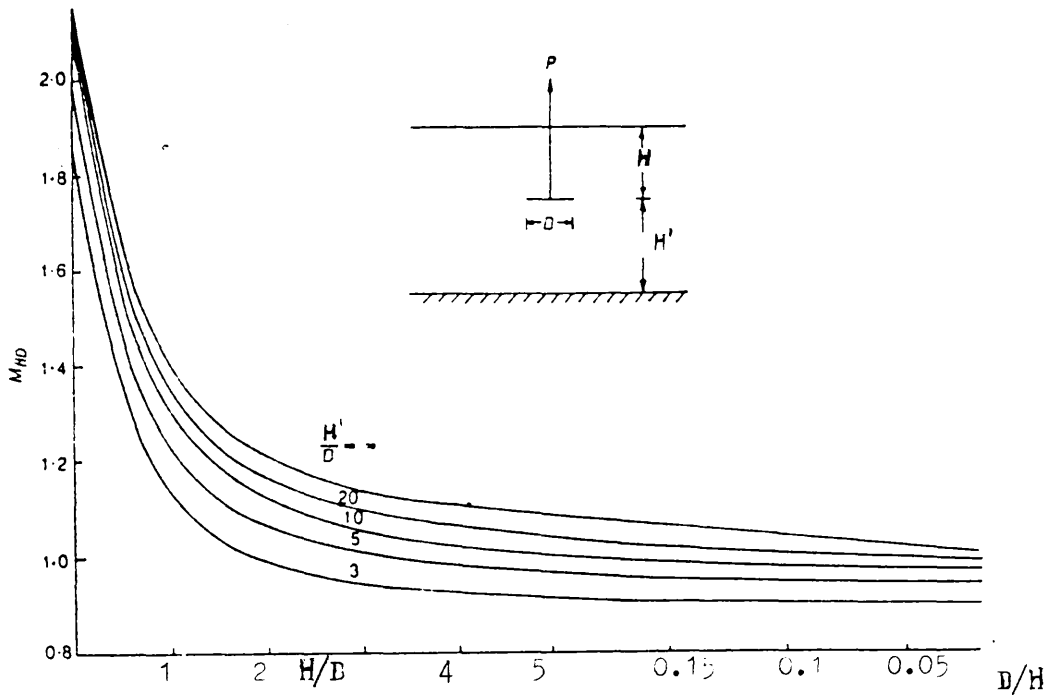

Fig 1.44 Effect of embedment and layer depth, Rowe & Booker 1981.

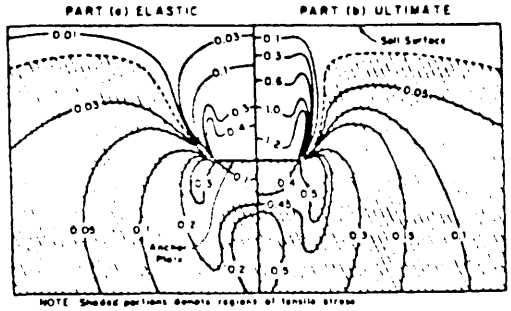

(a) Vertical stress.

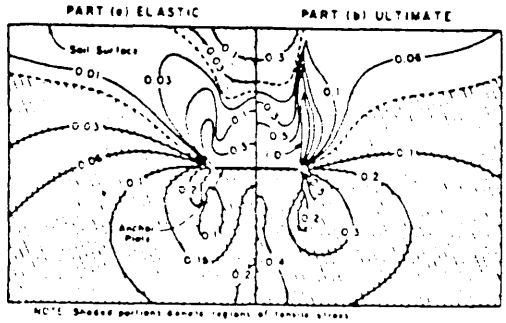

(b) Radial stress.

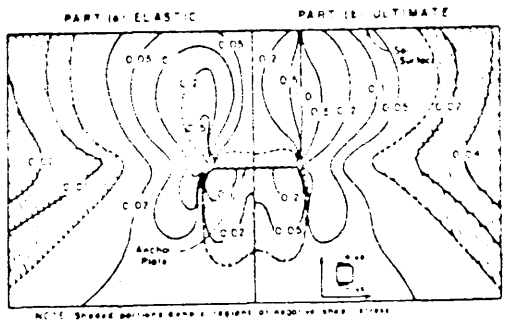

(c) Shear stress.

Fig. 1.4 Elastic and ultimate stress distribution, Davis & Sutherland [14].

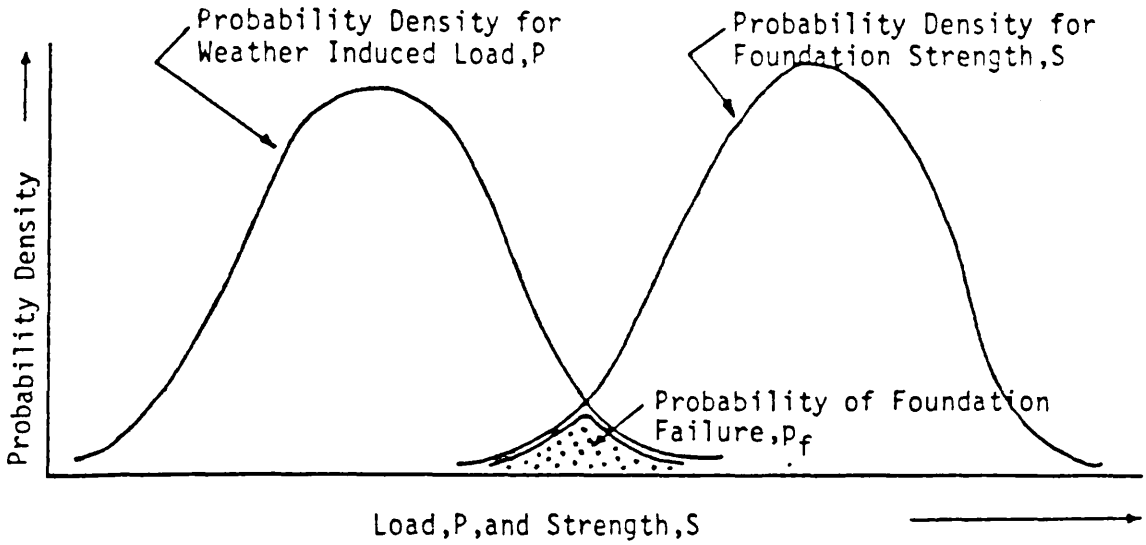

Fig 1.46 Probability of failure of a foundation under induced weather load, Cragg et al 1981.

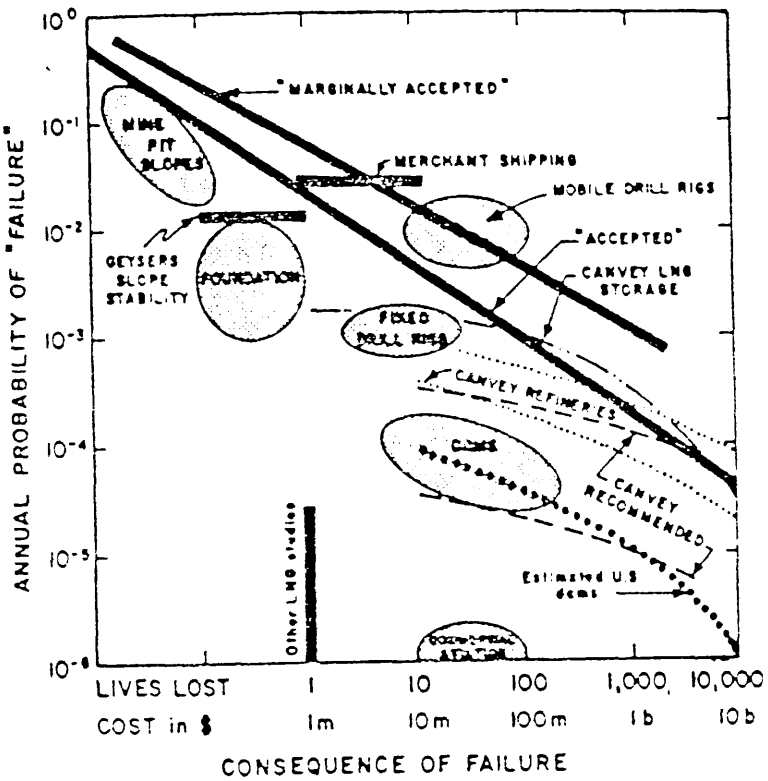

Fig 1.47 Risks for selected engineering projects, Cragg et al 1981.

2.1 INTRODUCTION :

In this analysis, the soil is assumed to be elastic, homogeneous and isotropic. It is assumed to sustain tensile stresses as well as compressive stresses. The load is uniformly distributed on the anchor plate which means that the anchor is considered to be flexible and it is assumed to be perfectly bonded to the soil below. The behaviour of soil loaded by both square and circular anchor buried at variable depths is studied. The present linear analytical technique uses the Mindlin(1936) solution for a point load acting beneath the surface of a semi– infinite mass.

2.2 ANALYSIS :

In an elastostatic analysis of homogeneous isotropic solids, the following field equations must be satisfied at all interior points, expressed in terms of cartesian tensors:

2.2.1 Governing Equations:

Equilibrium equations,

$$\sigma_{ij,i} + b_j = 0 \qquad (2.1)$$

where

b_j is the body force per unit volume,

σ_{ij} is the stress tensor, and the comma denotes partial differentiation with respect to the space variable.

Hooke's law ,

$$\sigma_{ij} = \lambda \delta_{ij} \epsilon_{kk} + 2 \mu \epsilon_{ij} \qquad (2.2)$$

where λ and μ are Lame's constants, and

δ_{ij} is the Kronecker delta.

Lame's constants are related to the conventional elastic constants E, G, (Young's modulus, shear modulus and Poisson's ratio, respectively) by the relations:

$$\lambda = \frac{E \nu}{(1 + \nu)(1 - 2\nu)} \qquad (2.3)$$

$$\mu = G = \frac{E}{2(1 + \nu)} \qquad (2.4)$$

Strain–displacement relation,

$$\epsilon_{ij} = \tfrac{1}{2} (u_{i,j} + u_{j,i}) \qquad (2.5)$$

where u_i is the i^{th} component of displacement vector.

The strain–displacement equation (2.5) may be substituted into Hooke's law (2.2) and the result in turn substituted into the equilibrium equation (2.3) to produce the governing equation:

$$\mu u_{i,jj} + (\lambda + \mu) u_{i,ji} + b_i = 0 \qquad (2.6)$$

which is called the Navier–Cauchy equation.

2.2.2 Fundamental (Point Force) Solution:

An embedded anchor applies pressures to the soil below ground level while the surface remains traction free everywhere. The fundamental point force solution to such problems was given by Mindlin in 1936. For illustrative purposes, the equation for vertical stress due to vertical point load is given in Appendix A. The complete stress tensor σ_{ij} due to a vertical point load P has the following form:

$$\sigma_{ij}(x) = F_{ij}(x,y) P(y) \qquad (2.7)$$

where

F_{ij} is a tensor function depending on the position of the load (y) and field point (x), and Poisson's ratio ν,

Expression (2.7) can also be written in an incremental form as:

$$d\sigma_{ij}(x) = F_{ij}\ (x,y)\ dP(y) \qquad (2.8)$$

2.3 NUMERICAL IMPLEMENTATION:

The stresses due to a distributed load w on the surface of the anchor plate is considered can be obtained by integration of equation (2.7), ie

$$d\sigma_{ij} = \int F_{ij}\ (x,y)\ dw\ dS(y) \qquad (2.8a)$$

By discretising the surface of loading into small elements, equation (2.8a) can be rewritten in the form:

$$d\sigma_{ij} = \sum_{n=1}^{N} F_{ij}\ (x,y_n)\ dw\ dS_n \qquad (2.8b)$$

where

dw is the increment of uniformly distributed load, over the surface S

y_n, dS_n are the position vector and the area of the n^{th} element, respectively.

N is the number of anchor elements.

Figure 2.1 shows how square and circular anchors may be divided into small elements. It also shows the XZ plane through the centre of the anchor where stresses are calculated.

2.3.1 Convergence Study:

Discretisation and numerical solution induce some errors. In this case, the error is a function of the dimensionless ratio r/D from the field point to the anchor, where the distance r is expressed as follows:

$$r = (r_i\ r_i)^{\frac{1}{2}}$$

and

$$r_i = x_i - y_i$$

To avoid excessive computer time, the number of elements is reduced for field points remote from the anchor, but sufficient number of elements are chosen for every field point such that the maximum error is less than 1%. Table 2.1 shows the variation of the error, for the vertical stress σ_{zz}, with respect to the ratio r/D and the number of elements N.

Table 2.1 Error in σ_{zz} along the anchor axis with number of elements for a square anchor:

r/D = 0.05		r/D = 0.10		r/D = 0.20		r/D = 0.50		r/D = 1/00	
N	ϵ	N	ϵ	N	ϵ	N	ϵ	N	ϵ
8	52%	4	52%	2	53%	2	1%	2	4%
16	11%	8	11%	4	11%	4	1%	4	1%
32	0	16	0	8	0	8	0	8	0

2.3.2 Stress Invariants:

The computer program determines several components of stress. The horizontal stress σ_{xx}, vertical stress σ_{zz}, and shear stress τ_{xz} are calculated at several field points, and then principal stresses and stress invariants in the XZ plane are determined. The major and the minor principal stresses are defined by the following expressions:

$$\sigma_1 = \tfrac{1}{2} (\sigma_{xx} + \sigma_{zz}) + \tfrac{1}{2} \left[(\sigma_{xx} - \sigma_{zz})^2 + 4 \tau_{xz}^2 \right] \quad (2.9)$$

$$\sigma_3 = \tfrac{1}{2} (\sigma_{xx} + \sigma_{zz}) - \tfrac{1}{2} \left[(\sigma_{xx} - \sigma_{zz})^2 + 4 \tau_{xz}^2 \right] \quad (2.10)$$

$$\frac{\sigma_1 + \sigma_3}{2} = \frac{\sigma_{xx} + \sigma_{zz}}{2} \quad (2.11)$$

$$\frac{\sigma_1 - \sigma_3}{2} = \frac{\left[(\sigma_{xx} - \sigma_{zz})^2 + 4 \tau_{xz}^2 \right]^{\frac{1}{2}}}{2} \quad (2.12)$$

2.3.3 Identification of Zones of Incipient Failure:

These quantities (σ_1 and σ_3) are necessary to determine the state of the soil under the anchor loading because the failure criteria are usually written in terms of principal stresses. As shown in Figure 2.3, the major principal stress σ_1 and the minor principal stress σ_3 represent the intersection points of the Mohr circle with the σ axis. The quantity $(\sigma_1 - \sigma_3)/2$ represents the radius of the Mohr circle, and

is equal to the maximum shear stress. The quantity $(\sigma_1+\sigma_3)/2$ represents the position of the centre of Mohr circle, which is along the σ axis and is equal to the stress.

The Mohr–Coulomb failure criterion is schematically interpreted by Figure 2.3 from where the following relation is deduced

$$AF = OA \sin\varphi$$

which can also be written:

$$\frac{\sigma_1 - \sigma_3}{2} = \frac{\sigma_1 + \sigma_3}{2} \sin\varphi \qquad (2.13.a)$$

or

$$\frac{\sigma_1 - \sigma_3}{\sigma_1 + \sigma_3} = \sin\varphi \qquad (2.13.b)$$

In other words, for cohesionless soils, when the ratio of maximum shear stress–to–mean stress is equal to $\sin\varphi$ the Mohr–Coulomb failure criterion is satisfied and yielding of the soil initiates.

2.3.4 In–situ Stresses:

In–situ stresses must be taken into account because they influence the initial yield stress level. The in–situ stresses are:

$$\sigma_{zz}^{0} = \gamma z$$

$$\sigma_{xx}^{0} = K_0 \gamma z \qquad (2.14)$$

where

$$K_0 = \frac{\nu}{(1 - \nu)} \qquad (2.15)$$

γ is the unit weight of soil,

z is the depth.

2.3.5 Current Stresses:

The current stress σ_{ij} are defined here as the summation of the in–situ stress σ_{ij}^{0} and the stress increment $d\sigma_{ij}$ due to an incremental pressure dw on the anchor plate, ie

$$\sigma_{ij} = \sigma_{ij}^{0} + d\sigma_{ij} \qquad (2.16.a)$$

or, explicitly,

$$\begin{cases} \sigma_{xx} = \sigma_{xx}^{0} + d\sigma_{xx} \\ \sigma_{zz} = \sigma_{zz}^{0} + d\sigma_{zz} \\ \tau_{xz} = d\tau_{xz} \end{cases} \qquad (2.14.b)$$

It is these current stresses which are plotted in Figures 2.4 to 2.40 . Figure 2.2 shows the grid of field points. This grid is finer in the region where the stress varies rapidly, which is the region immediately above the anchor edge in the case of pulled–out anchors. A singularity problem arises near the edge of the anchor where the stresses are discontinuous. The plots of the components of stresses show the contours converging to that point. Great care is necessary to resolve the stress field sufficiently accurately there. The contour plotting program which was used to display these data consists of the NAG graphical supplement routines, and uses the GHOST interface so that the user can store the results within a gridfile.

2.4 RESULTS:

The results presented here are a distillation of the results from a more comprehensive study presented in research report by Merouani and Davies[51]. The models analysed are a deep anchor (H/D= 12) and two shallow anchors (H/D= 1.5 and 2.5). For both deep and shallow anchors, two values of Poisson's ratio are considered; $\nu = 0.5$ and $\nu = 0.3$. The stresses were calculated at two different values of the uniform load; $w = 5\sigma_{za}$ and $w = 10\sigma_{za}$, where $\sigma_{za} = \gamma H$ is the initial vertical stress at the anchor level.

The cases shown in Figures 2.4 to 2.40 represent circular and square shallow anchors at depth–to–diameter (or depth–to–breadth) ratio H/D= 1.5, a shallow square anchor at H/D= 2.5 and a deep square anchor at H/D= 12. Associated with the shallow anchors are unit weights of soil $\gamma = 0.67$ for H/D= 1.5 and $\gamma = 0.4$ for H/D= 2.5 to give an initial vertical stress $\sigma_{za} = 1$ at anchor level, while for the deep anchor the initial vertical stress was considered to be constant and equal to unity.

It should be noted that tensile normal stresses are considered negative in these plots.

In the following, the stress components induced by uniformly distributed pressures on anchors are examined for shallow and deep anchors.

2.4.1 Deep Anchors:

The soil immediately above the anchor is subjected to a vertical upwards pressure Q= w/2, where w is the anchor pressure. In other words, the pressure exerted by the anchor is divided into equal parts; the remaining stress component relieves the compressive stress beneath the anchor.

a. Vertical stress:

The pressure bulb (Figure 2.4) for a deeply embedded square anchor (for $\nu = 0.5$) should have exactly the same shape as the one given by a square surface foundation. Comparisons were made between the predicted stress along the axis with those predicted by Poulos and Davis[65] in Table 3.14 of their text. The errors cannot be discriminated graphically. For instance, at z/D = 0.5 the theoretical solution is $\sigma_{zz} = 4.5$ including unit in-situ stress and the numerical solution is $\sigma_{zz} = 4.5$. The vertical stress in the soil immediately above the anchor is 6; i.e. the sum of the insitu stress $\sigma_{za} = 1$ and Q= 5. The contours intersect the anchor axis at right angles. This feature, denoting symmetry is common to all normal stress components.

b. Horizontal stress:

The horizontal stress σ_{xx} (Figure 2.5) is compressive in the region shown. In the soil immediately above the anchor the horizontal stress is 6. However it diminishes faster than the vertical stress with distance away from the anchor. At z/D= 0.5 on the centroidal axis, Tables 3.15 and 3.16[65] give the value $\sigma_{xx} = 1.74$ and an interpolated result from Figure 2.5 gives $\sigma_{xx} = 1.7$.

c. Shear stress:

Figure 2.6 shows that the shear stress τ_{xz} is negative in the region above the anchor, this means that an element of soil above the anchor would deform as

shown below. Contours tend to be parallel to the anchor axis near to that axis where the shear stress must be zero from symmetry considerations. The shear stress is largest over the edge of the anchor which represents a singularity point.

d. Major and minor principal stresses:

Contours of major principal stress and minor principal stress (Figure 2.7 and 2.8) are similar to those given by Lambe and Whitman[44] for a circular surface foundation. Along the anchor axis, the major principal stress is equal to the vertical stress and the minor principal stress is equal to the horizontal stress. The values of σ_1 and σ_3 were therefore checked along that axis.

e. Maximum shear stress:

Along the anchor axis, the magnitude of the maximum shear stress $(\sigma_1 - \sigma_3)/2$ (Figure 2.9) increase from zero at z/D= 0 to approximately 1.5 at z/D= 0.4, then decreases again for z/D>0.4. The region of maximum value of $(\sigma_1 - \sigma_3)/2$ forms an arc from the edge of the anchor towards its centroidal axis as shown.

f. Mean stress:

The contours of mean stress $(\sigma_1 + \sigma_3)/2$ (Figure 2.10) are similar to those of the major principal stress, particularly in the region near the anchor. The magnitude of this component of stress is 6 in the soil immediately above the anchor and decreases away from the anchor.

g. Stress ratio:

The contours of stress ratio $(\sigma_1 - \sigma_3)/(\sigma_1 + \sigma_3)$ (Figure 2.11) have almost the same shape as the contours of maximum shear stress. The magnitude increases to a maximum value at z/D= 0.8 on the centroidal axis and decreases thereafter. It would appear therefore that yield would start above the anchor edge and propagate inwards and upwards along the path indicated by the dotted line on the plot.

2.4.2 Shallow Anchors:

Since the depth− to− breadth ratio (H/D) in these plots is 1.5, the upper horizontal line on these plots represents the ground surface. Results from a shallow anchor with H/D= 2.5 will also be discussed. It can be noted that, in general, the shape of the contours of the stress components for both shallow and deep anchors are broadly the same.

a. Vertical stress:

Figure 2.12 shows that compressive vertical stresses near a shallow anchor are almost the same as those for deep anchor. However, away from the anchor, near the ground surface, the magnitudes of these stresses are smaller than those for a deep anchor. For example, Figure 2.12 gives at z/D= 1.0 σ_{zz}= 0.8 while for H/D= 12, Figure 2.4 gives σ_{zz}= 1.4 (in both cases the initial stresses are excluded). This is due to the fact that for the shallow anchor the vertical stress varies from Q= $5\sigma_{za}$ at the anchor level to zero at the ground level in a distance d= 1.5D, while for deep anchor the vertical stress varies from Q= $5\sigma_{za}$ at the anchor level to zero at the ground level in a larger distance d= 12D.

b. Horizontal stress:

The shape of these contours (Figure 2.13) is broadly similar to that for deep anchors (Figure 2.5). However, near the ground surface tensile horizontal stresses occur in this case. The magnitudes of the horizontal stresses are a little smaller than the ones of deep anchors even close to the anchor. For instance, at z/D= 0.25 σ_{xx}= 2 for shallow anchors and σ_{xx}= 2.2 for deep anchors.

c. Shear stress:

Figure 2.14 shows that the contours of shear stress τ_{xz} become parallel to the ground level where the shear stress is zero. If we consider the contours at z/D= 0.25 above the anchor edge, τ_{xz}= − 1.4 for a shallow anchor and τ_{xz}= − 1.1 for a deep anchor.

d. Major and minor principal stresses:

Figures 2.15 and 2.16 show that the contours of major and minor principal stresses are more nearly horizontal away from the anchor and their

magnitudes are smaller than the ones deep anchors. Figure 2.16 shows negative minor stresses appearing near the soil surface. This phenomenon was observed by Davie[16]. During tests on uplift capacity of circular anchors in cohesive soil cracks appeared at the surface of the soil around the anchor axis. These cracks are due to the tensile horizontal stresses shown in Figures 2.13 and 2.16.

The shape of the mean stress contours (Figure 2.18) is similar to that of major principal stress in this case as well.

e. Maximum shear stress:

Below the zone where tensile horizontal stresses appear, the contours of Figure 2.17 show a more regular shape, yet different from that of Figure 2.9 for deep anchors. Despite this fact, the magnitudes of these contours are in the same range (from 0.12 to 1.8) and show a similar local maximum at $z/D = 0.4$ along the anchor axis. The zone with the highest shear stress appears at the edge of the anchor and would expand with an increase of the anchor pressure W until reaching the centroidal axis.

f. Mean stress:

Just as the contours of horizontal and minor stresses, the contours of mean stress in Figure 2.18 indicate a zone of tensile stress near the ground surface. The contours also tend to be more nearly horizontal away from the anchor.

g. Stress ratio:

Figure 2.19 depicts the contours of stress ratio in the region close to the anchor, and shows that these contours are completely different from those obtained for a deep anchor. Contours are not plotted in the region where tensile horizontal stresses exist because they yield values which are not very useful there.

The contours plotted in figures 2.25 to 2.31 represent the stress distribution for a shallow square anchor at depth–to–breadth ratio $H/D = 2.5$. As a general rule, the shape and magnitudes of the stress components are intermediate between those for deep anchors and those for shallow anchors.

2.5 DISCUSSION OF RESULTS:

The effects of anchor shape, the depth–to–diameter ratio and Poisson's ratio are discussed in the following.

2.5.1 Effect of Anchor Shape:

Stresses due to loading of shallow square anchors (Figures 2.12 to 2.19) may be compared with those for circular anchors (Figures 2.20 to 2.26). In each case $\nu = 0.5$, $w = 10.\sigma_{za}$, $\gamma = 0.67$ and $H/D = 1.5$. In general, the shape of the contours are very similar for circular and square anchor plates and the difference cannot be easily discriminated graphically.

2.5.2 Effect of Embedment Depth:

The shape of the contours is approximately the same for both deep and shallow anchors but they are more nearly horizontal away from the anchor for shallow anchors. The decrease in the magnitude of normal stresses away from anchors is faster for shallow anchors than for deep ones. However, contours of shear stress τ_{xz} do not seem to be affected a great deal by the depth of embedment. It is particularly interesting to notice that tensile stresses appear near the soil surface in the zone around the anchor axis for shallow anchors, especially when that phenomenon was observed in experiments on clay soils by Davie[16].

2.5.3 Effect of Poisson's Ratio:

The effect of Poisson's ratio is shown through the plots representing two soils having different values of Poisson's ratio and loaded by a square anchor embedded at shallow depth ($H/D = 1.5$). Figures 2.20 to 2.26 are the results for a soil with $\nu = 0.5$ and Figures 2.34 to 2.40 for a soil with $\nu = 0.3$. The shape of the contours remains much the same for the various components of stress in the two soils. An increase of Poisson's ratio from 0.3 to 0.5 induces an increase in the magnitudes of vertical, horizontal, major, minor and mean stress, and a decrease in the magnitudes

of shear stress τ_{xz} and maximum shear stress in the general region above the anchor. For example, the results given by the plots at z/D= 0.5 are σ_{zz}= 3.6 for ν= 0.5 and σ_{zz}= 3.0 for ν= 0.3.

2.5.4 Incipient Yield:

It seems paradoxical to use the term 'yield' in a chapter which deals with an elastic analysis of solids. However, in this case only initiation of yield of the material considered is implied. Therefore, the contours of stress ratio which have been plotted only hint at the zone of incipient yielding. Thus, Figures 2.11 and 2.19 only suggest that the modes of failure of deep and shallow anchors might be different. Nevertheless, the evidence from laboratory tests indicates that this is a valid conclusion.

2.6 *CONCLUSION:*

In this elastic analysis, several assumptions have been made. Obviously, some of these assumptions limit the applicability of the analysis but on the other hand some useful insights into the stress distribution around anchors have been obtained.

Parameters such as depth of embedment, anchor shape and Poisson's ratio of soil were considered, and their effects on the soil behaviour under working load conditions were studied. The contours showing zones of incipient yield have different shapes for deep and shallow anchors. However, the question of whether Figures 2.11 and 2.19 are presenting two different modes of failure cannot be answered at this stage. Therefore, a more realistic non– linear analysis is required before any sensible conclusion can be drawn.

In the following chapters the finite element method and appropriate soil constitutive laws are used for this purpose.

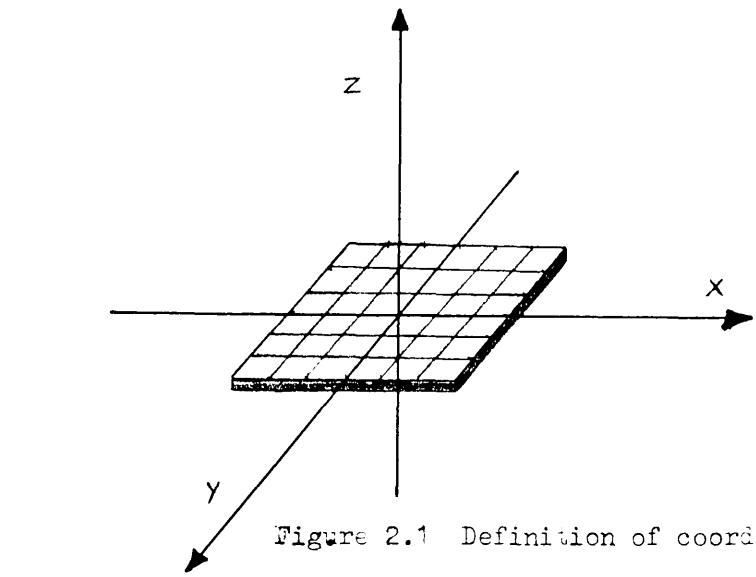

Figure 2.1 Definition of coordinate axes.

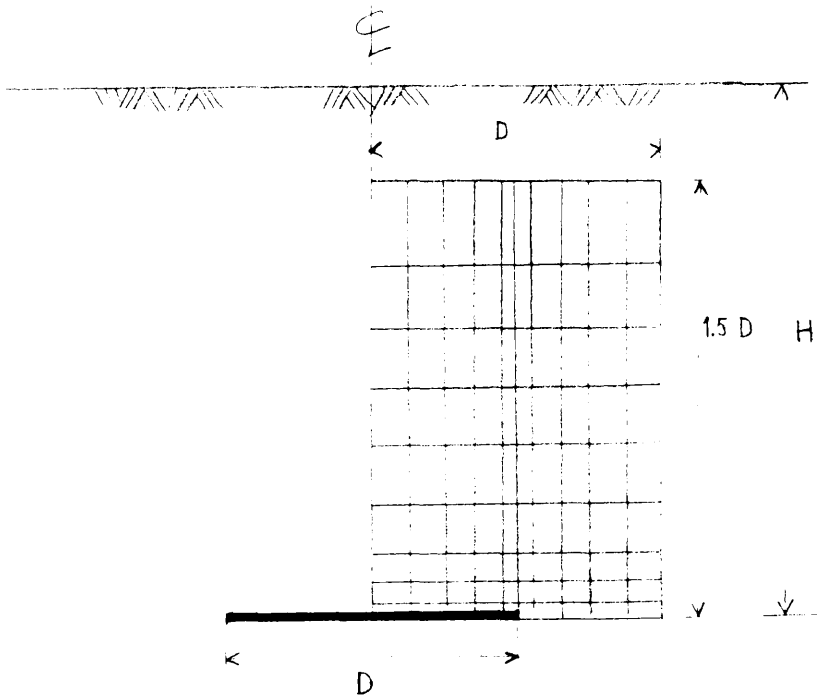

Figure 2.2 Anchor position and sampling points.

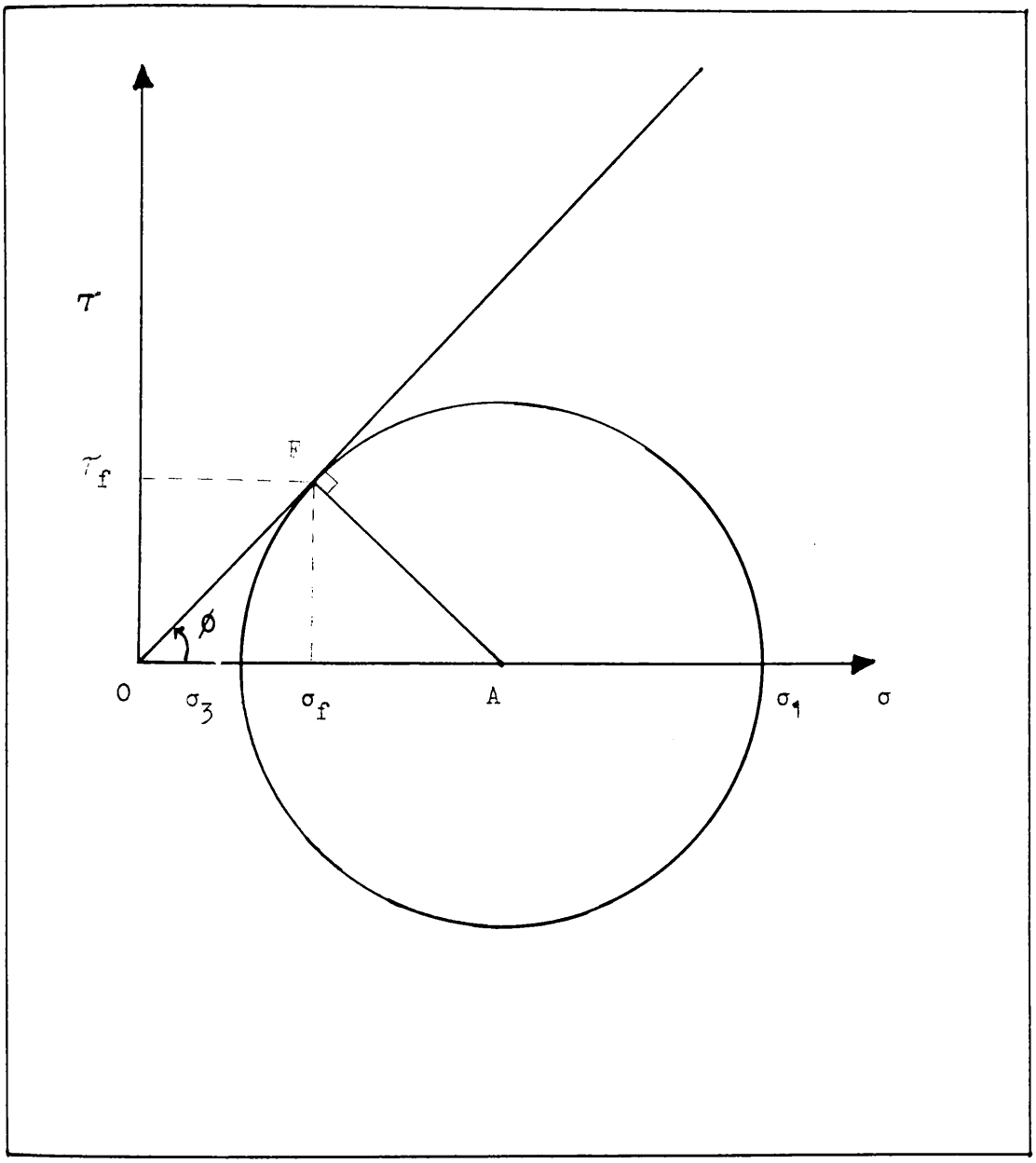

Figure 2.3 Mohr-Coulomb failure criterion.

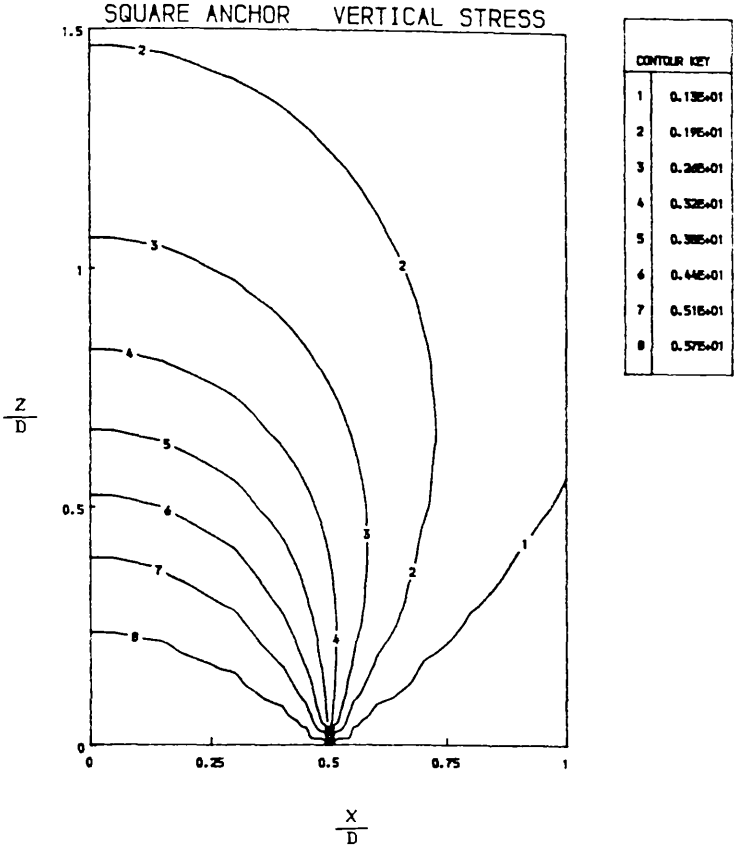

Figure 2.4 $\frac{H}{D} = 12$ $\sigma_z^0 - \sigma_x^0 = 1$

$\nu = 0.5$ $\frac{W}{\sigma_{za}} = 10$

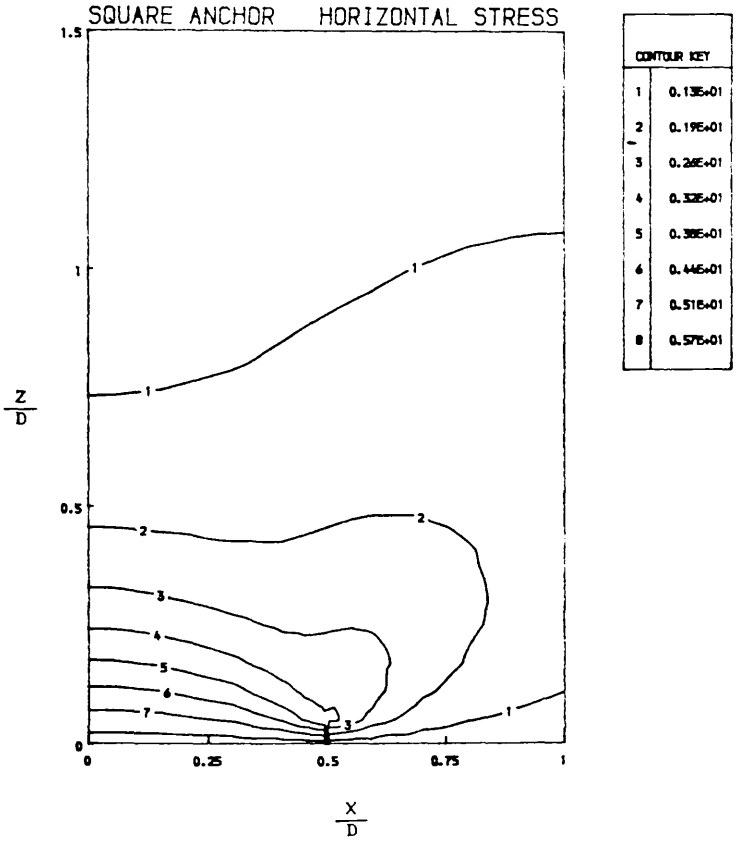

Figure 2.5 $\frac{H}{D} = 12$ $\sigma_z^0 - \sigma_x^0 = 1$

$\nu = 0.5$ $\frac{W}{\sigma_{za}} = 10$

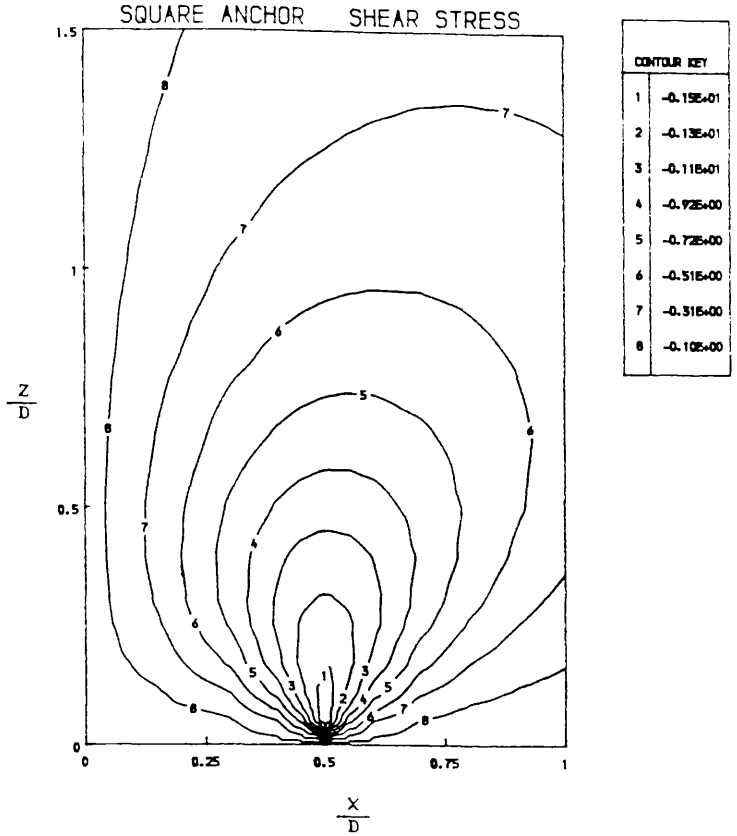

Figure 2.6 $\frac{H}{D} = 12$ $\sigma_z^0 = \sigma_x^0 = 1$
$\nu = 0.5$ $\frac{W}{\sigma_{za}} = 10$

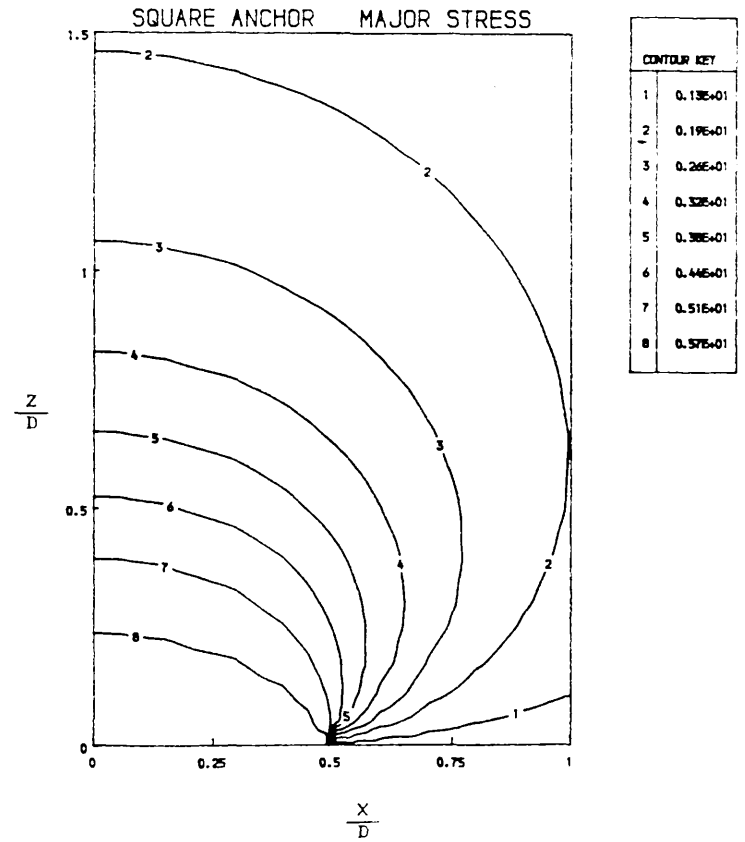

Figure 2.7 $\frac{H}{D} = 12$ $\sigma_z^0 = \sigma_x^0 = 1$
$\nu = 0.5$ $\frac{W}{\sigma_{za}} = 10$

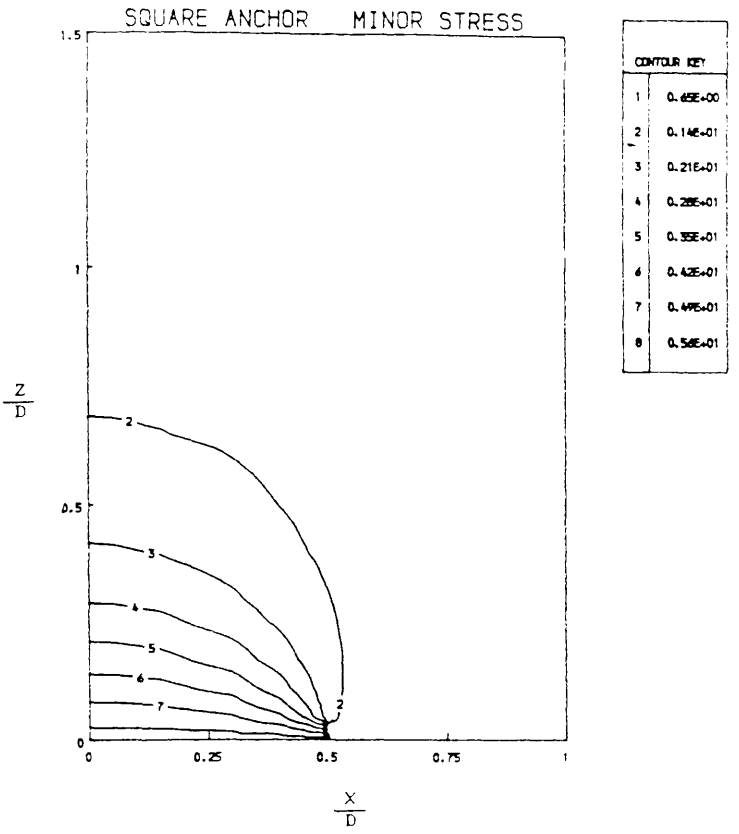

Figure 2.8 $\frac{H}{D} = 12$ $\sigma_z^o = \sigma_x^o = 1$
$\nu = 0.5$ $\frac{W}{\sigma_{za}} = 10$

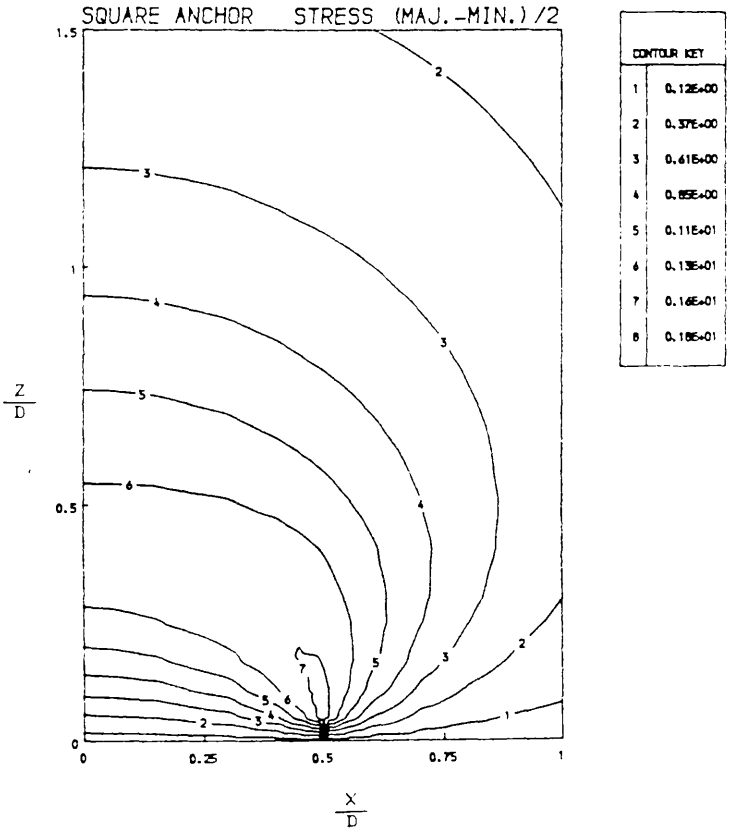

Figure 2.9 $\frac{H}{D} = 12$ $\sigma_z^o = \sigma_x^o = 1$
$\nu = 0.5$ $\frac{W}{\sigma_{za}} = 10$

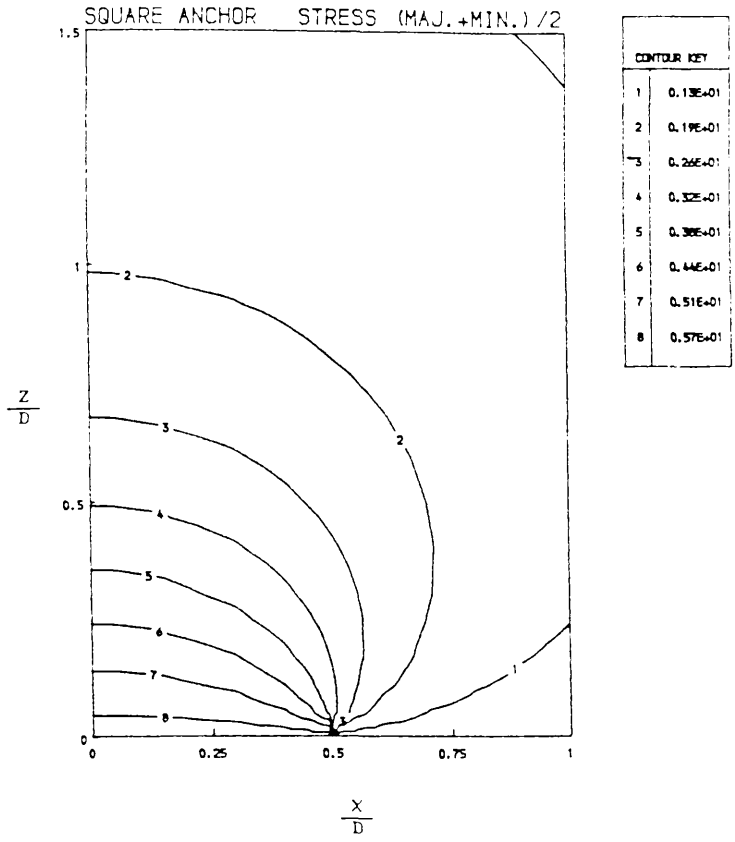

Figure 2.10 $\frac{H}{D} = 12$ $\sigma_z^o = \sigma_x^o = 1$ $\nu = 0.5$ $\frac{W}{\sigma_{za}} = 10$

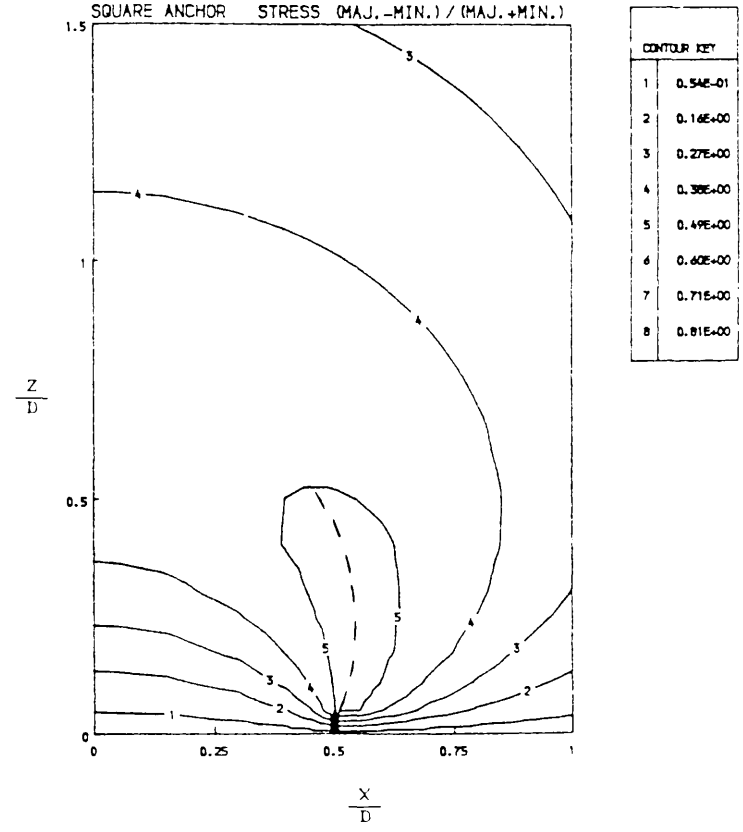

Figure 2.11 $\frac{H}{D} = 12$ $\sigma_z^o = \sigma_x^o = 1$ $\nu = 0.5$ $\frac{W}{\sigma_{za}} = 10$

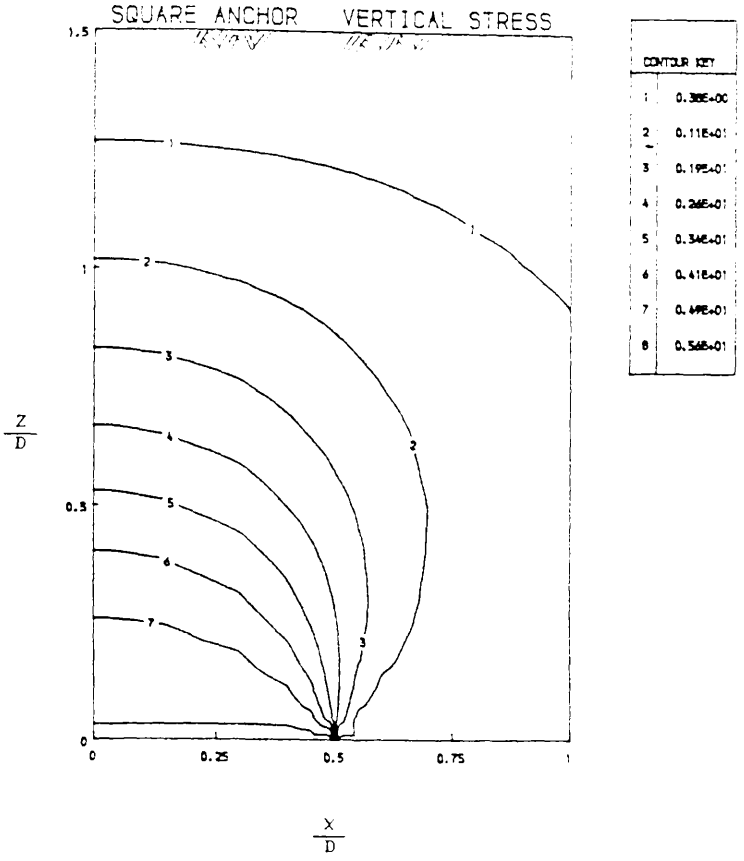

Figure 2.12 $\frac{H}{D} = 1.5 \quad \gamma = \frac{2}{3}$
$\nu = 0.5 \quad \frac{W}{\sigma_{za}} = 10$

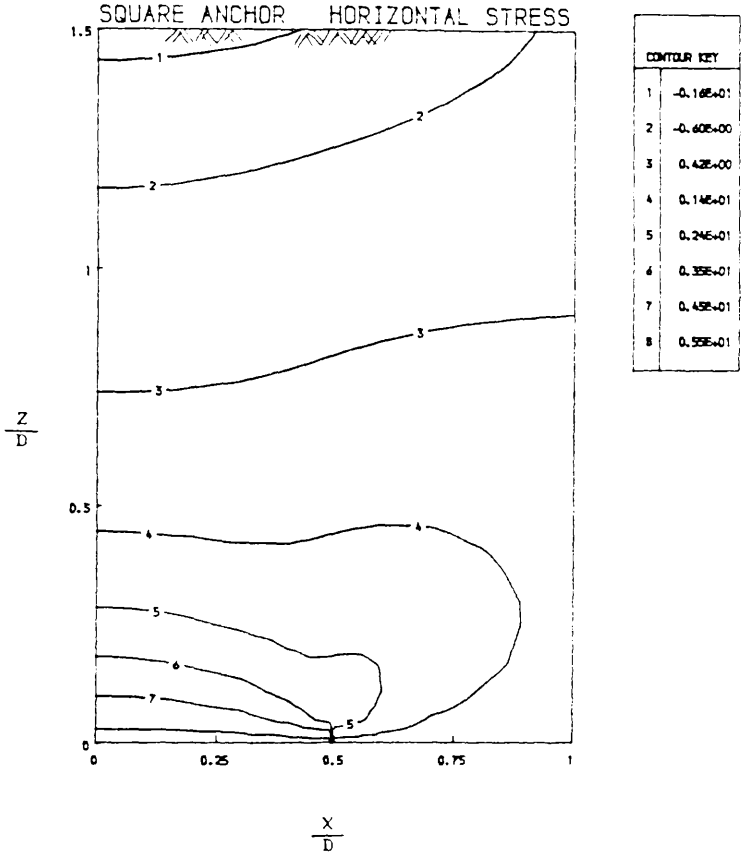

Figure 2.13 $\frac{H}{D} = 1.5 \quad \gamma = \frac{2}{3}$
$\nu = 0.5 \quad \frac{W}{\sigma_{za}} = 10$

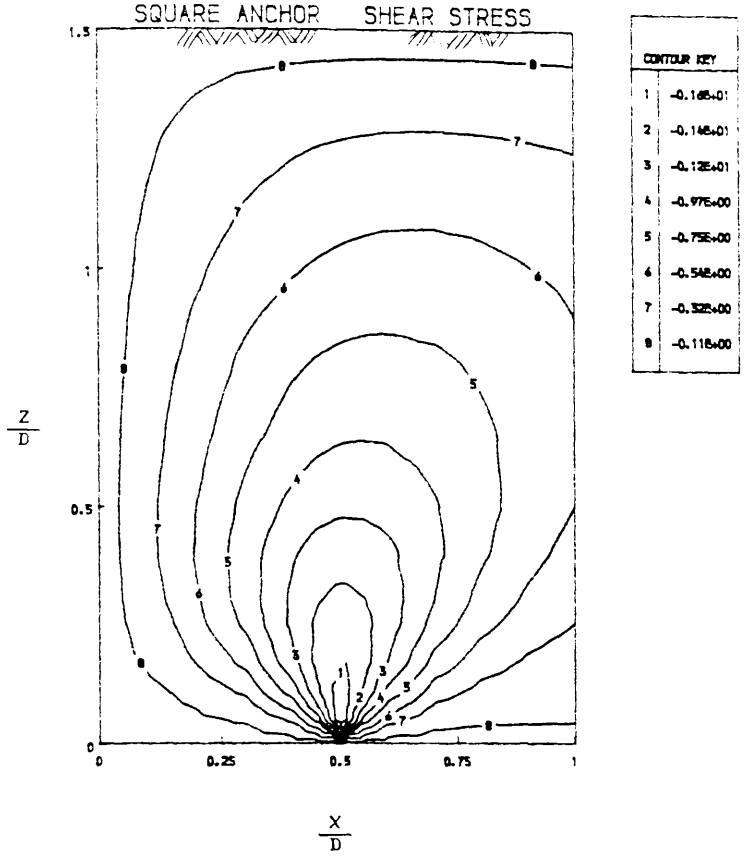

Figure 2.14 $\frac{H}{D} = 1.5 \quad \gamma = \frac{2}{3}$

$\nu = 0.5 \quad \frac{W}{\sigma_{za}} = 10$

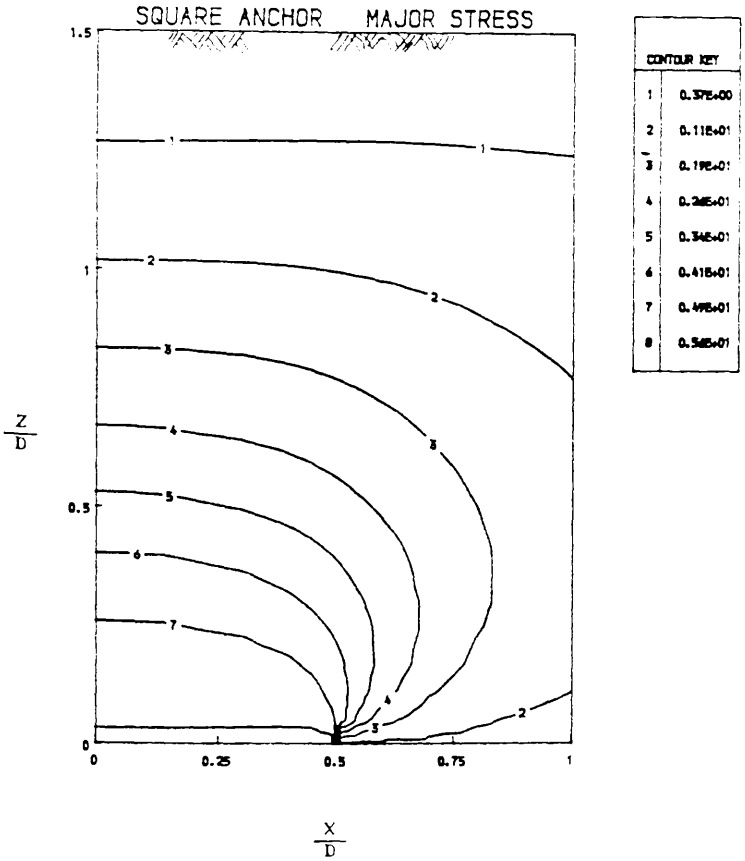

Figure 2.15 $\frac{H}{D} = 1.5 \quad \gamma = \frac{2}{3}$

$\nu = 0.5 \quad \frac{W}{\sigma_{za}} = 10$

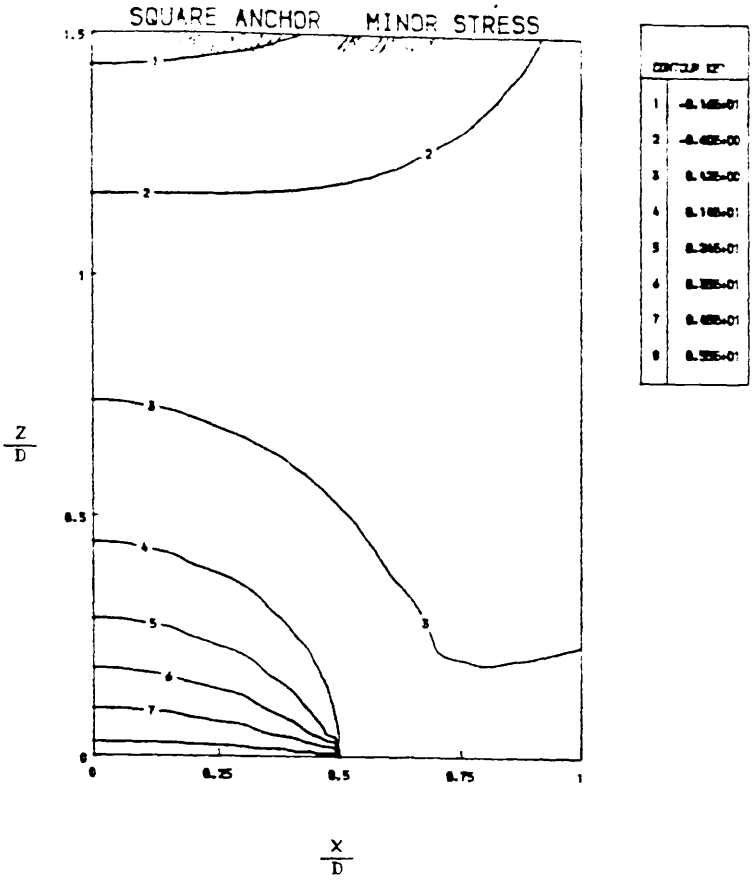

Figure 2.16 $\frac{H}{D} = 1.5 \quad \gamma = \frac{2}{3}$
$\nu = 0.5 \quad \frac{W}{\sigma_{za}} = 10$

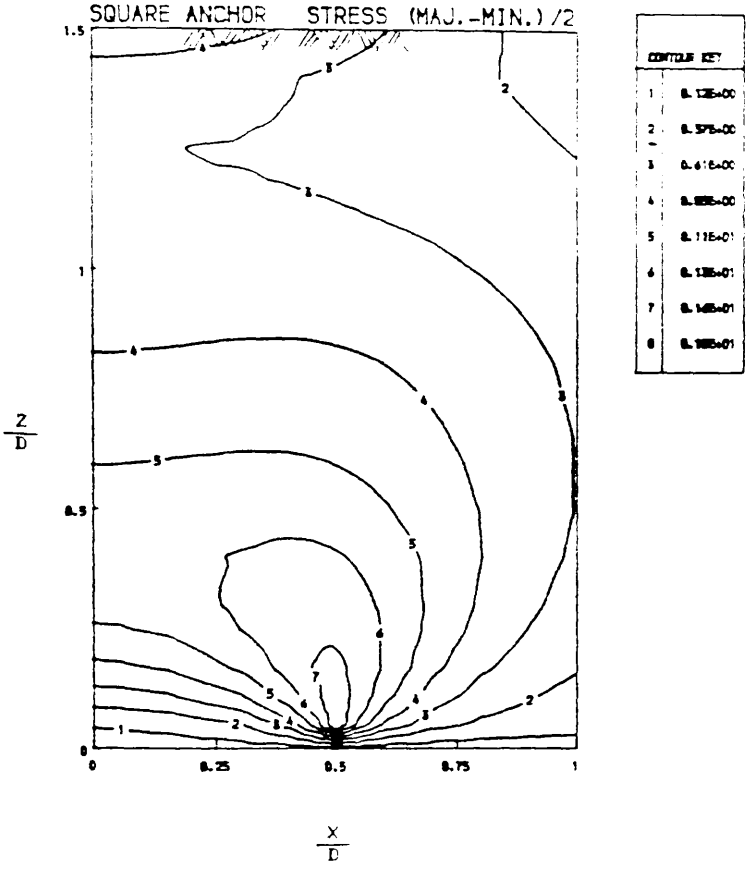

Figure 2.17 $\frac{H}{D} = 1.5 \quad \gamma = \frac{2}{3}$
$\nu = 0.5 \quad \frac{W}{\sigma_{za}} = 10$

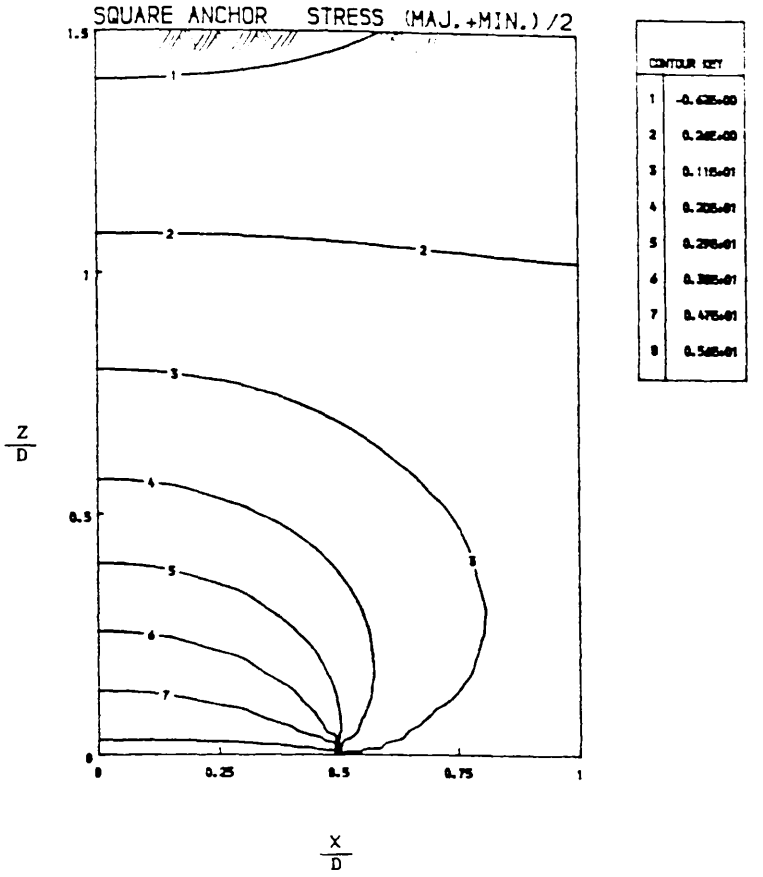

Figure 2.18 $\frac{H}{D} = 1.5 \quad \gamma = \frac{2}{3}$

$\nu = 0.5 \quad \frac{W}{\sigma_{za}} = 10$

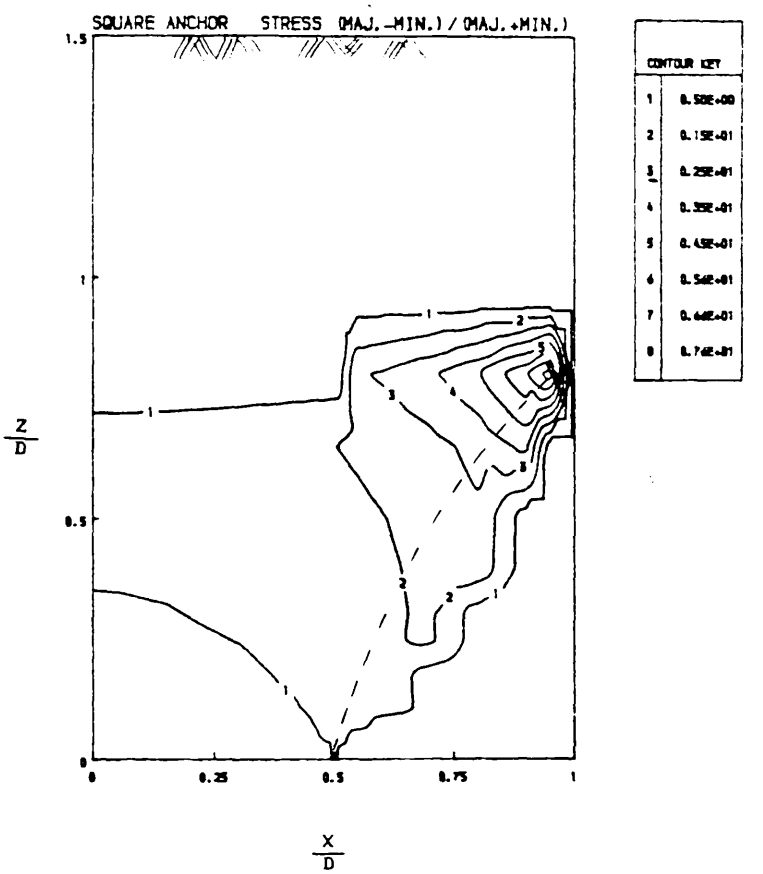

Figure 2.19a $\frac{H}{D} = 1.5 \quad \gamma = \frac{2}{3}$

$\nu = 0.5 \quad \frac{W}{\sigma_{za}} = 10$

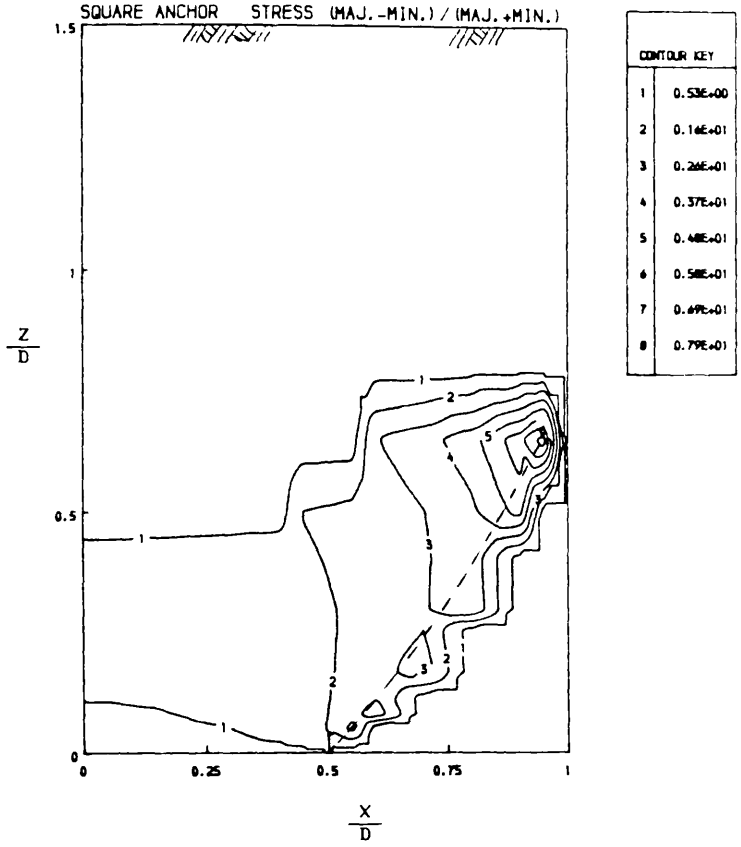

Figure 2.19b $\frac{H}{D} = 1.5 \quad \gamma = \frac{2}{3}$

$\nu = 0.3 \quad \frac{W}{\sigma_{za}} = 10$

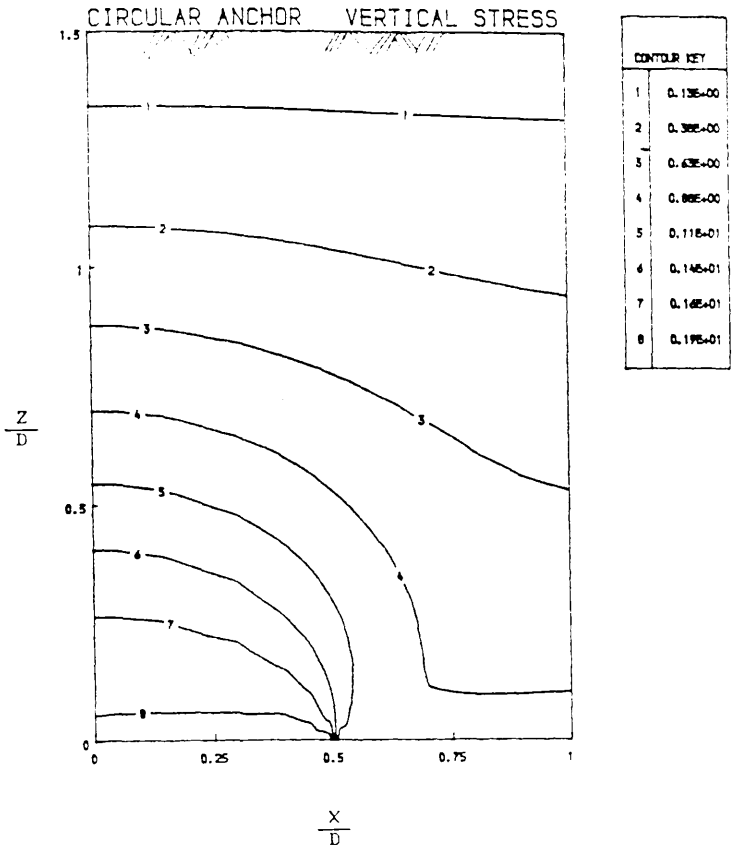

Figure 2.20 $\frac{H}{D} = 1.5 \quad \gamma = \frac{2}{3}$

$\nu = 0.5 \quad \frac{W}{\sigma_{za}} = 10$

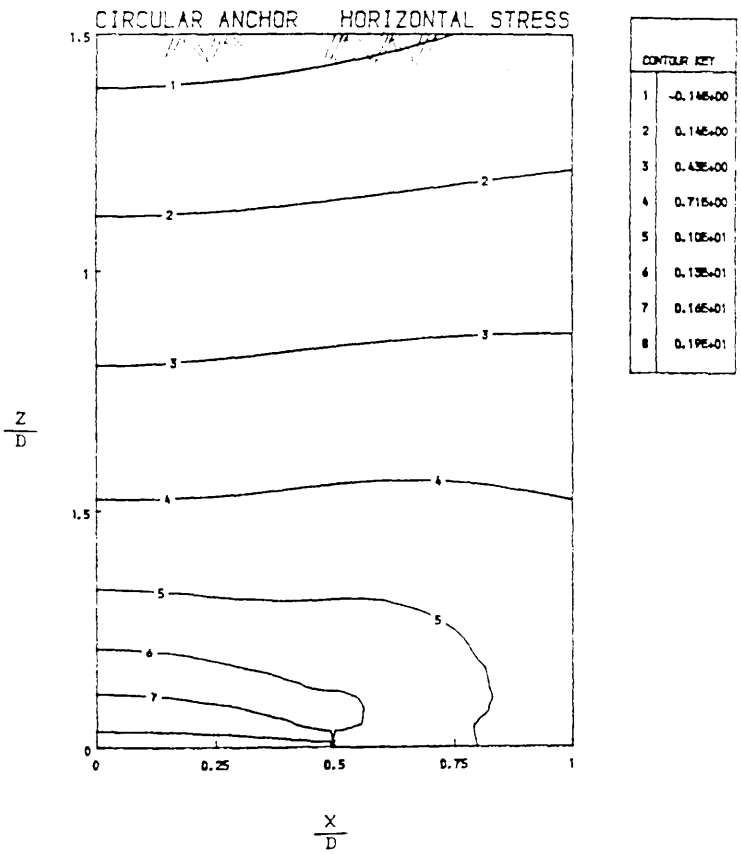

Figure 2.21 $\frac{H}{D} = 1.5 \quad \gamma = \frac{2}{3}$

$\nu = 0.5 \quad \frac{W}{\sigma_{za}} = 10$

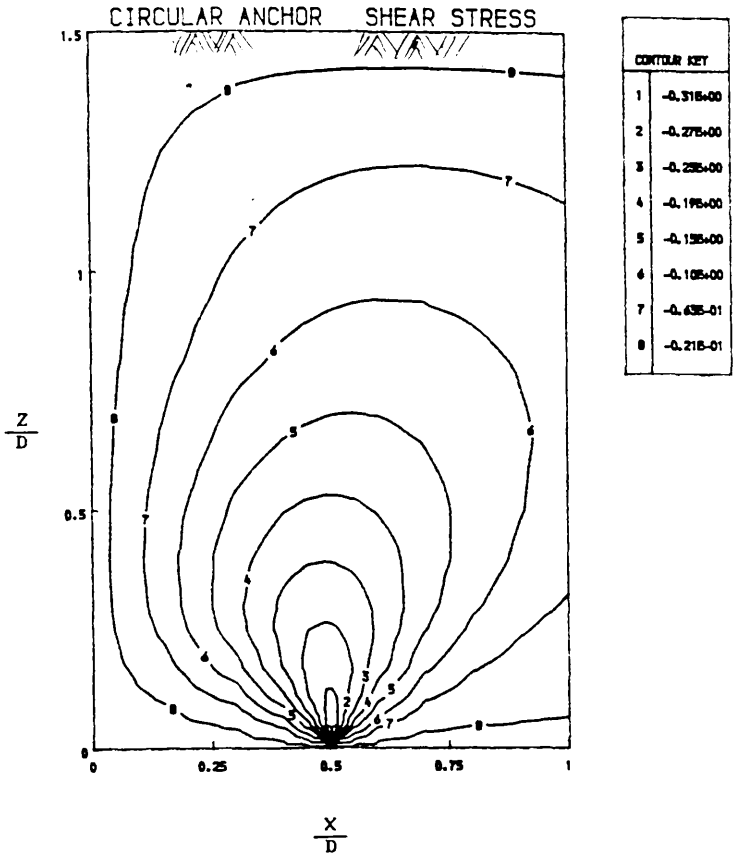

Figure 2.22 $\frac{H}{D} = 1.5 \quad \gamma = \frac{2}{3}$

$\nu = 0.5 \quad \frac{W}{\sigma_{za}} = 10$

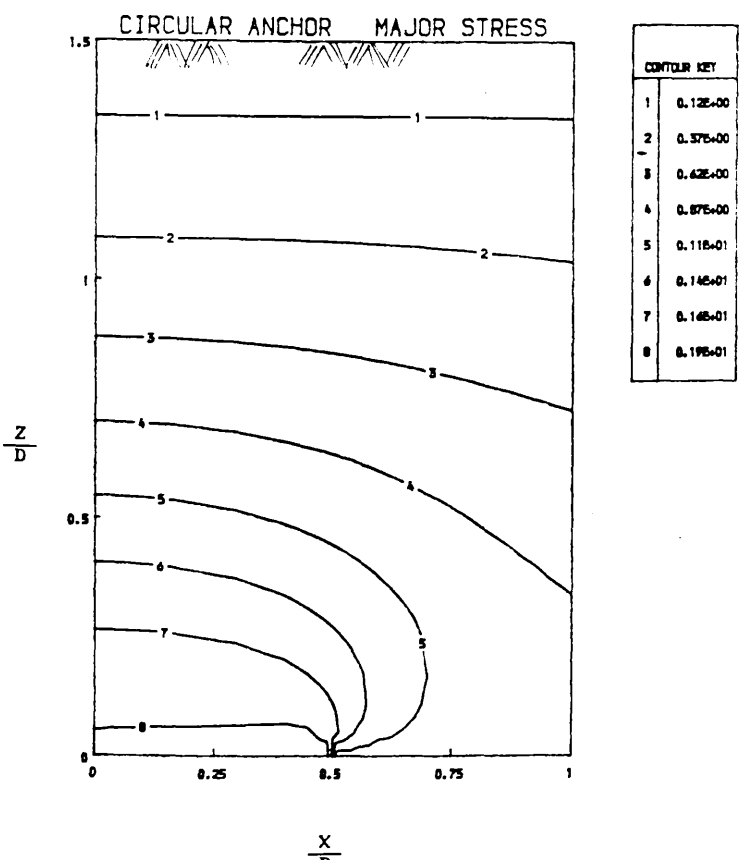

Figure 2.23 $\frac{H}{D} = 1.5 \quad \gamma = \frac{2}{3}$

$\nu = 0.5 \quad \frac{W}{\sigma_{za}} = 10$

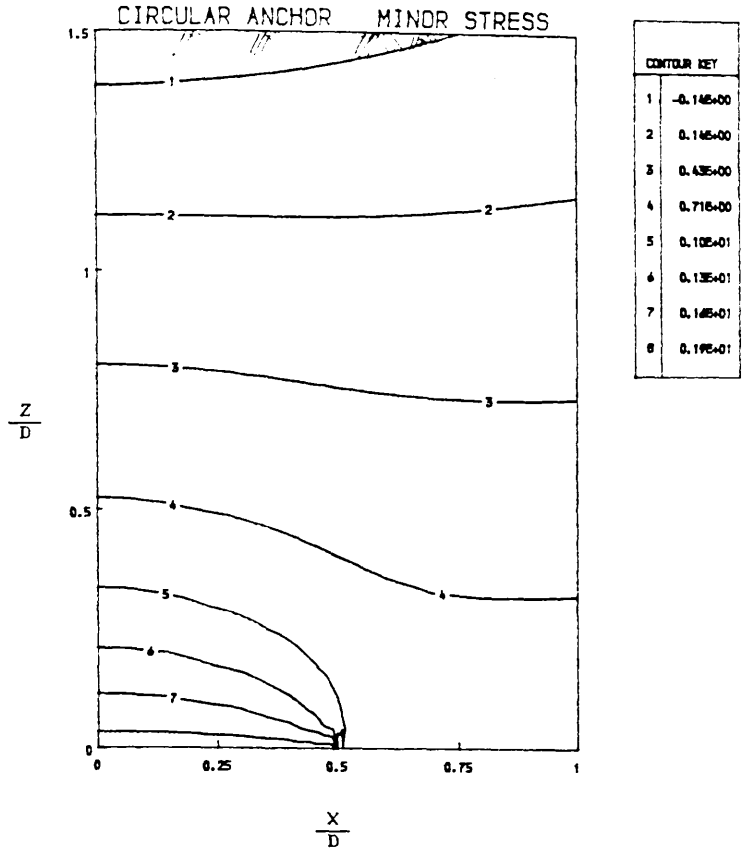

Figure 2.24 $\frac{H}{D} = 1.5 \quad \gamma = \frac{2}{3}$
$\nu = 0.5 \quad \frac{W}{\sigma_{za}} = 10$

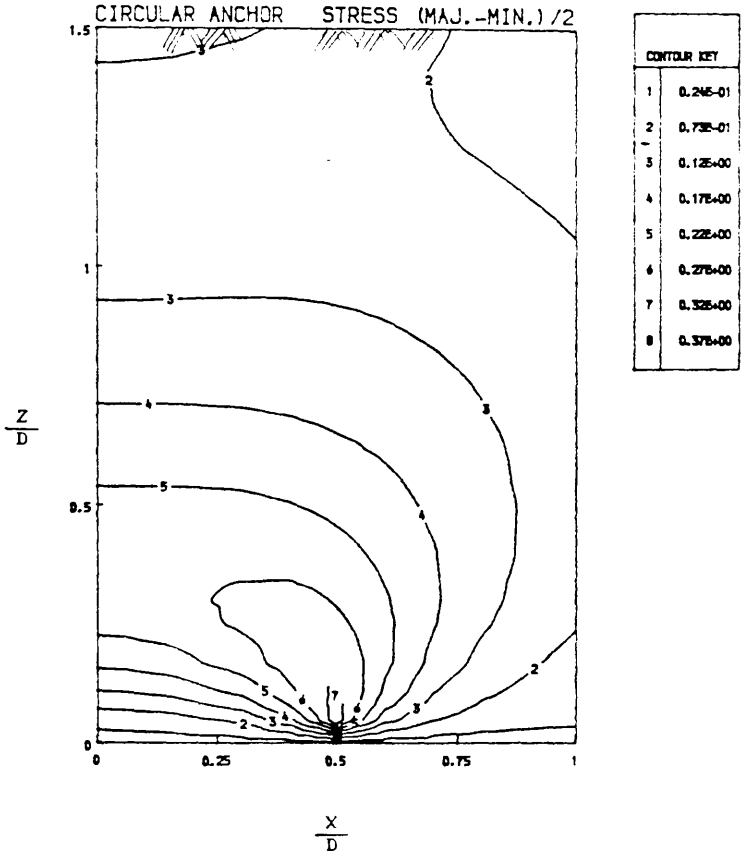

Figure 2.25 $\frac{H}{D} = 1.5 \quad \gamma = \frac{2}{3}$
$\nu = 0.5 \quad \frac{W}{\sigma_{za}} = 10$

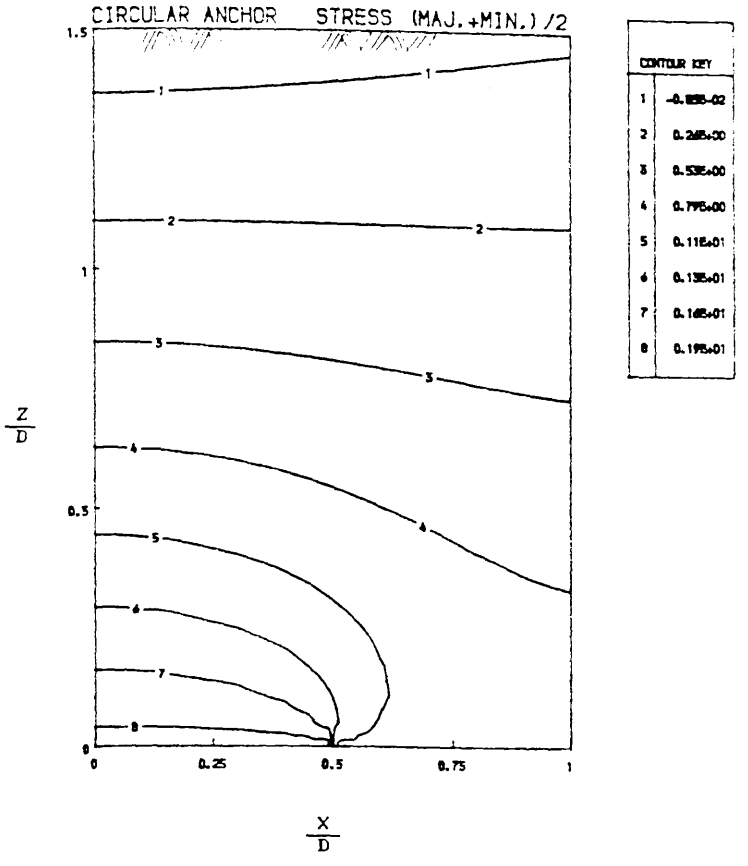

Figure 2.26 $\frac{H}{D} = 1.5 \quad \gamma = \frac{2}{3}$

$\nu = 0.5 \quad \frac{W}{\sigma_{za}} = 10$

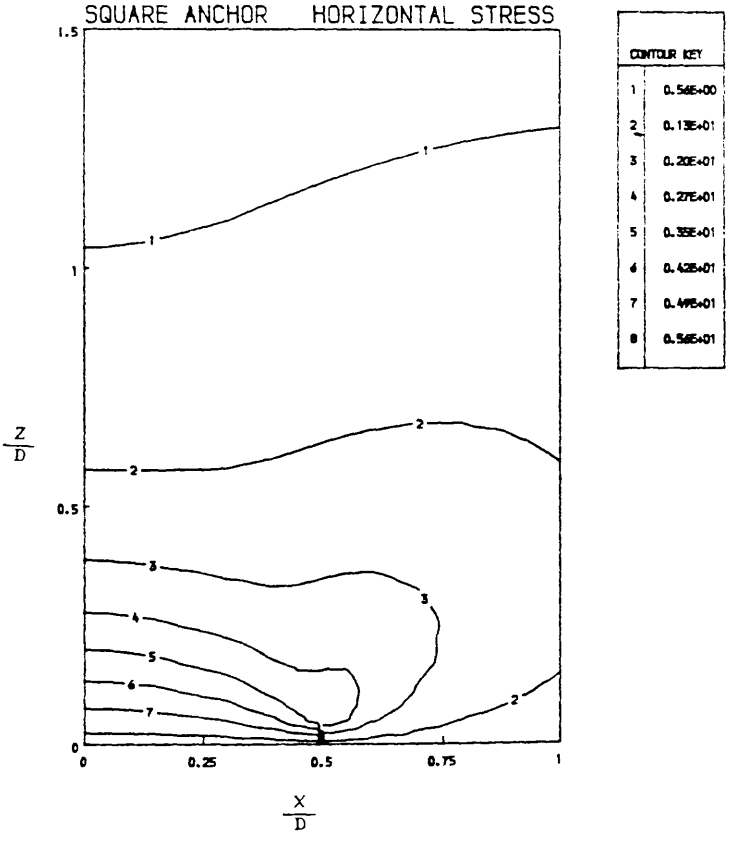

Figure 2.27 $\frac{H}{D} = 2.5 \quad \gamma = 0.4$

$\nu = 0.5 \quad \frac{W}{\sigma_{za}} = 10$

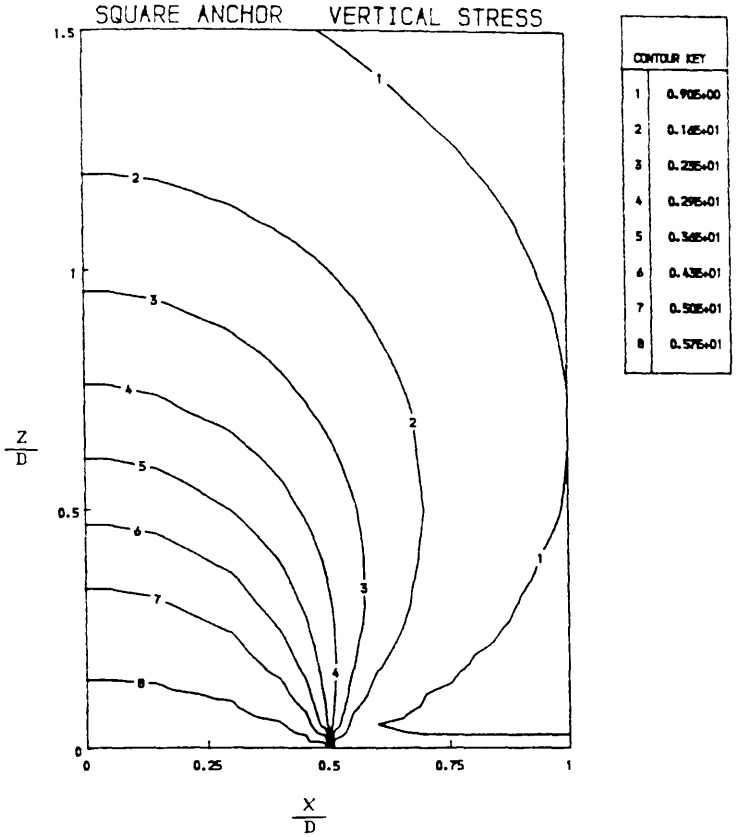

Figure 2.28 $\frac{H}{D} = 2.5 \quad \gamma = 0.4$
$\nu = 0.5 \quad \frac{W}{\sigma_{za}} = 10$

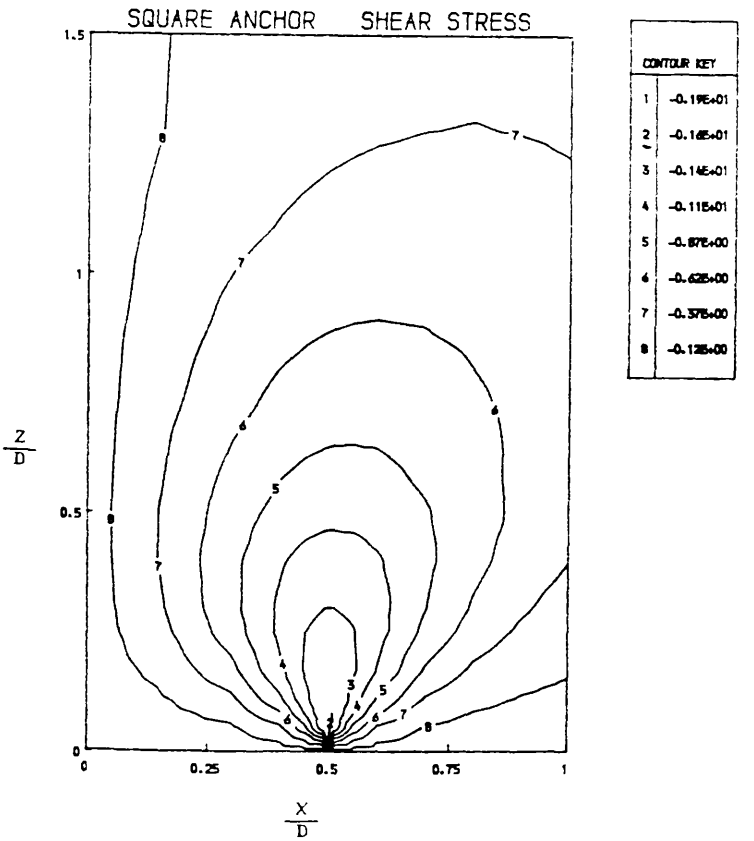

Figure 2.29 $\frac{H}{D} = 2.5 \quad \gamma = 0.4$
$\nu = 0.5 \quad \frac{W}{\sigma_{za}} = 10$

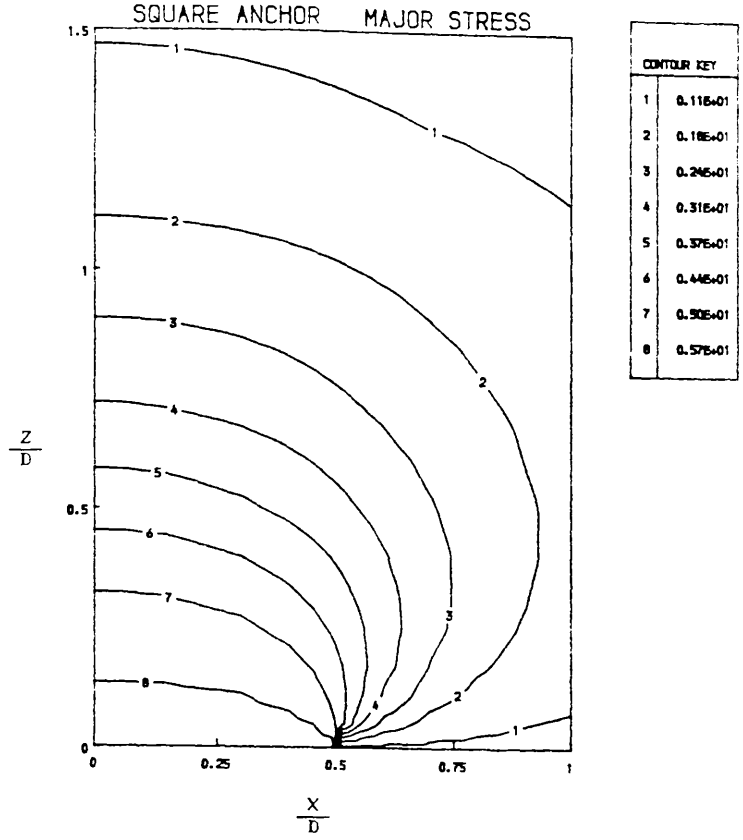

Figure 2.30 $\frac{H}{D} = 2.5 \quad \gamma = 0.4$
$\nu = 0.5 \quad \frac{W}{\sigma_{za}} = 10$

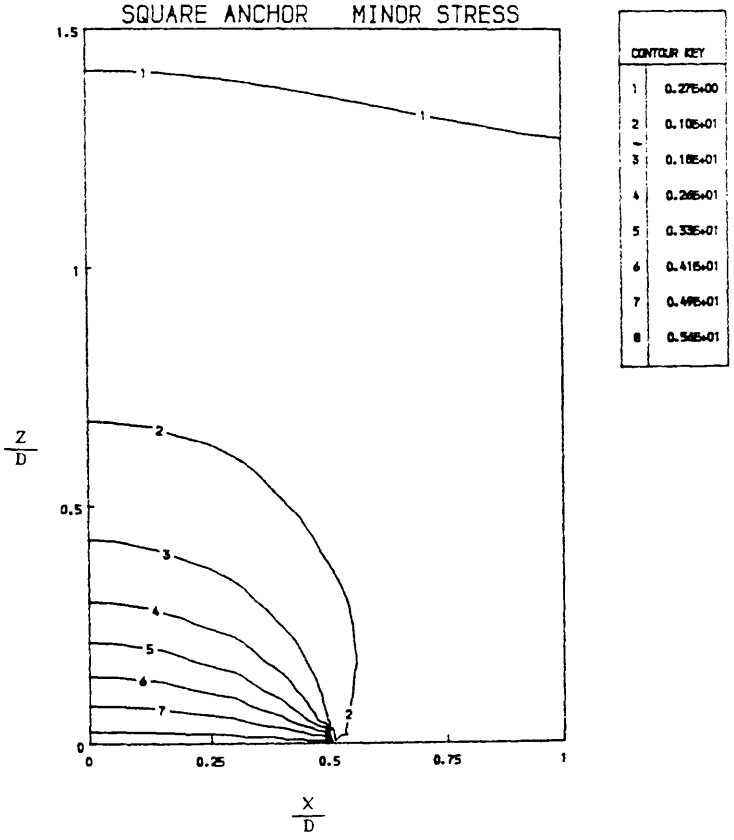

Figure 2.31 $\frac{H}{D} = 2.5 \quad \gamma = 0.4$
$\nu = 0.5 \quad \frac{W}{\sigma_{za}} = 10$

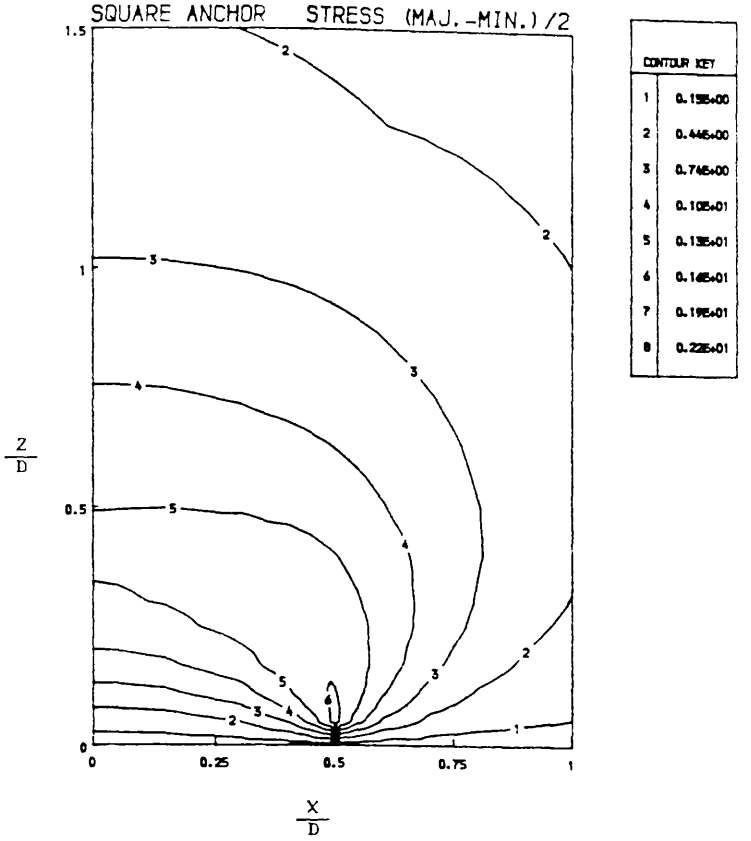

Figure 2.32 $\frac{H}{D} = 2.5 \quad \gamma = 0.4$
$\nu = 0.5 \quad \frac{W}{\sigma_{za}} = 10$

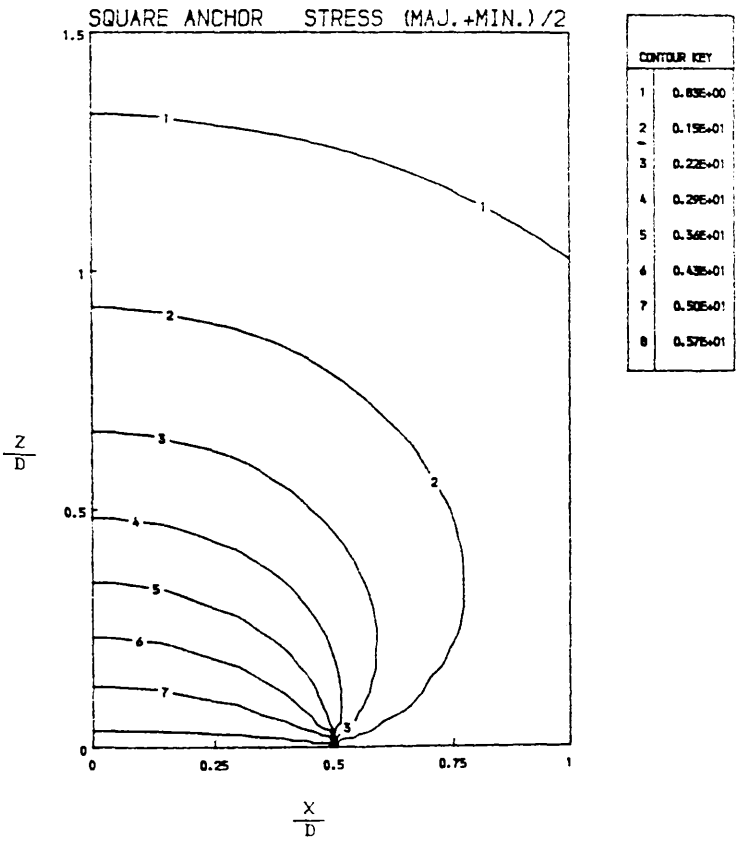

Figure 2.33 $\frac{H}{D} = 2.5 \quad \gamma = 0.4$
$\nu = 0.5 \quad \frac{W}{\sigma_{za}} = 10$

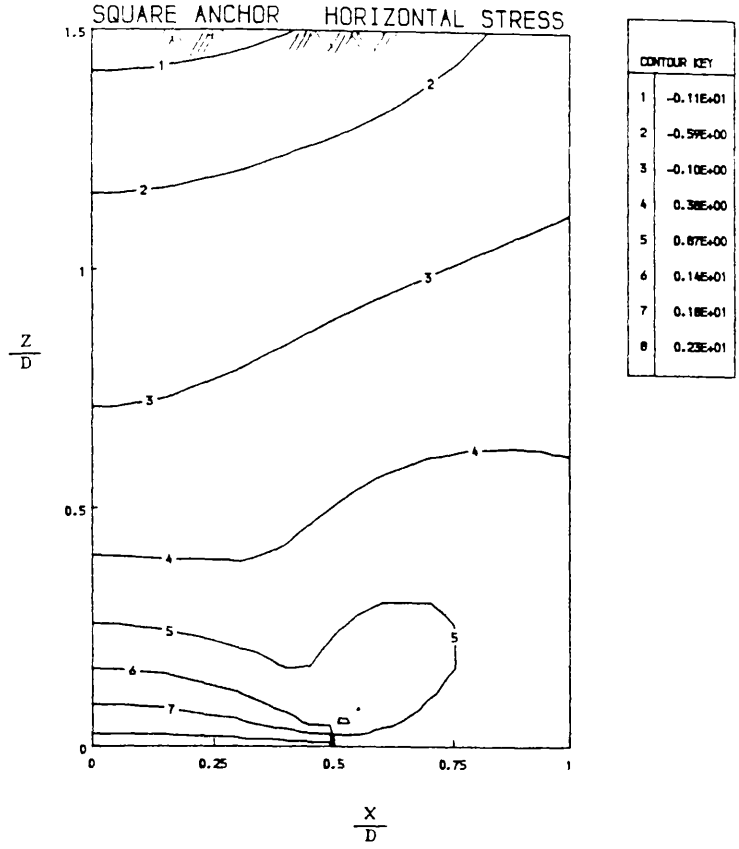

Figure 2.34 $\frac{H}{D} = 1.5 \quad \gamma = \frac{2}{3}$
$\nu = 0.3 \quad \frac{W}{\sigma_{za}} = 10$

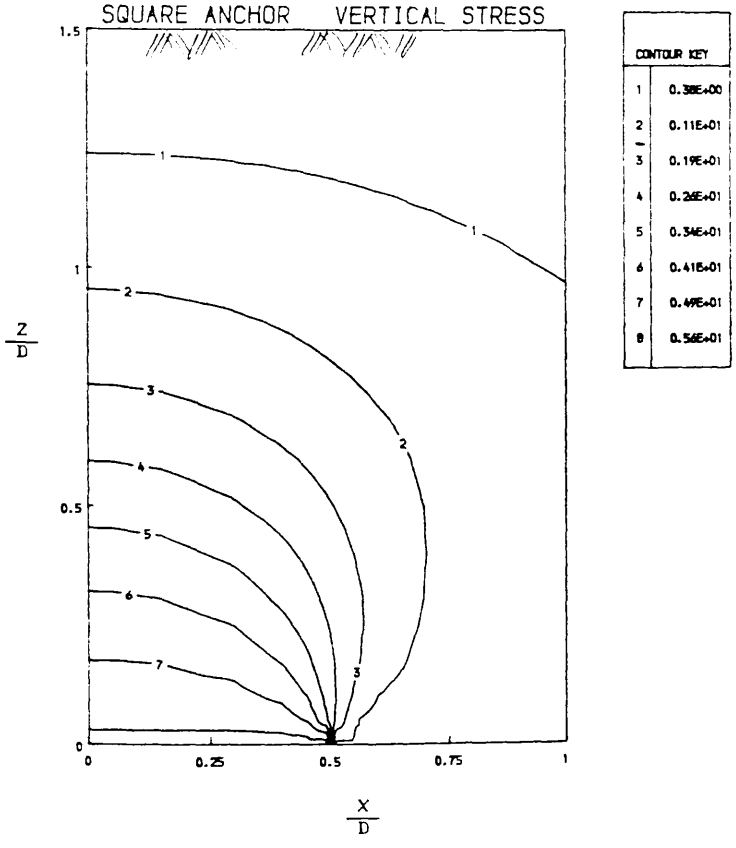

Figure 2.35 $\frac{H}{D} = 1.5 \quad \gamma = \frac{2}{3}$
$\nu = 0.3 \quad \frac{W}{\sigma_{za}} = 10$

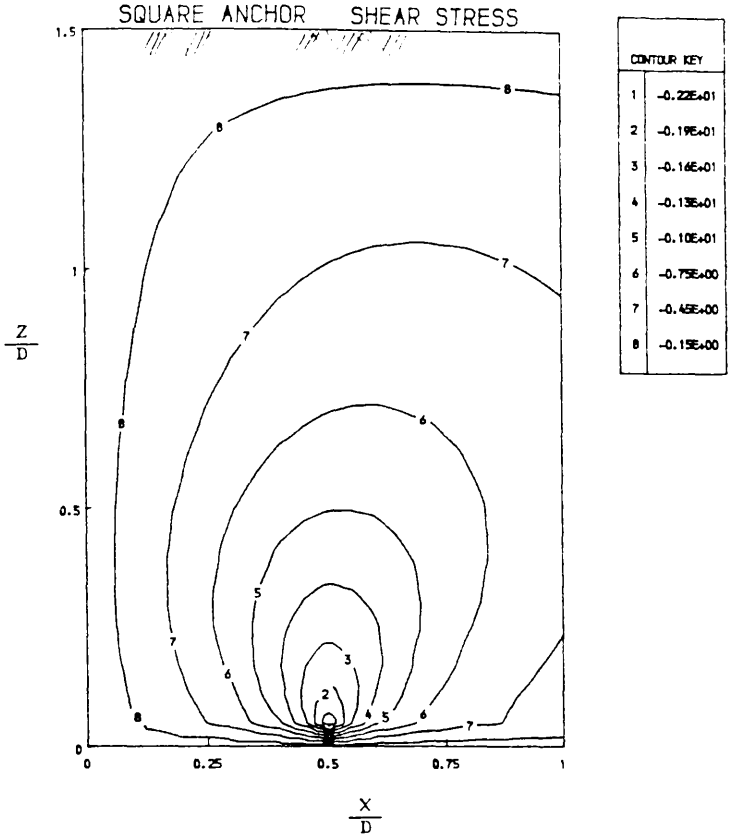

Figure 2.36 $\frac{H}{D} = 1.5 \quad \gamma = \frac{2}{3}$
$\nu = 0.3 \quad \frac{W}{\sigma_{za}} = 10$

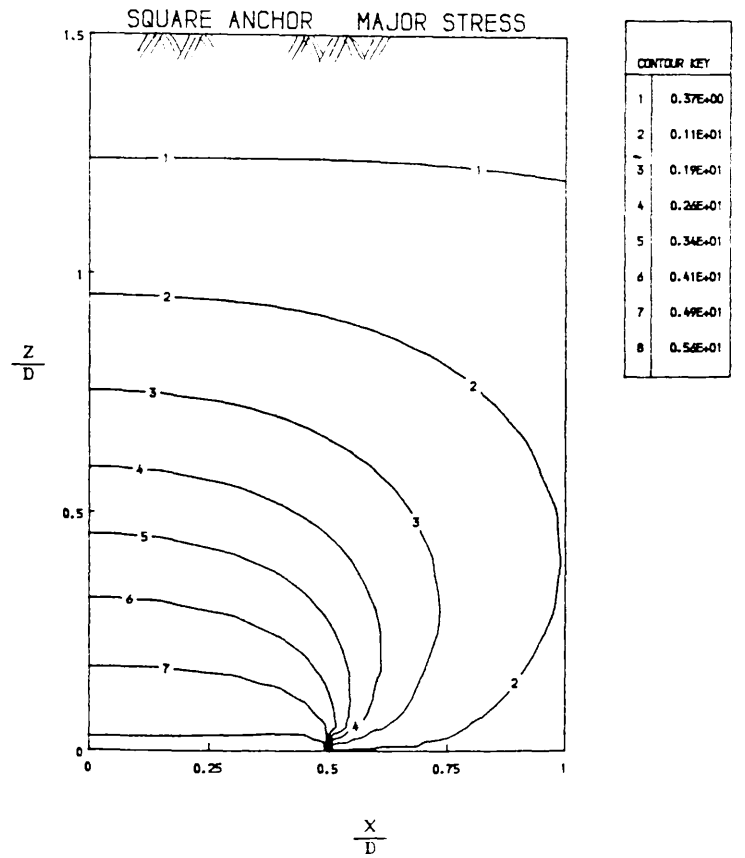

Figure 2.37 $\frac{H}{D} = 1.5 \quad \gamma = \frac{2}{3}$
$\nu = 0.3 \quad \frac{W}{\sigma_{za}} = 10$

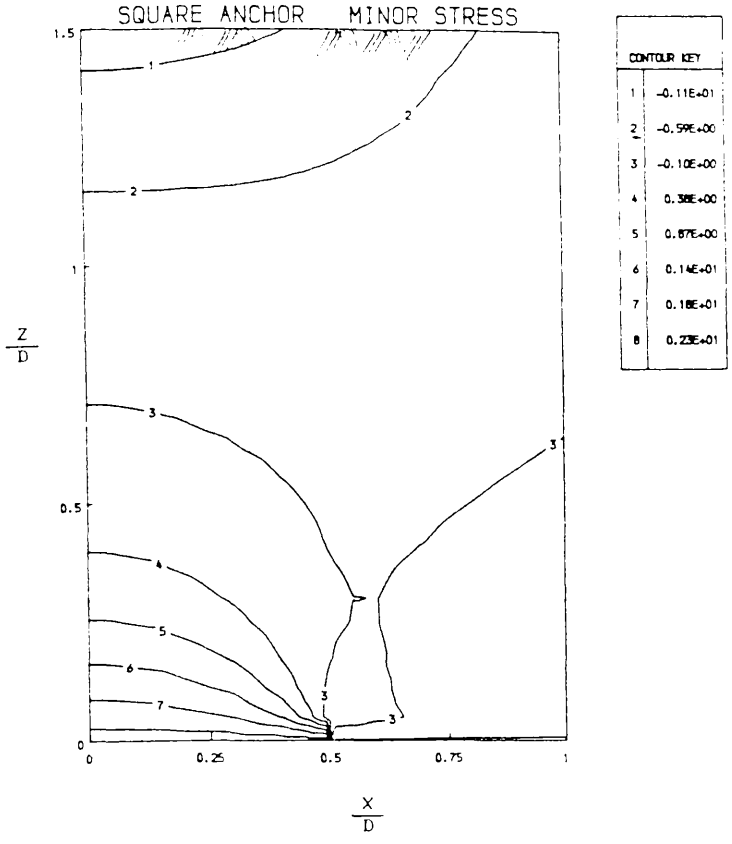

Figure 2.38 $\frac{H}{D} = 1.5 \quad \gamma = \frac{2}{3}$
$\nu = 0.3 \quad \frac{W}{\sigma_{za}} = 10$

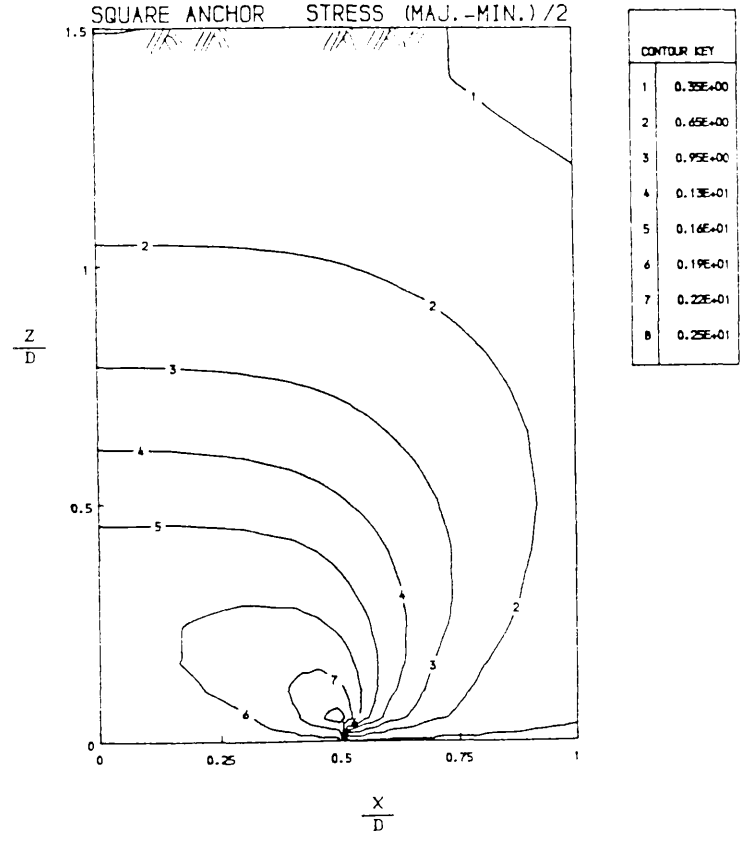

Figure 2.39 $\frac{H}{D} = 1.5 \quad \gamma = \frac{2}{3}$
$\nu = 0.3 \quad \frac{W}{\sigma_{za}} = 10$

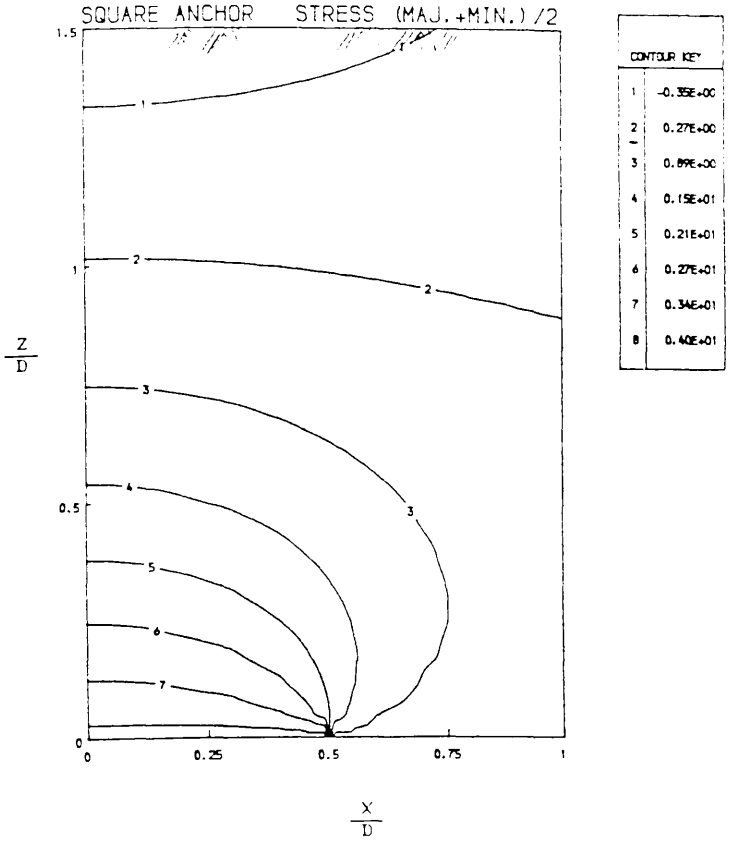

Figure 2.40 $\frac{H}{D} = 1.5 \quad \gamma = \frac{2}{3}$

$\nu = 0.3 \quad \frac{W}{\sigma_{za}} = 10$

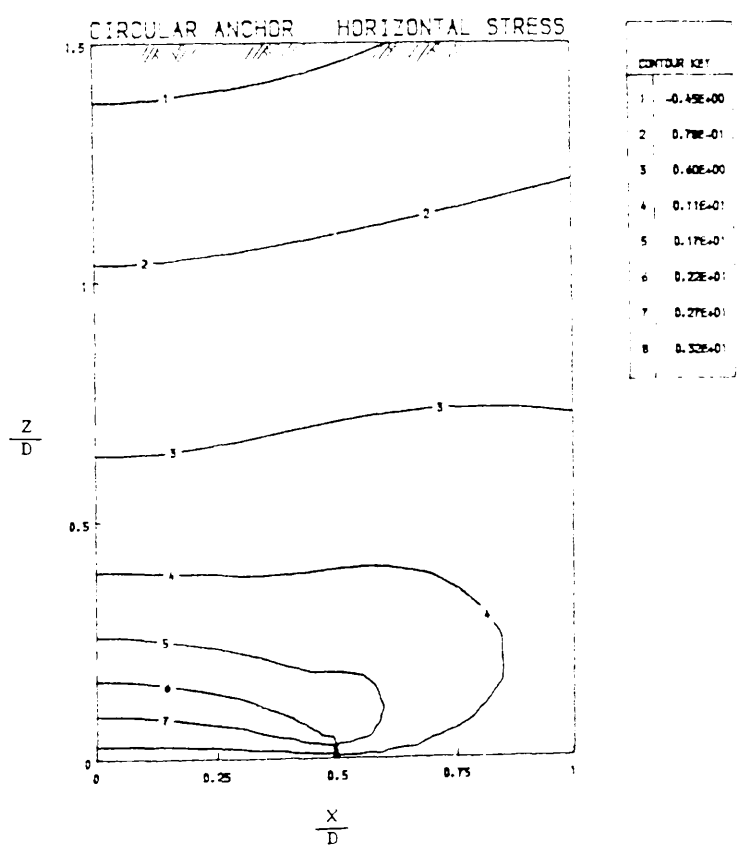

Figure 2.41 $\frac{H}{D} = 1.5 \quad \gamma = \frac{2}{3}$

$\nu = 0.5 \quad \frac{W}{\sigma_{za}} = 5$

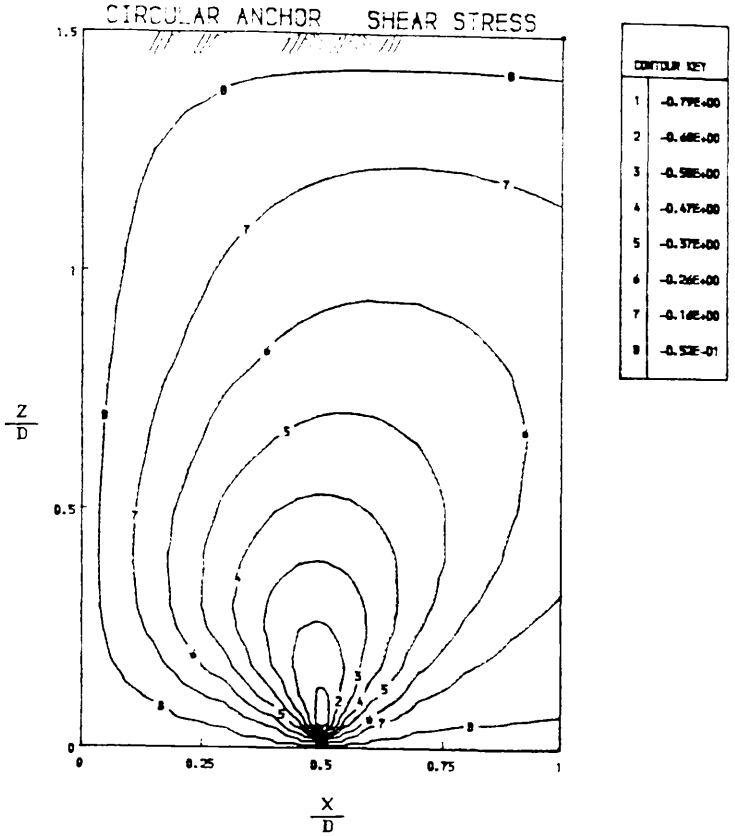

Figure 2.42 $\frac{H}{D} = 1.5 \quad \gamma = \frac{2}{3}$

$\nu = 0.5 \quad \frac{W}{\sigma_{za}} = 5$

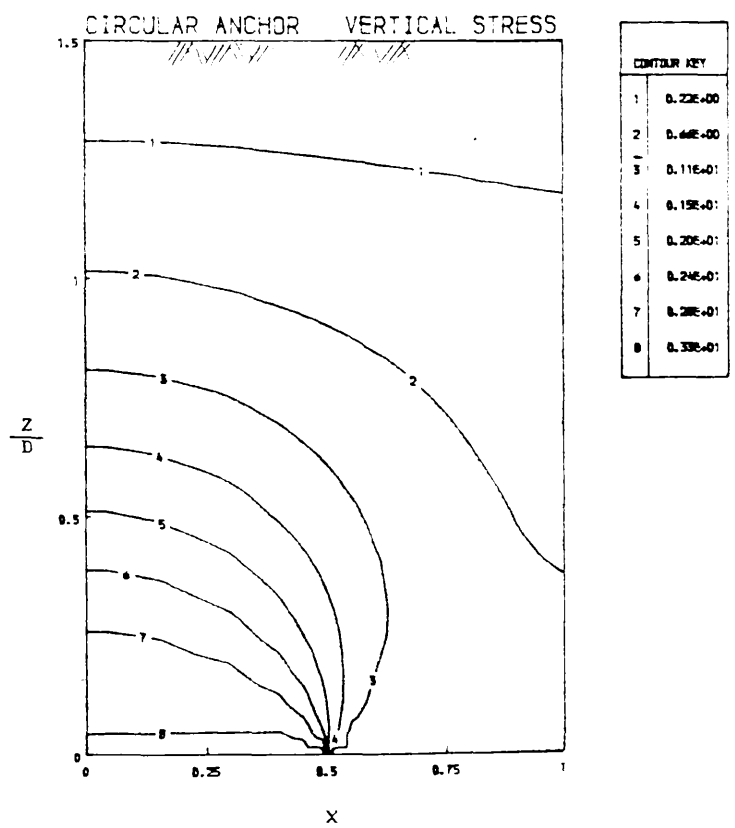

Figure 2.43 $\frac{H}{D} = 1.5 \quad \gamma = \frac{2}{3}$

$\nu = 0.5 \quad \frac{W}{\sigma_{za}} = 5$

CHAPTER 3 CONSTITUTIVE LAWS

3.1 INTRODUCTION:

Realistic *constitutive* (*stress–strain*) *laws* are essential if reliable results are to be obtained using numerical methods of analysis. However, in general, advances in numerical analysis have far exceeded knowledge of the behaviour of materials. As a consequence, very often, results from numerical procedures may be of limited or doubtful validity.

This imbalance has spurred research into the theoretical formulation of constitutive laws and measurement of material parameters. The former involves use of continuum mechanics whereas the latter hinges on accurate measurement of the parameters using sophisticated equipment.

The simplest constitutive laws used in engineering are linear models such as Hooke's law. This law is valid only for a very limited class of materials because many engineering systems are nonlinear at load levels of interest. This is particularly true for soils. In consequence, it is necessary to examine the more complicated theory of elastoplastic flow.

3.2 ELASTO–PLASTICITY:

Many authors such as Desai and Siriwardane[21], Hill[32], Naylor and Pande[59] and Salencon[74] have written books on the subject of elasto– plasticity. The basic concepts are outlined here for completeness.

When solids are unloaded, they may or may not return to their original state. If they return to their original state when the load is removed, the response is

termed elastic. Loading cycles in which part of the deformation is permanent are termed elasto– plastic.

Most materials behave elastically up to a certain level of stress. A typical stress– strain curve for a metal under uniaxial tension is shown in Figure 3.1. When the load is increased, the material behaves elastically up to point A, and regains the original state if the load is removed. If the metal is loaded beyond point A, say up to point B, and then unloaded, there will be some permanent or irrecoverable deformation in the body, and the material is said to have undergone plastic deformations. The stress– strain response depicted in Figure 3.1 exemplifies hardening behaviour, ie, the yield stress on reloading from C is now greater than the original yield stress.

When the metal is loaded from A to B, both elastic and plastic deformations occur, and this is called elastoplastic behaviour. Hence, the total strain ϵ can be written as the summation of the elastic strain ϵ^e and the plastic strain ϵ^p:

$$\epsilon = \epsilon^e + \epsilon^p \qquad (3.1)$$

Because the reloading paths do not follow the original loading path, the strains will be dependent on the stress history. Elasto– plastic behaviour is thus characterised by history– dependent deformation.

3.2.1 Yield Criterion / Function:

The yield criterion can be defined as the limit of elastic deformations, expressed as a function of the stress level. For a one– dimensional state of stress, the yield criterion can be easily defined in terms of the uniaxial compressive stress or uniaxial tensile stress σ_y. However, under multiaxial states of stress, a mathematical expression involving all the stress components is required.

In the case of a uniaxial loading, the yield function may be expressed in the form:

$$f(\underline{\sigma},R) = 0 \qquad (3.2)$$

And for uniaxial loading, this simplifies to:

$$\sigma - \sigma_y(\epsilon^p) = 0 \qquad (3.3)$$

where:

$\underline{\sigma}$ is the stress tensor,

R is the hardening parameter,

σ and σ_y are the uniaxial stress and the yield stress, respectively.

The form of these expressions must be based on experimental observations. The hardening parameter R is usually a function of the plastic strains, that is:

$$R = R(\underline{\epsilon}^p) \qquad (3.4)$$

The yield function $f=0$ is represented, in principal stresses space, by a surface called the yield surface (Figure 3.2). When $f<0$ the behaviour of the material is elastic but when $f=0$ the behaviour of the material is elasto– plastic and the material is in a state of yield. $f>0$ is a physically inadmissible state of stress.

3.2.2 Elementary Yield Criteria:

Experimental evidence shows that the yielding of a metal is not affected significantly by hydrostatic pressure. This assumption leads to the conclusion that the yield criterion depends essentially only on the state of deviatoric stress. Therefore, the yield function for metals can be expressed in terms of the invariants of the deviatoric stress tensor as:

$$f(J_2, J_3, R) = 0 \qquad (3.5)$$

where J_2 and J_3 are the second and the third invariants of the deviatoric stress tensor.

$$J_2 = \tfrac{1}{2}\, s_{ij}\, s_{ij} \qquad (3.6)$$

$$J_3 = {}^1/_3\, s_{ij}\, s_{jk}\, s_{ki} \qquad (3.7)$$

and

$$s_{ij} = \sigma_{ij} - {}^1/_3\, \sigma_{kk}\, \delta_{ij} \qquad (3.8)$$

Von Mises and Tesca yield criteria are the most widely used in metal plasticity and, also, for clays in the case of undrained behaviour (with respect to

total stresses).

a) Von Mises Yield Criterion

According to this theory, yield will initiate when the second invariant of the deviatoric stress tensor reaches a certain value. This criterion was proposed by Von Mises in 1913. According to this criterion,

$$f = J_2 - k^2 \qquad (3.9)$$

where k is a material constant to be determined from experiments. Figure 3.3 shows the Von Mises yield surface in principal stress space.

b) Tresca Yield Criterion

According to this criterion (Tresca, 1864), yielding occurs when the maximum shear stress reaches some value. In general, the Tresca criterion can be expressed in terms of principal stresses as:

$$f = \sigma_{max} - \sigma_{min} - 2k = 0 \qquad (3.10)$$

where k is the material constant.

If a total stress analysis is carried out, this criterion is applicable to saturated clay soils under undrained conditions when k becomes equal to c_u, the "undrained shear strength". Figure 3.4 shows the Tresca yield criterion in principal stress space.

c) Mohr–Coulomb Yield Criterion:

The yield criteria described in the previous sections assume that yielding of the material is independent of the hydrostatic stress. However, for effective stress analyses of soils such criteria are not relevant. According to the Mohr–Coulomb criterion, the shear strengths of soils increase with increasing normal effective stress on the failure plane:

$$\tau = c + \sigma \tan\varphi \qquad (3.11)$$

where:

τ is the shear stress on the failure plane,

σ is the normal effective stress on the failure plane,

c is the cohesion of the material,

φ is the angle of internal friction.

This yield criterion is shown in principal stress space and Π– plane in Figure 3.5. In terms of principal stresses, Mohr– Coulomb's criterion becomes:

$$\frac{\sigma_1 - \sigma_3}{2} = \frac{\sigma_1 - \sigma_3}{2} \sin\varphi + c \cos\varphi \qquad (3.12)$$

According to this criterion, the yield strength in "compression" is higher than that in "extension", (Figure 3.5b) in the triaxial test sense. It should be noted that the Mohr– Coulomb criterion is expressed in terms of maximum and minimum principal stresses, and hence does not incorporate the effect of intermediate principal stress. Therefore, the description of the Mohr– Coulomb criterion in terms of conventional forms of stress invariants becomes difficult. The simplest way to describe the criterion is in terms of the Lode angle θ where:

$$\theta = -\frac{1}{3} \sin^{-1}\left[-\frac{3\sqrt{3}}{2} \frac{J_3}{J_2^{1.5}}\right] \qquad (3.13)$$

$$-\pi/6 \leqslant \theta \leqslant \pi/6$$

Figure 3.6 shows $\sqrt{J_2}$, I_1 and θ forming cylindrical coordinates in principal stress space. The space diagonal represents states of equal– all– round stress, or mean stress. $\sqrt{J_2}$, or the deviatoric stress, measures the deviation from this and θ measures the orientation in the normal or Π plane.

The set of invariants I_1, J_2 and θ can be used to describe the Mohr– Coulomb criterion conveniently in three– dimensional stress– space in the form;

$$f = \frac{I_1}{3}\sin\theta + \sqrt{J_2}\cos\theta - \frac{\sqrt{J_2}}{3}\sin\varphi\sin\theta - c\cos\varphi = 0 \qquad (3.14)$$

where $I_1 = \sigma_1 + \sigma_2 + \sigma_3$

When $\varphi = 0$, the Mohr-Coulomb criterion reduces to the Tresca criterion.

3.2.3 Hardening Behaviour:

Hardening is said to occur when the yield stress of a material increases during elasto–plastic loading. Figure 3.8 depicts hardening, softening and ideal (elastic–perfectly plastic) material behaviour in response to uniaxial loading. Hardening can be related to the degree of plastic straining which the material has suffered (or the amount of work dissipated during this straining) in changing the state of the material. Hence, the terms "strain hardening" or "work hardening" are often used to describe this phenomenon.

For multiaxial states of stress (Figure 3.9), hardening may involve an expansion of the yield surface (isotropic hardening) or translation (kinematic hardening) or a combination of both. Kinematic hardening is necessary to describe such phenomena as the Bauschinger effect in cyclic loading (Figure 3.7).

3.2.4 Plastic Potential, Flow Rule

It is assumed that the flow of material at yield is governed by some function of current stresses called the plastic potential – by analogy with Newtonian potential functions. The plastic potential Q assumes a similar form to the yield function f and is expressed as:

$$Q(\underline{\sigma}) = 0 \qquad (3.16)$$

The normality principle states that the plastic strain increment tensor is linearly related to the gradient of the plastic potential through the stress point, ie,

$$d\underline{\epsilon}^P = d\lambda \frac{\partial Q(\underline{\sigma})}{\partial \underline{\sigma}} \qquad (3.17)$$

where $d\lambda$ is a non−negative scalar called the plasticity multiplier

The plastic potential is said to be associated when the yield function and the plastic potential are defined by the same expression ($f = Q$). In associated flow, the material satisfies the normality condition with respect to the yield surface, ie:

$$d\underline{\epsilon}^p = d\lambda \frac{\partial f}{\partial \underline{\sigma}} \qquad (3.18)$$

For geological materials, the equation of the plastic potential is often different from that of yield surface; that means that the flow is non−associated. However, for simplicity associated flow is often assumed in practice.

3.2.5 Formulation of Stress−Strain Relation:

The aim of this section is to gather the threads together to obtain the relation between stress and strain increments during elasto−plastic flow. The objective is then to seek the form of D^{ep} in the equation:

$$d\underline{\sigma} = D^{ep}\, d\underline{\epsilon} \qquad (3.19)$$

where $d\underline{\sigma}$ and $d\underline{\epsilon}$ are increments of the stress and total (elastic plus plastic) strain tensors and D^{ep} is the elasto−plastic constitutive matrix. Firstly, the additivity postulate can be used to write:

$$d\underline{\epsilon} = d\underline{\epsilon}^e + d\underline{\epsilon}^p \qquad (3.20)$$

where $\underline{\epsilon}^e$ and $\underline{\epsilon}^p$ denote elastic and plastic components of strain, respectively.

Secondly, the stresses are related to the elastic components $d\underline{\epsilon}^e$ of the strains through an elastic matrix D^e, that is:

$$d\underline{\sigma} = D^e\, d\underline{\epsilon}^e \qquad (3.21)$$

Substituting (3.20) in (3.21) leads to:

$$d\underline{\sigma} = D^e\, (d\underline{\epsilon} - d\underline{\epsilon}^p) \qquad (3.22)$$

Thirdly, the plastic strain increments are related to the flow rate, ie:

$$d\underline{\epsilon}^p = d\lambda \frac{\partial Q}{\partial \underline{\sigma}} \qquad (3.23)$$

Fourthly, the yield function is given by:

$$f(\underline{\sigma},R) = 0 \qquad (3.24)$$

in which $R = R(\underline{\epsilon}^p)$ is the hardening parameter.

It is a fundamental assumption that during plastic yield the stress remains on the yield surface. This 'consistency condition' implies that:

$$df(\underline{\sigma},R) = 0 \qquad (3.25)$$

Expanding this relation by the chain rule yields:

$$\frac{\partial f}{\partial \underline{\sigma}}^T d\underline{\sigma} + \frac{\partial f}{\partial R} \frac{\partial R}{\partial \underline{\epsilon}^p} d\underline{\epsilon}^p = 0 \qquad (3.26)$$

Substituting (3.21) and (3.23) into (3.20) leads to:

$$d\underline{\epsilon} = [D^e]^{-1} d\underline{\sigma} + d\lambda \frac{\partial Q}{\partial \underline{\sigma}} \qquad (3.27)$$

Substituting (3.24) into (3.26) leads to:

$$\frac{\partial f}{\partial \underline{\sigma}}^T d\underline{\sigma} + \frac{\partial f}{\partial R} \frac{\partial R}{\partial \underline{\epsilon}^p} d\lambda \frac{\partial Q}{\partial \underline{\sigma}} = 0 \qquad (3.28)$$

Defining a parameter H by:

$$\frac{\partial f}{\partial \underline{\sigma}}^T d\underline{\sigma} = H\, d\lambda \qquad (3.29)$$

and substituting in (3.28) gives:

$$H = - \frac{\partial f}{\partial R} \left[\frac{\partial R}{\partial \underline{\epsilon}^p}\right]^T \frac{\partial Q}{\partial \underline{\sigma}} \qquad (3.30)$$

Multiplying equation (3.27) by $(\partial f/\partial \underline{\sigma})^T D^e$ and replacing the matrix product $D^e [D^e]^{-1}$ by the identity matrix, leads to:

$$\frac{\partial f}{\partial \underline{\sigma}} D^e d\underline{\epsilon} = \frac{\partial f}{\partial \underline{\sigma}} d\underline{\sigma} + \frac{\partial f}{\partial \underline{\sigma}} D^e d\lambda \frac{\partial Q}{\partial \underline{\sigma}} \qquad (3.31)$$

Eliminating $\frac{\partial f}{\partial \underline{\sigma}} d\underline{\sigma}$ by (3.29) and rearranging, gives:

$$\lambda = \frac{1}{A} \frac{\partial f}{\partial \underline{\sigma}}^T D^e d\underline{\epsilon} \qquad (3.32)$$

in which

$$A = H + \frac{\partial f}{\partial \underline{\sigma}}^T D^e \frac{\partial Q}{\partial \underline{\sigma}} \qquad (3.33)$$

Rearranging (3.31) leads to:

$$d\underline{\sigma} = D^e \, d\underline{\epsilon} - d\lambda \, D^e \frac{\partial Q}{\partial \underline{\sigma}} \qquad (3.34)$$

Substitution of (3.32) into (3.33) gives the required relation between $d\underline{\sigma}$ and $d\underline{\epsilon}$, ie equation (3.34).

The elasto-plastic constitutive matrix D^{ep} is then:

$$D^{ep} = D^e - \frac{1}{A} D^e \frac{\partial Q}{\partial \underline{\sigma}} \frac{\partial f}{\partial \underline{\sigma}}^T D^e \qquad (3.35)$$

For associated flow, the function Q is replaced by the yield function f.

3.3 CAM CLAY MODELS BASED ON THE CRITICAL STATE CONCEPT:

The ultimate objective of this chapter is to conduct a numerical investigation of some constitutive models for sand. However, since the behaviour of sand is rather complicated, we consider first the simple Cam clay model in order to develop some understanding of the fundamentals of soil behaviour.

3.3.1 Introduction:

Roscoe et al.[75] proposed models for the yielding of soils based on the theory of plasticity. The basic state parameters used in the development of the critical state models are the mean effective stress p, deviatoric stress q, and the void ratio e. With respect to the cylindrical triaxial configuration, these parameters take the forms described below for the axisymmetric condition, $\sigma_2 = \sigma_3$:

$$p = \frac{\sigma_1 + 2\sigma_3}{3} = \frac{I_1}{3} \qquad (3.36)$$

$$q = \sigma_1 - \sigma_3 = [3 \, J_2]^{\frac{1}{2}} \qquad (3.37)$$

It is also convenient to define the volumetric strain ϵ_v and the distortional strain ϵ_d as follows:

$$\epsilon_v = \epsilon_1 + 2\epsilon_3 \tag{3.38}$$

$$\epsilon_d = 2\,(\epsilon_1 - \epsilon_3)/3 \tag{3.39}$$

3.3.2 Concept of Critical Void Ratio (Critical Density):

When a loose soil sample is sheared, it passes through progressive states of yielding before reaching a state of collapse. The yielding continues until the material reaches a critical void ratio, after which the void ratio remains constant during subsequent deformation (Figure 3.10). That is, the material reaches a state in which no volume change takes place during further shearing. This state is called the critical state and the corresponding void ratio is called the critical void ratio. When a dense soil sample is sheared to failure, it reaches a peak shear stress as shown in Figure 3.10a. Initially the material compacts, and then it dilates until the volumetric strain reaches a constant value which corresponds to its critical value. It has been observed that a soil with a void ratio lower than the critical value (dense soil) deforms in such a manner as to increase its volume, whereas at a void ratio higher than the critical value (loose soil) the deformations will decrease the volume.

3.3.3 Associated– Modified Cam Clay:

The constitutive laws on which this model is based are very simple and, as the name suggests, involve an associated flow rule. The theory on which this model is founded is summarised in the following.

Consolidation behaviour:

The elasto– plastic model is partly based on observations of consolidation and swelling behaviour . During consolidation, along AB (Figure 3.11), the void ratio of the material decreases according to the following equation:

$$e = e_1 - \lambda \ln(p/p_1) \tag{3.40}$$

where λ, the slope of the consolidation curve, is a fundamental material parameter.

p_1 is some reference stress on the consolidation curve.

If the material follows the path BC the soil swells as a consequence of reduction in the effective mean stress, and the expression is for void ratio becomes:

$$e = e_0 - \kappa \ln(p/p_0) \qquad (3.41)$$

where κ, the slope of the rebound curve, is also a fundamental material parameter,and p_0 is the past maximum mean effective stress (yield stress). Void ratio changes along the swelling line are reversible, ie, elastic.

The two previous equations can be written in an incremental form:

$$de = - \lambda \, dp/p \qquad (3.40a)$$

$$de^e = - \kappa \, dp/p \qquad (3.41b)$$

Recalling:

$$de = de^e + de^p$$

and noting that:

$$d\epsilon_v = \frac{de}{1+e} \qquad (3.42)$$

then

$$d\epsilon_v^p = - \frac{\lambda - \kappa}{1+e} \quad \frac{dp}{p} \qquad (3.43)$$

Since p_0 takes the role of the hardening parameter the strain hardening relationship is:

$$dp_0 = - \frac{1+e}{\lambda-\kappa} \, d\epsilon_v^p \, p_0 \qquad (3.44)$$

Yield function and plastic flow:

The expression of the yield function for the associated modified Cam clay is the ellipse shown in Figure 3.12.

$$f = p^2 - pp_0 + (q/M)^2 = 0 \qquad (3.45)$$

where M is the slope of the Mohr–Coulomb line in p–q space.

For triaxial compression ($\sigma_2 = \sigma_3$),

$$M = \frac{6 \sin\varphi}{3 - \sin\varphi} \qquad (3.46)$$

Because the failure line lies below the ellipse for overconsolidated soils, this implies softening behaviour in such soils. Of course, for associated flow, the plastic potential and the yield function are identical, ie,

$$Q = f \qquad (3.47)$$

Derivatives

Before calculating any derivatives involved in the constitutive equations some parameters need to be defined for the case of axisymmetric problem. First, the mean effective stress:

$$p = \frac{\sigma_r + \sigma_\theta + \sigma_z}{3} \qquad (3.48)$$

and the deviatoric stress,

$$q = \{ \tfrac{1}{2} [(\sigma_z-\sigma_r)^2 + (\sigma_z-\sigma_\theta)^2 + (\sigma_\theta-\sigma_r)^2 + 6\,\tau_{rz}^2] \}^{\frac{1}{2}} \qquad (3.49)$$

and the elastic constitutive matrix

$$[D^e] = \frac{E}{(1+\nu)(1-2\nu)} \begin{bmatrix} 1-\nu & \nu & \nu & 0 \\ & 1-\nu & \nu & 0 \\ & \text{SYM.} & 1-\nu & 0 \\ & & & \frac{1-2\nu}{2} \end{bmatrix} \qquad (3.50)$$

The following derivatives are substituted into the the elasto–plastic stiffness matrix.

$$\frac{\partial f}{\partial \underline{\sigma}} = \frac{\partial f}{\partial p}\frac{\partial p}{\partial \underline{\sigma}} + \frac{\partial f}{\partial q}\frac{\partial q}{\partial \underline{\sigma}} \qquad (3.51)$$

$$\frac{\partial Q}{\partial \underline{\sigma}} = \frac{\partial f}{\partial \underline{\sigma}} \qquad (3.52)$$

$$\frac{\partial p}{\partial \underline{\sigma}} = \begin{bmatrix} \frac{1}{3} & \frac{1}{3} & \frac{1}{3} & 0 \end{bmatrix}^T \qquad (3.53)$$

$$\frac{\partial q}{\partial \underline{\sigma}} = \frac{3}{2q} \begin{bmatrix} \sigma_z-p & \sigma_r-p & \sigma_\theta-p & 2\tau_{rz} \end{bmatrix}^T \qquad (3.54)$$

$$\frac{\partial f}{\partial p} = 2p - p_0 \tag{3.55}$$

$$\frac{\partial f}{\partial q} = \frac{2q}{M^2} \tag{3.56}$$

$$\frac{\partial Q}{\partial p} = \frac{\partial f}{\partial p} \tag{3.57}$$

$$\frac{\partial Q}{\partial q} = \frac{\partial f}{\partial q} \tag{3.58}$$

$$\frac{\partial f}{\partial p_0} = - p \tag{3.59}$$

And from the flow rule we derive the following equations:

$$d\epsilon_v^p = d\lambda \frac{\partial Q}{\partial p} \tag{3.60}$$

and

$$d\epsilon_d^p = d\lambda \frac{\partial Q}{\partial q} \tag{3.61}$$

The elasto-plastic constitutive matrix is hence:

$$[D^{ep}] = [D^e] - \frac{[D^e] \frac{\partial Q}{\partial \underline{\sigma}} \frac{\partial f}{\partial \underline{\sigma}}^T [D^e]}{\frac{\partial f}{\partial \underline{\sigma}}^T [D^e] \frac{\partial Q}{\partial \underline{\sigma}} - \frac{\partial f}{\partial p_0} \frac{dp_0}{d\epsilon_v^p} \frac{\partial Q}{\partial p}} \tag{3.62}$$

3.3.4 Results:

A computer program, listed in the appendix, simulating the response of associated Cam clay was written. Several example problems were solved by this program and two of these are discussed below. The first example represents the predicted undrained behaviour of Cam clay in a conventional triaxial test in compression. The second one shows the predicted drained behaviour of Cam clay under K_0 condition. In the first case, two "samples" with different values of over-consolidation ratio (O.C.R.= 1.25 and O.C.R.= 5) were considered. In the second example, a third sample with a value of overconsolidation ratio O.C.R.= 10 was also analysed.

The fundamental parameters of the clay used in these examples ran were:

λ = 0.14

κ = 0.05

ν = 0.20

e = 1.00

φ = 30.0°

p_0 = 125 kPa

Figure 3.13 shows the predicted effective and total mean stress during undrained loading of normally consolidated (wet) and overconsolidated (dry) Cam clay.

The total stress path has a constant slope of 3/1 as shown in the figure. However, the effective stress path is vertical at the beginning (elastic behaviour) until it intersects the yield surface. The path then passes through successive states of yielding before it attains the failure state represented in Figure 3.13 by the critical state line of slope M. The hardening behaviour of normally consolidated (or wet) clays is shown by a continuous expasion of the subsequent yield surfaces until collapse. But, the effective stress path predicted for an over–consolidated (or dry) clay shows continuous contraction of the yield surface (softening) until the critical state line is attained.

The predicted stress–strain behaviour of associated Cam clay is shown in Figure 3.14 where the shear stress, for over–consolidated clay, increases up to a peak value then decreases to the critical state value. However, the shear stress in the normally consolidated clay increases continuously up to failure. This means, that the material hardens. It is worth noting that the stress strain behaviour of normally consolidated clay is similar to that of dense sand and the behaviour of normally consolidated clay is similar to that of loose sand as shown in Figure 3.10.

The pore water pressure response predicted during undrained triaxial compression is shown in Figure 3.15. In an over–consolidated clay the pore pressure increases up to a peak value then decreases until reaching a negative value. Therefore, if the soil sample were to be remoulded by somebody with wet hands, it would suck up water and dry that person's hands, hence the term 'dry'. The pore water pressure response depicted in Figure 3.15 by a normally consolidated clay shows a continuous increase of the pore pressure. This positive pore pressure would cause water to drain out of the soil which explains why normally consolidated soils are called 'wet'.

Figure 3.16 shows the effective stress paths followed by three samples of Cam clay having the same past maximum effective stress p_0 but different initial mean effective stress p. The three curves start from different positions then converge to form one straight line under K_0 loading, ie:

$$d\epsilon_2 = d\epsilon_3 = 0$$

Figure 3.17 shows the predicted stress–strain relations corresponding to the test conditions described previously. For the normally consolidated clay, the strain increases continuously with the deviatoric stress. For over–consolidated clays, a nonlinear elastic stress–strain response at low stress levels is followed by plastic flow at constant deviatoric stress. Finally, the soil hardens progressively.

3.4 ROWE'S STRESS–DILATANCY RELATION:

The angle of dilatancy (or shortly, dilatancy) may be described as the change in volume that is associated with the shear distortion of an element of granular material. Consider a pack of spheres arranged in a state of packing which is as dense as possible. If any shear distortion occurs, the relative positions of the spheres must change, and the total volume of the pack must increase. This volume change is termed dilatancy.

The stress– dilatancy equation is the name given to the particular equation (flow rule) developed by Rowe[68,69], namely:

$$R = K\ D \tag{3.63}$$

where

$$R = \frac{\sigma_1}{\sigma_3} \tag{3.64}$$

and

$$D = -\ c\ \frac{d\epsilon_3^p}{d\epsilon_1^p} \tag{3.65}$$

c = 2 for compression,

c = ½ for extension, and

c = 1 for plane strain.

The coefficient K is an energy ratio.

$$K = \tan^2\ (\tfrac{1}{4}\ \pi + \tfrac{1}{2}\ \varphi_f) \tag{3.66}$$

where φ_f is an angle of friction which depends on relative density and stress state, and

$$\varphi_\mu \leqslant \varphi_f \leqslant \varphi_{cv} \tag{3.67}$$

where

φ_μ is the angle of friction between the mineral particles, and φ_{cv} is the angle of friction at the critical void ratio.

Some particular values of φ_f are given in the following.

Triaxial compression and extension:

– dense sand before peak: $\varphi_f = \varphi_\mu$

– dense sand at large strains: $\varphi_f = \varphi_{cv}$

– loose sand for any strain level: $\varphi_f = \varphi_{cv}$

Plane strain:

$$\varphi_f = \varphi_{cv}$$

Rowe's stress– dilatancy equation is used by Vermeer[89] as the flow rule for cone hardening in a model which is discussed later in this chapter.

3.5 STRAIN SOFTENING IN SANDS:

There are a number of materials, including sand, which exhibit a phenomenon called strain–softening. Materials which exhibit such softening are characterised by a stress–strain response in which the stress rises monotonically with strain to a peak, and then decreases with further increase in strain (Figure 3.8b). In the following section, experimental observations and results obtained by various authors are discussed.

3.5.1 Experimental Observations:

The evidence of strain–softening in sands comes essentially from standard triaxial compression tests on dense specimens. It is well known that, because of friction between the end platens and the specimen and the development of various bifurcation modes, it is difficult in such tests to maintain a state of homogeneous deformation within the specimen as the deformation progresses. It was shown by Hettler and Vardoulakis[33] that experiments with perfect boundary conditions (ideally lubricated) and perfectly homogeneous material cannot ensure, in general, homogeneous deformation, since various modes of bifurcation develop. Examples of such instabilities are barreling, bulging, necking and shear banding.

Careful testing of sand by Denam[18], Hettler[35], Vardoulakis[82,85,86], Hettler and Vardoulakis[33] and many others have established that when sand is deformed homogeneously in triaxial compression very little or no strain–softening occurs at axial strains up to at least 10%. For larger strains, bifurcation modes develop, producing subsequent non–homogeneous deformation accompanied by pronounced strain–softening. More recent work by Vardoulakis et al[83] shows how a tiny zone of inhomogeneity expands and creates a shear band.

3.5.2 Numerical Modelling:

Pietruszczak and Mroz[64], Nayak and Zienkiewicz[58] and others have implemented analyses in which the constitutive relations allow for strain–softening. Other researchers have approached the problem in different ways. For example, Desai's viewpoint[22] on strain–softening is that the degradation associated with strain–softening can be considered to be caused by disruption in the internal constitution of the material due to formation of discontinuities such as microcracks, fractures, and voids. Hence, softening material is no longer continuous and a plasticity model that is based on the theory of continua may no longer be applicable. For him, an alternative solution would be to combine the continuum model with appropriate modification of the numerical technique to allow for the discontinuities. This approach poses many difficulties.

3.5.3 Concluding Remarks:

The studies quoted previously demonstrate that the strain–softening observed in the conventional triaxial tests on dense sands is not a true material property but the result of inhomogeneous deformation due to either end plate friction or instability modes. Drescher and Vardoulakis[23] drew the following conclusion based on Hettler's work: "These results mean that true material softening is very slow and can be neglected for relatively large strains after the limiting state has been reached.". A more recent paper by Muhlhaus and Vardoulakis[55] stated that shear bands have a thickness and that this thickness was a small multiple of the mean grain size as Roscoe[67] hypothesized. It is clearly very difficult to include strain softening (as generally understood) in analyses of boundary value problems since continuum models are antithetical to softening. In the following section, we consider one of the leading continuum models for sand.

3.6 VERMEER'S MODEL FOR SAND:

Several constitutive models for sands exist in literature including those proposed by Desai[20], Lade [43], Pietruszczak and Mroz[64], Nova and Wood [60], Nova[61,62], etc... for both monotonic and cyclic loading. Vermeer's model was chosen for study herein because it uses a relatively small number of parameters and is more general than most. In the following, the history of this model and the theory on which it is based are briefly given.

3.6.1 History:

The first version of Vermeer's model [87] was based on data from triaxial tests. The model has two yield surfaces, a distortion (or cone) yield surface and a consolidation (or cap) yield surface. The names cap and cone are related to the shapes of the associated yield surfaces (Figure 3.19). The expression for the total strain is

$$\epsilon = \epsilon^e + \epsilon^p + \epsilon^c \qquad (3.68)$$

where

ϵ is the total strain,

ϵ^e is the elastic strain,

ϵ^p is the plastic strain related to the cone yield surface, and

ϵ^c is the plastic strain related to the cap yield surface.

In 1978, Vermeer established a more general three–dimensional theory using the failure criterion defined by Matsuoka and Nakai[50]. Kenter and Vermeer then derived the corresponding plane strain equations and analysed some boundary value problems by means of the finite element method. In 1980–1981, Vermeer[88] presented a new version of the model in principal stress space using five parameters. This represented an improvement over the previous version which involved seven parameters.

3.6.2 Basic Concepts:

The latest version of Vermeer's model[89] is based on four empirical laws. The first one is a non–incremental Hookean law for the elastic strains. The second law describes the shear dilatancy involving a close approximation of Rowe's stress–dilatancy equations. The third law is a hyperbolic relation between the shear strain and the shear stress. Finally, there is a power law for the volumetric strain in compression. Plasticity theory is used as a framework for unifying these elements into a coherent whole.

3.6.3 Elastic Strains:

The elastic behaviour of the soil is assumed to be nonlinear. Vermeer adopted a non–incremental Hookean law using the secant shear modulus G_s.

$$\epsilon_i^e = \frac{1}{2\,G_s}\,\sigma_i \qquad i = 1,2,3 \qquad (3.69)$$

with

$$G_s = G_0 \left[\frac{\sigma}{p_0}\right]^{1-\beta} \qquad (3.70)$$

and

$$\sigma = \left[\frac{1}{3}\,\sigma_i\,\sigma_i\right]^{\frac{1}{2}} \qquad (3.71)$$

β, G_0 and p_0 are three model parameters.

In his Grenoble paper[89], during the workshop conference, Vermeer took $G_0 = 75$ MPa, $p_0 = 200$ kPa (p_0 is an arbitrary reference stress) and $\beta = \frac{1}{4}$ for dense Karlsruhe sand. These elastic strains are actually the derivatives of a complementary strain–energy function W with the property:

$$\epsilon_i^e = \frac{\partial W}{\partial \sigma_i} \qquad (3.72)$$

where

$$W = W_0\,\sigma^{1+\beta} \qquad (3.73)$$

and

$$W_0 = \frac{3}{2\,G_0}\,\frac{p_0^{1-\beta}}{1+\beta} \qquad (3.74)$$

the energy function leads to the expression:

$$\epsilon_i^e = \frac{\partial W}{\partial \sigma_i} = \frac{\sigma_i}{2\ G_s} \qquad (3.75)$$

as expressed earlier by equation (3.69).

This expression can also be written in an incremental form which is:

$$d\epsilon_i^e = \frac{\partial^2 W}{\partial \sigma_i\ \partial \sigma_j}\ d\sigma_j = \frac{1}{2\ G_s}\left[\ \delta_{ij} - \frac{1-\beta}{\sigma_k\ \sigma_k}\ \sigma_i\ \sigma_j\ \right] d\sigma_j \qquad (3.76)$$

where δ_{ij} is the Kronecker delta.

3.6.4 Failure:

The failure criterion suggested by Matsuoka and Nakai[50] was used by Vermeer. This is a smooth approximation of the Mohr–Coulomb failure surface. This surface is easier to implement than the six sided Mohr–Coulomb pyramid shown in Figure 3.5. The failure criterion is:

$$f^1 = -3p\ I_2 + A_p\ I_3 = 0 \qquad (3.77)$$

where

$$-3\ p = \sigma_1 + \sigma_2 + \sigma_3 \qquad (3.78)$$

$$I_2 = -\sigma_1\ \sigma_2 - \sigma_2\ \sigma_3 - \sigma_3\ \sigma_1 \qquad (3.79)$$

$$I_3 = \sigma_1\ \sigma_2\ \sigma_3 \qquad (3.80)$$

It should be noted that compressive normal stresses are negative according to Vermeer's sign convention. The material parameter A_p defined as follows:

$$A_p = \frac{9 - \sin^2\varphi_p}{1 - \sin^2\varphi_p} \qquad (3.81)$$

where φ_p is the peak friction angle determined from triaxial test.

Figure 3.38 shows the failure surface in the deviatoric plane. In plotting the failure criterion in the deviatoric plane of principal stress space, it is convenient to define the deviatoric stresses,

$$s_i = \sigma_i + p \qquad (3.82)$$

and the invariants:

$$J_2 = s_i\, s_i \qquad (3.83)$$

$$J_3 = s_1\, s_2\, s_3 \qquad (3.84)$$

Substituting the identities

$$I_2 = -3\, p^2 + \tfrac{1}{2}\, J_2 \qquad (3.85)$$

and

$$I_3 = -\, p^3 + \tfrac{1}{2}\, p\, J_2 + {}^1/_3\, J_3 \qquad (3.86)$$

in equation (3.77), this becomes:

$$(3 + \sin^2\varphi_p)\, p\, J_2 + {}^1/_3\, (9 - \sin^2\varphi_p)\, J_3 = 8 \sin^2\varphi_p\, p^3 \qquad (3.87)$$

3.6.5 Cone Hardening Behaviour:

Cone hardening generally provides the major component of plastic strain.

a/ Yield function:

For isotropic hardening, the failure surface is the limiting position of an expanding "pre–failure" yield surface (Fig 3.39). Vermeer defined the cone hardening yield function as a smooth approximation to the six–sided Mohr–Coulomb pyramid. In principal stress space, this surface has a shape similar to a cone, as the name suggests. This yield function is:

$$f^p = -\, 3\, p\, I_2 + \frac{9 - \sin^2\varphi_m}{\cos^2\varphi_m}\, I_3 \qquad (3.88)$$

where φ_m is the mobilised friction angle which increases with the plastic distortion γ^p and the stress level σ. The shape of this yield function is shown in Fig 3.19 in the p–q plane.

b/ Flow rule:

The flow rule is:

$$d\epsilon_i^p = d\gamma^p \,.\, \frac{\partial Q^p}{\partial \sigma_i} \qquad (3.89)$$

or explicitly,

$$d\epsilon_i^p = d\gamma^p \,.\left[\frac{\sqrt{2}\,.\, s_i}{(3\, s_i\, s_i)^{\frac{1}{2}}} + \frac{4}{9}\,.\, \frac{\sin\varphi_m - \sin\varphi_{cv}}{1 - \sin\varphi_m . \sin\varphi_{cv}} \right] \qquad (3.90)$$

where $d\gamma^p$, the rate of plastic distortion, is:

$$d\gamma^p = \left[{}^3/_2 \; de_i^p . de_i^p \right]^{\frac{1}{2}}$$

with

$$de_i^p = d\epsilon_i^p - {}^1/_3 \; d\epsilon_{kk}^p$$

The plastic distortion is the controlling hardening parameter for cone hardening. For this law, the flow rule can only be integrated numerically. Although it is not necessary to define the plastic potential function explicitly, it is convenient for understanding the flow rule. For the cone hardening law Vermeer could not find a proper plastic potential, but he managed to find the "updated plastic potential".

$$Q^p = ({}^2/_3 \; s_i \; s_i)^{\frac{1}{2}} - \frac{4}{3} \; \frac{\sin\varphi_m - \sin\varphi_{cv}}{1 - \sin\varphi_m . \sin\varphi_{cv}} \; p \qquad (3.91)$$

In the evaluation of $\partial Q/\partial\sigma_i$, φ_m has to be treated as a constant, whereas φ_m depends on the stress level. It can be seen from equation (3.91) that the updated plastic potential is a cone that gives a circle in the deviatoric plane (Fig 3.18). Initially Vermeer proposed a non–associated flow rule[89] that proved to be more accurate than this one. However, that flow rule was considered to be too complex and too costly for use in finite element programs.

c/ Validation of the Cone Hardening Law:

In 1963, Kondner and Zelasko[42] published results from triaxial tests with constant value of mean pressure and proposed a hyperbolic equation for the distortion γ:

$$\gamma = |\epsilon_1 - \epsilon_3| = B \; \frac{M_p \cdot q/p}{M_p - q/p} \qquad (3.92)$$

if $M_m = q/p$

then

$$M_p = \max M_m = \frac{6 \sin\varphi_p}{3 - \sin\varphi_p} \qquad (3.93)$$

Using the expression of B proposed by Hansen[31]:

$$B = B_0 \left[\frac{p}{p_0} \right]^{\beta} = \frac{p_0}{2 G_0} \left[\frac{p}{p_0} \right]^{\beta} \qquad (3.94)$$

The cone hardening law is obtained by dividing the shear strain equation into an elastic and a plastic part. The elastic part is obtained by assuming that plastic strain rate vanishes in the beginning of deviatoric loading, ie:

$$\gamma^e = B \cdot q/p \tag{3.95}$$

thus

$$\gamma^p = B \frac{(q/p)^2}{M_p - q/p} \tag{3.96}$$

If $p \simeq \sigma$, equations (3.95) and (3.96) become:

$$\gamma^e \simeq \frac{1}{2 G_s} q \tag{3.97}$$

and

$$\gamma^p \simeq \frac{\sigma}{2 G_s} \frac{(q/p)^2}{M_p - q/p} \tag{3.98}$$

Equation (3.97) coincides with equation (3.69) which defines elastic strains and equation (3.98) defines the cone hardening parameter in the model.

Using the results of various tests, Tatsuoka and Ishihara[81] have published empirical contours. Figure 3.39 shows the contours obtained by these authors (a) and Vermeer[89] (b) of shear strain γ. In another paper, Tatsuoka and Ishihara[81], and also Stroud[78] presented results of yield point tests and concluded that the shear strain contours may be approximated by yield loci. This observation is exploited by Vermeer in this model.

3.6.6 Cap Hardening:

Cap plastic strains are introduced to describe the plastic volumetric strain observed in isotropic loading and not expressed by the cone hardening law.

a/ Yield function:

The yield cap describes the plastic contraction in isotropic and anisotropic compression. In principal stress space, the yield cap is a sphere as indicated in Figure 3.19. The stress measure σ with definition (3.71) is constant for all stress

points on the cap. The cap yield function is:

$$f^c = \sigma - \sigma^c \tag{3.99}$$

b/ Flow rule:

The cap flow rule is associated. A hardening parameter ϵ^c is now introduced by defining

$$\epsilon^c = \int_0^t d\epsilon^c \, dt \tag{3.100}$$

where

$$d\epsilon^c = \left[3 \, d\epsilon_i^c \, d\epsilon_i^c \right]^{\frac{1}{2}} \tag{3.101}$$

From the consistency equation(3.26), the G_s equation(3.70), and substituting the whole in the flow rule equation, namely:

$$d\epsilon_i^c = \frac{1}{h^c} \frac{\partial f^c}{\partial \sigma_i} \frac{\partial f^c}{\partial \sigma_j} d\sigma_j = \frac{1}{3 h^c} \frac{\sigma_i \sigma_j}{\sigma_k \sigma_k} d\sigma_j \tag{3.102}$$

we obtain:

$$d\epsilon_i^c = \frac{\alpha \beta}{2 G_s} \frac{\sigma_i \sigma_j}{\sigma_k \sigma_k} d\sigma_j \tag{3.103}$$

3.6.7 Stress– Dilatancy Theory in the Model:

The stress– dilatancy relation used by Vermeer is that due to Rowe[69]. However, Vermeer expressed the stress dilatancy equation in terms of the angle of dilatancy ψ_m.

In the case of planar deformation ($d\epsilon_2 = 0$), the definition of the dilatancy angle is:

$$\sin\psi_m = \frac{d\epsilon_1 + d\epsilon_3}{d\epsilon_3^p + d\epsilon_1^p} \tag{3.104}$$

Vermeer noted that the angle φ_f introduced by Rowe varied by only a few degrees. For simplicity Vermeer assumed $\varphi_f = \varphi_{cv}$. Rowe's parameters R and K may be

defined as follows:

$$R = \frac{1 + \sin\varphi_m}{1 - \sin\varphi_m} \tag{3.105}$$

$$K = \frac{1 + \sin\varphi_m}{1 - \sin\varphi_{cv}} \tag{3.106}$$

And hence the stress-dilatancy equations are:

- triaxial compression $\quad \frac{2\, d\epsilon_3^p}{d\epsilon_1^p} = -\frac{R}{K}$

- triaxial extension $\quad \frac{d\epsilon_1^p}{2\, d\epsilon_3^p} = -\frac{R}{K}$

Equation (3.104) can also be written as:

$$\sin\psi_m = \frac{R - K}{R + K} = \frac{\sin\varphi_m - \sin\varphi_{cv}}{1 - \sin\varphi_m \sin\varphi_{cv}} \tag{3.107}$$

For triaxial compression it follows from the stress-dilatancy theory:

$$\frac{d\epsilon_1^p + 2\, d\epsilon_3^p}{|d\epsilon_3^p - d\epsilon_1^p|} = \frac{R - K}{\frac{1}{2} R + K} = \frac{4 \sin\psi_m}{3 - \sin\psi_m} \simeq \frac{4}{3} \sin\psi_m \tag{3.108}$$

Similarly, for triaxial compression, it follows that:

$$\frac{d\epsilon_1^p + 2\, d\epsilon_3^p}{|d\epsilon_1^p - d\epsilon_3^p|} = \frac{R - K}{R + \frac{1}{2} K} = \frac{4 \sin\psi_m}{3 + \sin\psi_m} \simeq \frac{4}{3} \sin\psi_m \tag{3.109}$$

These last two stress–dilatancy equations show that the stress–dilatancy theory gives approximately $4\sin\psi_m/3$, whereas the model gives exactly $4\sin\psi_m/3$ since the flow rule can be written:

$$d\epsilon_i^p = d\gamma^p \cdot \left[\frac{\sqrt{2} \cdot s_i}{(3\, s_i\, s_i)^{\frac{1}{2}}} + \frac{4}{9} \sin\psi_m \right] \tag{3.110}$$

Rowe's stress–dilatancy theory involves no equation for intermediate states between triaxial compression and triaxial extension, but Vermeer's model allows interpolation between these two extremes.

3.7 RESULTS FROM VERMEER'S MODEL:

A series of tests (experimental) were simulated by a computer program based on Vermeer's model. Triaxial tests, isotropic loading, p–constant loading, and loading and unloading under K_0 conditions were simulated by the program. The results are shown in Figures 3.20 to 3.35. The data utilized in the computations are those for a dense Karlsruhe sand.

$G_0 = 75$ MPa $\qquad \beta = 0.25$

$\alpha = 0.88$ $\qquad \varphi_p = 43°$

$\varphi_{cv} = 32°$ $\qquad p_0 = 200$ kPa

3.7.1 Elastic Behaviour:

The elastic stress–strain relation is expressed in two forms; an incremental form as expressed by equation (3.86) and a secant form as expressed by equation (3.85). The two forms are shown in Figure 3.21 where the deviatoric stress is plotted against the deviatoric strain. This plot shows that the incremental form converges to the secant form from (which it is derived) for small values of stress increments. A stress increment of 10% of the confining pressure gives a difference of 0.4 % of the deviatoric strain under triaxial conditions, which is negligible.

To check the independence of the elastic strain from the followed stress path, a sand sample is loaded under the three stress paths depicted in Figure 3.20. The volumetric strain obtained at the end of stress path 1 should be equal to the volumetric strain at the end of stress paths 2 and 3, which means:

$$\epsilon_{v_1}^{e} = \epsilon_{v_2}^{e} + \epsilon_{v_3}^{e} \qquad (3.111)$$

For a sample at an initial confining pressure $\sigma_3 = 200$ kPa, the isotropic compression (path 2) gave $\epsilon_{v_2}^{e} = -0.09\%$ (Figure 3.22), the loading at p–constant (path 3) gave $\epsilon_{v_3} = 0.08\%$ (Figure 3.23) and the triaxial loading (path 1) gave $\epsilon_{v_1} = -0.01\%$ (Figure 3.24). Path independence is therefore satified. The same verification process

was carried out on the samples with initial confining pressures $\sigma_3 = 80$ kPa and $\sigma_3 = 400$ kPa.

3.7.2 Results from Triaxial Tests:

The tests were performed on three samples at different confining pressures (p= 80kPa, 200 kPa and 400 kPa). Figure 3.25 shows the stress paths followed by these three samples during the simulated triaxial tests. The top point of each stress path corresponds to the stress level where failure occurs. When the initial stress is $\sigma_3 = 80$ kPa, the soil sample fails when the mean stress attains the maximum value p= 185 kPa. This mean stress corresponds to $\sigma_2 = \sigma_3 = 80$ kPa and $\sigma_1 = 400$ kPa. The second sample, tested under a confining stress $\sigma_3 = 200$ kPa, attained failure when the mean stress p= 460 kPa which corresponds to $\sigma_1 = 990$ kPa. And in the third case where $\sigma_3 = 400$ kPa, failure occurs at p= 930 kPa, that is $\sigma_1 = 1990$ kPa. Figure 3.26 depicts the stress– strain behaviour of the components of strain (elastic, cap hardening and cone hardening) taken separately, and taken together (total strain or elasto– plastic strain). The elastic and the cap hardening components of strain are very small relative to the cone hardening strain. For high values of deviatoric stress the curves of the cone hardening component and total strain merge. The reason why the elastic and cap component of strain are very small is that the samples tested are in a dense state. As the soil tested had a little volume of voids, it could not contract much more. This is especially true for the case shown in these figures where the confining pressure is very high (400 kPa). In Figure 3.26, the curve of deviatoric stress q versus shear strain γ shows the continuous hardening behaviour of the material.

Figure 3.27 shows the stress– strain behaviour of dense Karlsruhe sand with, this time, the normalized deviatoric strain γ_n instead of the usual deviatoric strain γ. The relation between γ and γ_n is:

$$\gamma_n = \gamma \, (p_0/p)^{\beta} \qquad (3.112)$$

The experimental results obtained from triaxial tests are in good agreement with the the predictions made by Vermeer's model in terms of normalized strains: this is shown by Figures 3.36 and 3.37.

Figures 3.28 and 3.29 show the relation between mean stress p, volumetric strain ϵ_v and normalized volumetric strain ϵ_{vn}, for different confining pressures. The three plots depict similar behaviour. When a sample of sand is sheared it contracts in a first stage and then dilates until reaching the state of failure described previously. The maximum value of volumetric strain attained during dilation of the material is very large with respect to that of contraction. The maximum volumetric strain during dilation is about 14 times that of contraction for a sample at confining pressure σ_3 = 400 kPa. This could be predicted for a dense sand where the peak value of dilatancy is large (ψ_p = 14°) and the porosity is small (n= 0.35).

Figures 3.30 and 3.31 show the relation between Mm = q/p and the shear strain γ or normalized shear strain γ_n. These figures show the stress ratio Mm increasing with further increase of the total strain and then tending to an asymptotic limit at Mp = 1.77 . The only difference between the two graphs is the larger strains given by the normalized shear strain γ_n. Here again it is clear that the effects of cap hardening and elastic response (for dense sand) are very small relative to the effect of cone hardening.

Figures 3.32 and 3.33 depict the relation between the volumetric strain, (or normalized volumetric strain) and the stress ratio Mm (= q/p). The curve of Mm versus total volumetric strain shows a contraction of the sample of sand up to a certain value of Mm (Mm $\simeq$ 1.3) and then expansion up to failure. In this case, at a confining pressure σ_3= 400 kPa the maximum volumetric strain during dilation is about 17 times that of contraction.

Figure 3.34 shows the predicted relation between the volumetric strain ϵ_v and the deviatoric strain ϵ_d during triaxial loading. The sand contracts initially and

then dilates at an almost constant rate. A similar curve was obtained by Hetler and Vardoulakis[33] from experiments done on the same sand.

The stress path depicted in Figure 3.35 is that for dense Karlsruhe sand subjected to:

a – isotropic loading from p= 0 to p= 200 kPa

b – isotropic unloading from p= 200 kPa to p= 80 kPa

c – loading under K_0 condition from p= 80 kPa to p= 930 kPa

d – unloading under K_0 condition from p= 930 kPa to p= 110 kPa

This plot shows the variation of the mean stress p along the space diagonal depicted by the axis q = 0. In this case, the only strains undergone by the material are due to elastic straining and cap hardening. The deviatoric stress increases thereafter during loading under K_0 condition and the stress path depicted rises at an almost constant slope of 3/2.5. Finally the deviatoric stress decreases during K_0 unloading until it reaches the axis of isotropic loading.

3.8 CONCLUSIONS:

A review of elasto–plastic (flow) theory, on which most constitutive laws for sands are based has been given as an aid to the understanding of the basic concepts. Some important phenomena, such as softening and dilatancy have been discussed in some detail since these are of particular relevance to granular materials. Because of these complexities, a simple model (Cam clay) was examined in detail at the outset in order to explore aspects of the numerical implementation of such models.

From a review of several constitutive models for sands, Vermeer's model, which has the merit of being relatively simple yet comprehensive, has been studied in depth. The predictions given by the model have been compared with experimental data and yielded good agreement in most cases.

However Vermeer's model does not describe softening behaviour because this is not a material property of a continuum but a phenomenon which results from material inhomogeneities or non–uniformity of loading. Nevertheless, the cone flow rule in this model incorporates Rowe's stress–dilatancy relation and in this respect the model has much to recommend it.

One of the conclusions drawn by Vermeer was: "*For triaxial conditions the model prediction coincides with the Mohr–Coulomb criterion, whereas deviations occur for intermediate states between triaxial compression and triaxial extension.*". The reason for that is that the major strain component (cone hardening) was based on a smooth approximation of the Mohr–Coulomb criterion and the models equations were set up (or verified) for triaxial compression or triaxial extension.

For this reason among others (particularly the absence of intrinsic softening) it was decided that little advantage would be gained by implementing the model into the finite element code. Instead, a simple elastic–perfectly plastic model based on the Mohr–Coulomb failure criterion was employed in the subsequent finite element analyses. The advantages of this model are that only two material parameters need to be defined and that the associated flow rule permits use of a standard (symmetric) equation solver. Clearly, there is scope for analysis using more complex models but it is unclear whether this would yield significant advantage. Perhaps a better approach is to adapt finite element methods to cater for softening.

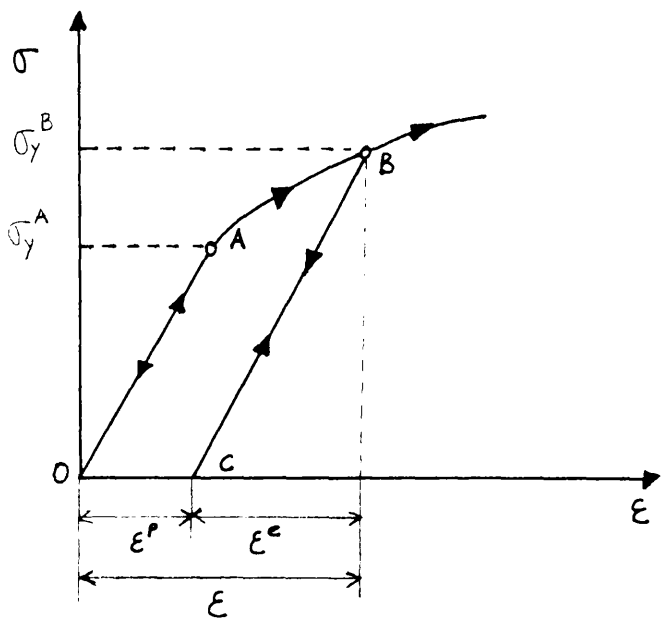

Figure 3.1 Recoverable and irrecoverable strains.

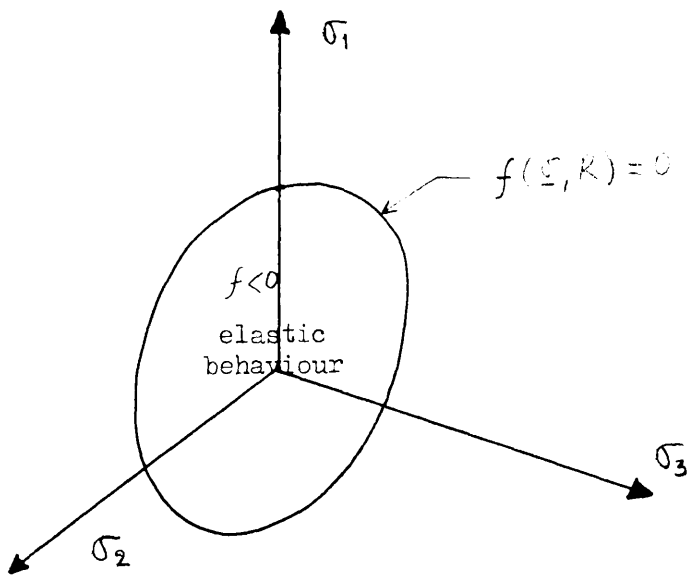

Figure 3.2 Yield function.

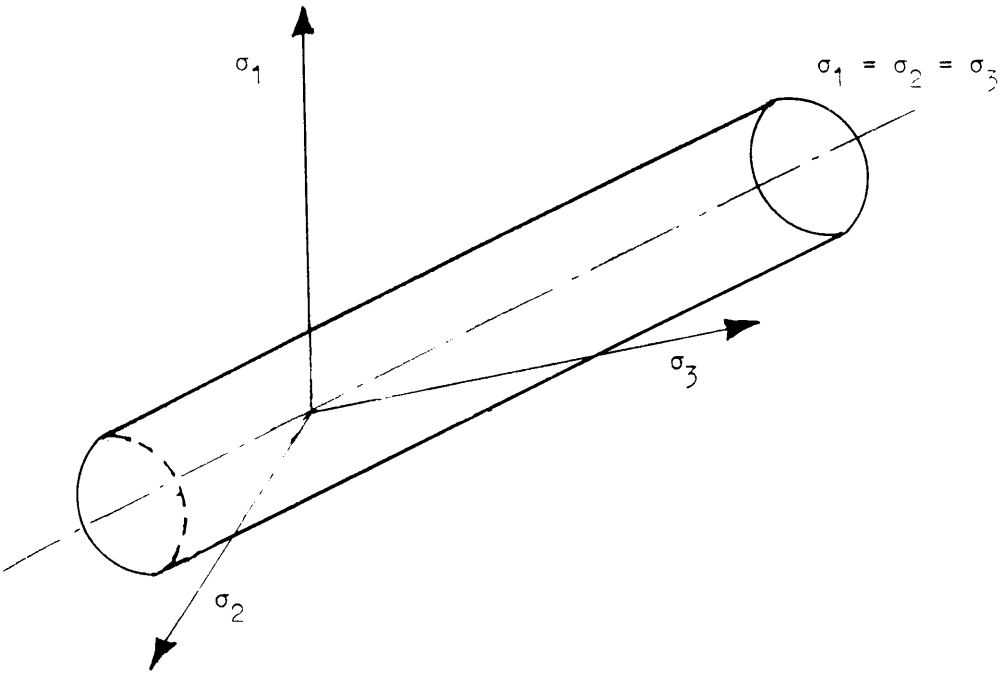

Figure 3. 3 Von Mises yield criterion.

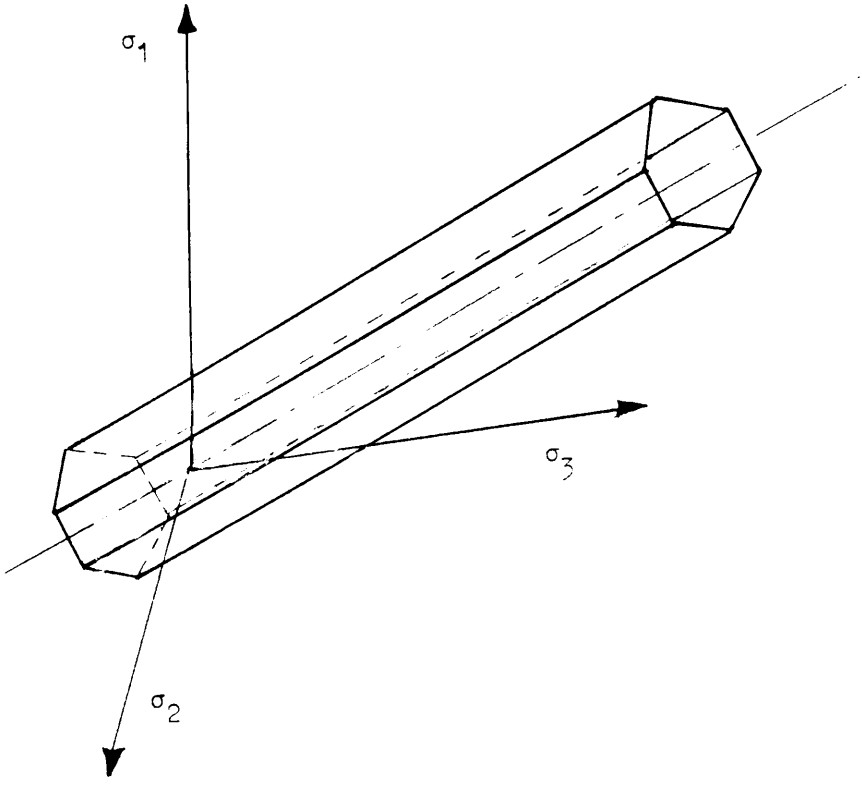

Figure 3. 4 Tresca yield criterion.

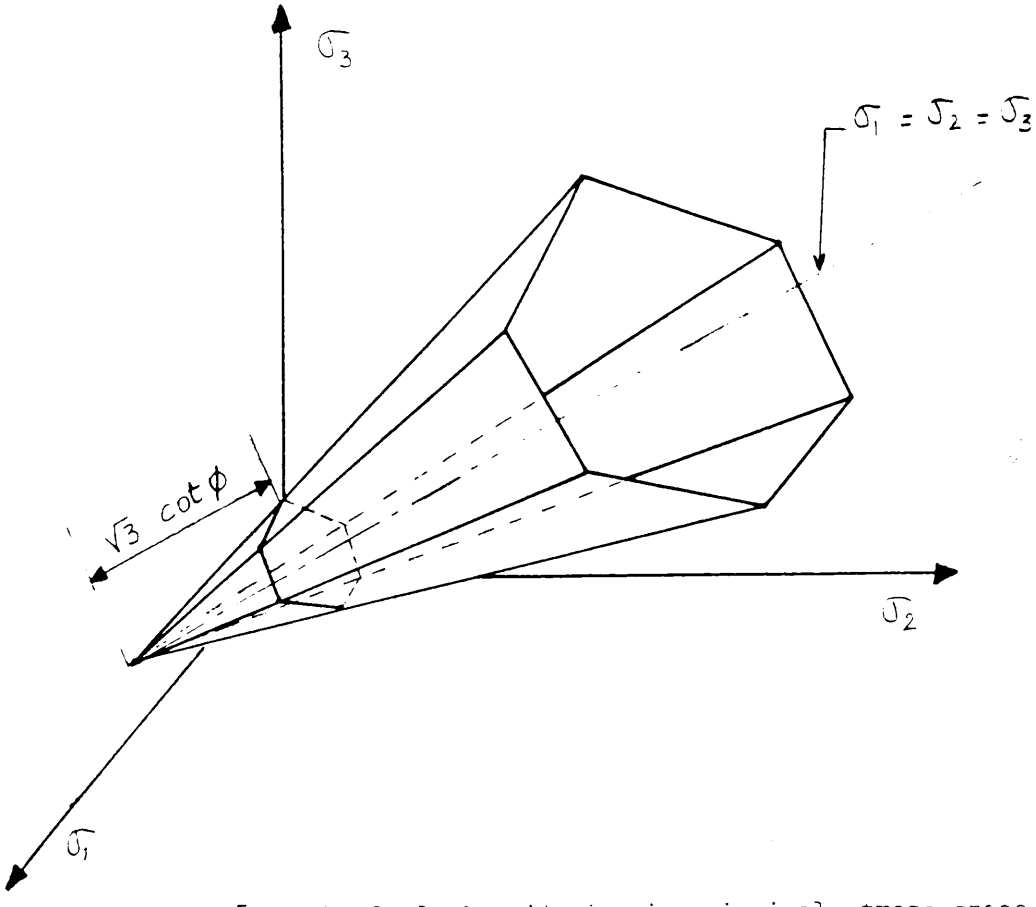

Figure 3.5a Mohr-Coulomb criterion in principal stress space.

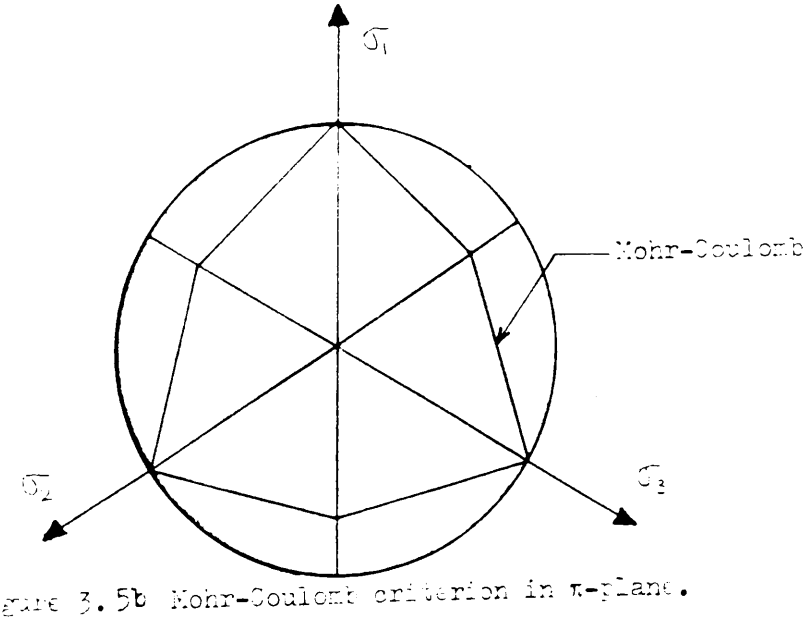

Figure 3.5b Mohr-Coulomb criterion in π-plane.

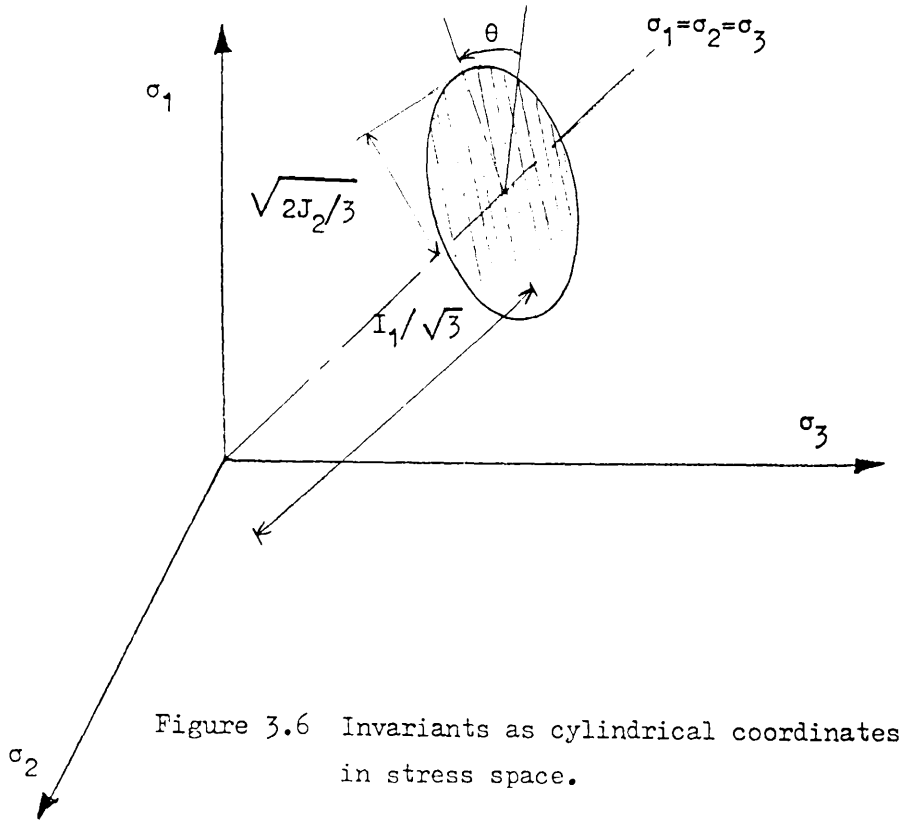

Figure 3.6 Invariants as cylindrical coordinates in stress space.

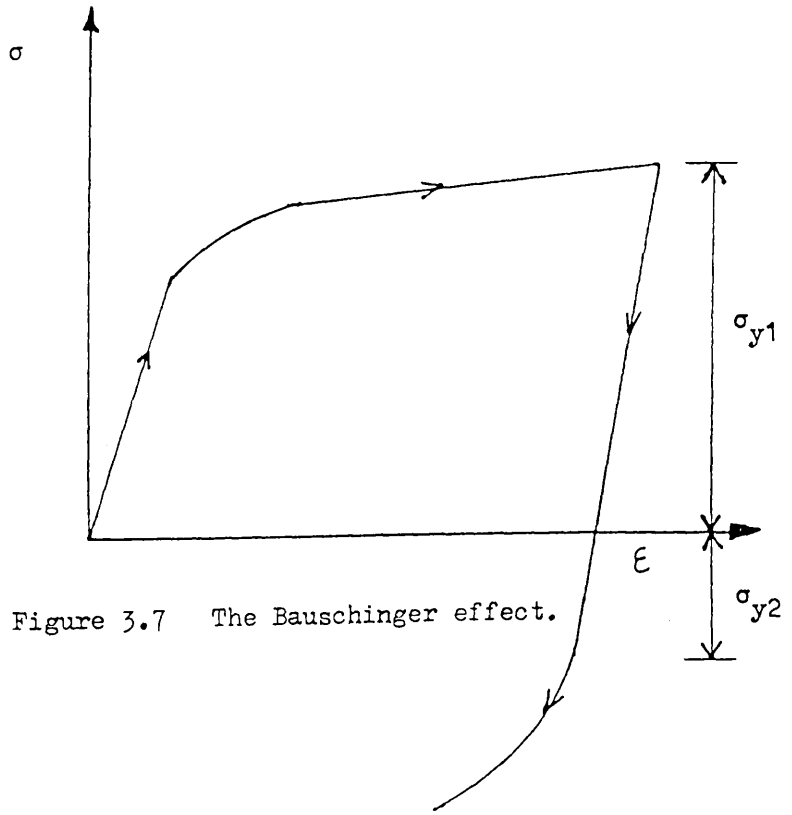

Figure 3.7 The Bauschinger effect.

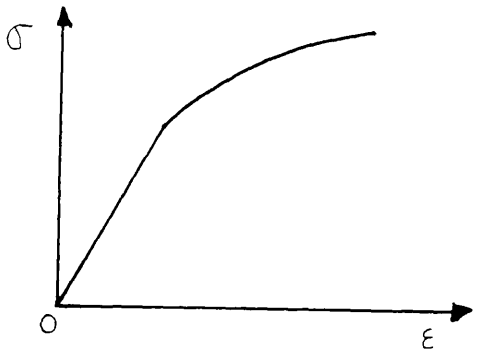

(a)

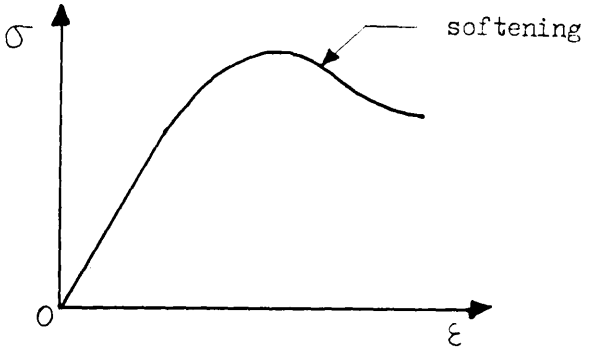

(b)

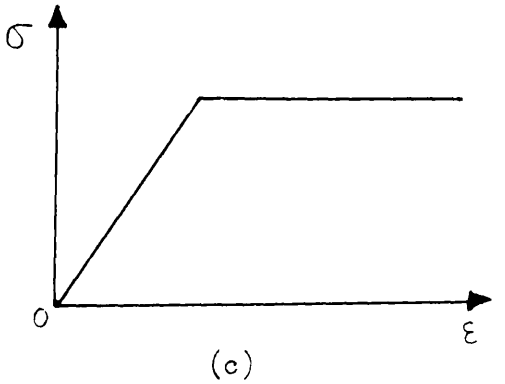

(c)

Figure 3.8 Stress-strain behaviour of :
a) hardening material
b) softening material
c) elastic-perfectly plastic material

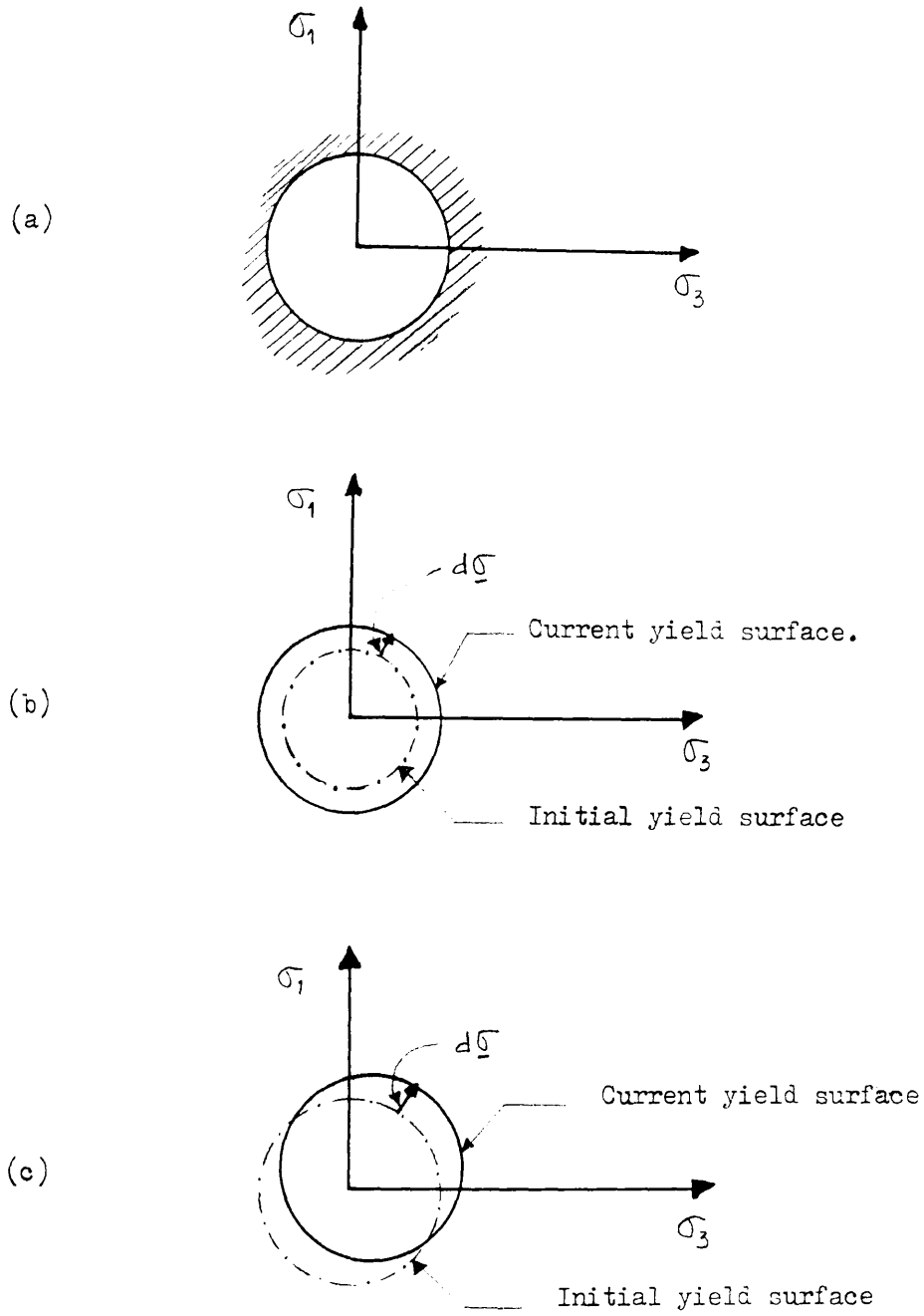

Figure 3.9 Models of strain hardening behaviour

a) Elastic-perfectly plastic

b) Isotropic strain hardening

c) Kinematic strain hardening

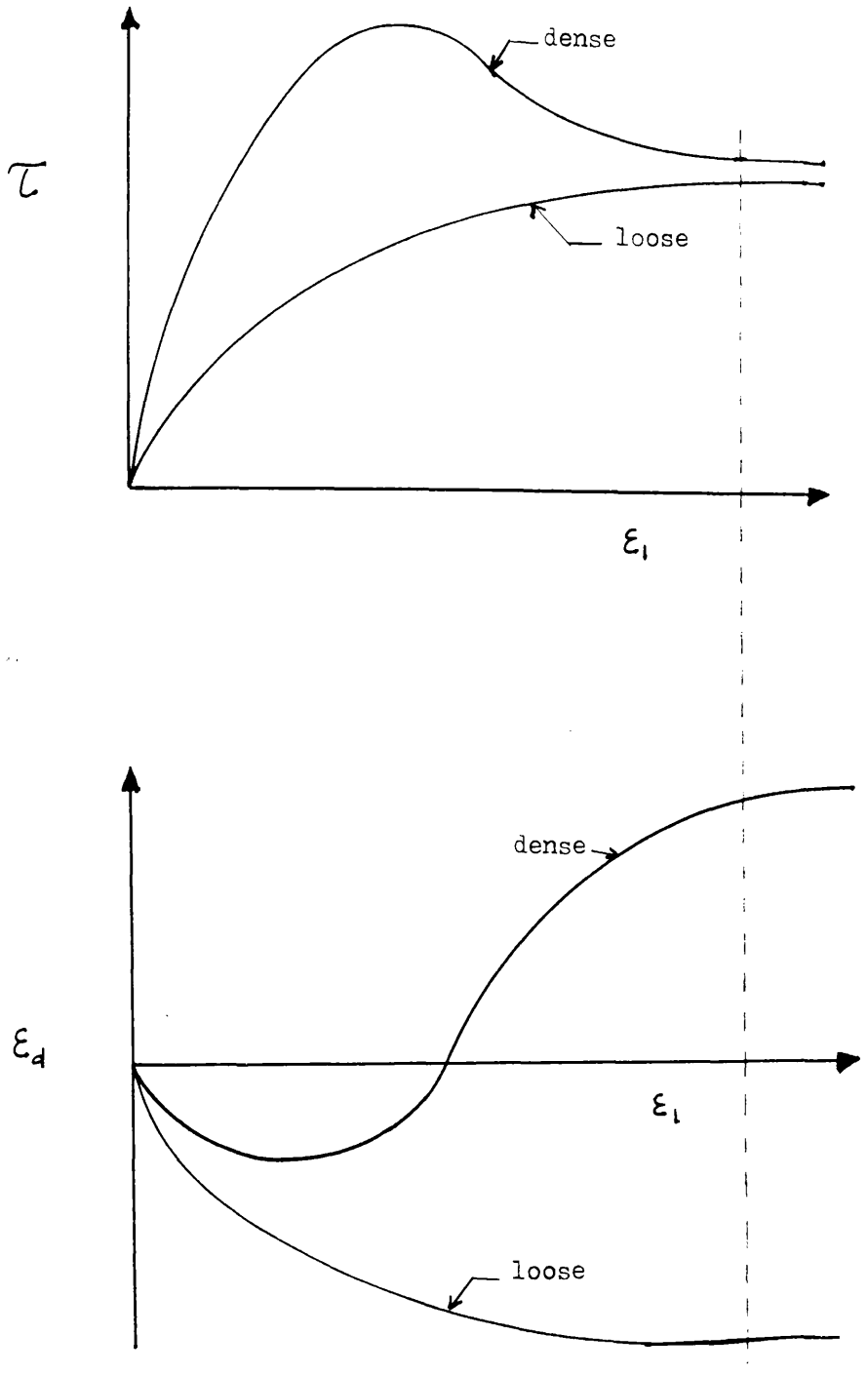

Figure 3.10 Behaviour of loose and dense soils.

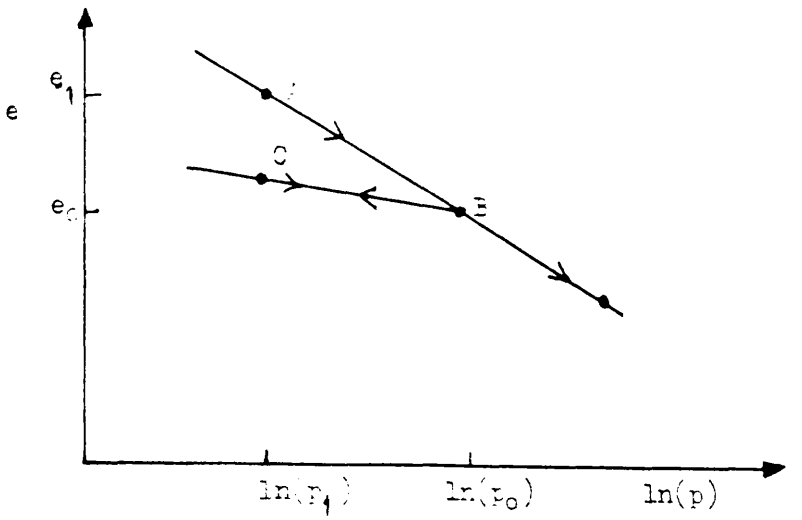

Figure 3.11 Consolidation and swelling behaviour.

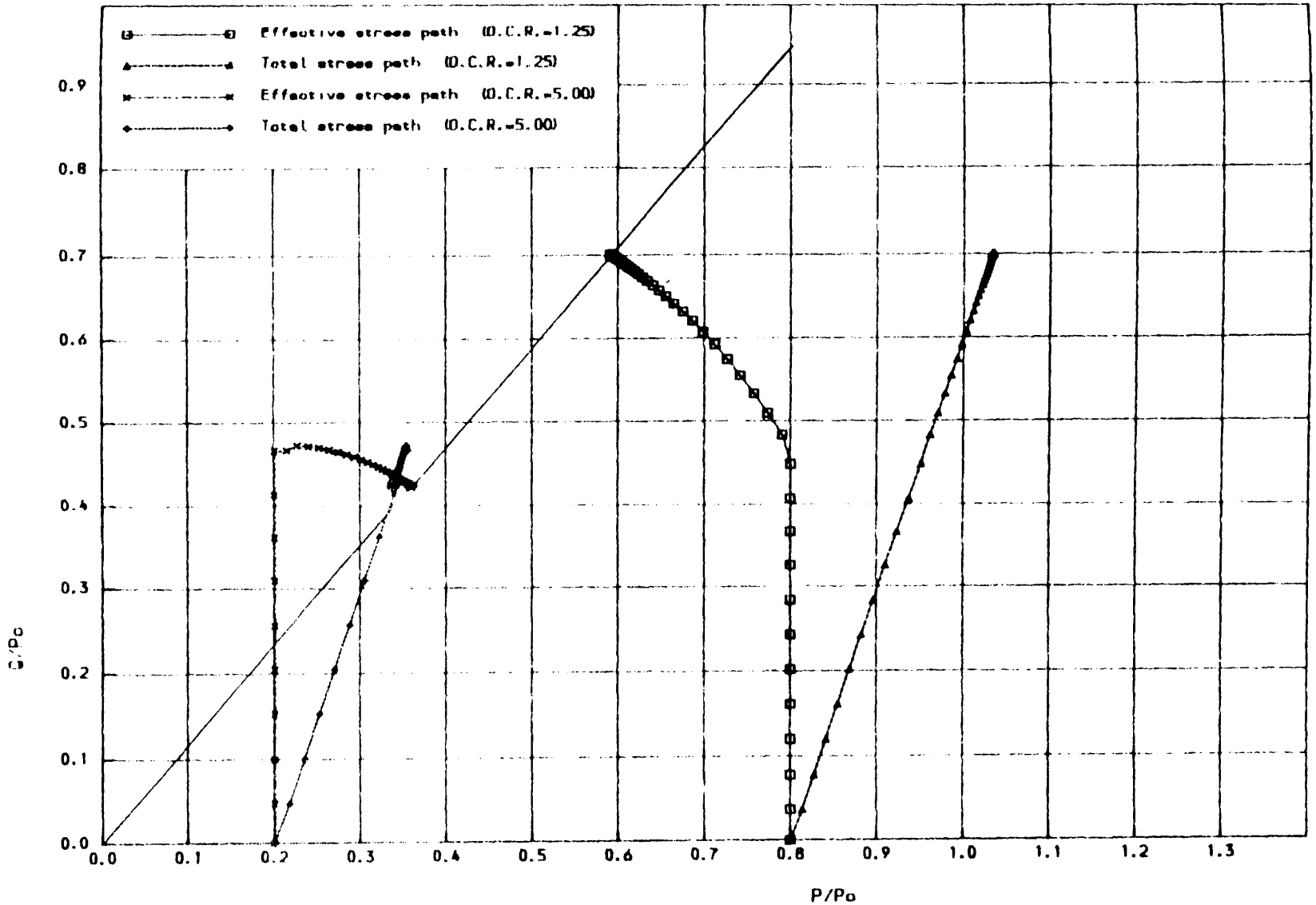

FIG. 3.13 PREDICTED STRESS PATHS OF ASSOCIATED CAM-CLAY IN TRIAXIAL TEST
(Compression , Po=125 KPa , ϕ =30°)

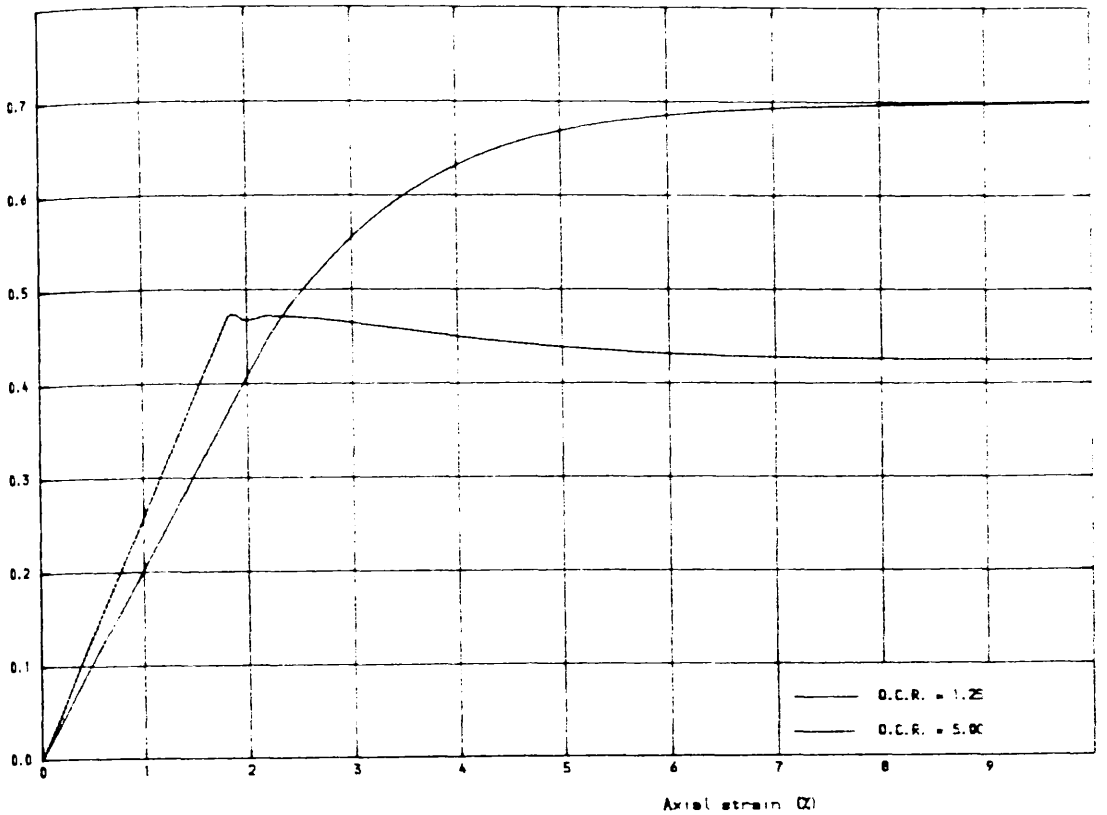

FIG. 3.14 PREDICTED STRESS-STRAIN BEHAVIOUR OF ASSOCIATED CAM-CLAY
(Triaxial compression , P_o=125 kPa , ϕ=30°)

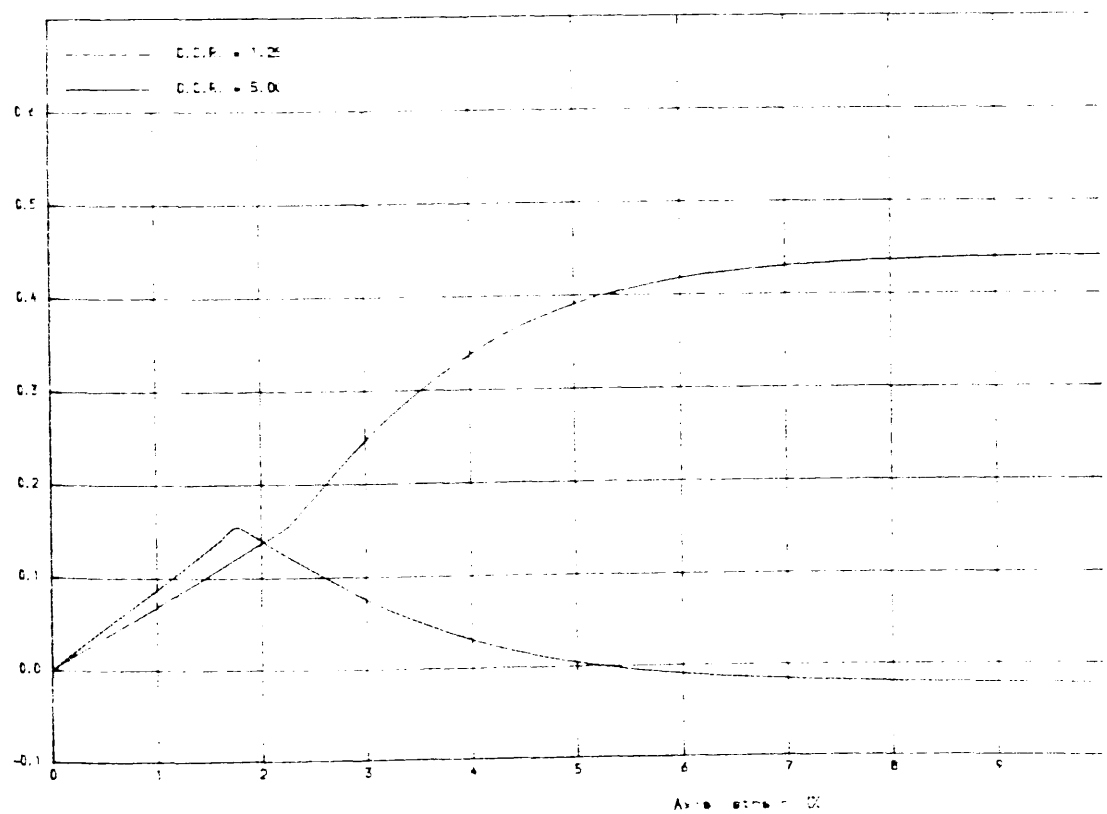

FIG. 3.15 PREDICTED PORE WATER PRESSURE RESPONSE OF ASSOCIATED CAM-CLAY
(Triaxial compression , P_o=125 kPa , ϕ=30°)

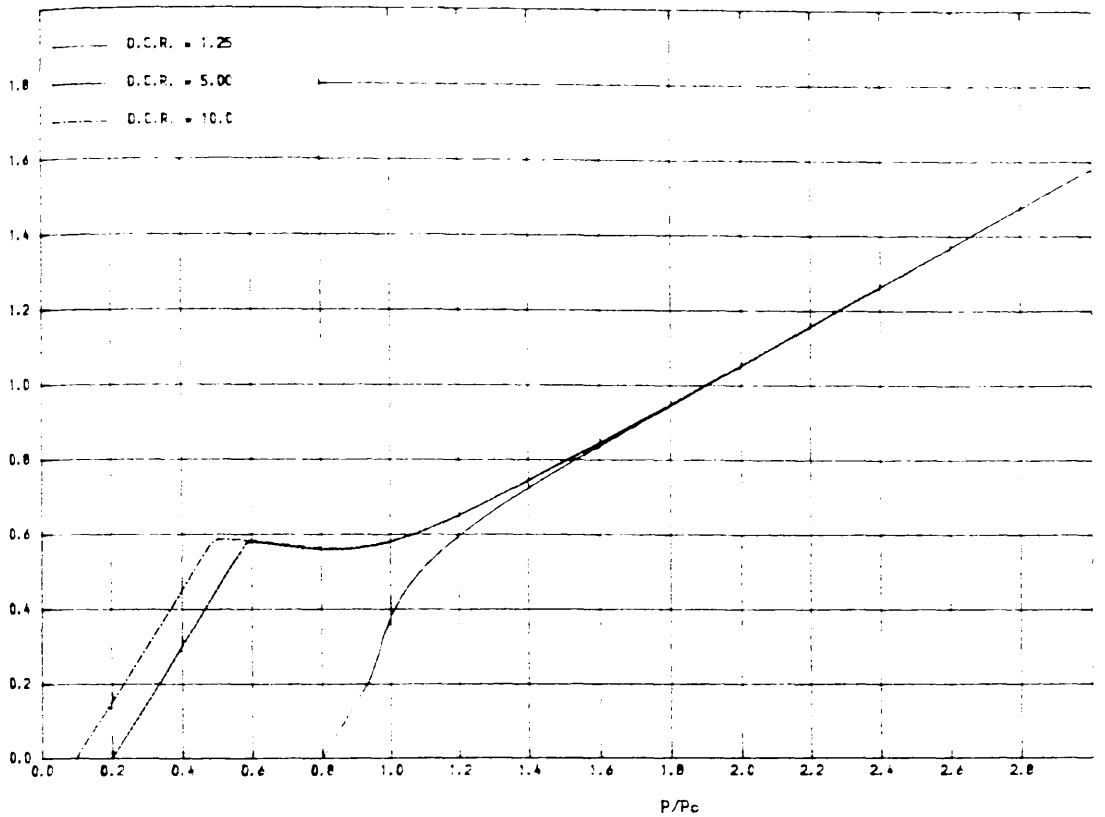

FIG. 3.16 STRESS PATHS OF ASSOCIATED CAM-CLAY IN DRAINED TEST
(Compression test , Ko consolidation , Pc s.=0.2 , Pc=125 kPa)

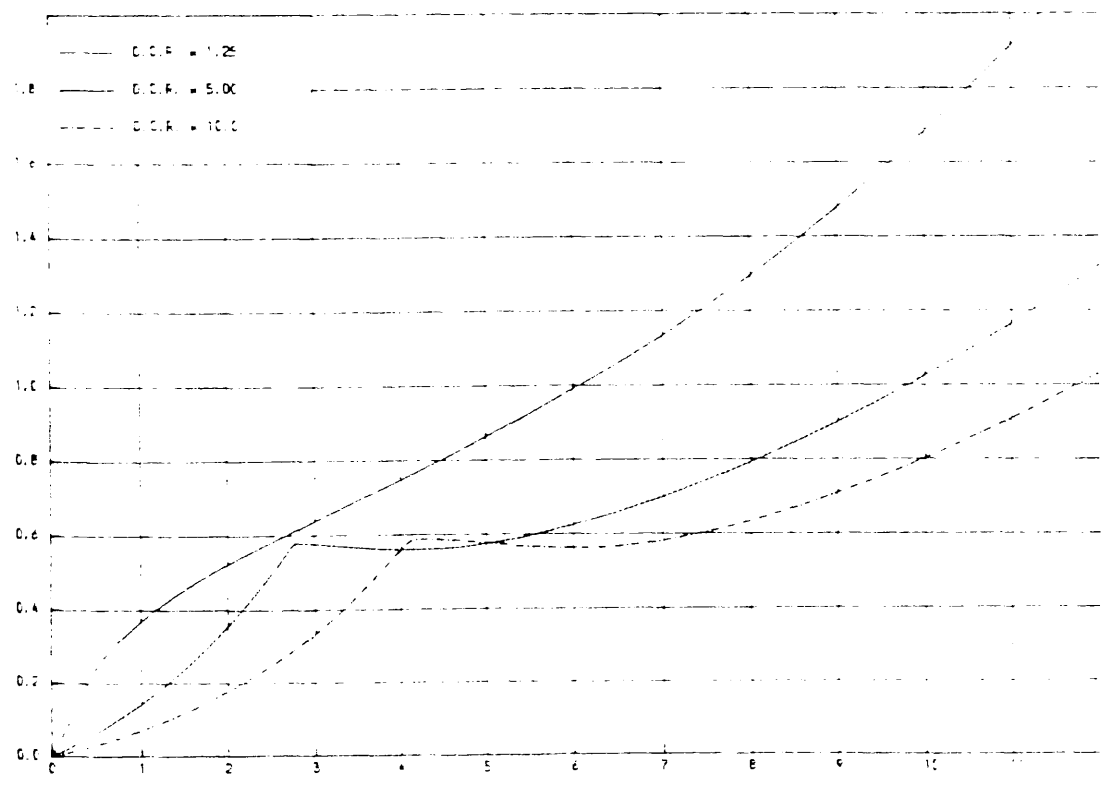

FIG. 3.17 STRESS-STRAIN BEHAVIOUR OF ASSOCIATED CAM-CLAY IN DRAINED TEST
(Compression test , Ko consolidation , Pc s.=0.2 , Pc=125 kPa

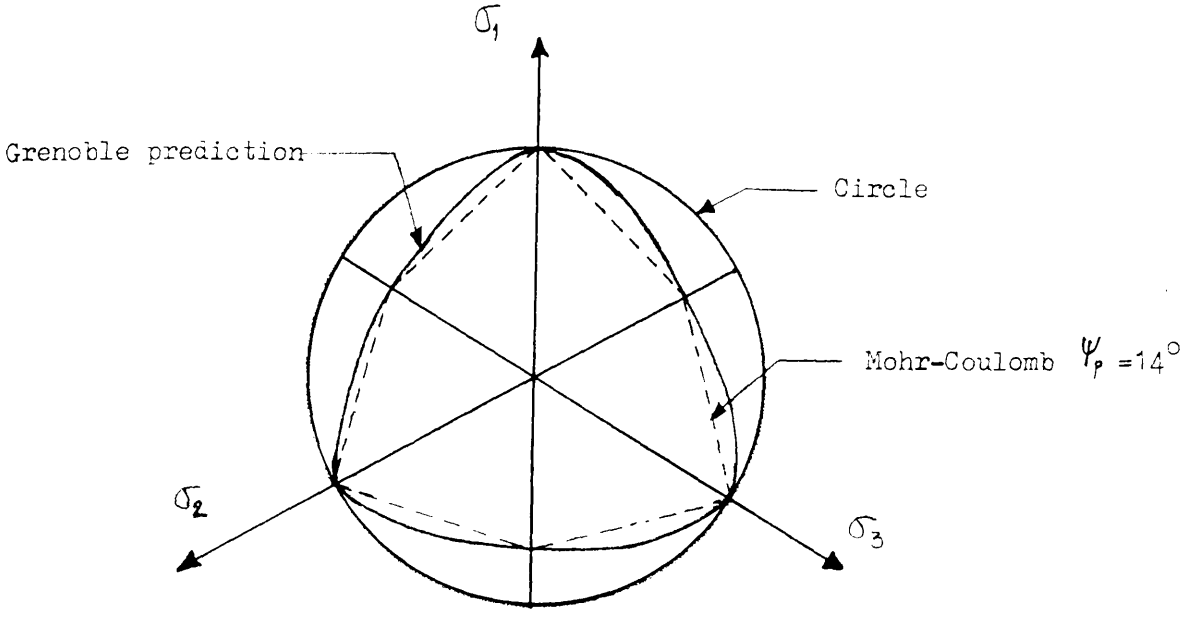

Figure 3.18 Plastic potentials for cone hardening in deviatoric view (Vermeer, 1982)

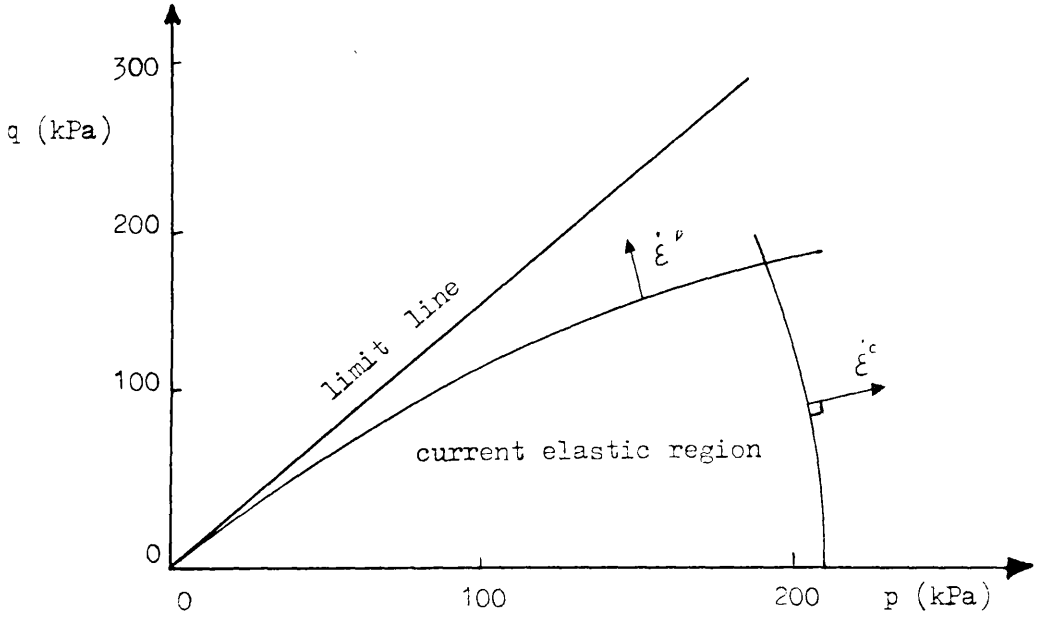

Figure 3.19 Yield cone for $\dot{\varepsilon}^p$ and yield cap for $\dot{\varepsilon}^c$

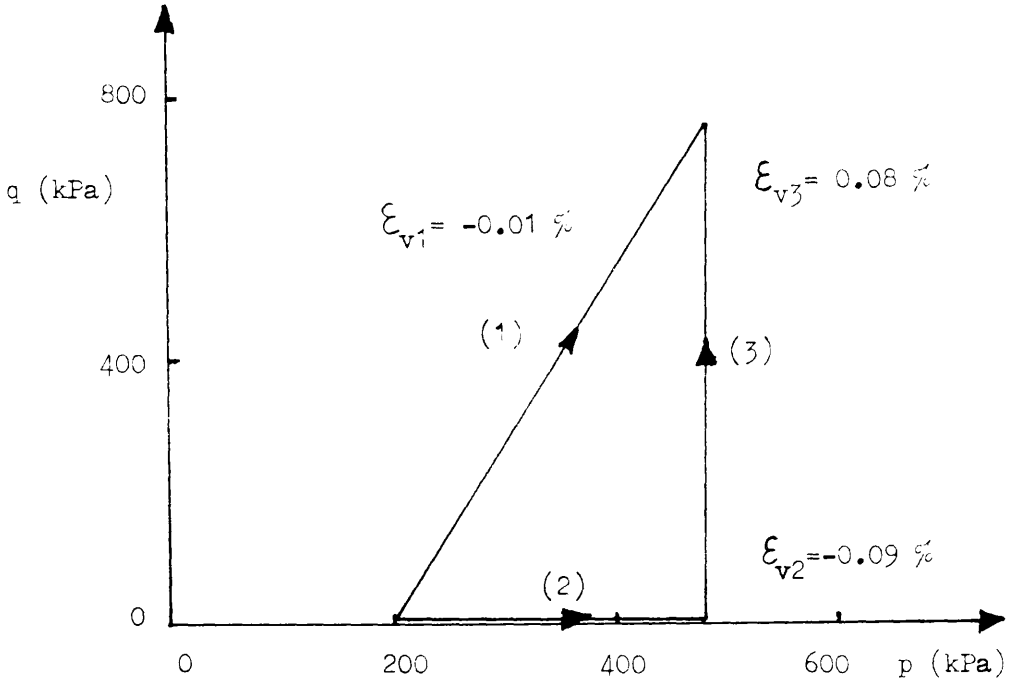

Figure 3.20 Elastic stress paths

1) triaxial compression

2) isotropic loading

3) p-constant loading

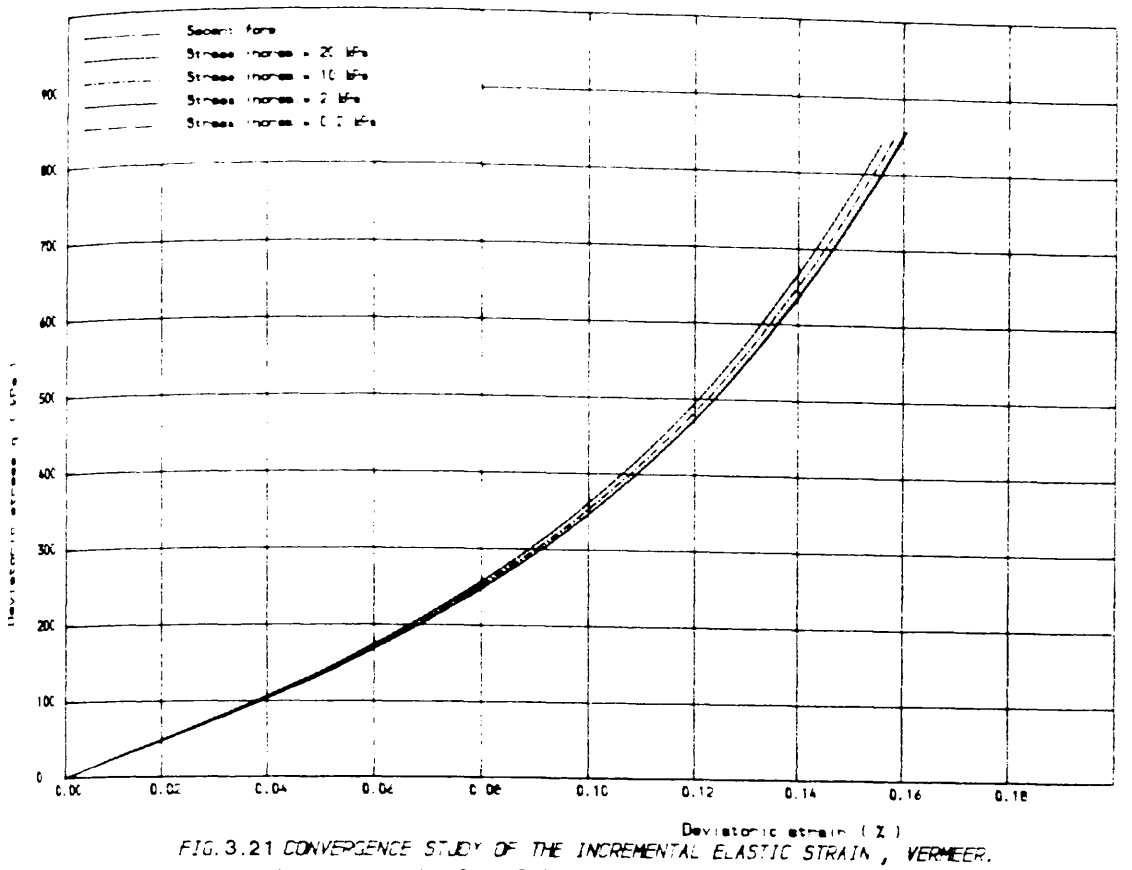

FIG. 3.21 CONVERGENCE STUDY OF THE INCREMENTAL ELASTIC STRAIN , VERMEER.
(Karlsruhe sand , S gas3=200 kPa , Triaxial test)

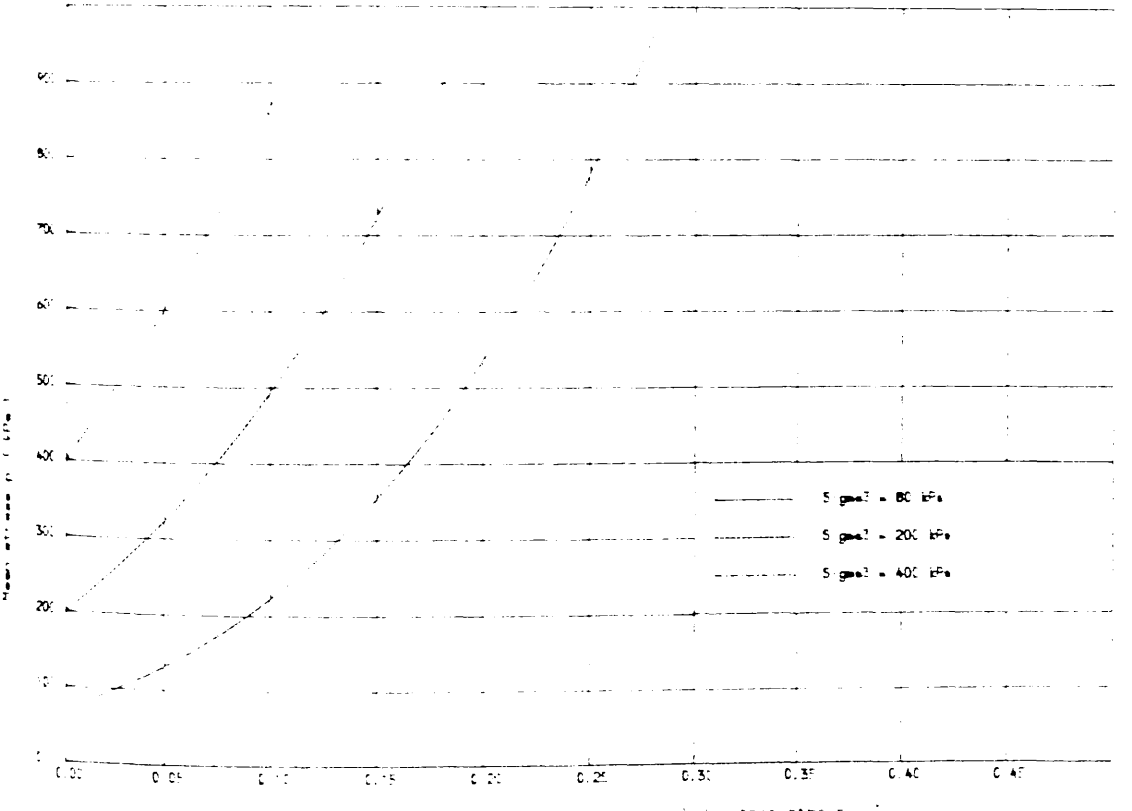

FIG. 3.22 ELASTIC STRESS-STRAIN BEHAVIOUR IN ISOTROPIC LOADING , VERMEER
(Karlsruhe sand , Pa=200 kPa)

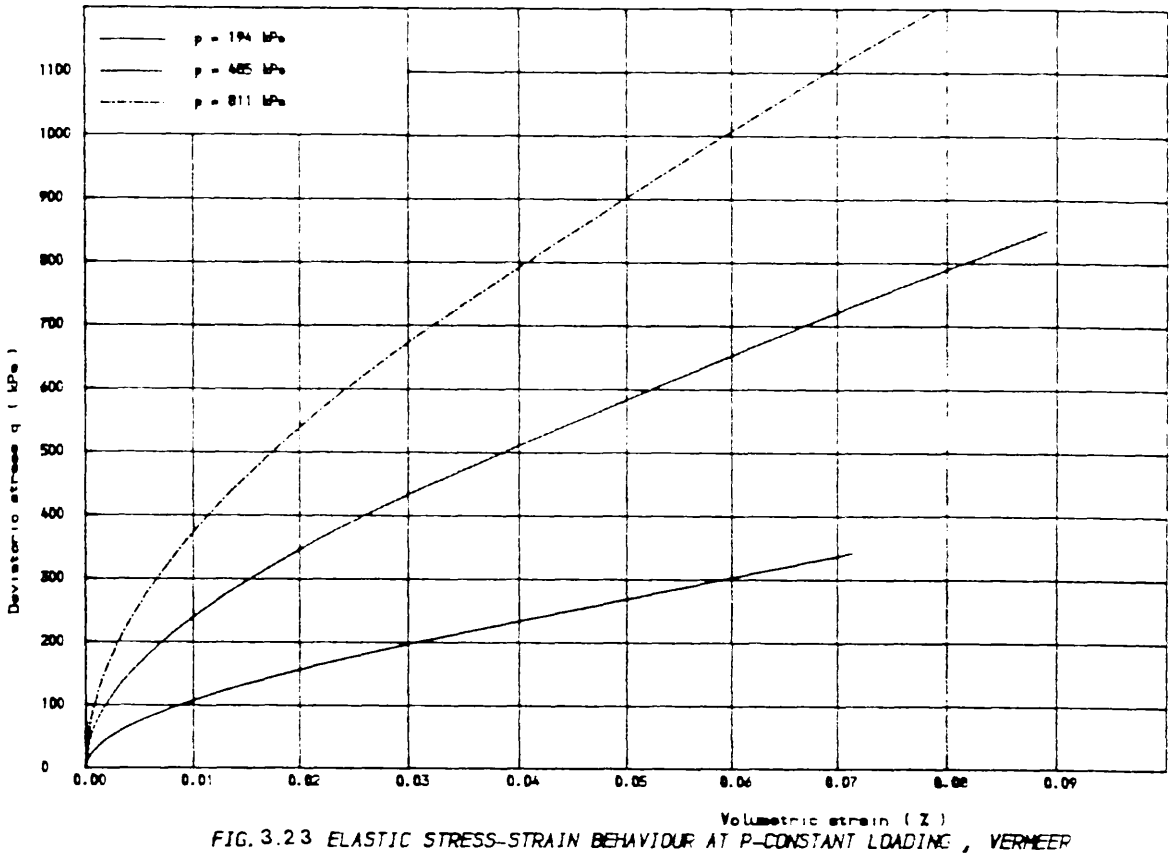

FIG. 3.23 ELASTIC STRESS-STRAIN BEHAVIOUR AT P-CONSTANT LOADING , VERMEER
(Karlsruhe sand , Po=200 kPa , Incremental form)

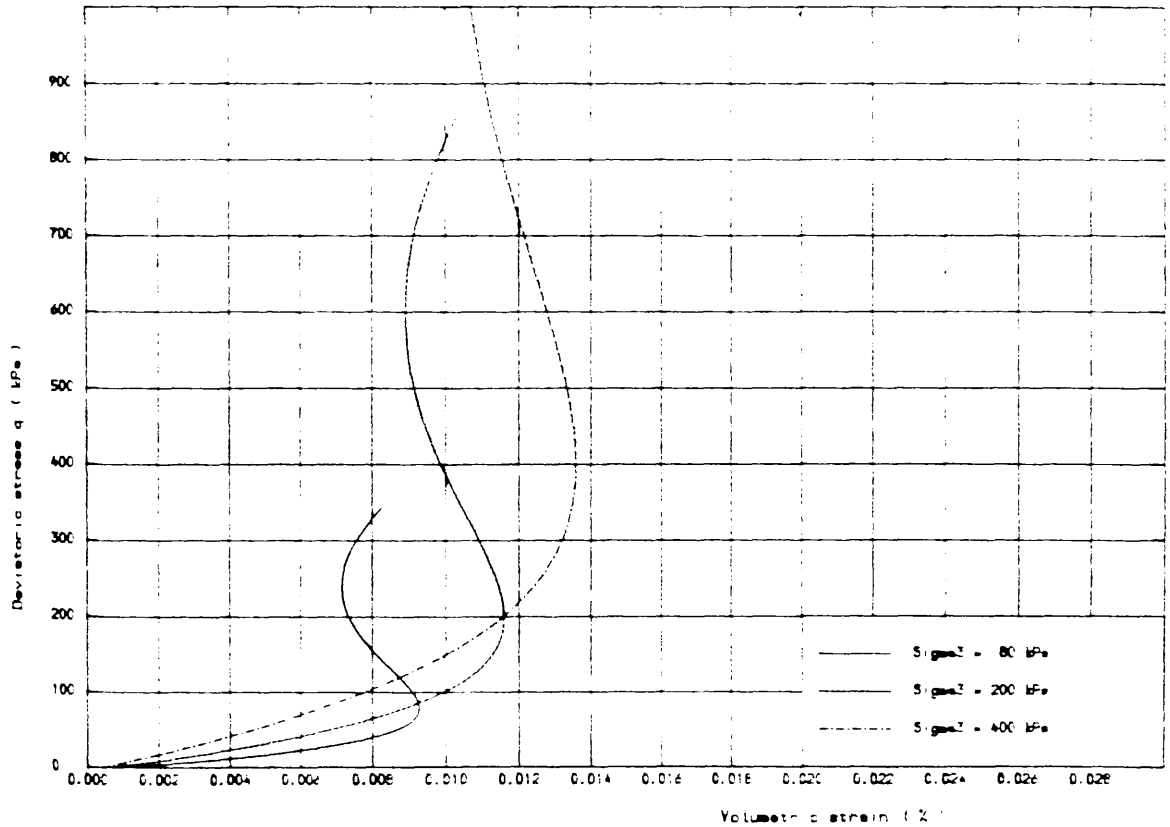

FIG. 3.24 ELASTIC STRESS-STRAIN BEHAVIOUR IN TRIAXIAL COMPRESSION , VERMEER
(Karlsruhe sand , Po=200 kPa , Incremental form)

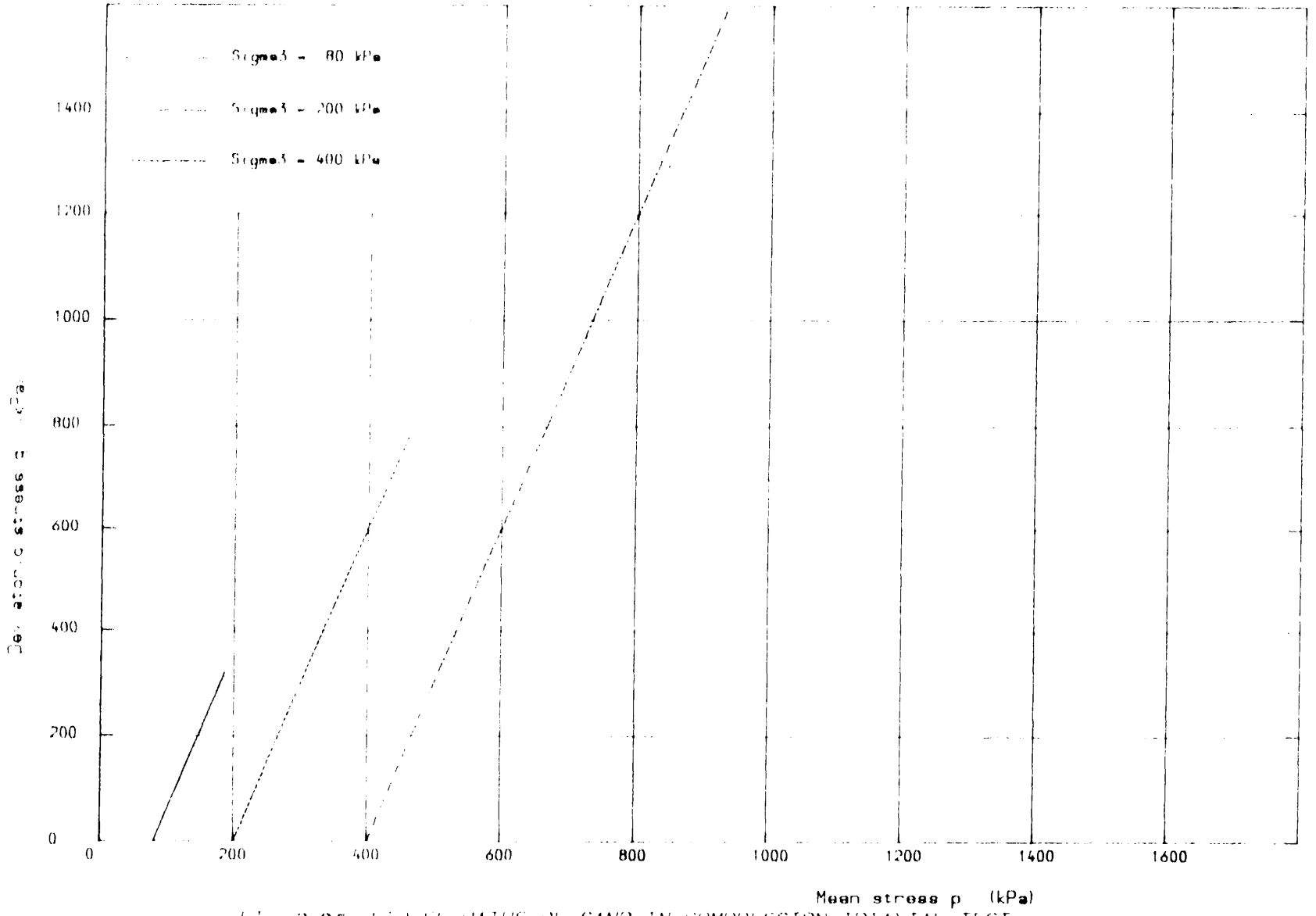

Fig. 3.25 STRESS PATHS OF SAND IN COMPRESSION TRIAXIAL TEST

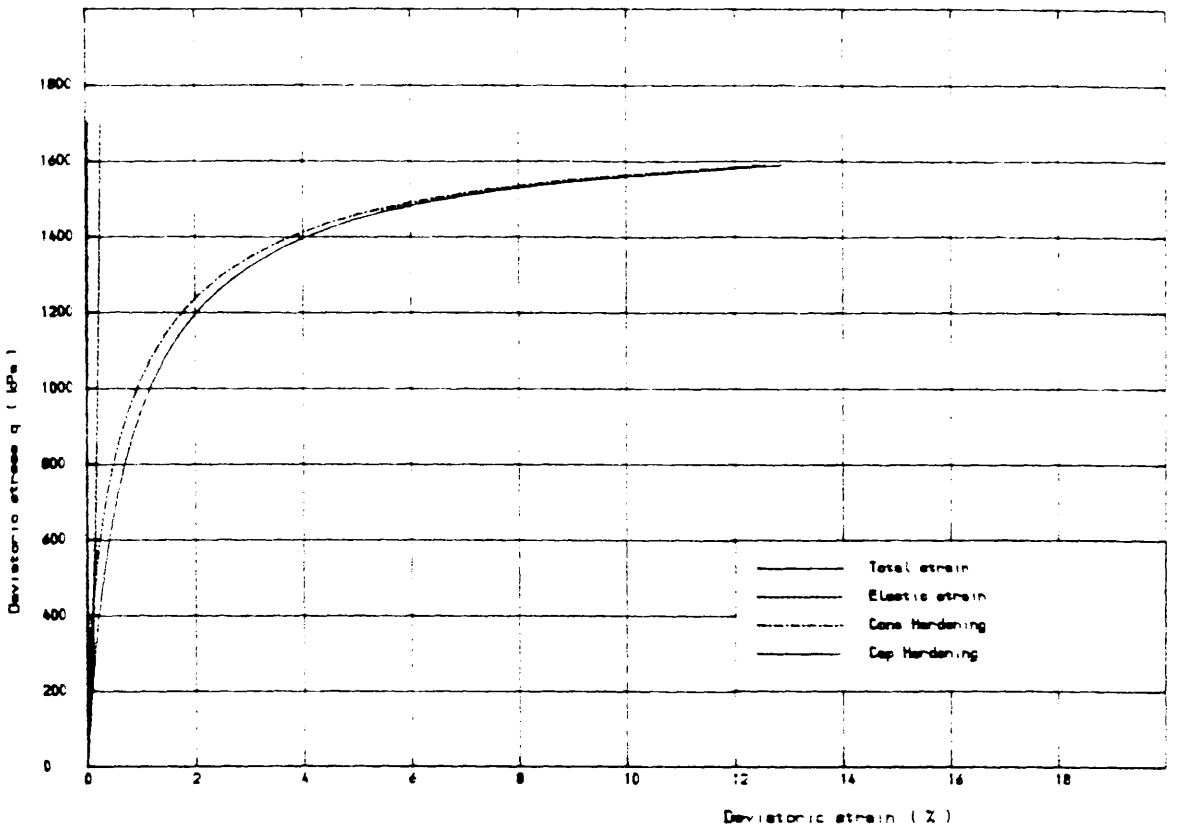

FIG.3.26 VARIOUS COMPONENTS OF STRAIN AND TOTAL STRAIN IN TRIAXIAL TEST
(Karlsruhe sand , Beta=0.25 , Go=75 MPa , Po=200 kPa , Sigma3=400 kPa)

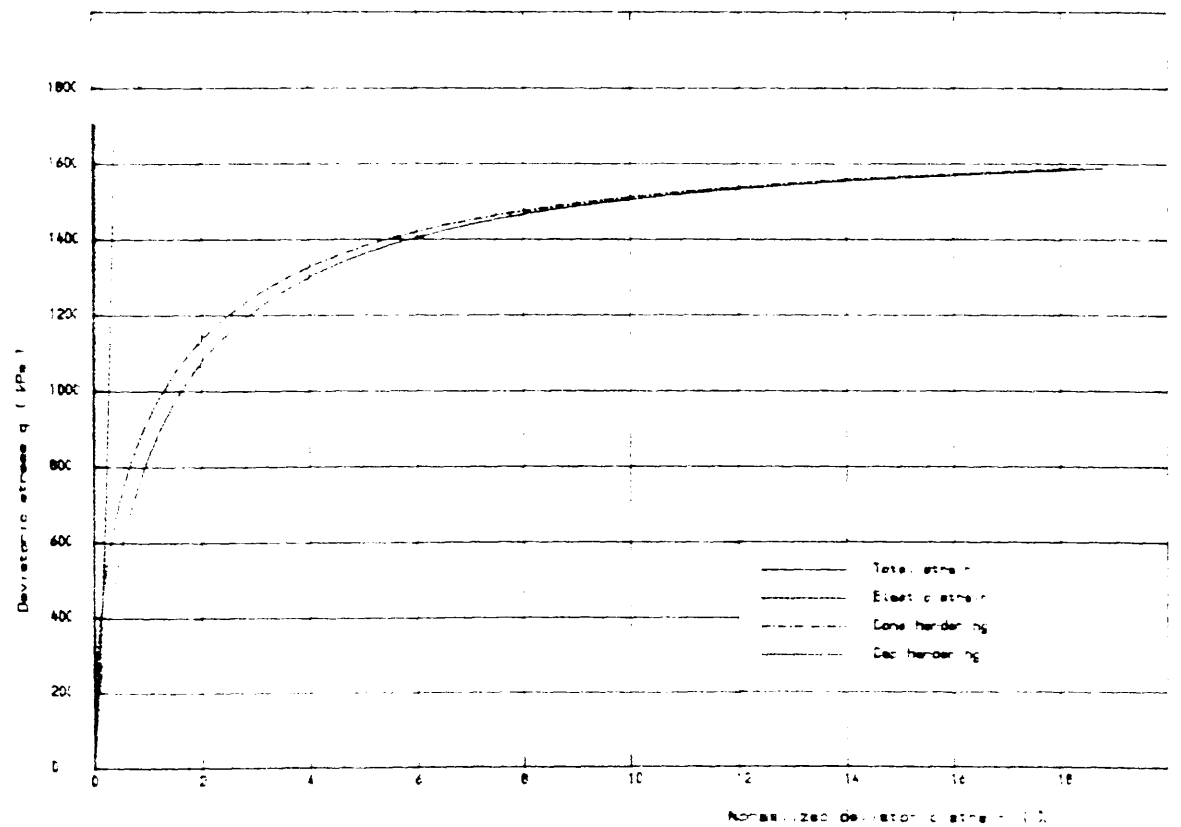

FIG.3.27 VARIOUS COMPONENTS OF STRAIN AND TOTAL STRAIN IN TRIAXIAL TEST
(Karlsruhe sand , Beta=0.25 , Go=75 MPa , Po=200 kPa , Sigma3=400 kPa)

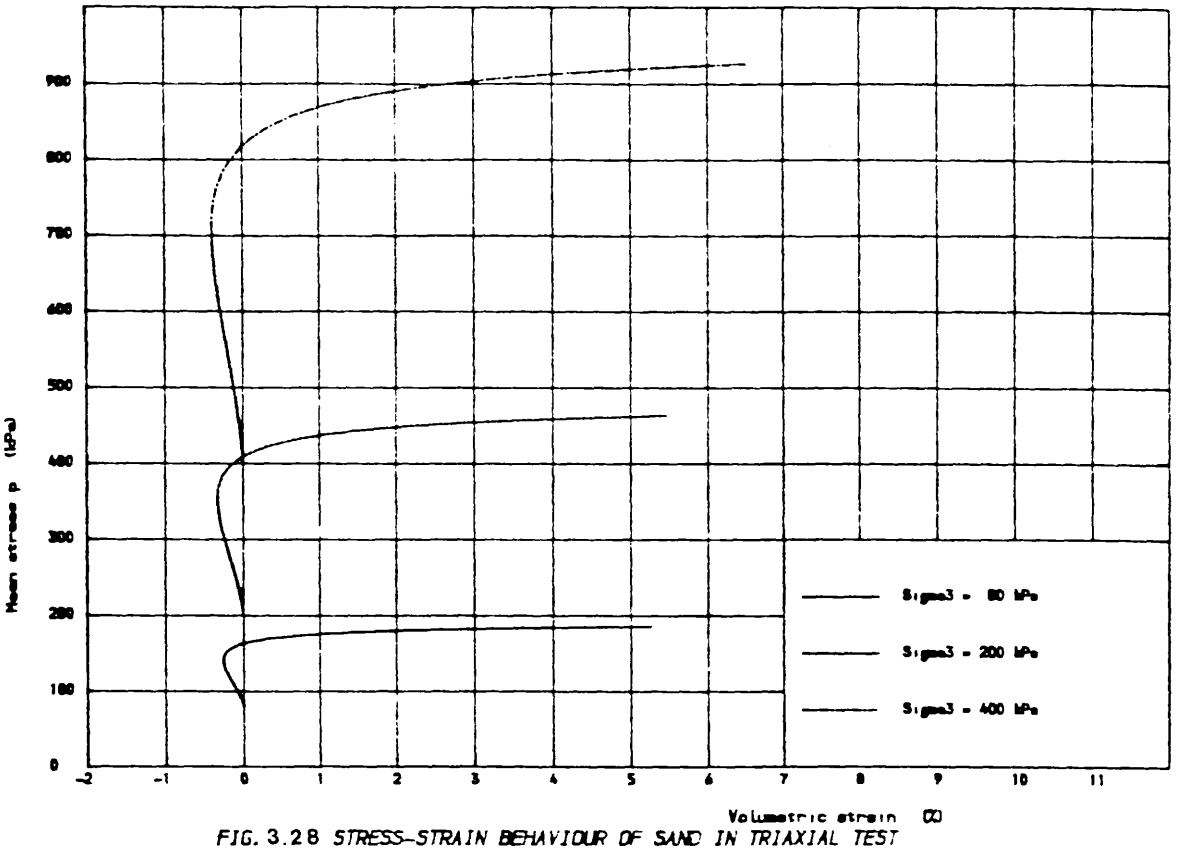

FIG. 3.28 STRESS-STRAIN BEHAVIOUR OF SAND IN TRIAXIAL TEST
(Dense Karlsruhe sand , Po=200 kPa , Go=75 MPa)

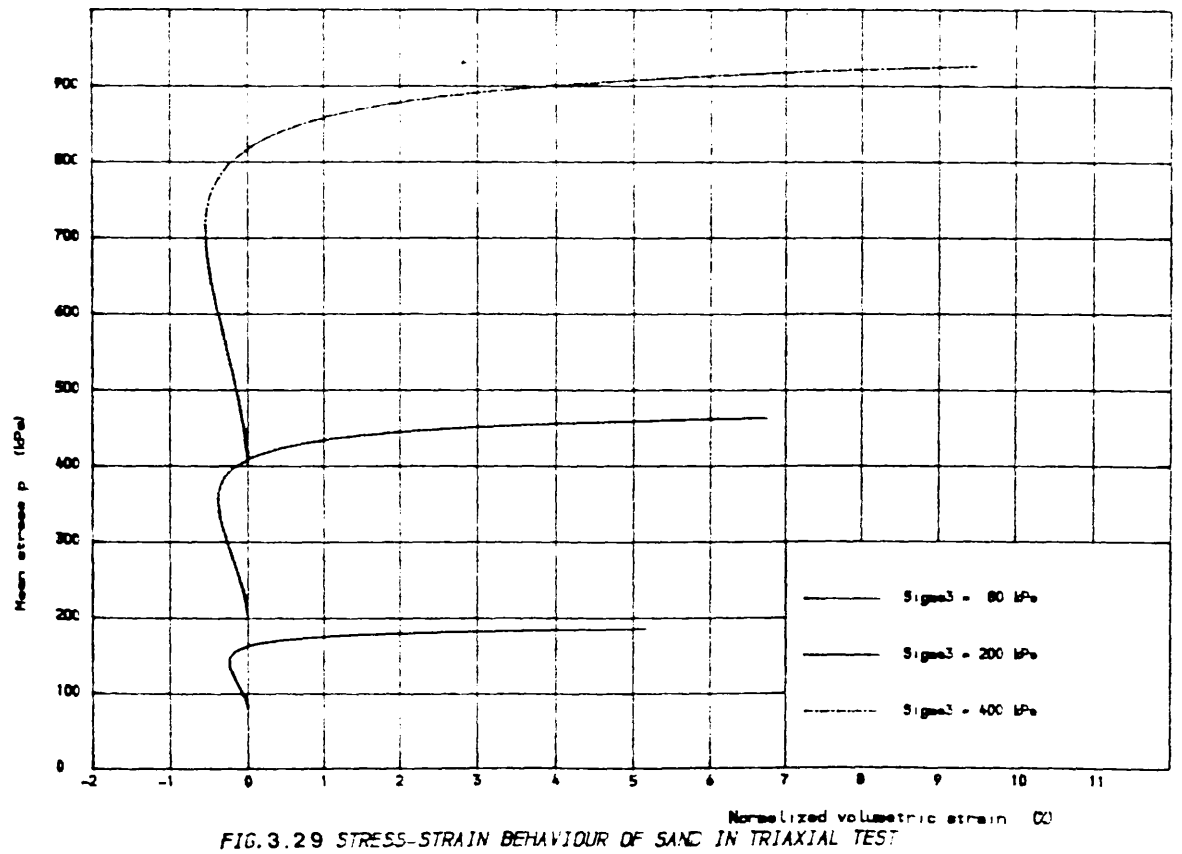

FIG. 3.29 STRESS-STRAIN BEHAVIOUR OF SAND IN TRIAXIAL TEST
(Dense Karlsruhe sand , Compression , Po=200 kPa , Go=75 MPa)

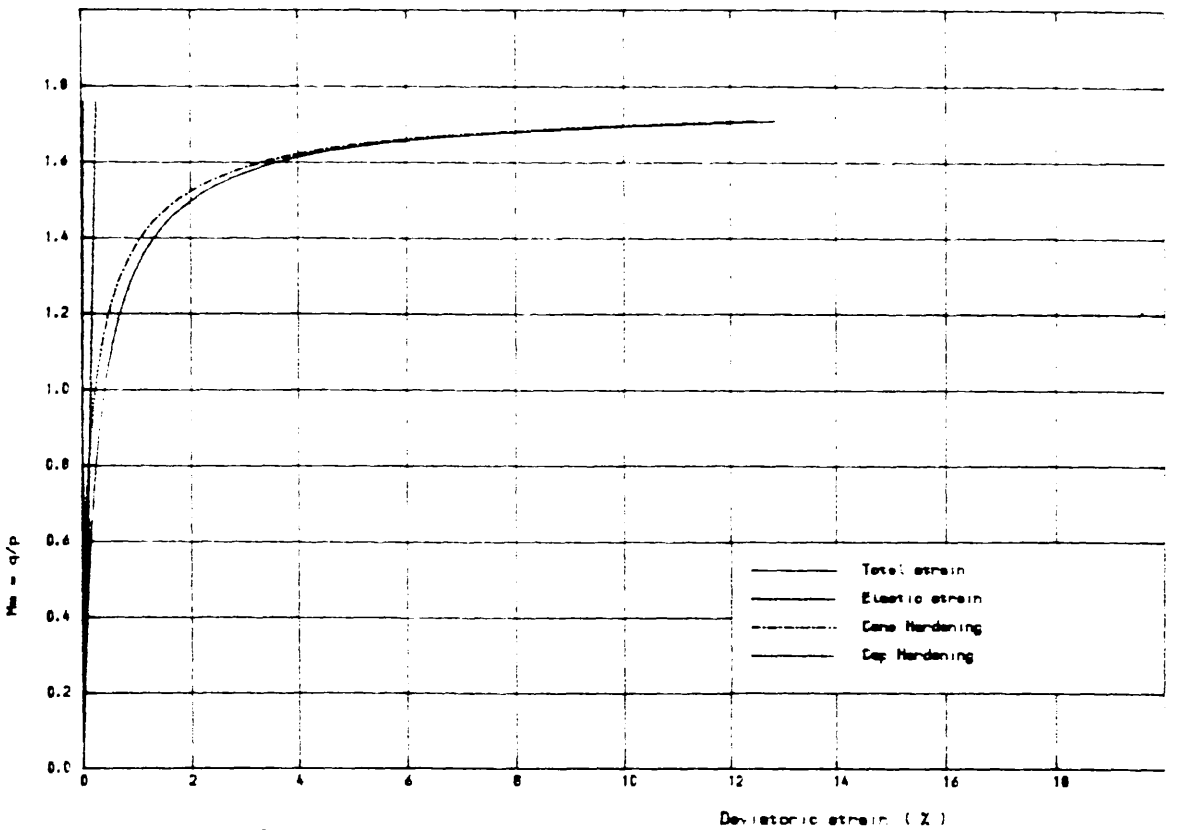

FIG.3.30 VARIOUS COMPONENTS OF STRAIN AND TOTAL STRAIN IN TRIAXIAL TEST
(Karlsruhe sand , Beta=0.25 , Go=75 MPa , Po=200 kPa , Sigma3=400 kPa)

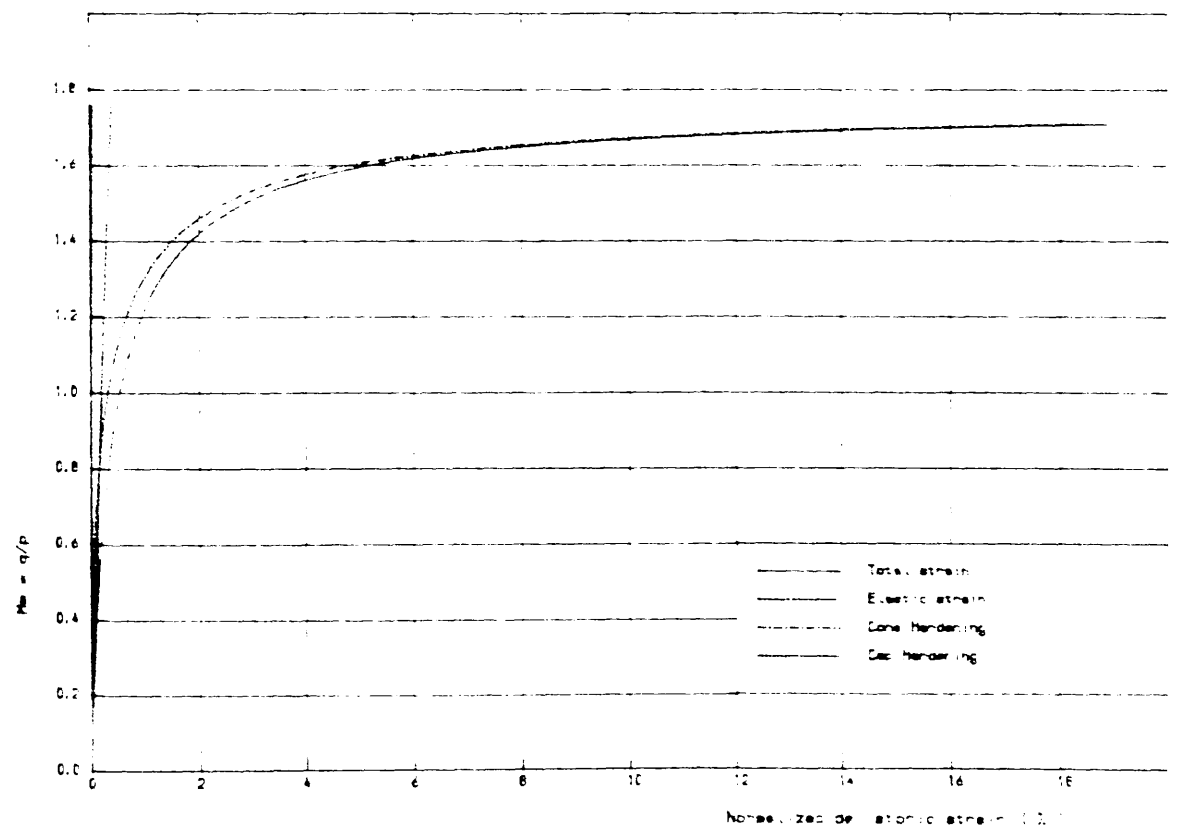

FIG.3.31 VARIOUS COMPONENTS OF STRAIN AND TOTAL STRAIN IN TRIAXIAL TEST
(Karlsruhe sand , Beta=0.25 , Go=75 MPa , Po=200 kPa , Sigma3=400 kPa)

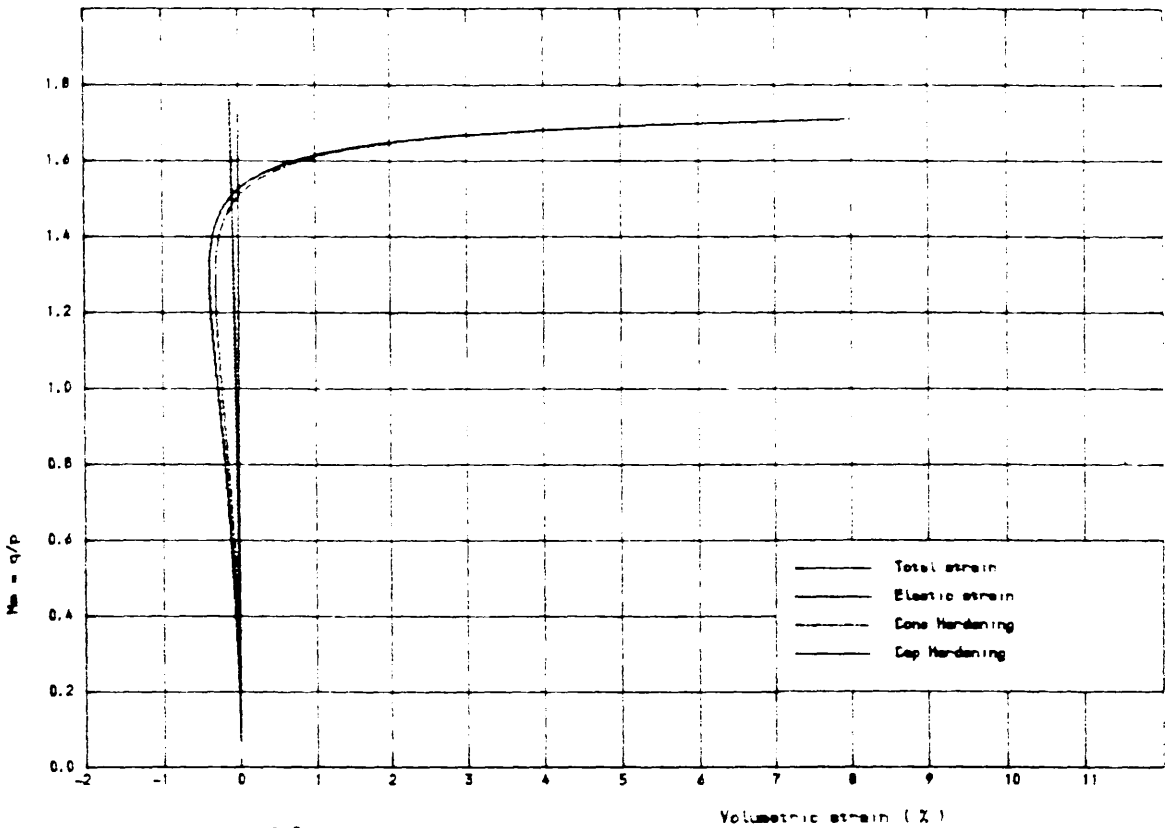

FIG. 3.32 VARIOUS COMPONENTS OF STRAIN AND TOTAL STRAIN IN TRIAXIAL TEST
(Karlsruhe sand , Beta=0.25 , Go=75 MPa , Po=200 kPa , Sigma3=400 kPa)

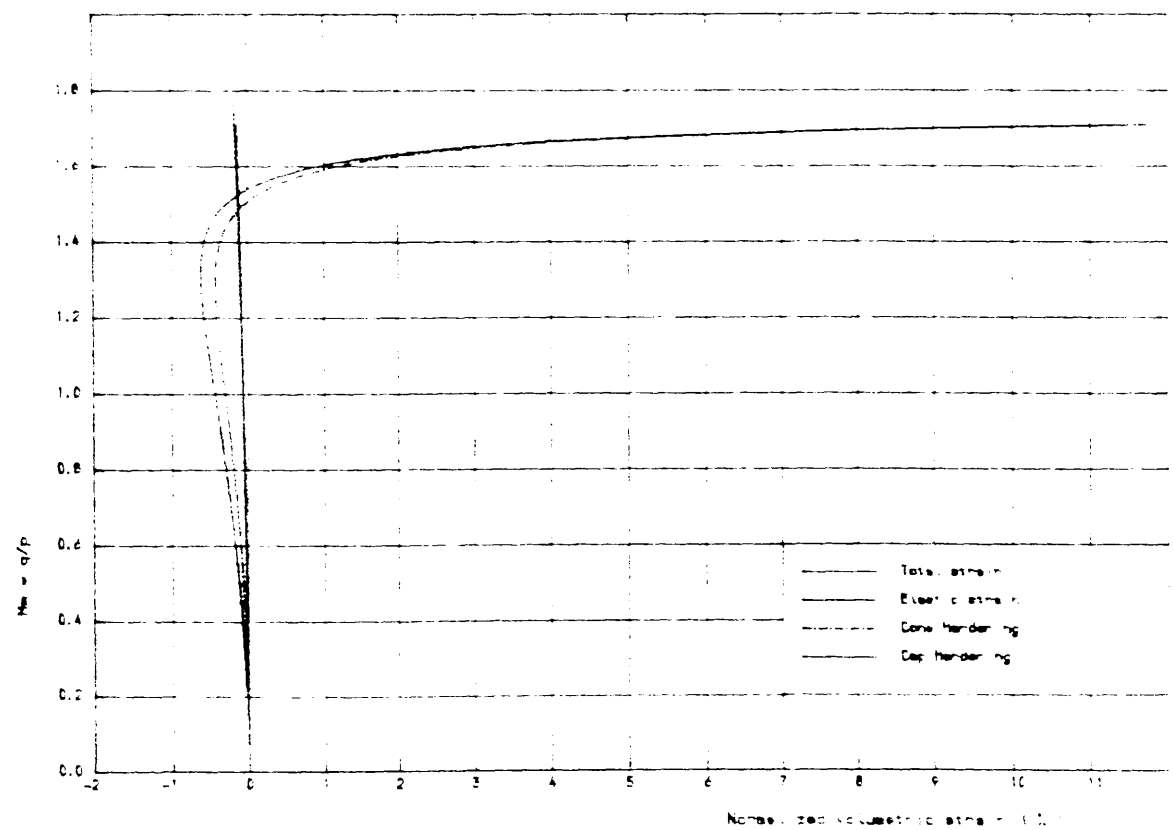

FIG. 3.33 VARIOUS COMPONENTS OF STRAIN AND TOTAL STRAIN IN TRIAXIAL TEST
(Karlsruhe sand , Beta=0.25 , Go=75 MPa , Po=200 kPa , Sigma3=400 kPa)

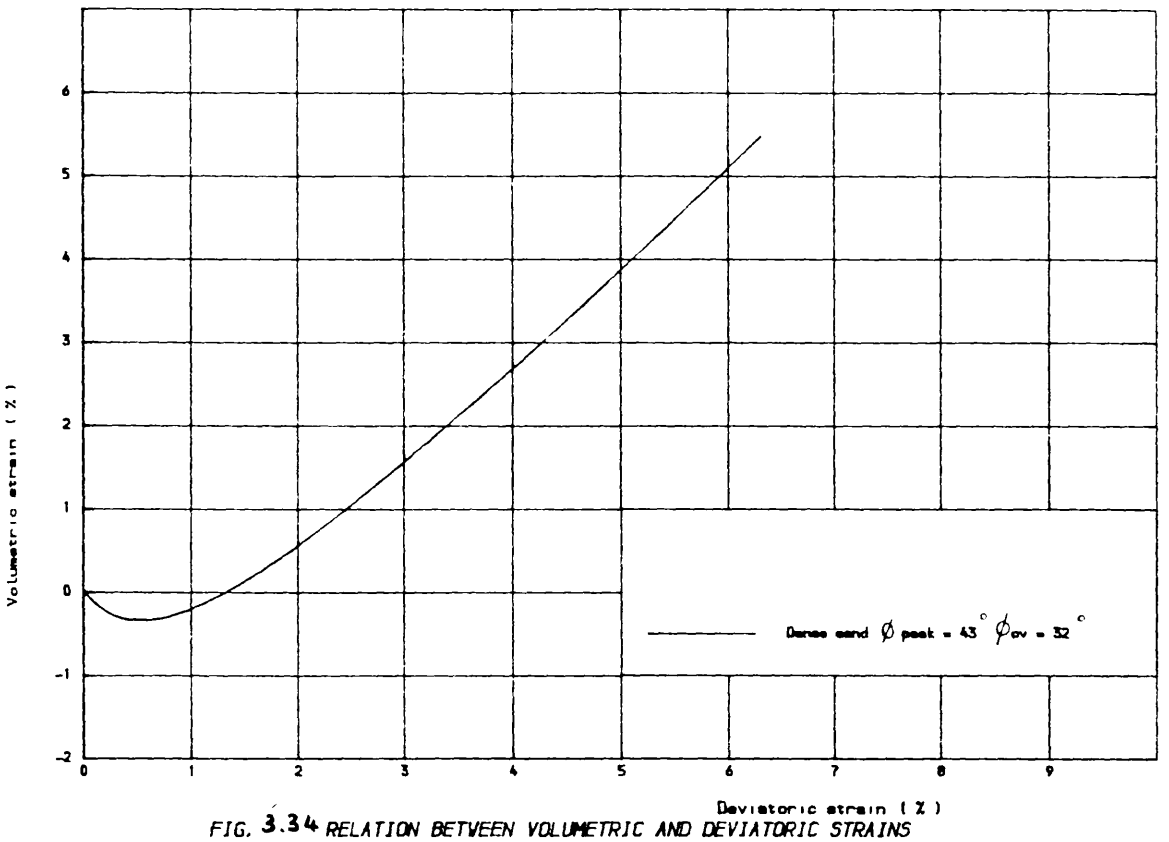

FIG. 3.34 RELATION BETWEEN VOLUMETRIC AND DEVIATORIC STRAINS
(Karlsruhe sand , Triaxial compres. , Sigma3=200 kPa)

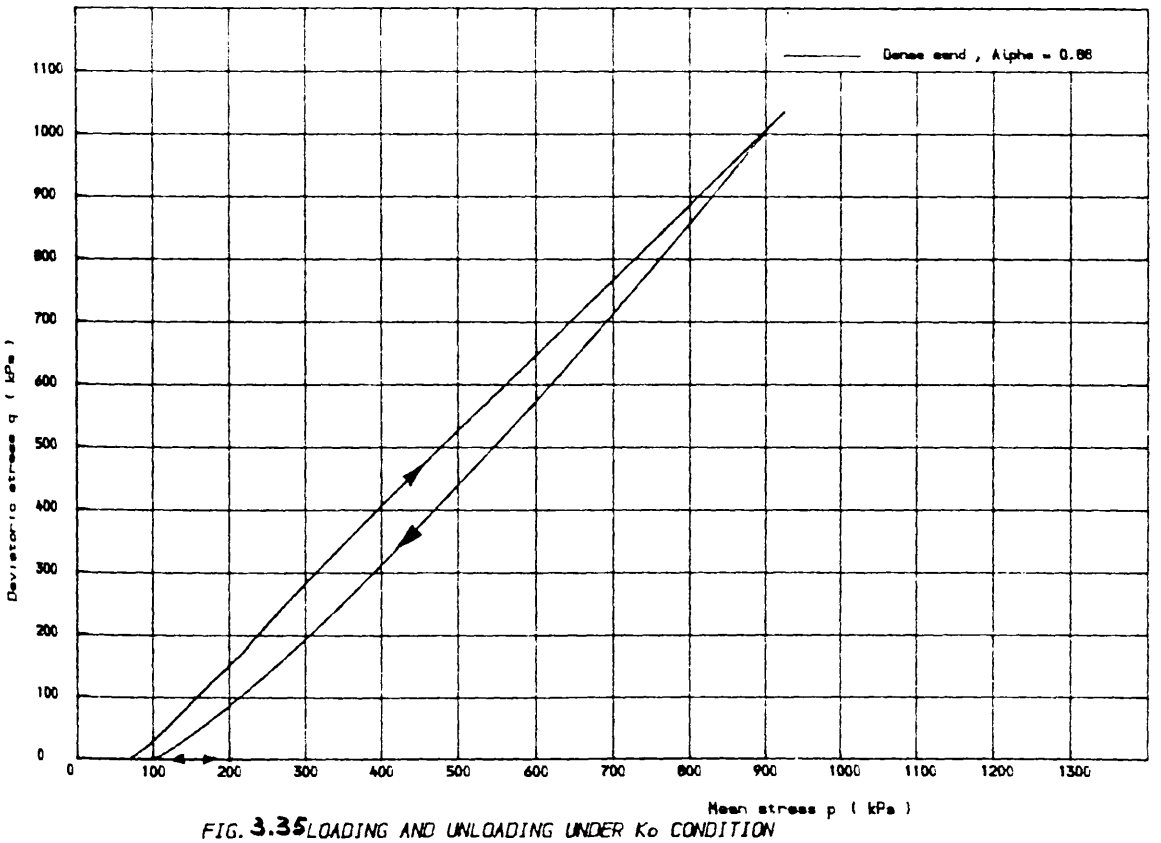

FIG. 3.35 LOADING AND UNLOADING UNDER Ko CONDITION
(Dense Karlsruhe sand , Po=200 kPa , Go=75 MPa)

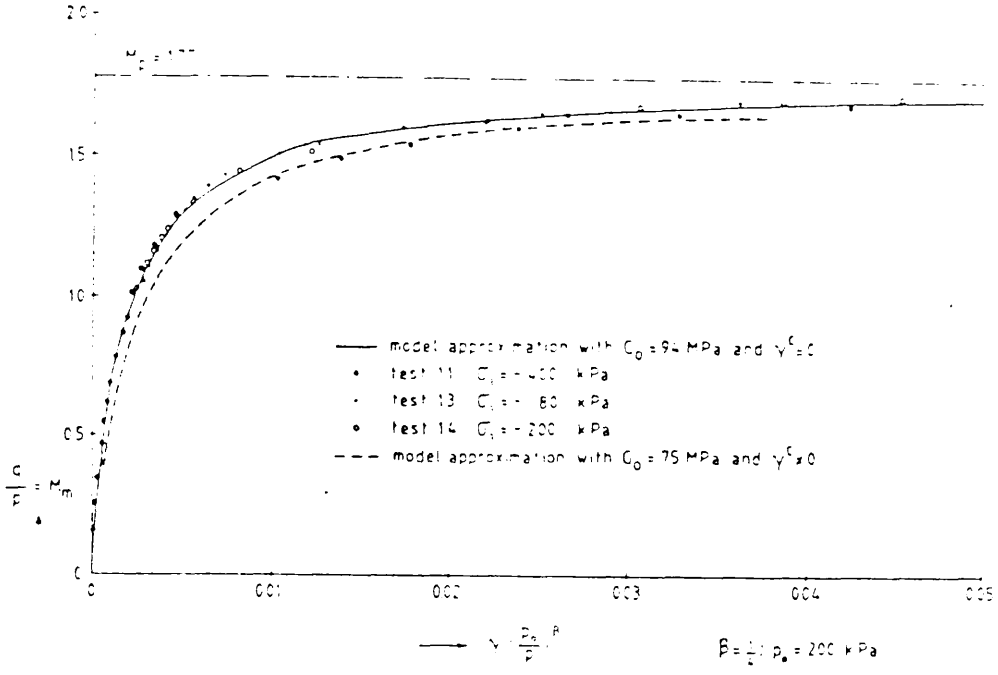

Figure 3.36 Predictions and results from constant cell pressure tests, Vermeer 1982.

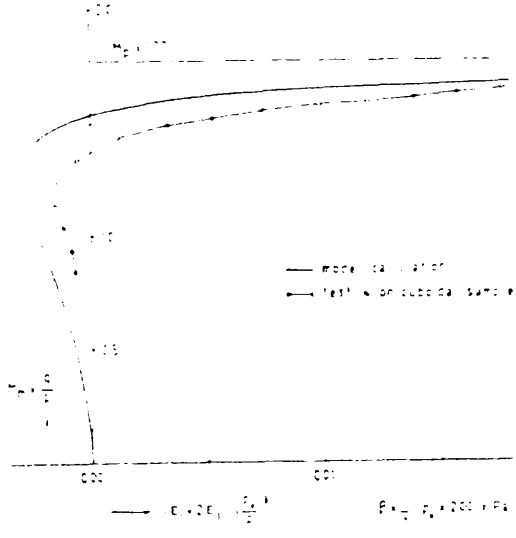

Figure 3.37 Predictions and test results from constant cell pressure tests in triaxial ramble, Vermeer 1982.

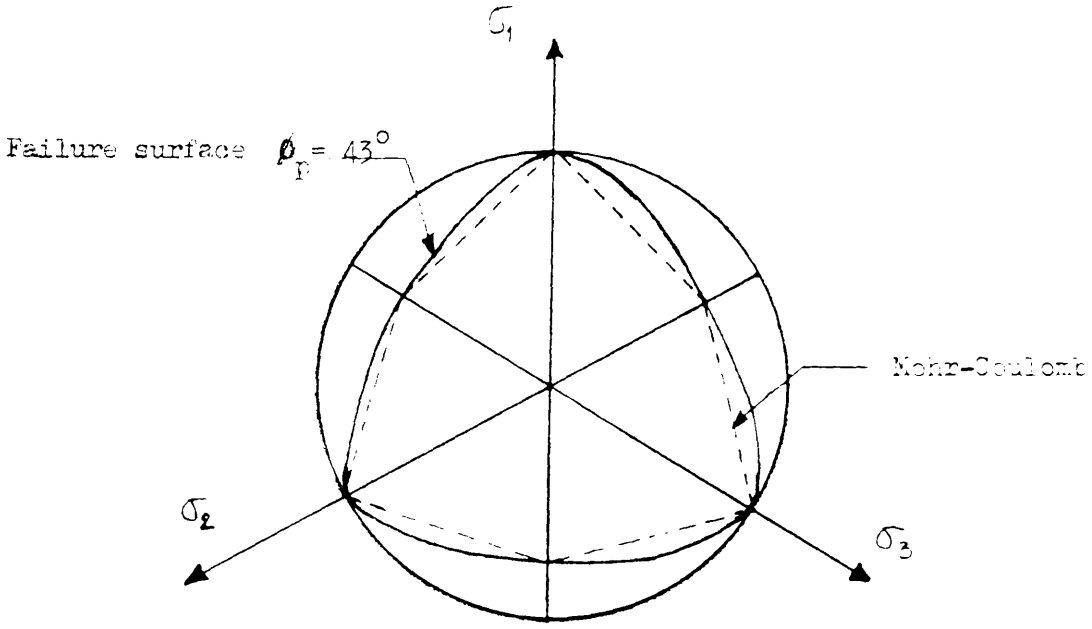

Figure 3.38 Failure surface in deviatoric plane.

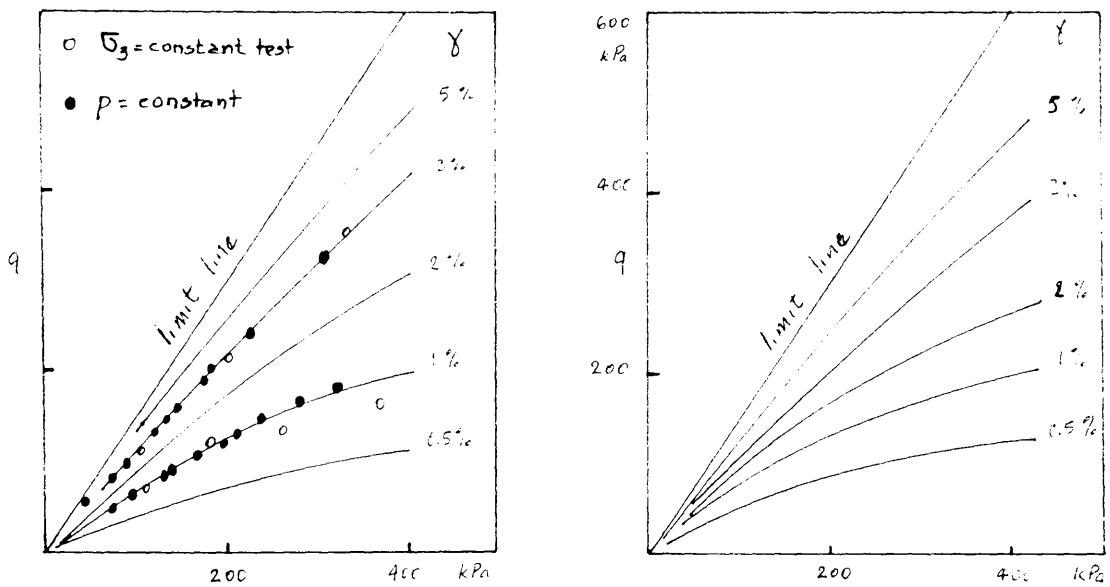

Figure 3.39 Yield loci.

4.1 INTRODUCTION :

In this chapter a short summary of the finite element method will be given together with a description of the computer program used in this analysis of ground anchors. A more complete treatment of the finite element method is given by many authors notably Zienkiewicz[96], Naylor and Pande[59] and Owen and Hinton[63]. Enhancements to the program to allow for initial stresses are then described. A study of the parameters having influence on the convergence of the solution process is described and finally, the parameters having a major effect on the behaviour and pull–out capacity of plate anchors are examined.

4.2 FINITE ELEMENT THEORY:

The finite element method is an approximation technique which represents continua by equivalent discrete systems. Consequently, continua with infinite degrees of freedom are approximated by equivalent systems with finite numbers of degrees of freedom. The successive stages constituting the finite element algorithm are described in the following sections.

4.2.1 Discretisation:

The starting point of the analysis is the division of the system into finite elements. Eight basic elements are illustrated in Fig 4.1. For geotechnical work, the triangular and quadrilateral elements for plane strain or axisymmetric analysis are most commonly used. The elements most often used in such analyses are the so–called 8–noded Serendipity elements; they have four corner nodes and four

midside nodes. There seems to be a consensus that these so-called 'parabolic' elements which have one midside node offer the best results. These elements are termed isoparametric: that is, the equations describing the shape of their boundaries are the same as those describing the variation of the nodal unknowns (e.g. displacements) across the element. Selection of the size and shape of elements is a matter of experience and intuition. Generally, elements should be smaller where the displacement gradients are steepest, i.e where there are rapid changes in stress and strain as shown in Fig 4.6.

4.2.2 Shape Function:

The shape (interpolation) functions define the variation of quantities across elements in terms of the nodal values. Let V stand for the value of the quantity at some point r, z then :

$$V = \sum_{i=1}^{n} N_i \, V_i \qquad (4.1)$$

where,

N_i is the shape function for node i,

n is the number of nodes in the element, and

V_i is the value of the quantity at node i.

The shape functions for the 8-node Serendipity element are shown in Fig 4.2.

for corner nodes:

$$N_i = \tfrac{1}{4} (1 + \zeta\zeta_i) (1 + \eta\eta_i) (\zeta\zeta_i + \eta\eta_i - 1) , \qquad i = 1,3,5,7 \qquad (4.2a)$$

for midside nodes:

$$N_i = \tfrac{1}{2} \zeta_i^2 (1 + \zeta\zeta_i) (1 - \eta^2) + \tfrac{1}{2} \eta_i (1 + \eta\eta_i) (1 - \zeta^2), \quad i = 2,4,6,8 \qquad (4.2b)$$

where ξ and η are the intrinsic coordinates of any point within the element. By definition, ξ and η have values in the interval $[-1,+1]$.

4.2.3 Coordinate Transformation:

Transformations from local (ξ,η) to global coordinates (x,y) are necessary. These include expressions for the incremental area dA = dr.dz in terms of $d\xi$ and

$d\eta$, and the cartesian shape function derivatives, i.e $\partial N_i/\partial r$ and $\partial N_i/\partial z$, given $\partial N_i/\partial \zeta$ and $\partial N_i/\partial \eta$.

By definition, the incremental area is:

$$dA = | J | \, d\zeta . d\eta \tag{4.3}$$

where $|J|$ is the determinant of the jacobian matrix J, and :

$$J = \begin{bmatrix} \dfrac{\partial r}{\partial \xi} & \dfrac{\partial z}{\partial \eta} \\ \dfrac{\partial r}{\partial \eta} & \dfrac{\partial z}{\partial \xi} \end{bmatrix} \tag{4.4}$$

The partial derivatives $\partial r/\partial \zeta$, etc... may be obtained from the shape function derivatives with respect to ξ, η and the nodal coordinates. Thus, by differentiating equation (4.1) we obtain:

$$\frac{\partial r}{\partial \xi} = \sum_{i=1}^{n} \frac{\partial N_i}{\partial \xi} . \, x_i \tag{4.5}$$

Explicit expressions for $\partial N_i/\partial \zeta$ and $\partial N_i/\partial \eta$ are readily obtained by differentiating equations (4.2a) and (4.2b).

To obtain the cartesian shape function derivatives the following chain rule is needed,

$$dN_i = \frac{\partial N_i}{\partial r} \, dr + \frac{\partial N_i}{\partial z} \, dz \tag{4.6}$$

Partial differentiation of (4.6) with respect to ζ and η in turn gives the following relation :

$$\begin{bmatrix} \dfrac{\partial N_i}{\partial \xi} \\ \dfrac{\partial N_i}{\partial \eta} \end{bmatrix} = \begin{bmatrix} \dfrac{\partial r}{\partial \xi} & \dfrac{\partial z}{\partial \xi} \\ \dfrac{\partial r}{\partial \eta} & \dfrac{\partial z}{\partial \eta} \end{bmatrix} \begin{bmatrix} \dfrac{\partial N_i}{\partial r} \\ \dfrac{\partial N_i}{\partial z} \end{bmatrix} \tag{4.7}$$

Inversions gives explicit expressions for the cartesian derivatives, ie:

$$\begin{bmatrix} \dfrac{\partial N_i}{\partial r} \\ \dfrac{\partial N_i}{\partial z} \end{bmatrix} = \frac{1}{|J|} \begin{bmatrix} \dfrac{\partial z}{\partial \eta} & -\dfrac{\partial z}{\partial \xi} \\ -\dfrac{\partial r}{\partial \eta} & \dfrac{\partial r}{\partial \xi} \end{bmatrix} \begin{bmatrix} \dfrac{\partial N_i}{\partial \xi} \\ \dfrac{\partial N_i}{\partial \eta} \end{bmatrix} \tag{4.8}$$

This expression (4.8) completes the transformations needed for axisymmetric applications.

4.2.4 Strain– Displacement Relations:

The displacements may be expressed as :

$$\underline{u} = (u,w)^T \tag{4.9}$$

where u and w are the displacements in the r and z directions,respetively.

The components of strain are :

$$\underline{\epsilon} = (\epsilon_r, \epsilon_\theta, \epsilon_z, \gamma_{rz})^T \tag{4.10}$$

where for small displacements, the strains are given as :

$$\begin{aligned} \epsilon_r &= \frac{\partial u}{\partial r} \\ \epsilon_\theta &= \frac{u}{r} \\ \epsilon_z &= \frac{\partial w}{\partial z} \\ \gamma_{rz} &= \frac{\partial u}{\partial z} + \frac{\partial w}{\partial r} \end{aligned} \tag{4.11}$$

For finite element applications it is necessary to relate strains to the displacements at element nodes $\underline{\delta}^e$. Using equation (4.1) to express u and w in terms of nodal displacement gives :

$$\underline{\epsilon} = B\ \underline{\delta}^e \tag{4.12}$$

The matrix B consists of a row of n submatrices B_i which for axisymmetric problems take the form:

$$B = \begin{bmatrix} \frac{\partial N_i}{\partial r} & 0 \\ \frac{N_i}{r} & 0 \\ 0 & \frac{\partial N_i}{\partial z} \\ \frac{\partial N_i}{\partial z} & \frac{\partial N_i}{\partial r} \end{bmatrix} \tag{4.13}$$

The need for the shape function cartesian derivatives is now apparent.

4.2.6 Stress–Strain Relations:

In general, the stress–strain relations can be expressed in the incremental form:

$$d\underline{\sigma} = D\ d\underline{\epsilon} \qquad (4.14)$$

where $\underline{\sigma} = (\sigma_r, \sigma_\theta, \sigma_z, \tau_{rz})^T$,in which $\sigma_r, \sigma_\theta, \sigma_z$ are the normal stresses in the r, θ and z directions and τ_{rz} is the shear stress in the rz plane. D is the constitutive matrix. Its components are constant for linear elastic materials and takes the form of equation (3.50). For nonlinear materials, the constitutive relations are stress dependent. The matrix D is symmetric for associated flow as shown in the previous chapter.

4.2.6 Stiffness Equations:

The global stiffness matrix equation which relates nodal forces to displacements is assembled from the individual element stiffness matrices.

Element stiffness matrices:

A typical element is assumed to be in equilibrium under a set of nodal forces $\underline{F^e}$ associated with displacements $\underline{\delta^e}$. Any external loadings are assumed to be applied at the nodes.

The use of the principle of virtual work forms the basis for the derivation of the relationship between nodal displacements and loads. A set of virtual displacements $\underline{\delta}^*$ is applied to the nodes. Let the stress at a point in the element be $\underline{\sigma}$ and the strain corresponding to the virtual displacements be $\underline{\epsilon}^*$. Equating the work done externally at the nodes to that done internally gives:

$$\underline{\delta}^{*T}.\ \underline{F^e} = \int \underline{\epsilon}^{*T}.\ \underline{\sigma}\ dV \qquad (4.15)$$

From equation (4.14), and noting the fact that (4.14) must hold true for any arbitrary virtual displacement, then:

$$\underline{F^e} = \int B^T\ \underline{\sigma}\ dV \qquad (4.16)$$

In geotechnical applications, equation (4.16) can be used to determine the equivalent nodal forces corresponding to the initial stresses.

Since the loading is applied by small increments, the relations used have an incremental form. By using the stress–strain equation (3.19), re–arranging, replacing $\underline{\epsilon}$ by (4.12) and susbtituting in (4.16) :

$$\underline{F}^e = \int B^T D B \underline{\delta} \, dV + \int B^T \underline{\sigma}_0 \, dV \qquad (4.17)$$

And in this case $\underline{\delta}$ is the actual nodal displacements vector.

Another way to write (4.18) would be :

$$\underline{F}^e = K^e . \underline{\delta}^e + \underline{F}_{\sigma 0} \qquad (4.18)$$

where:

$K^e = \int B^T D B \, dV$ is the element stiffness matrix and

$\underline{F}_{\sigma 0} = \int B^T \underline{\sigma}_0 \, dV$ element nodal forces due to initial stresses

Assembly:

The global stiffness equations are obtained by superimposing the element stiffness matrices, as a consequence of the compatibility and equilibrium conditions at nodes common to adjacent elements. The global matrix K (and load vector $\underline{R}$ where $\underline{R} = \underline{F} - \underline{F}_{\sigma 0}$) is thus assembled from element matrices K^e giving the overall stiffness equation :

$$K . \underline{\delta} = \underline{R} \qquad (4.19)$$

which can be solved for $\underline{\delta}$.

4.2.7 Solution Techniques for Nonlinear Problems:

The solution to nonlinear problems must proceed in an incremental manner since the solution at any stage depends not only on the current displacements of the structure but also on the previous loading history.

Tangential stiffness method:

In this method, the stiffness matrix $K(\delta)$ is assembled at the beginning of each increment of load. The load increments should, in theory, be infinitesimally small. However, with finite increments, at the end of the increment, equilibrium conditions

will not be satisfied, and :

$$K(\underline{\delta}) \cdot \Delta\underline{\delta} - \Delta\underline{R} = \underline{\Psi}(\underline{\delta}) \neq 0 \qquad (4.20)$$

where $\underline{\Psi}(\underline{\delta})$ is the residual load vector.

Iterations may be applied within load increments with the aim to make $\underline{\Psi}(\underline{\delta})$ tend to zero, and element stiffnesses are recomputed during each iteration of each load increment. The technique is illustrated schematically in Fig 4.3 for a one–dimensional problem. The use of this method in strain softening situations, where the tangent stiffness is negative, may lead to numerical instability.

Initial stiffness method:

If the stiffness matrix is not updated and instead the original (elastic) stiffness matrix is used, complete reduction of the stiffness matrix at each step can be avoided. In this case, complete equation solution need only be performed for the first iteration and subsequent approximations to the nonlinear solution obtained, via the expression

$$K \cdot \Delta\underline{\delta} - \Delta\underline{R} = \underline{\Psi}(\underline{\delta}) \qquad (4.21)$$

Since the same stiffness matrix K is employed at each stage, the reduced matrix can be stored and subsequent solutions merely necessitate the reduction of the right hand side $\underline{\Psi}(\underline{\delta})$ terms. This has the immediate advantage of significantly reducing the computing cost per iteration but reduces the convergence rate as can be seen in Fig 4.4. This method is said to be unconditionally convergent and can be employed (with care) for strain softening materials.

For the analysis of ground anchors in sand, this latter solution technique was employed since the tangential stiffness method failed to converge.

4.3 PROGRAM :

The finite element program used in this study was based on a nonlinear computer code developed by Owen and Hinton[63] for axisymmetric problems.

4.3.1 Description:

This finite element program PLAST uses four–, eight– and nine–node isoparametric quadrilateral elements. The eight–node Serendipity element was used in the finite element mesh. Point loads, gravity and distributed edge loadings can be handled by the program, as well as loading due to initial stresses and non–zero prescribed displacements . Four yield criteria are available: Von Mises, Tresca, Drucker–Prager and Mohr–Coulomb. The Mohr–Coulomb criterion employed in this study was used in conjunction with an associated flow rule. The equation solution is carried out by the frontal method. One subroutine assembles the contributions from each element to form the global stiffness matrix K and the global load vector $\underline{R}$ and also solves the resulting set of simultaneous equations by Gaussian direct elimination. PLAST offers four nonlinear solution algorithms. Two of them are basic techniques termed *the initial stiffness method* and *the tangential stiffness method*. The other two algorithms are obtained by combinination of these two .

4.3.2 Enhancements:

Some enhancements were necessary before the program could be used for this study. In brief, this involved writing code to set up the initial stress state since the original incremental loading procedure assumed proportional loading.

A subroutine which sets the initial stresses in the soil was therefore added. The listing is given in the appendix. The equivalent nodal forces due to the initial stress tensor $\underline{\sigma}_0$ are:

$$\underline{F}_{\sigma 0} = \int B^T \, \underline{\sigma}_0 \, dV \qquad (4.22)$$

The initial stresses here are the gravity stresses based on an elastic response. In addition, complementary boundary and anchor displacements must be specified at this stage.

A mesh generation routine was also added to the program. This save time and helped to avoid errors during the rather tedious task of data input.

4.4 SOIL–ANCHOR MODEL :

For a three–dimensional soil mass which is symmetrical about its centreline axis (which coincides with the z axis) and which is subjected to loads and boundary conditions that are symmetrical about this axis, the behaviour is independent of the circumferential coordinate θ. Figure 4.5 shows a typical axisymmetic solid. The volume of soil, represented by the cylinder, shows the soil which is most affected by the the anchor loading.

The circular anchor is assumed to be rigid and very thin and no relative displacement is assumed to occur between the anchor and the soil in contact. The radius of the axisymmetric solid is fixed to be large enough to ensure that the truncated boundary does not affect the anchor response. At the same time the computing cost, which is dependent of the mesh size and other parameters, should be minimised. A compromise between cost and accuracy is therefore necessary. A typical mesh which gives reasonably accurate results but without containing an unreasonable number of elements, is shown in Fig 4.6 .

To determine the optimum mesh pattern, a detailed convergence study is necessary.

4.5 FINITE ELEMENT RESULTS:

The numerical results are presented in three stages; first a detailed study of the convergence of the solution process is carried out. Secondly, a parametric study which includes the effects of the soil characteristics, anchor plate embedment and initial stress state on the behaviour of anchor plates is described. Finally, a comparison of these finite element results with experimental results taken from literature is discussed.

The program was ran on an ICL 3980 computer using the VME operating system. The values of the cpu– time are therefore related to this particular mainframe. In the following examples, the anchor diameter (D) is 2m and the

depths of embedment (H) varies from 5m to 20m. The soil characteristics are:

E= 100 MPa , ν= 0.3, γ= 20 kN/m^3 and φ= 35°

Where other values than these are used, these are noted explicitly. An attempt has been made to normalize the results so that they are applicable to a wider range of data than those mentioned above.

4.5.1 Failure Load:

The results of model and field tests on anchor plates suggest that very large plastic deformations occur before collapse. In particular as the embedment ratio H/D increases, more extensive plastic deformation occurs before collapse. Rowe and Davis[72] reported that at greater depths of embedment, the deformations before collapse are so large that "practical" failure may be deemed to have occurred at a load less than the true collapse load. For deep anchors, use of the true collapse loading in conjunction with typical factors of safety of 2.5–3 would give working loads in the highly nonlinear range of behaviour and result in displacements much larger than would be predicted from an elastic analysis. The authors finally used the so–called "k_4 failure load" concept. This k_4 failure load is the load which produces four times the displacement that would have occurred if the soil remained elastic (Figure 5.1). This k_4 failure load concept is used in this study for both shallow and deep anchor.

4.5.2 Convergence Study:

In order to have confidence in the accuracy of the results obtained from finite element analyses, a convergence study in the elastic and elasto–plastic domains must be carried out. The main objective of this part of work is to reduce the computer cost while maintaining good accuracy. The sensitivity of the solution to the mesh size, boundary conditions, increment size, and convergence tolerance was studied for a shallow anchor. The results of this study are discussed below.

Precision:

Figure 4.9 shows that when the computer calculations are carried out in single precision the anchor pull−out capacity is different from that obtained with double precision calculations. Although the results are identical in the elastic domain, the difference is rather high (25% for δ= 10mm)for elasto−plastic behaviour and would affect a great deal the anchor pull−out capacity. Although the cost of double precision arithmetic is almost twice as much as that of single precision arithmetic (for the case of a shallow anchor at H/D= 2.5 , 30−element mesh). The use of double precision appears to be necessary to get reliable results. This conclusion is specific to the ICL computer which has a very short word length.

Mesh size:

Figure 4.10 depicts the load−displacement curves for the 16− , 30− , 49− and 100−element meshes shown in Figure 4.7 (a & b) for a shallow anchor (H/D= 2.5). The curves show that meshes with a lesser number of elements give a stiffer and unstable response. Meshes with larger number of elements give naturally more accurate results but larger cpu−time. The computations took over 3500 seconds for the 100−elements mesh, 1600 seconds for the 49−element mesh, 910 seconds for the 30−element mesh and 250 seconds for the 16−element mesh. The difference between responses of various meshes decreases when the displacement increases. From δ= 5mm onwards the responses converge and the effect of mesh size seems to become minor. For δ= 8mm, the variation of the load is about 7% for meshes with 30 and 49 elements with respect to that of 100 elements. For most problems involving shallow anchors, a 30−element finite element mesh was adopted since the the major objective here was to determine the collapse load.

Increment size:

The anchor was displaced in small successive increments of displacement and the respone was recorded for every increment. Figure 4.11 shows the load−displacement curves depicted by a shallow anchor with three different

displacement increments $\Delta\delta_1 = 0.2mm$, $\Delta\delta_2 = 0.5mm$ and $\Delta\delta_3 = 1mm$. From these plots, it can be seen that the increment size affects slightly the anchor pull-out capacity (less than 4% for $\Delta\delta = 0.2mm$ and $\Delta\delta = 0.5mm$). Since various embedment depths are considered, the use of dimensionless variables by introducing mechanical and geometrical properties of the soil-anchor system is required for normalizing the results. Therefore, in general a value of $\Delta\delta.E/D.\gamma.H = 0.25$ was chosen as the displacement increment.

Tolerance:

Because of equilibrium violation, extraneous residual forces develop in the iterative process of solution. The convergence criterion is based on a "tolerable" value of the residual. The criterion employed states that convergence occurs if the norm of the residual forces becomes less than the tolerance t:

$$\frac{[\sum_{i=1}^{N}(\Psi_i^r)^2]^{\frac{1}{2}}}{[\sum_{i=1}^{N}(f_i)^2]^{\frac{1}{2}}} \times 100 \leqslant t \qquad (4.23)$$

where f is the applied force vector,

$\underline{\Psi}$ is the residual force vector and r denotes the iteration number,

N is the total number of nodal points.

The convergence study on tolerance was carried out on an example of shallow anchor mesh of 30 elements. Figure 4.12 depicts load-displacement curves for four different values of tolerance : $t_1 = 5\%$, $t_2 = 2\%$, $t_3 = 1\%$ and $t_4 = 0.1\%$. These plots show that tolerances of 5% or 1% are insufficient because the load-displacement response of the anchor appears to be unstable. In this problem particularly, the tolerance of 2% gives, accidently, better results than for 1%. The execution of this problem took 440 seconds with a tolerance of 5%, 560 seconds with a tolerance of 2% and 910 seconds with a tolerance of 0.1%. For this problem using a tolerance of 0.1% , the number of iterations does not exceed 15. Although the computer time increases by 64% when the tolerance varies from 1% to 0.1%, a tight tolerance of 0.1% is necessary to obtain accurate results results.

Boundary Conditions:

The distance from the anchor axis to the bottom and lateral boundaries of the finite element mesh should be large enough to ensure that these boundaries will not have any effect on the pull–out capacity of the anchor. Therefore, a finite element mesh with the two boundary conditions (smooth (a) and rigid (b)) illustrated in Figure 4.13 was analysed. The slight effect of the boundary conditions on the pull–out capacity is shown in Figure 4.14. Contours of the vertical stress component for a shallow anchor at ultimate state represented in Figure 4.35 show horizontal lines with magnitudes equal to the insitu stresses near the lateral boundaries of the mesh. This shows that the stress distribution is unaffected by the boundary conditions. Therefore, with the given mesh dimensions, the boundary conditions do not have a major effect on the pull–out capacity of the anchor.

Cohesion:

The program is written to deal with c, φ materials. Therefore, in simulating sand behaviour, a very small value of cohesion must be provided in order to avoid numerical difficulties. Figure 4.15 shows the load–displacement curves for a shallow anchor assuming two values of cohesion, c= 100 Pa and c= 10 Pa. The two curves are similar between δ= 0 and δ= 6.5 mm ,then diverge somewhat between δ= 6.65 mm and 9 mm, then converge again for δ > 9 mm. For c= 100 Pa the computations took 910 seconds but rather longer for c= 10 Pa. Since the results are virtually identical, the higher value of cohesion was used in order to reduce computational time.

Scaling the Stress Point to the Yield Surface (Effect of MSTEP):

The incremental stress–strain relation are assumed to be valid for small increment sizes. If relatively large load increment sizes are permitted the process described by Owen and Hinton[63] and illustrated in Figure 4.16 can be used. The process of reducing the elastic stress to the yield surface is shown to end in the stress point D which is then scaled down to the yield surface to give point D'.

Greater accuracy can be achieved by relaxing the excess stress to the yield surface in several stages. The number of steps into which the excess stress AB is divided into is given by the following equation:

$$MSTEP = INTEGER(8.\Delta\sigma/c)+1$$

where $\Delta\sigma$ is the excess stress

c is the cohesion.

Obviously the greater the number of steps MSTEP, the greater the accuracy. However, $MSTEP_{max}= 30$ is sufficient as shown in Figure 4.17.

4.5.3 Parametric Study:

Suitable values of parameters such as mesh size, load increment size and tolerance have been determined from the convergence study. The influence of the boundary conditions on the uplift capacity of the anchor plate has also been studied and an appropriately sized region selected. Now, attention is focussed on the effect of soil properties, initial stress conditions and depth of embedment on the pull–out capacity of plate anchors. The effects of scale and, also, material inhogeneity are briefly considered. The magnitudes of the failure loads are defined using the k_4 failure load concept.

Angle of friction:

The effect of the friction angle φ on both shallow and deep anchors is studied. Figure 4.18 shows the load–displacement curves for a shallow anchor using four different types of sand ($\varphi= 30°$,35° ,40° and 45°). The plots show that the angle of friction has no effect on the soil response in the linear part of the curve. However, when the material behaviour is elasto–plastic the effect of the friction angle becomes significant and has a major effect on the anchor pull–out capacity. For instance, when the friction angle increases from 30° to 35°, the pull–out factor of this shallow anchor (H/D= 2.5) increases from 2.6 to 4.4, which represents a variation of 41%. However, an increase of the friction angle from 35° to 40° induces an increase of the pull–out factor of only 27% . Similar results are shown

in Figures 4.19 and 4.20 for anchors embedded at H/D= 5.0 and 10.0 respectively where variations in the angle of friction from 35° and 40° are depicted.

Embedment depth:

The effect of the depth of embedment ratio H/D has been investigated using anchor plates embedded at H/D= 2.5 (shallow anchor), H/D= 5 , and H/D= 10 (deep anchor). The results are summarised in Figure 4.21.a and 4.21.b. When the embedment ratio H/D increases the uplift capacity of the anchor increases. For instance, for a friction angle of 35° the ultimate load factor is 4.4 for a shallow anchor (H/D= 2.5), 6.2 for an anchor with H/D= 5 and 6.8 for a deep anchor (H/D= 10).

Insitu stress conditions:

The insitu stresses are calculated as follows:

$$\sigma_z^0 = \gamma z$$

$$\sigma_r^0 = \sigma_\theta^0 = K_0 \gamma z \qquad (4.24)$$

and $\tau_{rz}^0 = 0$

where K_0, the coefficient of earth pressure at rest, is taken as:

$$K_0 = \nu/(1-\nu) \qquad (4.25)$$

Figure 4.22 shows the load–displacement curves of three cohesionless soils for different initial stress conditions. These curves show that an increase of the coefficient of earth pressure at rest induces an increase of the anchor pull–out capacity. For instance, when K_0 increases from 0.43 to 0.54 the uplift capacity increases from 4.4 to 5.5, that is 25% of the initial value.

Inhomogeneity:

Sand whose Young's modulus of elasticity increases linearly with depth was considered which is probably a fair approximation to reality. The Young's modulus was assumed to vary as follows:

$$E = \mu.z$$

where μ is constant:

$$\mu = E_a/H$$

and $E_a = 100$ MPa, is the magnitude of the soil's Young modulus at the anchor level.

Since in finite element methods the material parameters are usually assumed to be constant within elements, the Young's modulus was assumed to vary in layers as shown in Figure 4.23.

Figure 4.24 shows the effect of soil inhomogeneity on the pull–out capacity of a shallow anchor (H/D= 2.5 and $\varphi = 35°$). For a homogeneous sand the ultimate uplift factor is 4.4 and for an inhomogeneous one it is 4.1, that is a difference of less than 7%. This indicates that the assumption of sand as a homogeneous material is convenient and does not induce a very large error in the results.

Scale:

In general, soil properties vary with depth. Therefore, the behaviour of plate anchors, whether they are tested in laboratory at reduced scale or on field at large scale, might be different. This possibility was investigated by simulating the behaviour of two plate anchors at depth of embedment ratio of 5 and different anchor diameters 2m and 0.2m. The Young's moduli were derived from Hardin et al's[39,40] equations for round–grained sands:

$$G = \frac{690\ (2.17-e)^2}{1+e}\ (p.p_A)^{\frac{1}{2}} \qquad (4.26)$$

where p_A is the atmospheric pressure (100kPa)

e is the voids ratio ($e \simeq 0.67$)

The stress conditions at rest are expressed by equation (4.24), therefore the mean stress p given by expression (3.36) becomes:

$$p = 2\gamma z/3 \qquad (4.27)$$

It is assumed that G is constant throughout the mass of soil (mesh) and equal to the value at anchor embedment depth. The relation between Young's modulus and shear modulus is:

$$E = 2(1+\nu)\ G \qquad (4.28)$$

After replacing z by H and, p_A and e by the values quoted above, the magnitudes of the Young's moduli obtained were:

for reduced scale E= 30 MPa

for large scale E= 100 MPa

Figure 4.25 depicts the response of a plate anchor at H/D= 5 tested on field ($E/\gamma H$= 500) and another one tested in laboratory ($E/\gamma H$= 1500). The normalized load capacity of the small scale anchor is rather higher than that of the large scale anchor. The pull−out factor is 6.2 for the large scale anchor and 6.5 for the reduced scale anchor. This difference may well be a numerical anomaly since this aspect of the study was not investigated further. Certainly, a scale effect might be expected and deserves further investigation.

Yielding Propagation:

Initiation and propagation of yielding in the sand around deep and shallow anchors is examined here. The friction angle of sand is 35°.

a/ Shallow anchors:

Figure 4.26 shows the propagation of yielding for a shallow anchor embedded at H/D= 2.5. Yielding initiates from the anchor edge and the ground surface near the anchor axis at 20% of the ultimate uplift load. These two small zones expand and propagate towards each other until they meet at a load equal to 60% of the ultimate anchor force. The resulting plastic zone then expands outwards in the direction normal to the anchor axis. However, the soil immediately above the anchor plate remains elastic. This is due to the fact that the stress state here is virtually hydrostatic. At the ultimate load, the shape of the plastic zone limit is reminiscent of the slip surfaces proposed by Balla[1] and Matsuo[49].

b/ Deep anchors:

Figure 4.27 shows yielding propagation in sand around a plate anchor embedded at H/D= 10. Yielding initiates near the edge of the anchor at 40% of the

ultimate uplift load. The major plastic zone is located above the anchor plate and propagates towards the soil surface. When the pull–out force reaches 90% of its ultimate value another yielding zone initiates at the ground surface near the anchor axis. An elastic zone above the anchor plate also exists for deep anchors.

Mesh Deformation:

Figure 4.28 shows the deformation of the sand around an anchor plate buried at shallow depth (H/D= 2.5). The region close to the anchor plate is most affected by the loading; more particularly points near the edge of the plate. Mesh elements located near the anchor edge undergo large displacements and 'necking' occurs in the elements situated below the anchor plate. However, the elements which are remote from the anchor axis retain their initial form and are relatively unaffected by the anchor loading.

Stresses Above and Below the Anchor Plate:

Figure 4.50 shows the vertical stress variation in the soil immediately above and below a deep anchor during loading. The anchor plate is buried at H/D= 10 and the friction angle is 35°. During loading, the vertical stress increases in the soil above the anchor and decreases in the soil below the anchor. Starting from the in–situ stress state described by equations (4.24) and (4.25), the anchor loading is applied incrementally. When the incremental vertical stress below the anchor reaches the magnitude of the initial stress at that point, the resulting stress becomes zero and a gap opens between the anchor plate and the soil below because sand has no tensile strength. In the mean time the vertical stress in the soil above the anchor increases continuously; initially in a linear manner.

Stress Distribution:

Contours representing the stress distributions due to the load of a rigid circular anchor plate are plotted for a shallow anchor (H/D= 2.5) in both elastic and ultimate states and for a deep anchor (H/D= 10) at ultimate state. The stress components and invariants shown in these plots are: radial stress σ_r, vertical stress

σ_z, circumferential stres σ_θ, shear stress τ_{rz}, mean stress p with definition (2.11), maximum shear stress τ_{max} with defintion (2.12) and stress ratio with definition (2.13.b). The anchor level is indicated by a dotted line.

a/ Shallow anchors:

Figures 4.29 to 4.35 show the stress distribution of various components of stress in the elastic state. The soil is assumed to sustain tensile stresses as well as compressive stresses. Only the incremental stresses are shown (ie neglecting the initial stresses) in order to emphasise the nature of the load transfer from the anchor to the surrounding soil. The main features noted for flexible anchors, studied in the second chapter of this thesis, are again evident in these plots. However, for rigid anchors, a pronounced stress singularity occurs over the edge of the anchor plate where the soil is strongly sheared.

Figures 4.36 to 4.42 show the stress distribution in sand around a rigid circular anchor at ultimate state. The value of the ultimate anchor mean pressure is 0.45 MPa. Contours of vertical stress shown in Figure 4.36 are horizontal in the region near the lateral boundary which shows that the anchor loading only effects the local region, around the anchor where the contours become markedly steeper. These remarks also apply to the radial, circumferential, mean and maximum shear stresses and suggest that as far as ultimate load predictions are concerned, accurate solutions can be obtained even with severely truncated mesh boundaries.

b/ Deep anchors:

Figure 4.43 to 4.49 show the stress distributions around a plate anchor buried in sand at H/D= 10. These data are very similar in type to those for shallow anchors and are presented for completeness without further comment.

4.5.4 Comparison With Experimental Results:

Figure 4.51 shows the variation of the uplift capacity of plate anchors with depth of embedment and various values of friction angle. The results from the finite element study are compared with the experimental results of Bemben and Kupferman[5]. These tests were carried out on two sands in a loose state. The first is a silty sand known as BBY sand ($\varphi = 36°$) and the second is a medium to fine sand known as Sunderland sand ($\varphi = 38°$). The finite element results appear to be in general agreement with these experimental results.

4.5 CONCLUSIONS:

The main stages constituting the general finite element algorithm have been described for the particular case of axisymmetry. Then followed a description of the program PLAST used in this analysis. Some enhancements to the program are also described. These involved the setting up of initial stresses and an incremental loading procedure with non-proportional loading. Subroutines for automatic mesh generation and in-situ stresses were added to the PLAST. After discretising the soil-anchor system, a convergence study which gave the optimum mesh pattern and suitable values of increment size and convergence tolerance, was carried out. At that stage a failure load criterion was defined and the "k_4 collapse load" concept proposed by Rowe and Davis[72] was adopted. Then, a parametric study including the effects of soil properties, initial soil conditions, and depth of embedment ratio on the pull-out capacities of plate anchors is described. Effects such as sand inhomogeneity and scale have been investigated. Obversation of the propagation of yielding in sand masses loaded by circular plate anchors embedded at deep and shallow depths has been particularly helpful for the understanding of the failure mechanisms. Contours of stress components and stress invariants in a soil mass loaded by a circular plate anchor are also plotted. These contours were plotted for shallow and deep anchors in elastic and ultimate states. Finally, the finite element

results were compared with experimental results of Bemben and Kupferman and generally good agreement was obtained. However, these data pertain to fairly loose (hardening) sands which do not present a very severe test of the power of finite element analyse for elasto_ plastic loading . A more sophisticated approach is necessary to obtain comparable results for analysis of anchors in dense sands.

however, in soil mechanics, fully plastic analysis are very difficult. Vermeer made the following remarks concerning his model in fully plastic analysis: "In relation to earlier versions of the present model, we presented several examples. However, extension towards problems concerning the ultimate bearing capacity appeared to be difficult." The veracity of these remarks are attested to by the difficulties experienced in this study and reported herein. Clearly, considerable further work will be necessary to obtain definitive numerical solutions for plate anchors capacity. Some suggestions are made in the following chapter to illuminate the path to this goal.

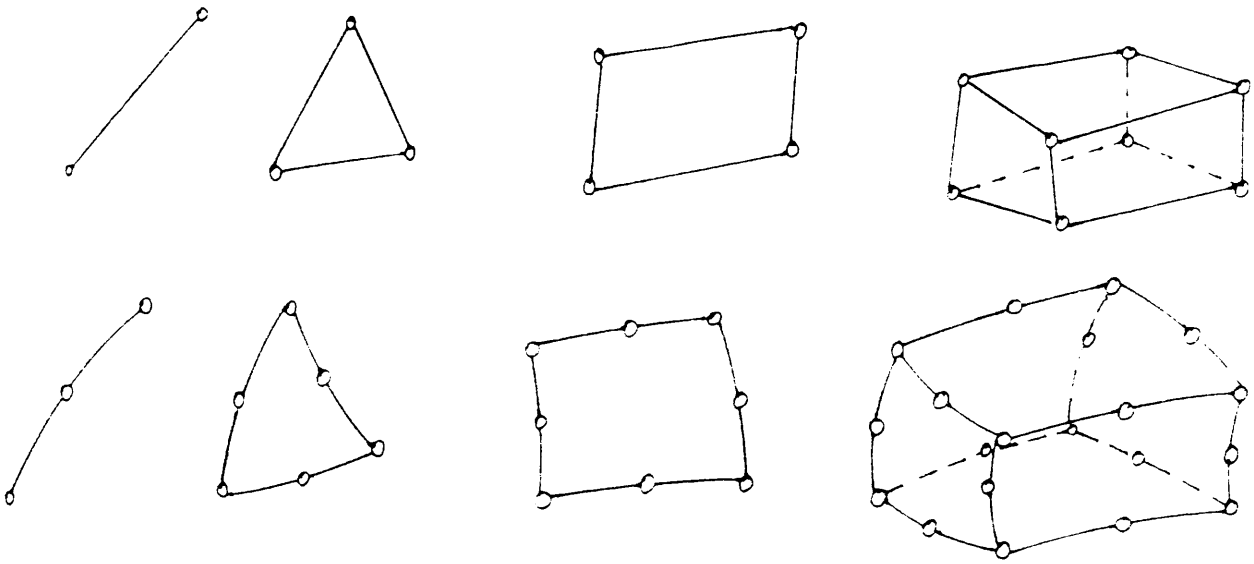

Figure 4.1 Some basic finite elements.

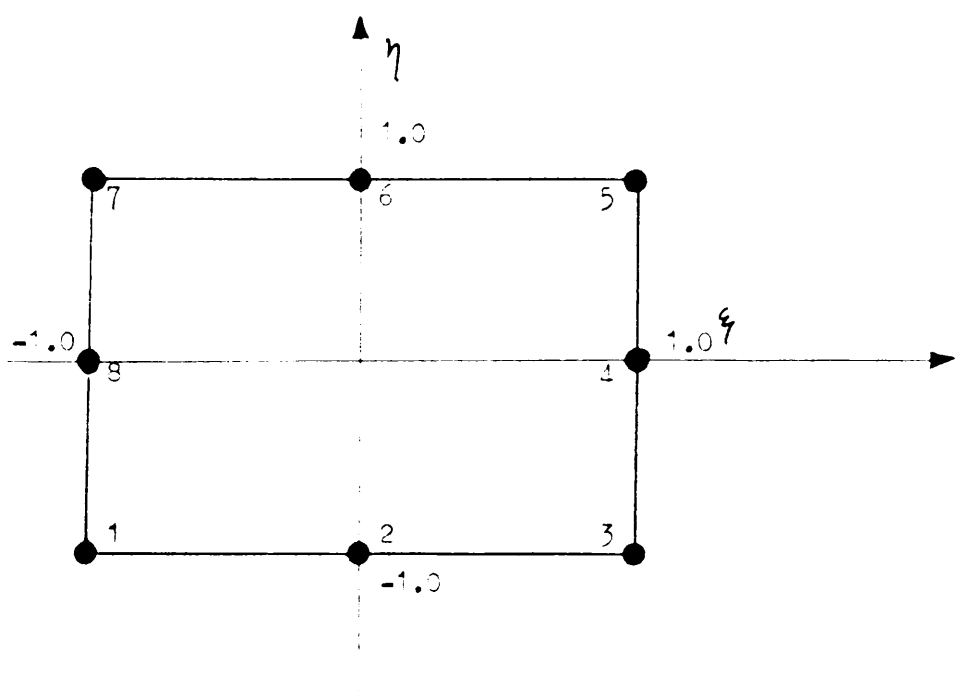

Figure 4.2 Eight-node Serendipity element.

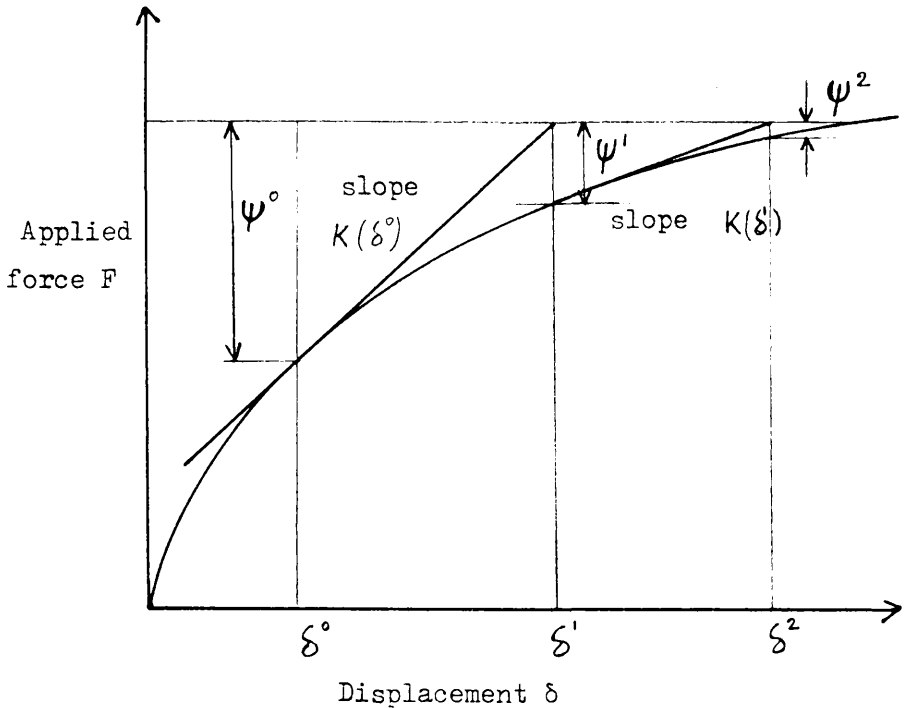

Figure 4.3 Tangential stiffness solution algorithm for a single degree of freedom.

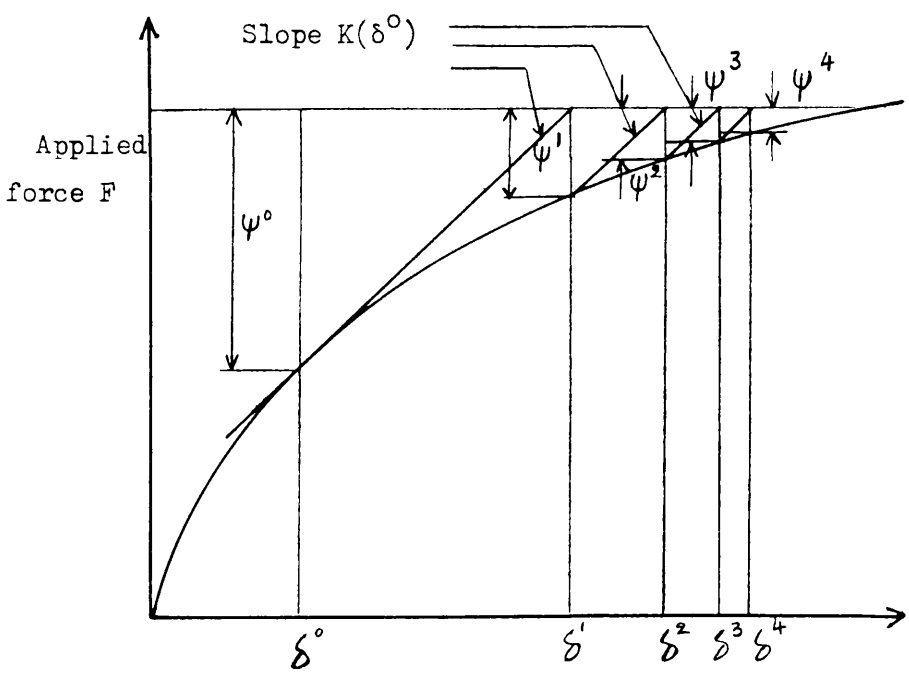

Figure 4.4 Initial stiffness solution algorithm for a single degree of freedom.

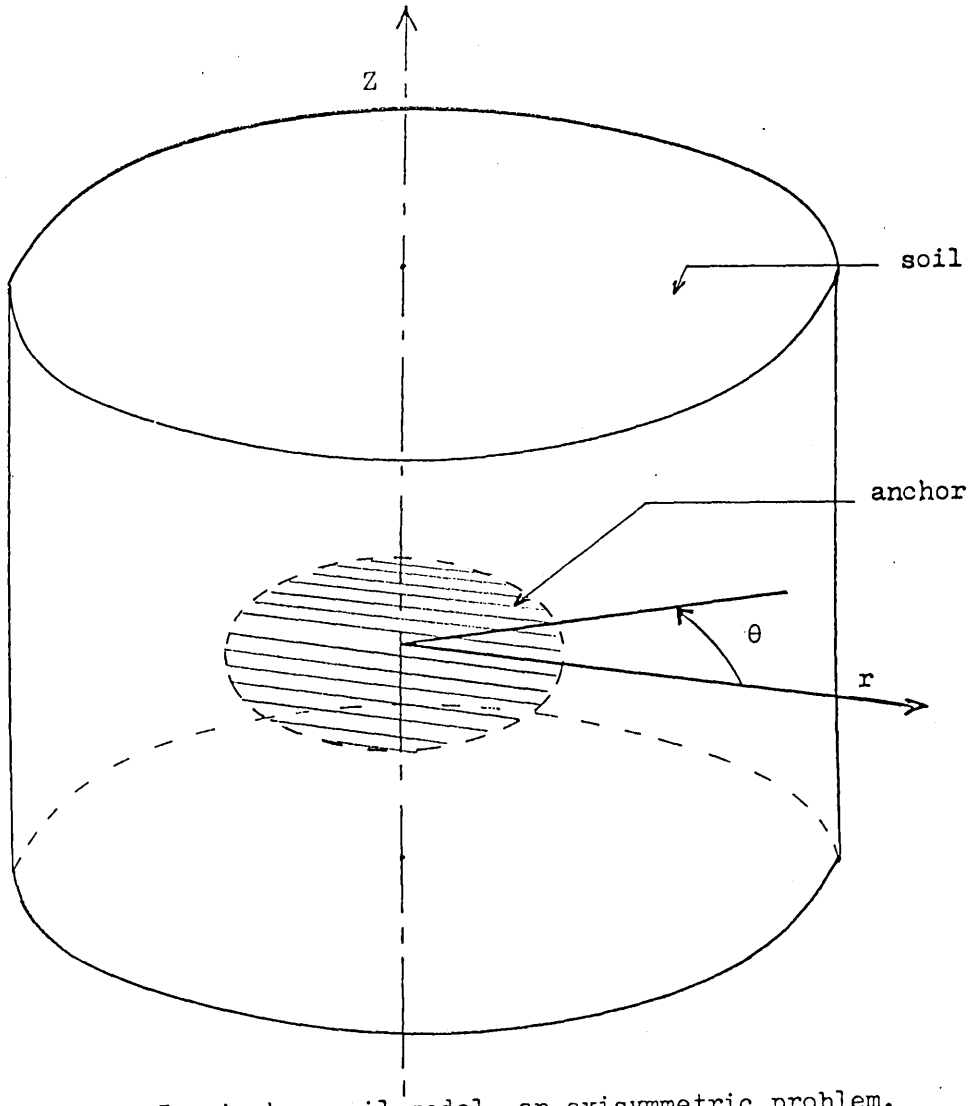

Figure 4.5 Anchor-soil model, an axisymmetric problem.

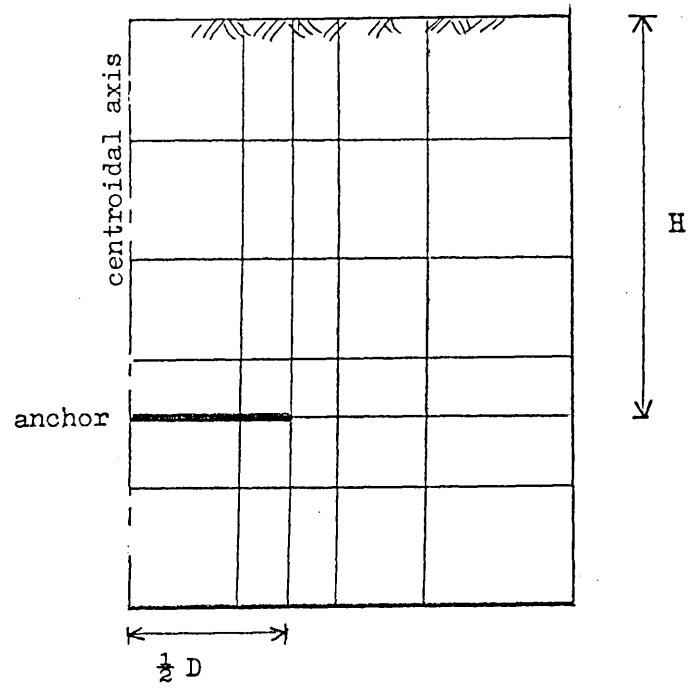

Figure 4.6 Finite element mesh for the problem of circular anchors in sand.

(1)

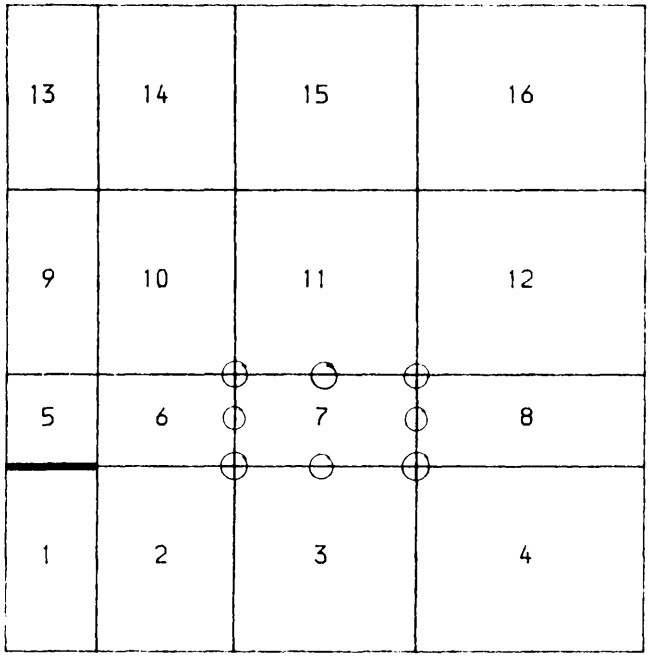

(2)

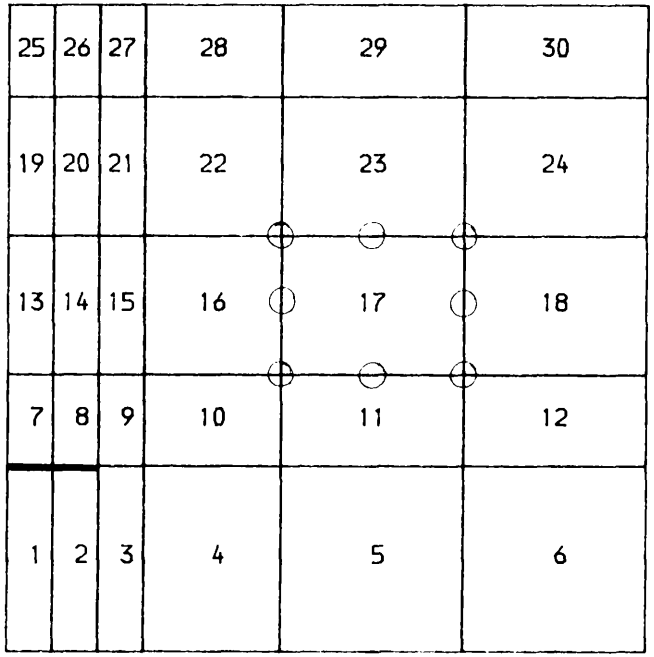

Figure 4.7a Finite element meshes for shallow anchor.

(3)

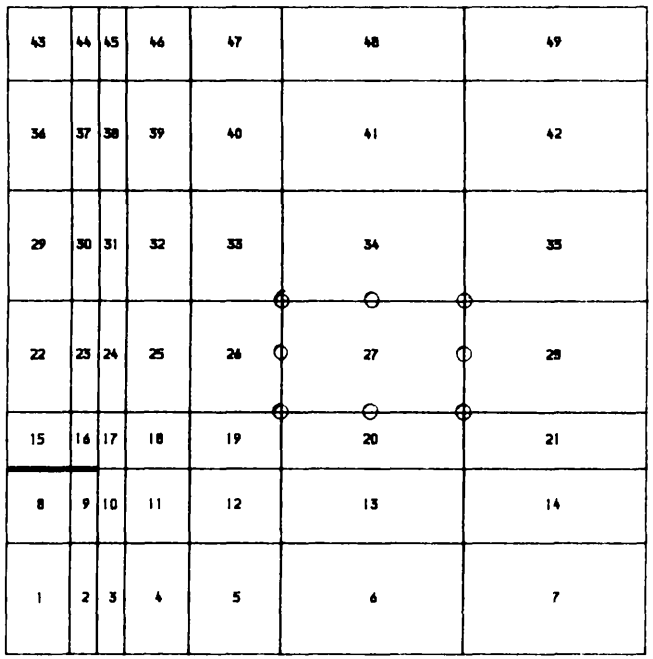

(4)

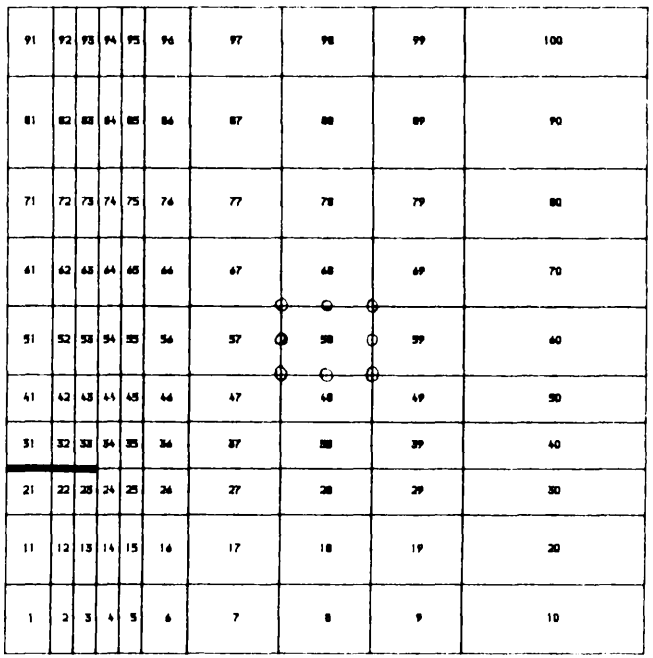

Figure 4.7b Finite element meshes for shallow anchor.

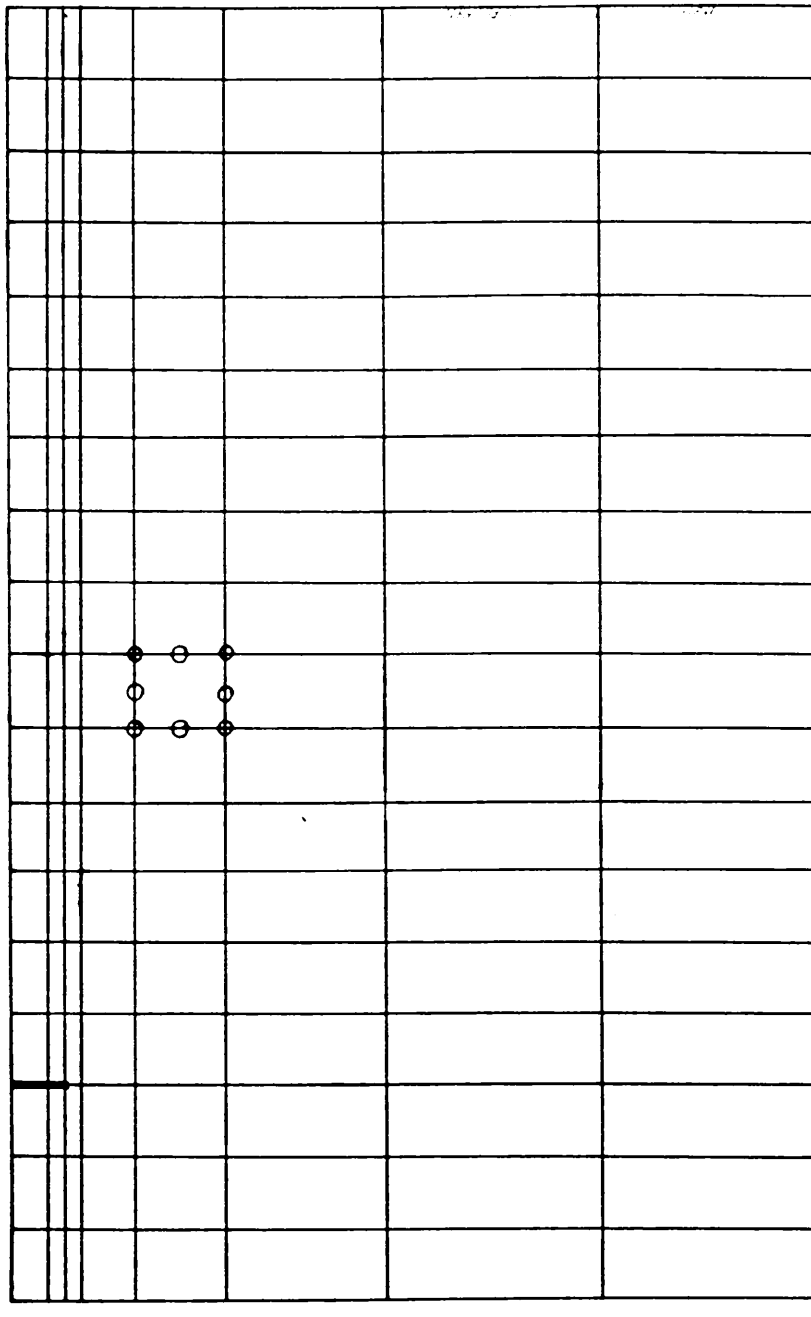

Figure 4.8Finite element mesh for deep anchor.

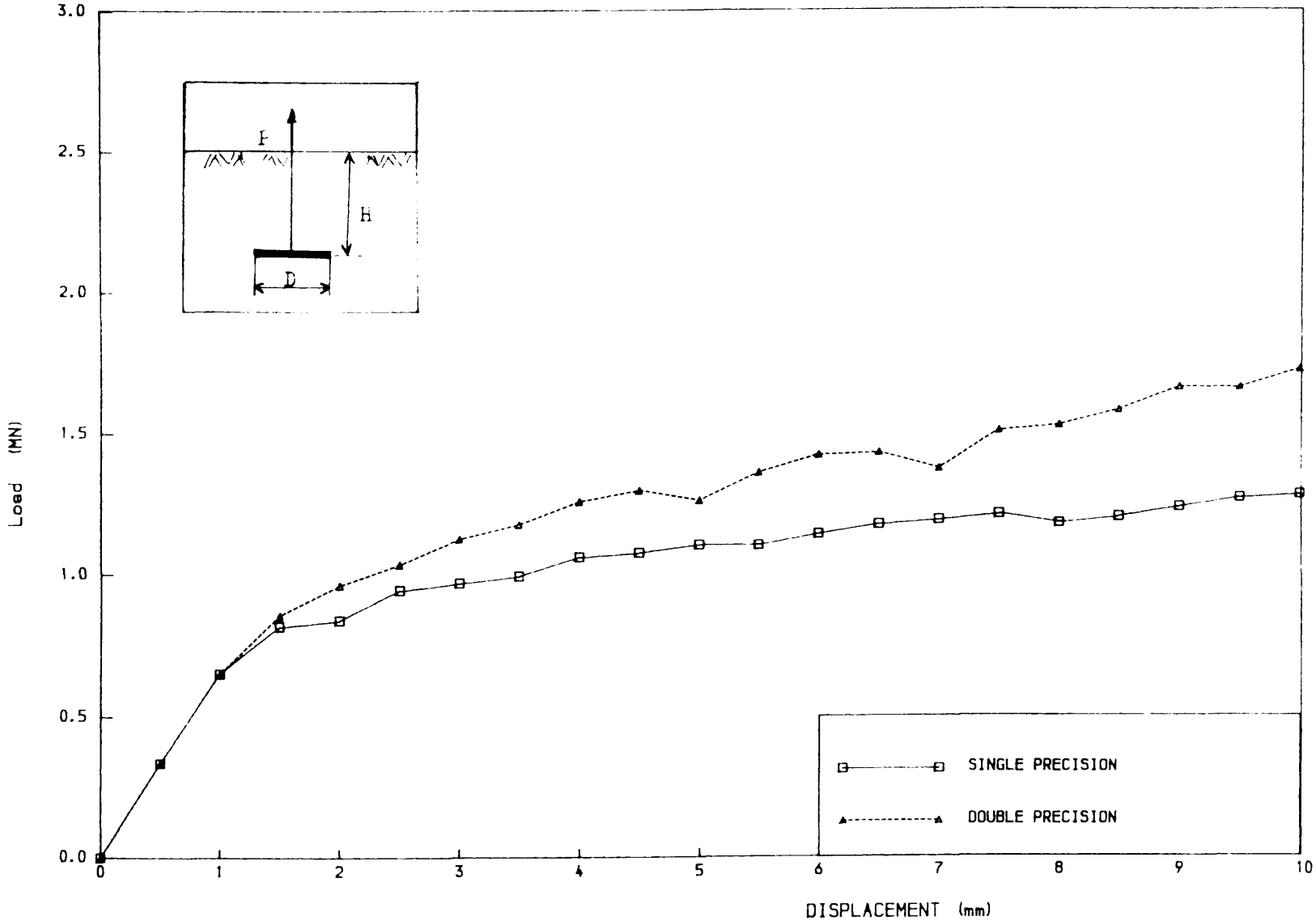

FIG. 4.9 LOAD-DISPLACEMENT CURVE FOR SHALLOW ANCHOR

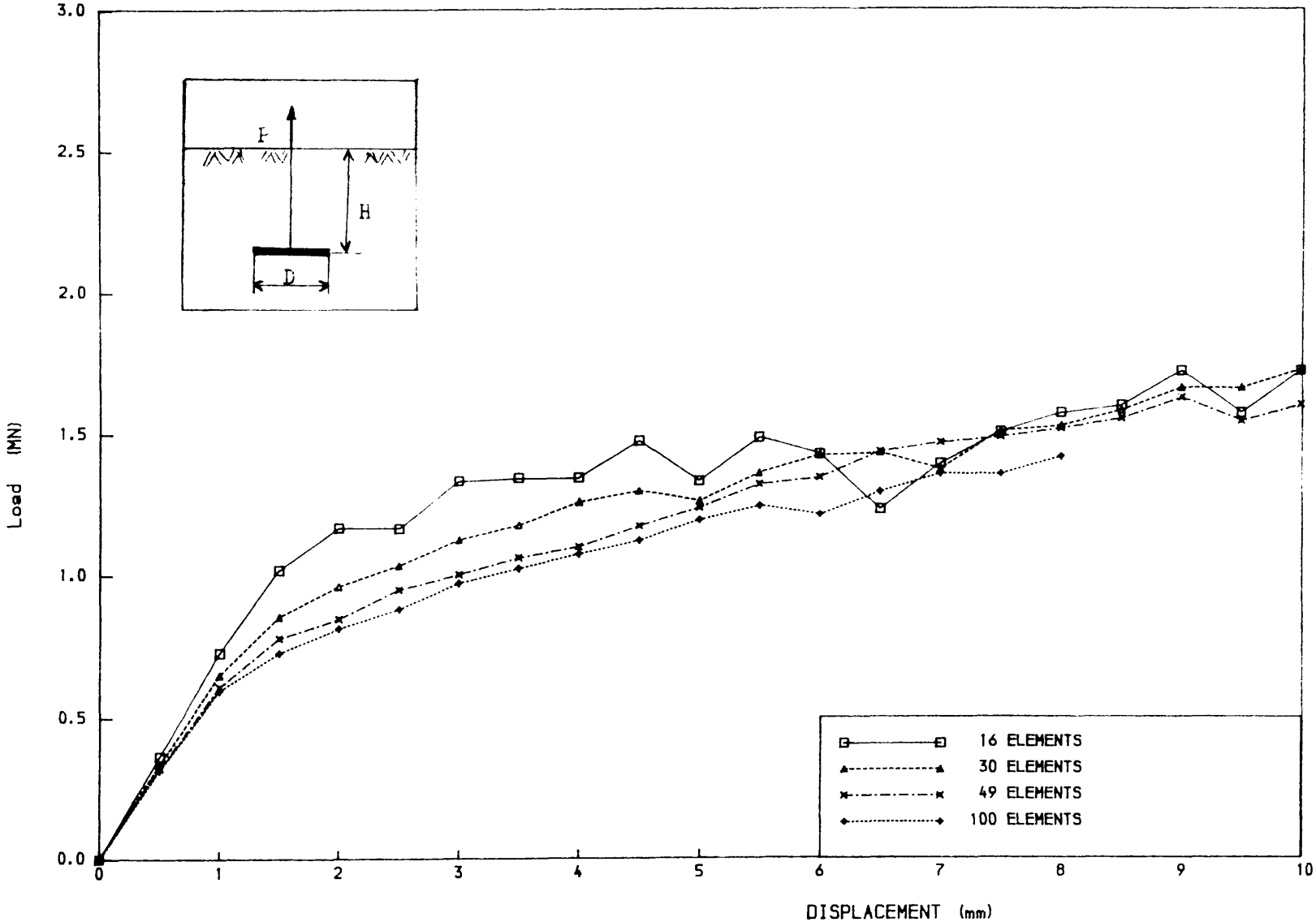

FIG.4.10 LOAD-DISPLACEMENT CURVE FOR SHALLOW ANCHOR

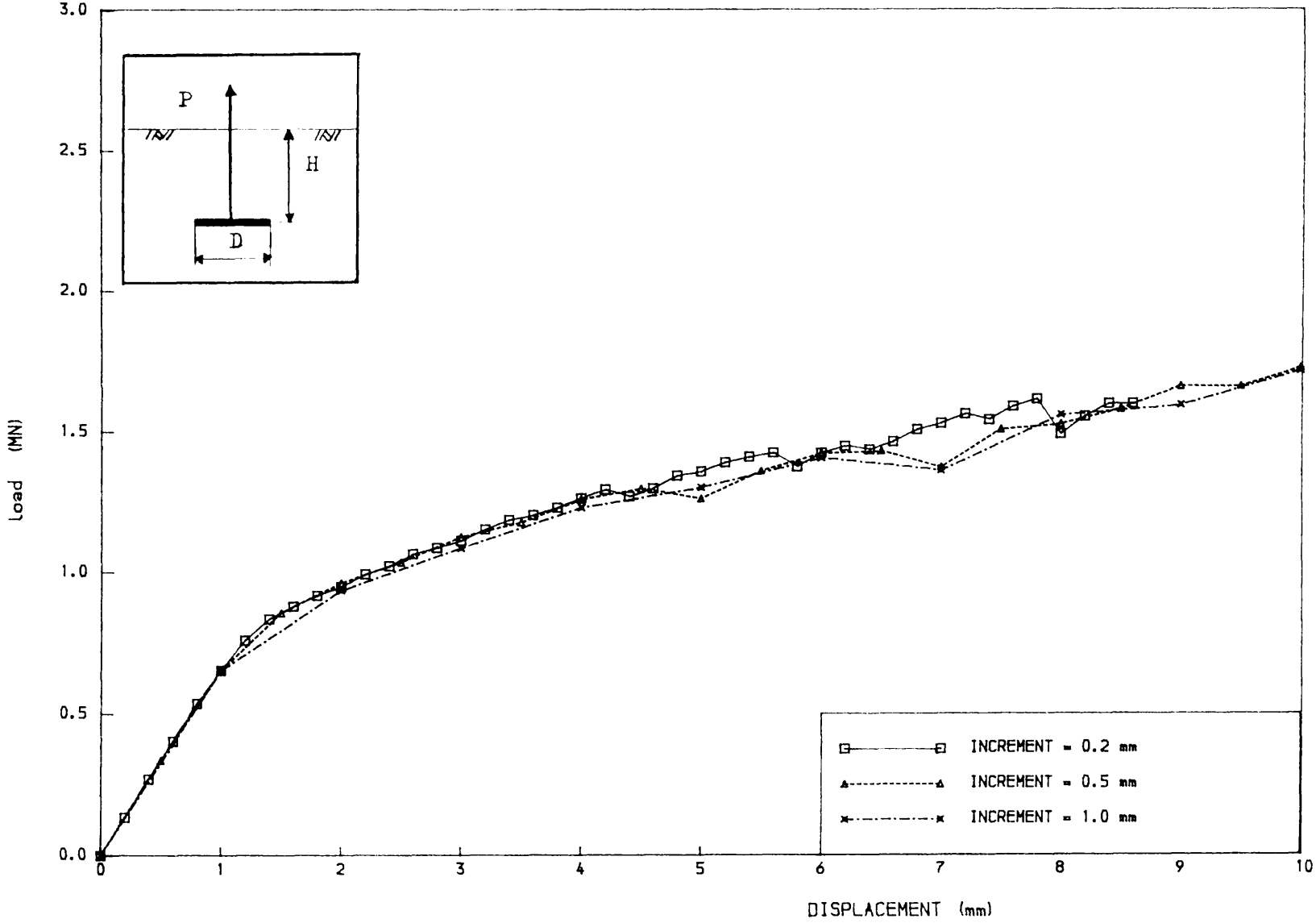

FIG 4.11 LOAD-DISPLACEMENT CURVE FOR SHALLOW ANCHOR

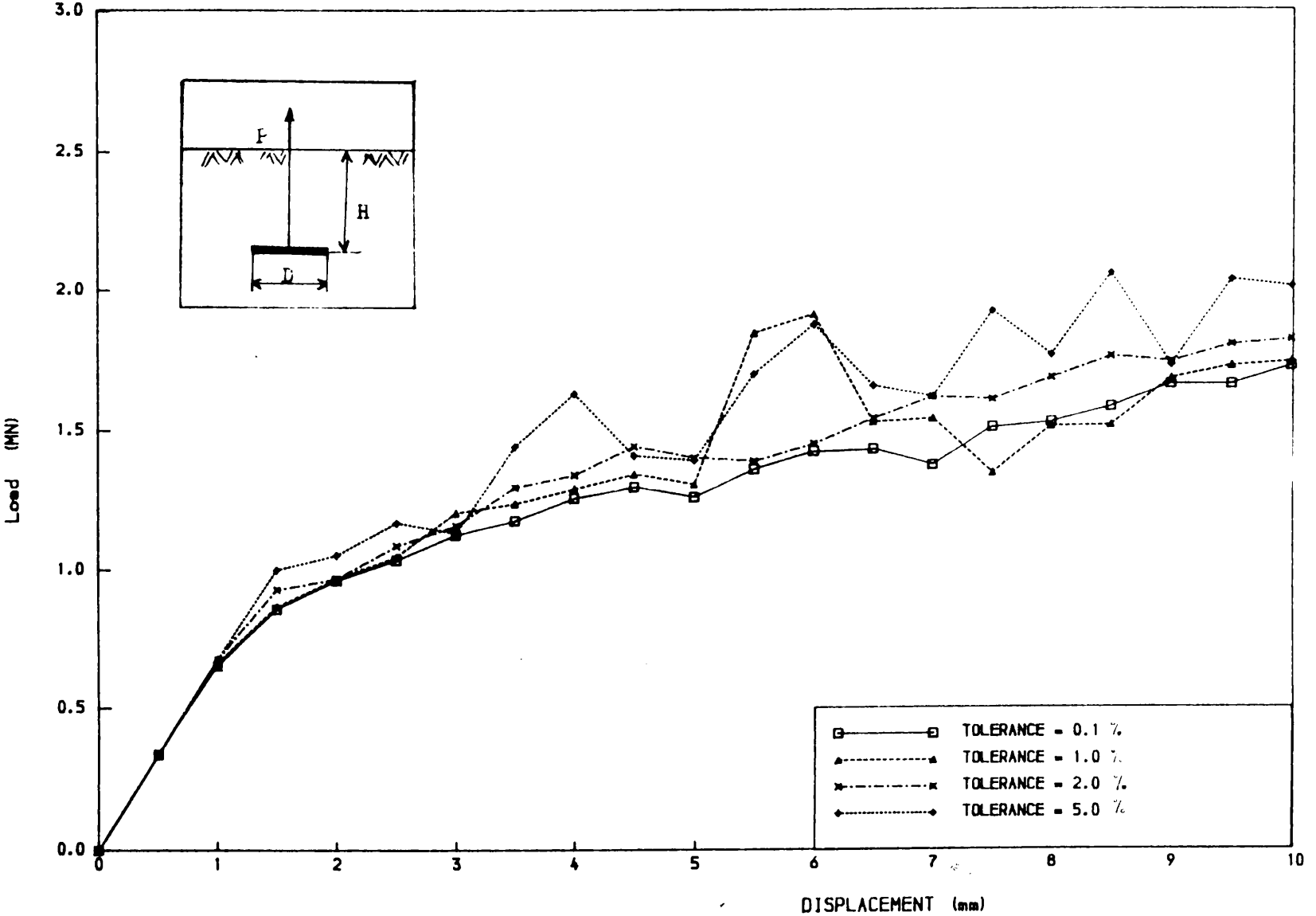

FIG.4.12 LOAD-DISPLACEMENT CURVE FOR SHALLOW ANCHOR

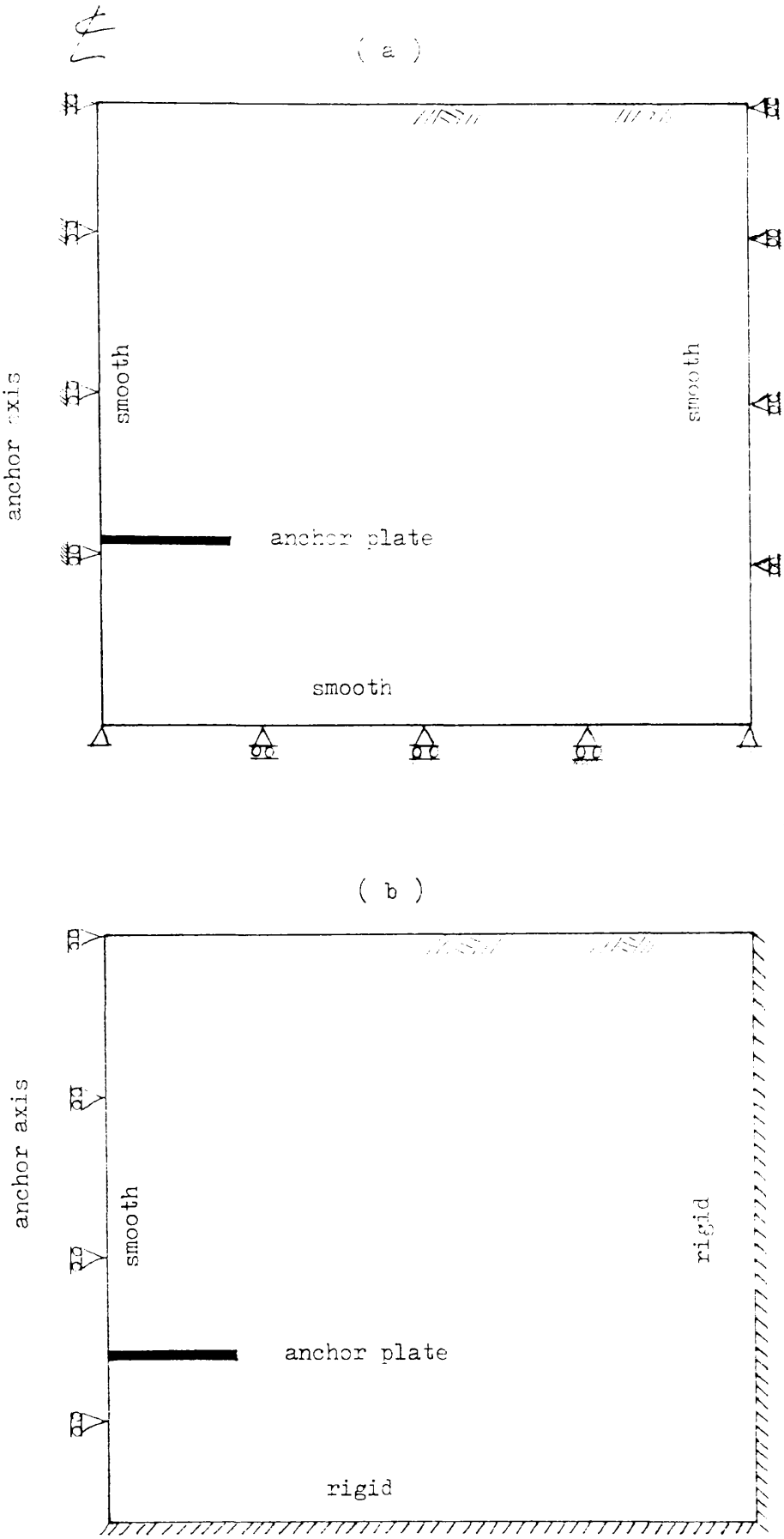

Figure4.13 Meshes with smooth (a) and rigid (b) boundary conditions.

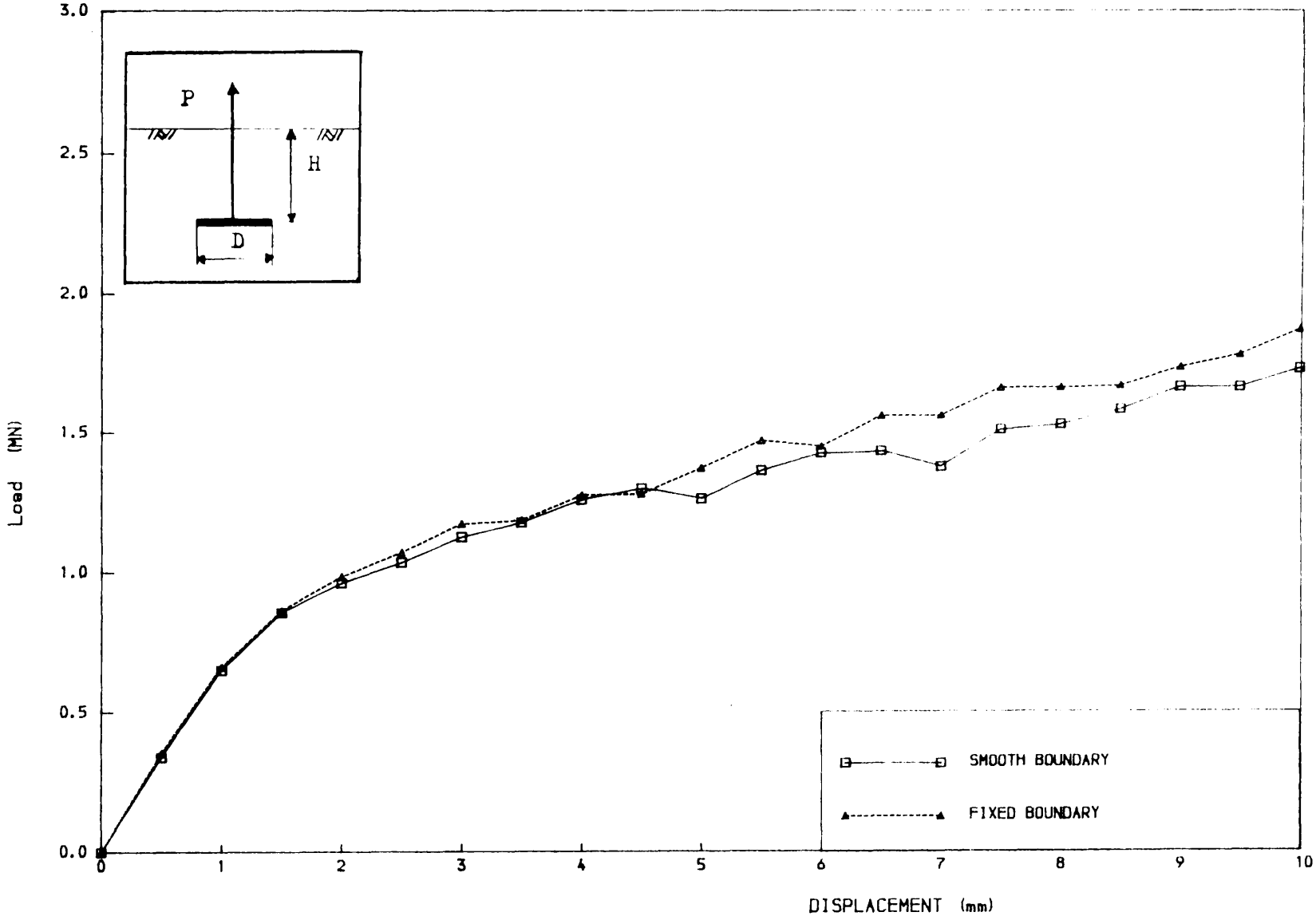

FIG 4.14 LOAD-DISPLACEMENT CURVE FOR SHALLOW ANCHOR

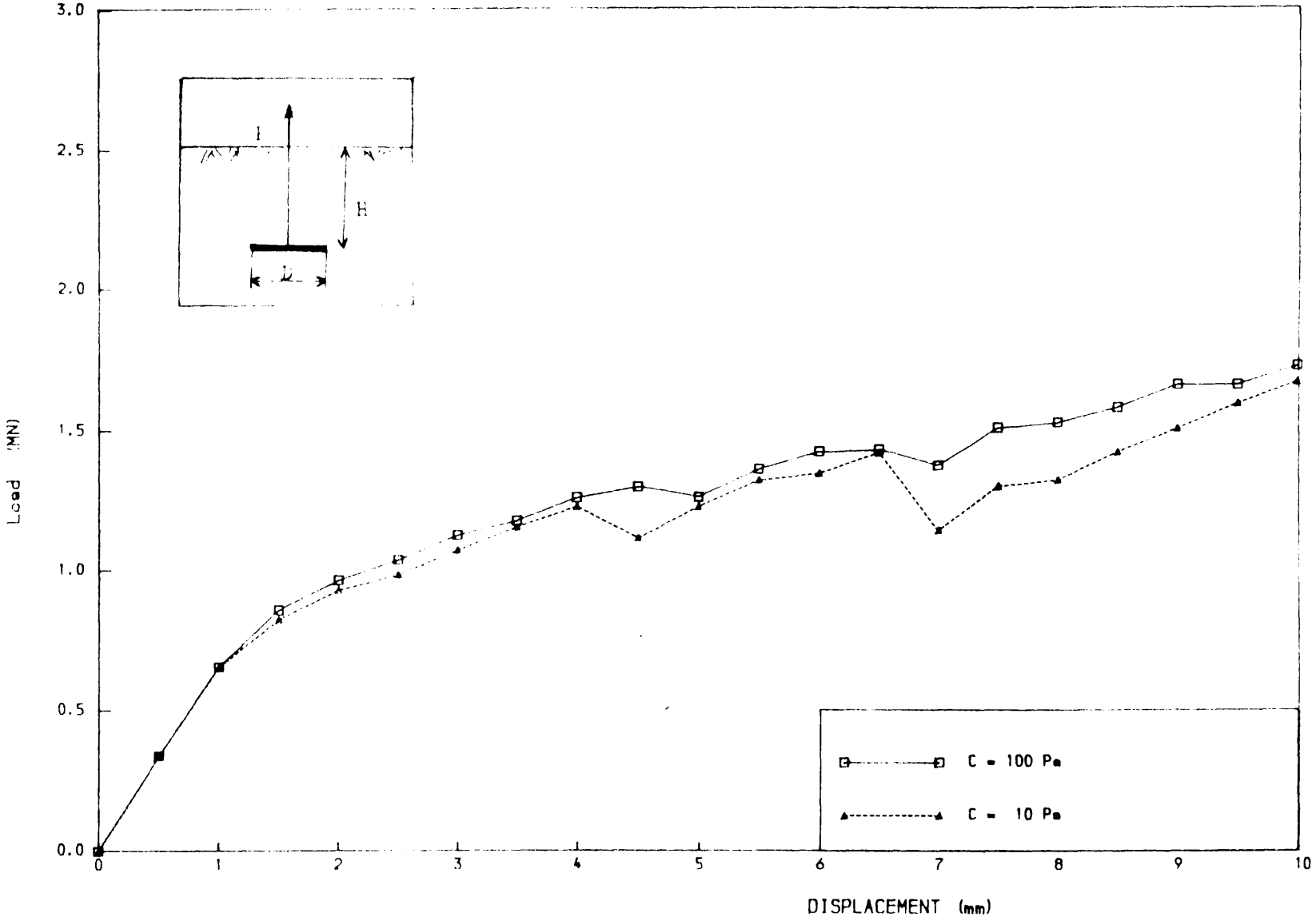

FIG. 5 LOAD DISPLACEMENT CURVE FOR SHALLOW ANCHOR

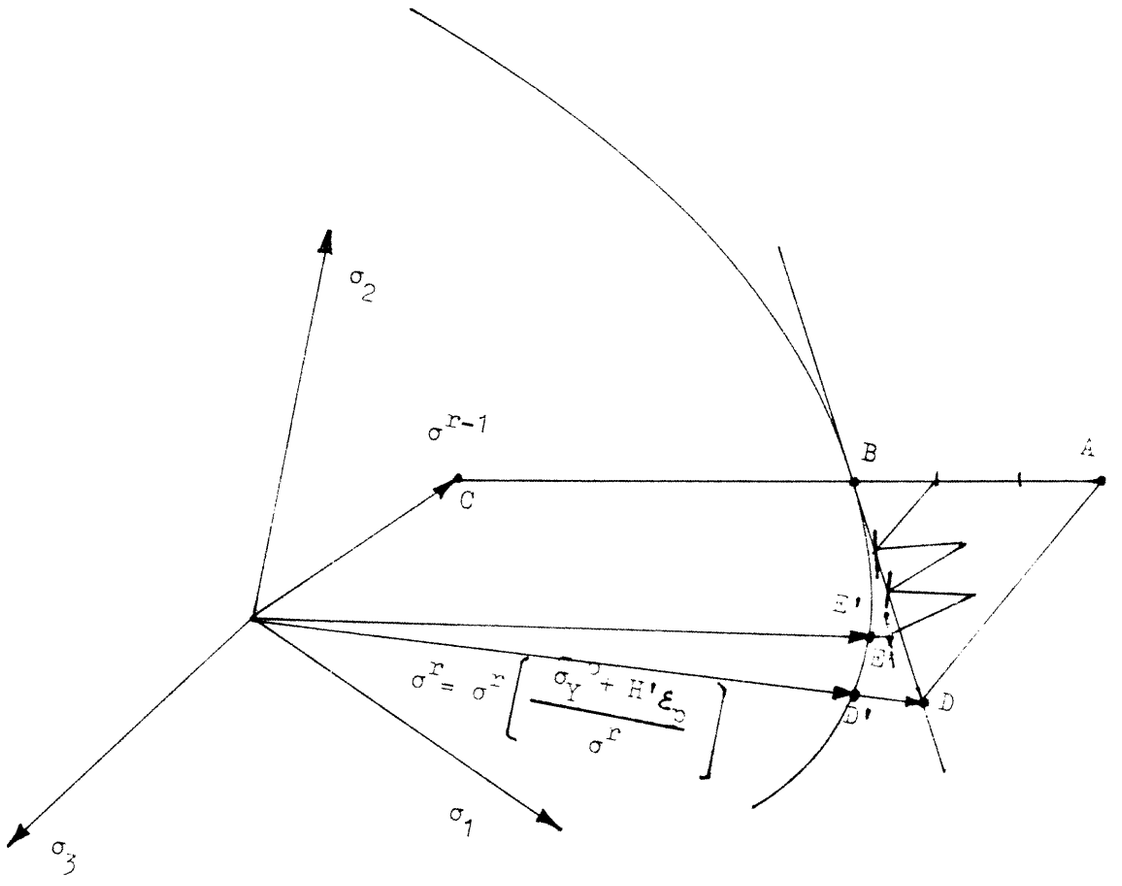

Figure 4.16 Process for reducing a stress point to the yield surface, Owen & Hinton.

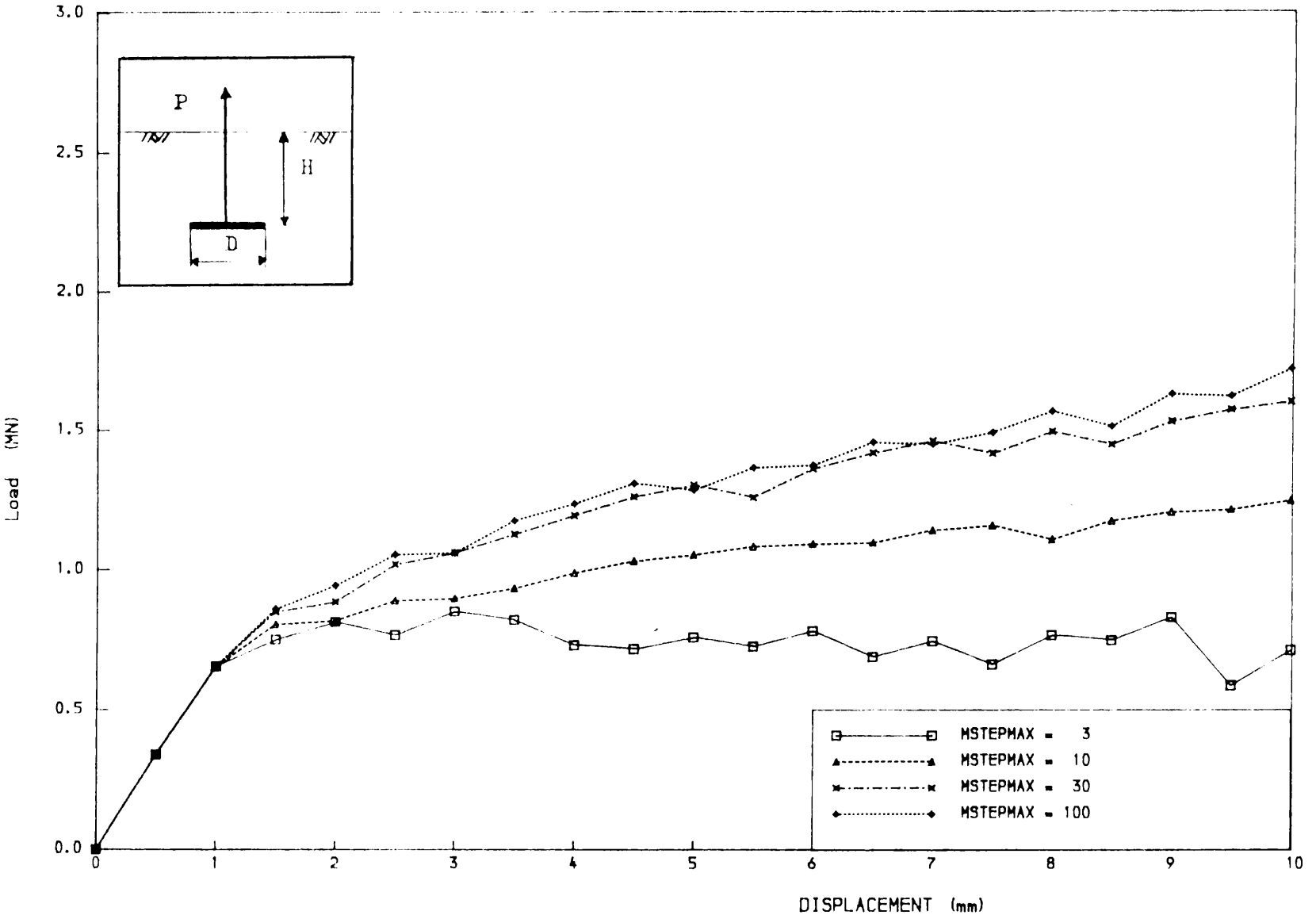

FIG 4.17 LOAD-DISPLACEMENT CURVE FOR SHALLOW ANCHOR

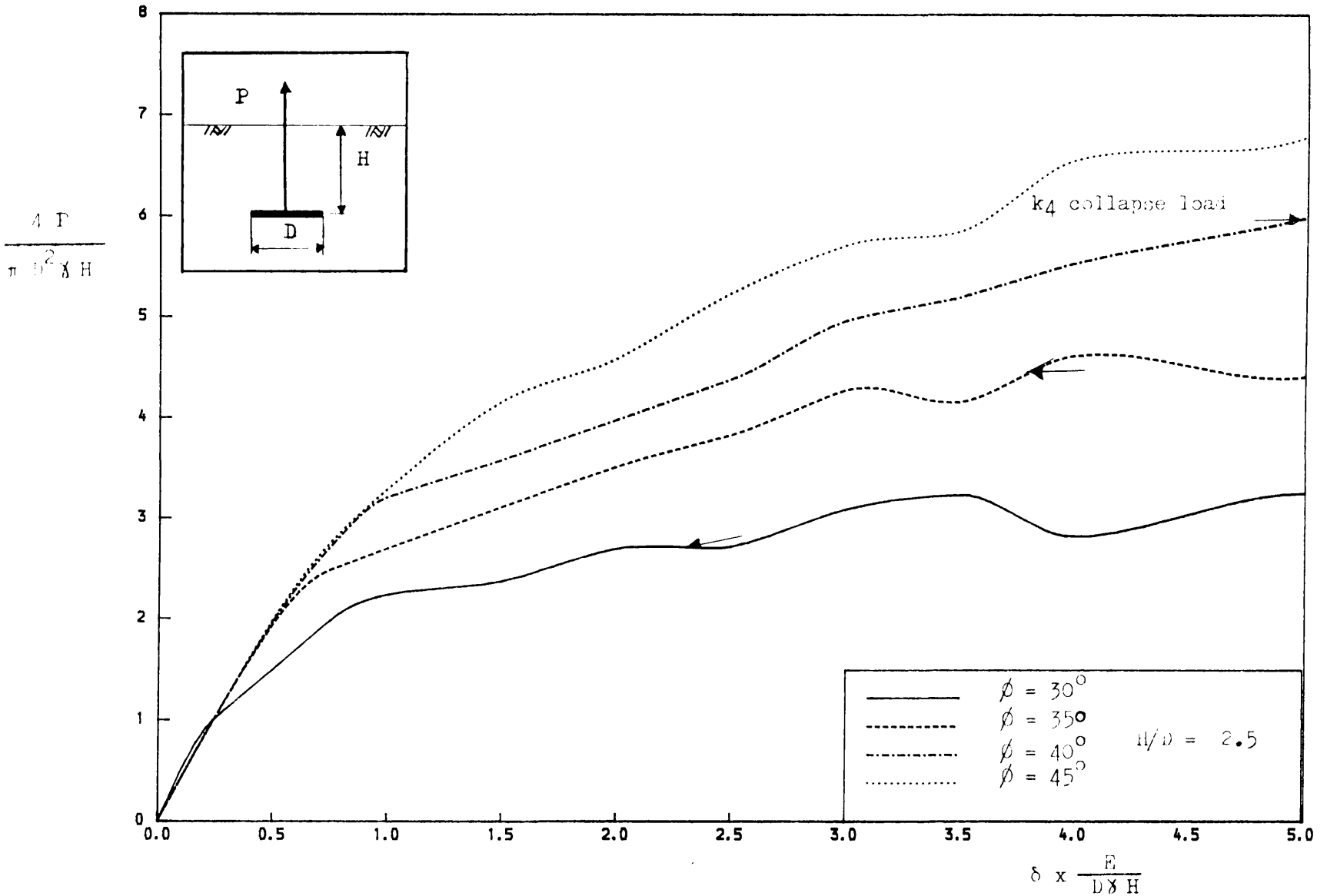

FIGURE 4.18 LOAD-DISPLACEMENT CURVE FOR SHALLOW ANCHOR

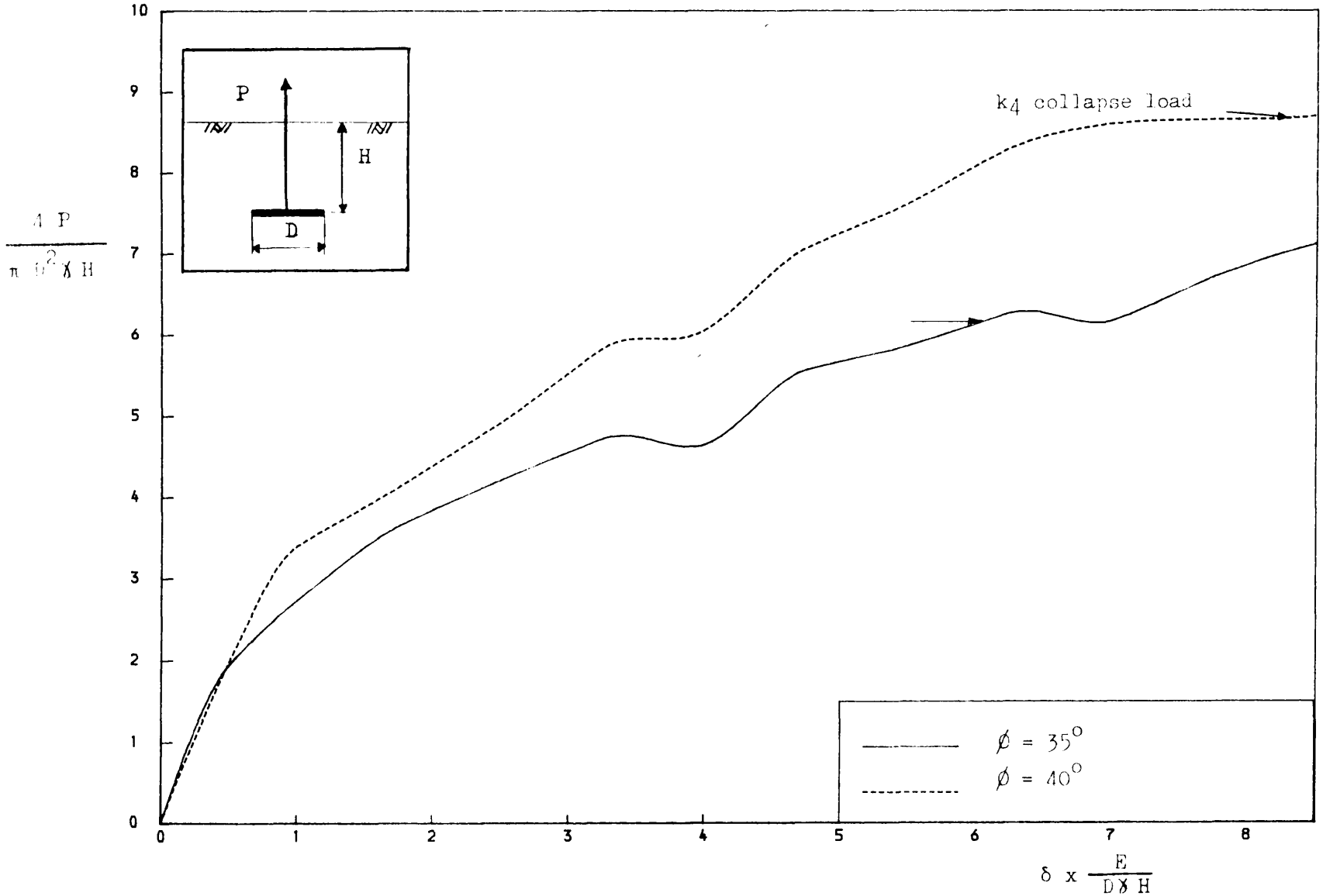

FIGURE 4.19 LOAD-DISPLACEMENT CURVE FOR ANCHOR AT H/D = 5

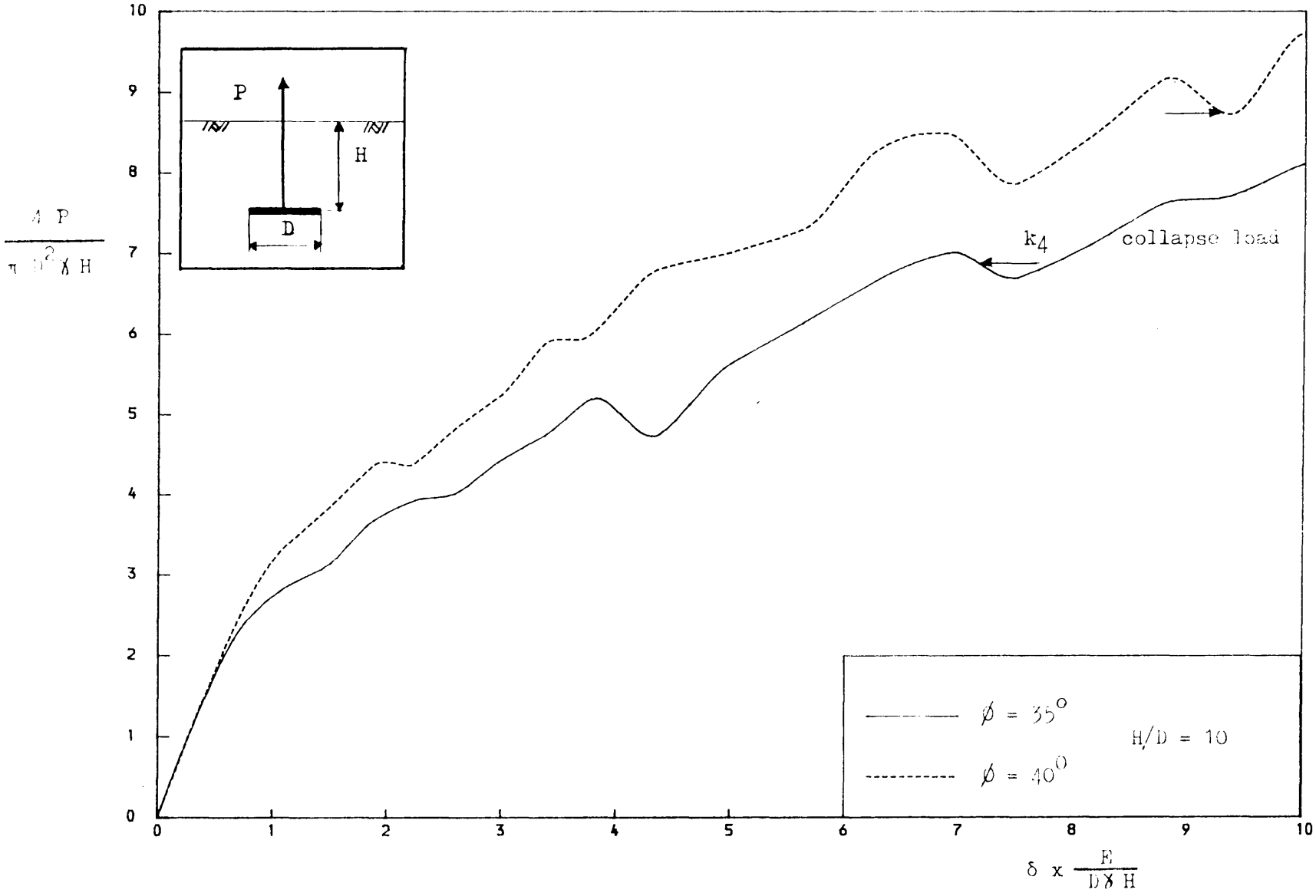

FIGURE 4.20 LOAD-DISPLACEMENT CURVE FOR DEEP ANCHOR

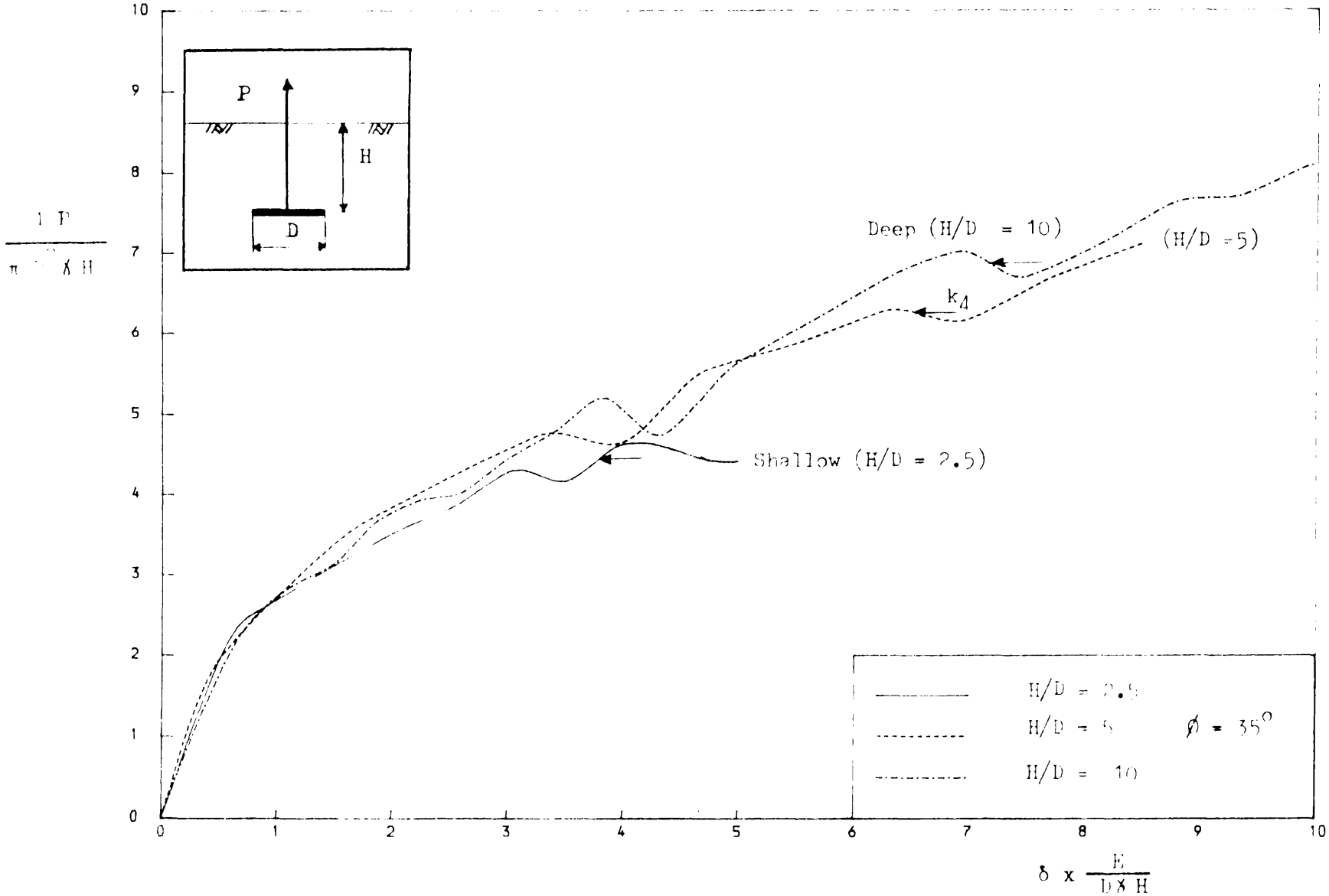

FIGURE 4.21 LOAD-DISPLACEMENT CURVE FOR ANCHORS

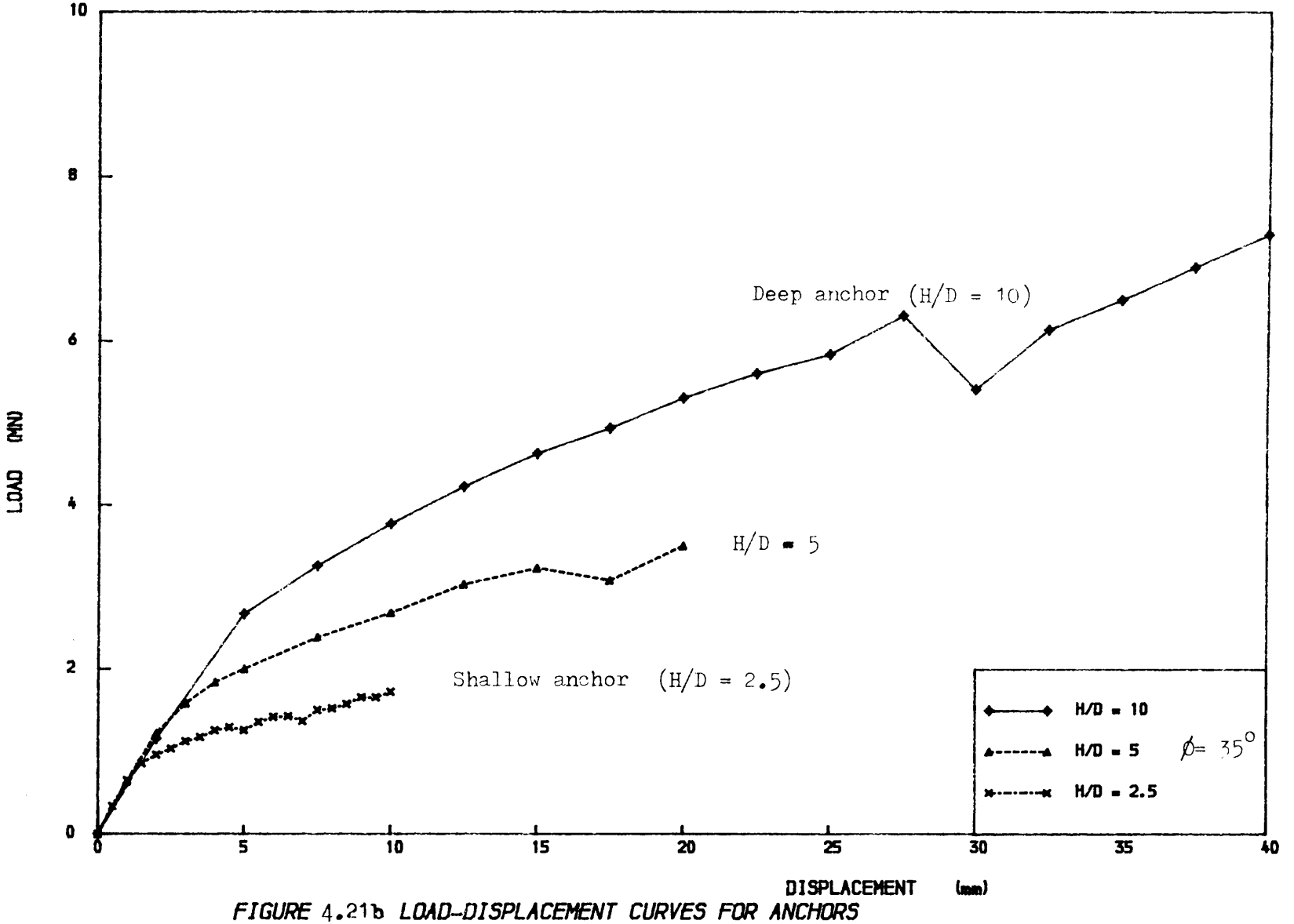

FIGURE 4.21b LOAD-DISPLACEMENT CURVES FOR ANCHORS

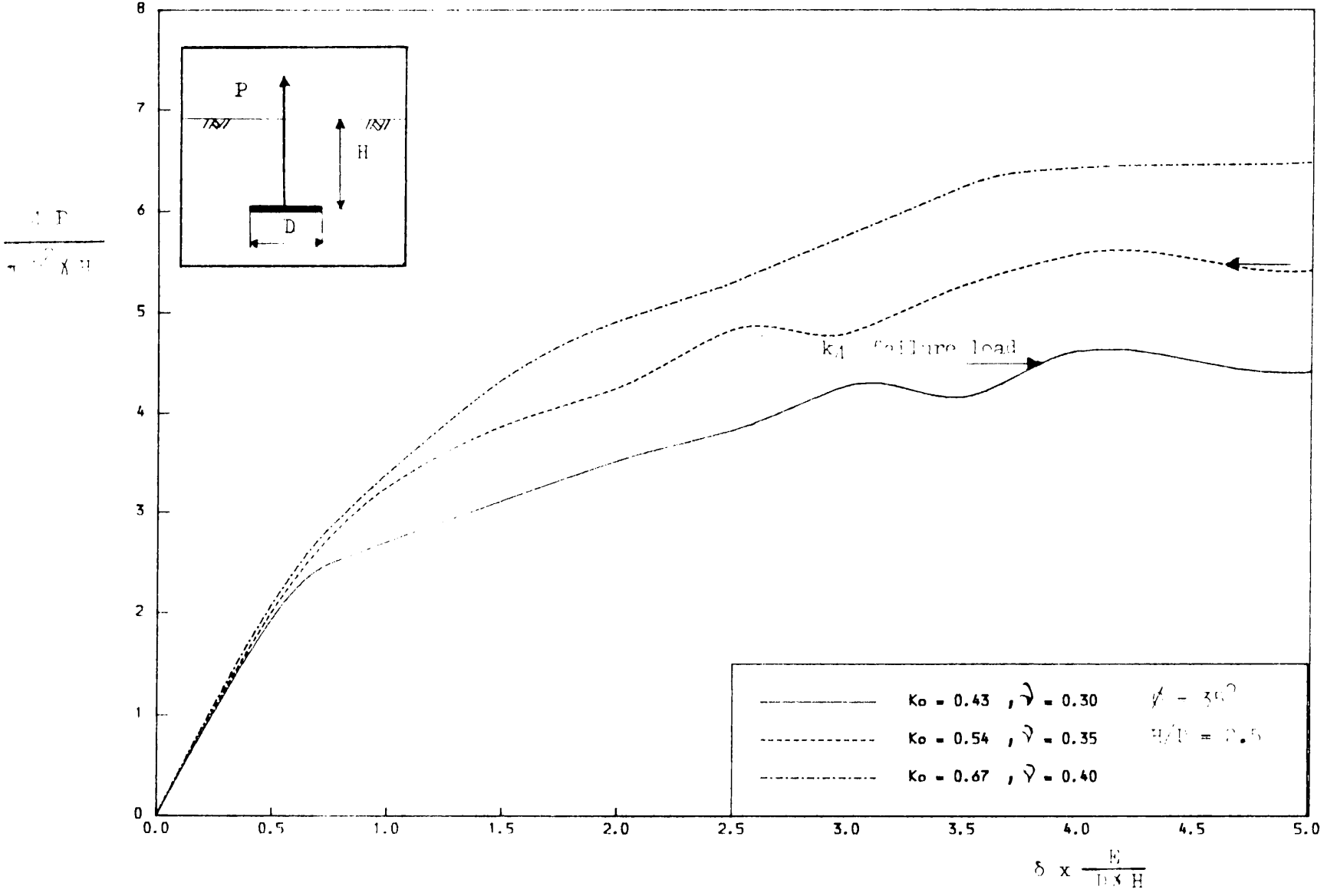

FIGURE [illegible] LOAD-DISPLACEMENT CURVE FOR SHALLOW ANCHOR

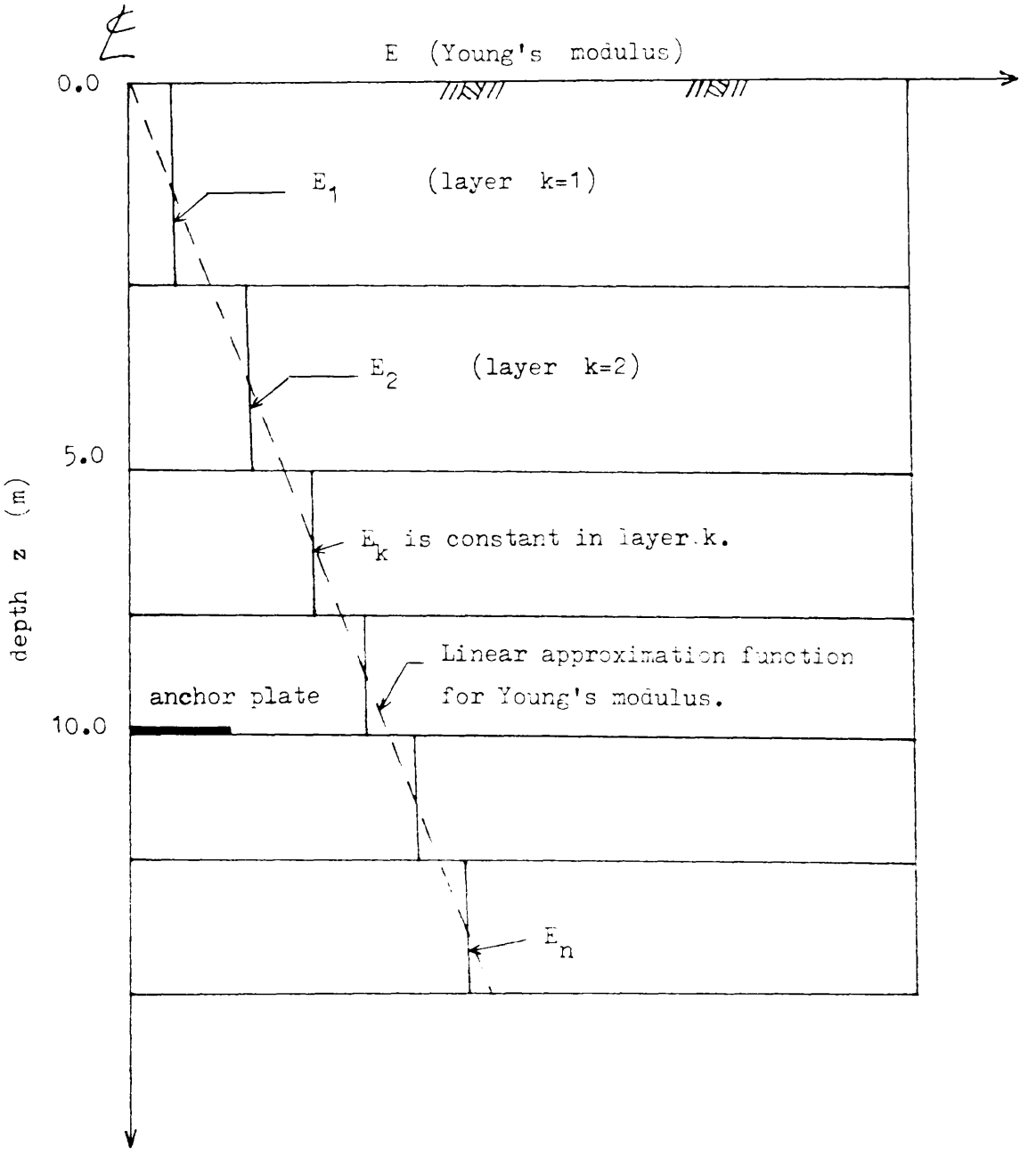

Figure 4.23 Variation of Young's modulus for inhomogeneous sand.

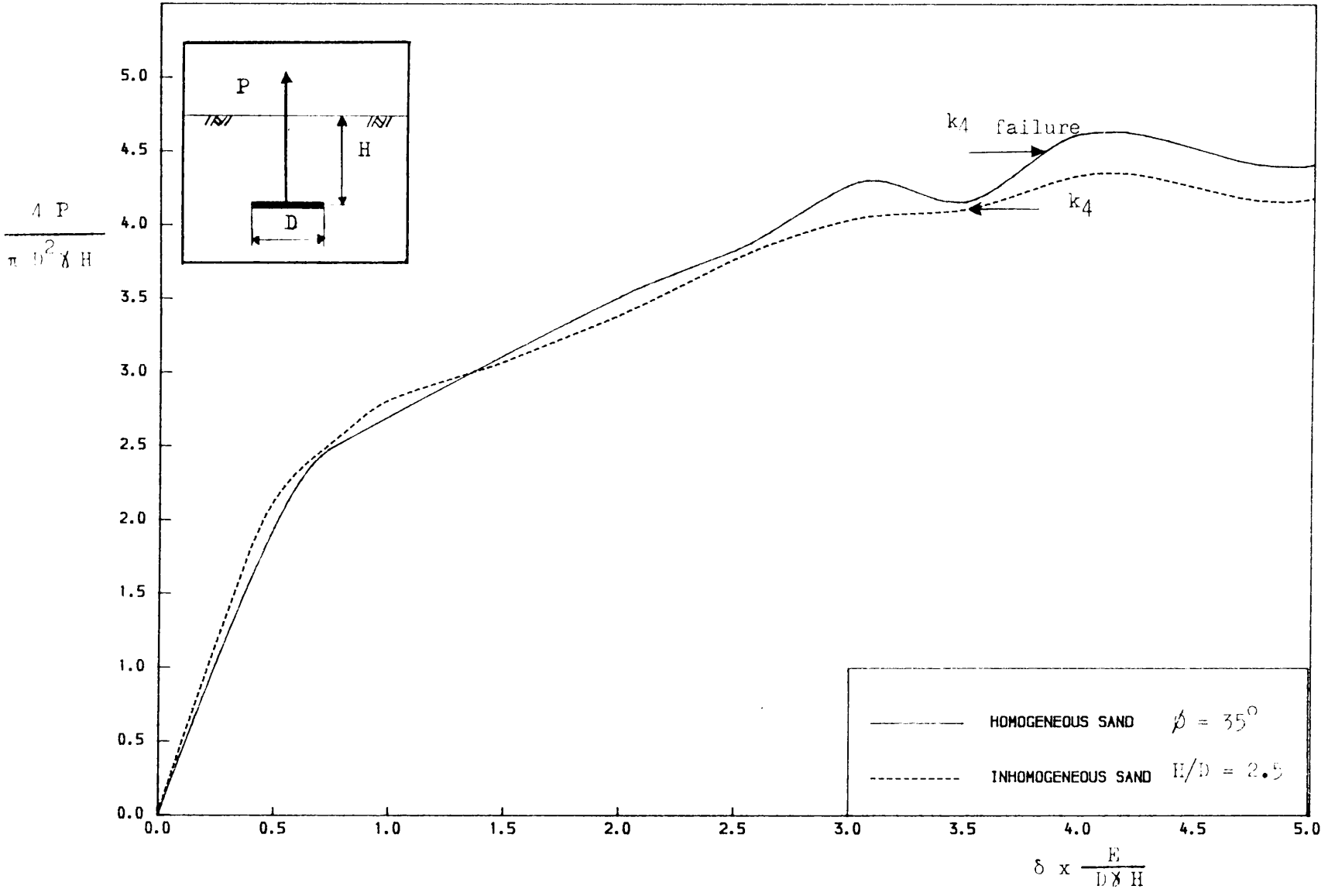

FIGURE 4.24 LOAD-DISPLACEMENT CURVE FOR SHALLOW ANCHOR

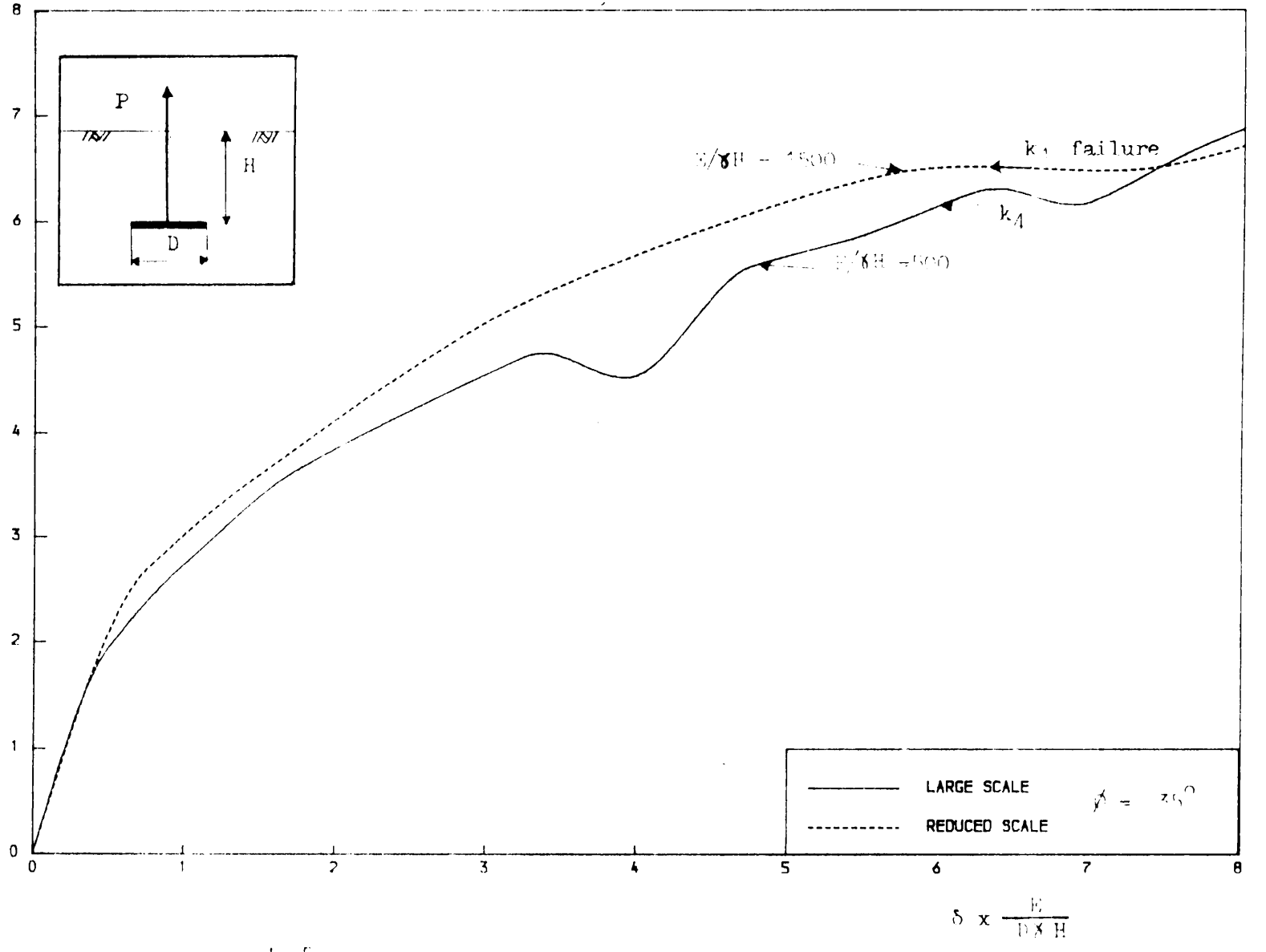

FIGURE 4.5 LOAD-DISPLACEMENT CURVE FOR ANCHOR AT H/D = 5

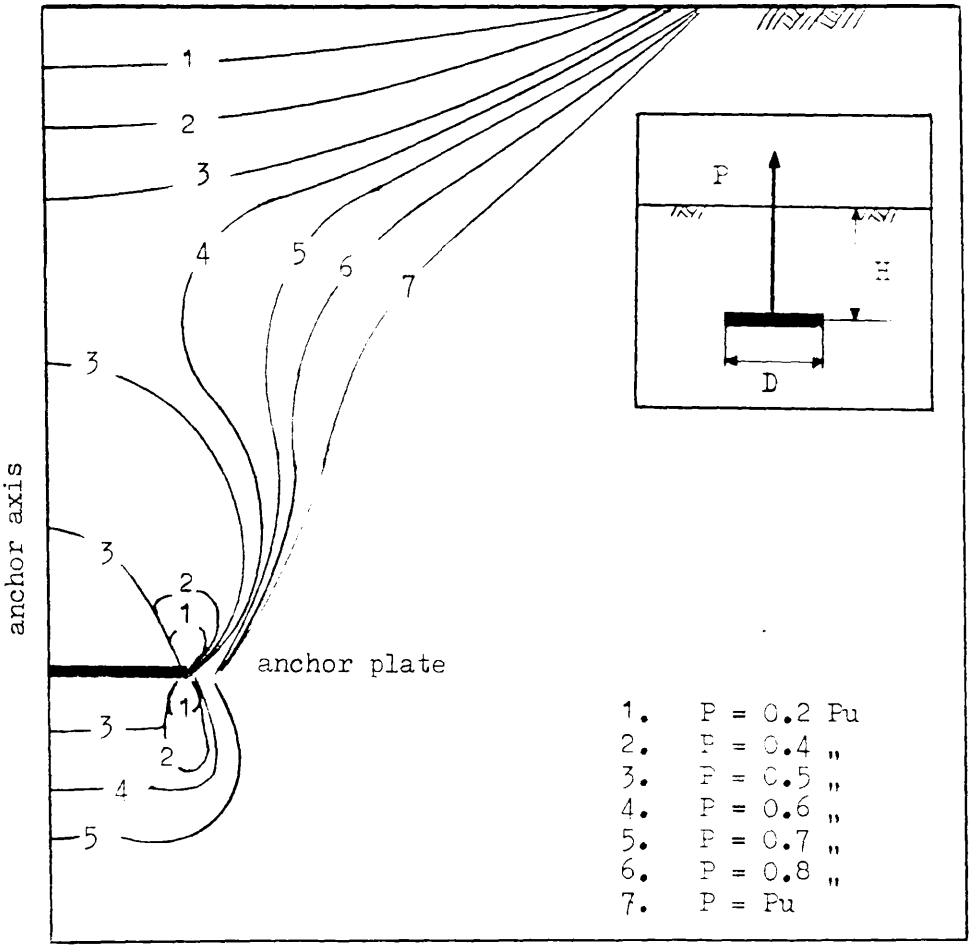

Figure 4.26 Propagation of yielding for shallow anchor.
(Pu = 1.4 MN , γ = 20 kN/m^3 , H/D = 2.5)

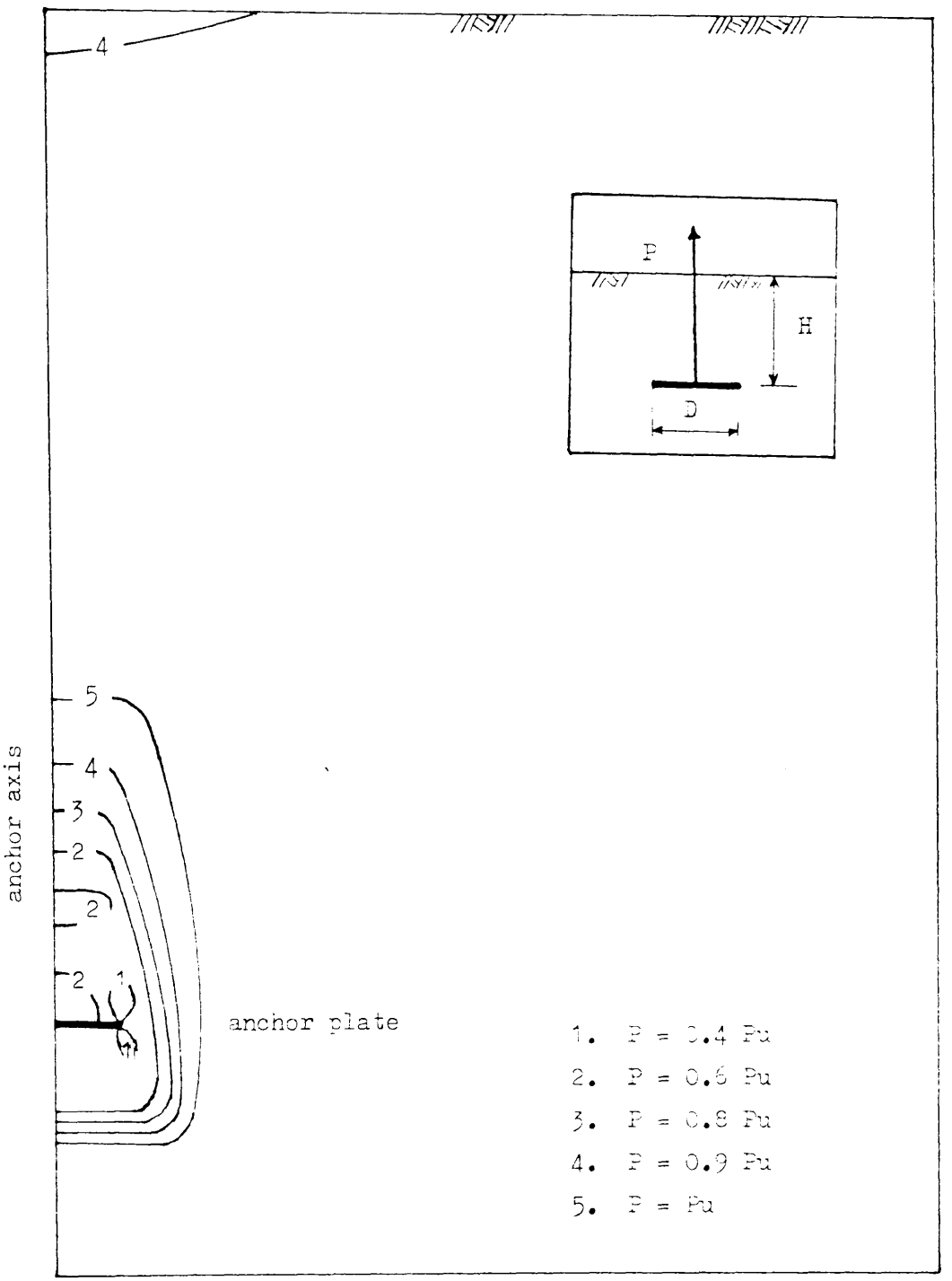

Figure 4.27 Propagation of yielding for deep anchor.
(Pu = 6.8 MN , γ = 20 kN/m^3 , H/D = 10)

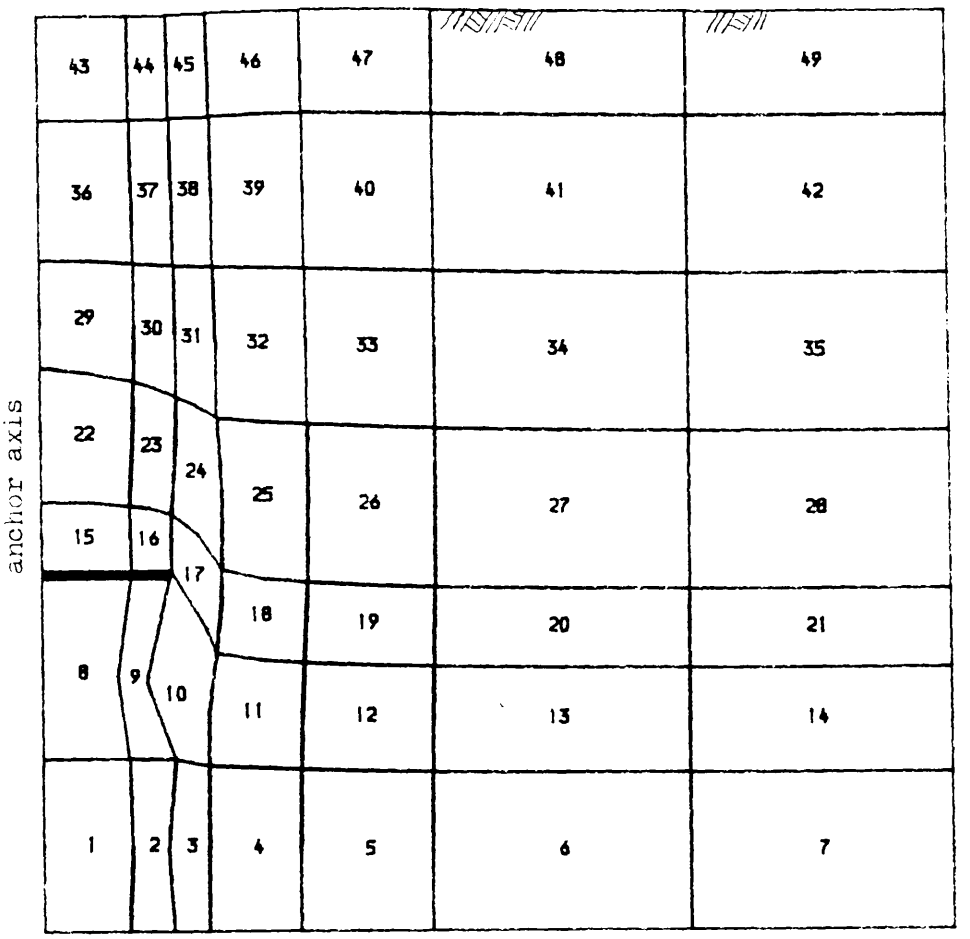

Figure 4.28 Deformation of soil under ultimate load of shallow anchor (displacement x 100).

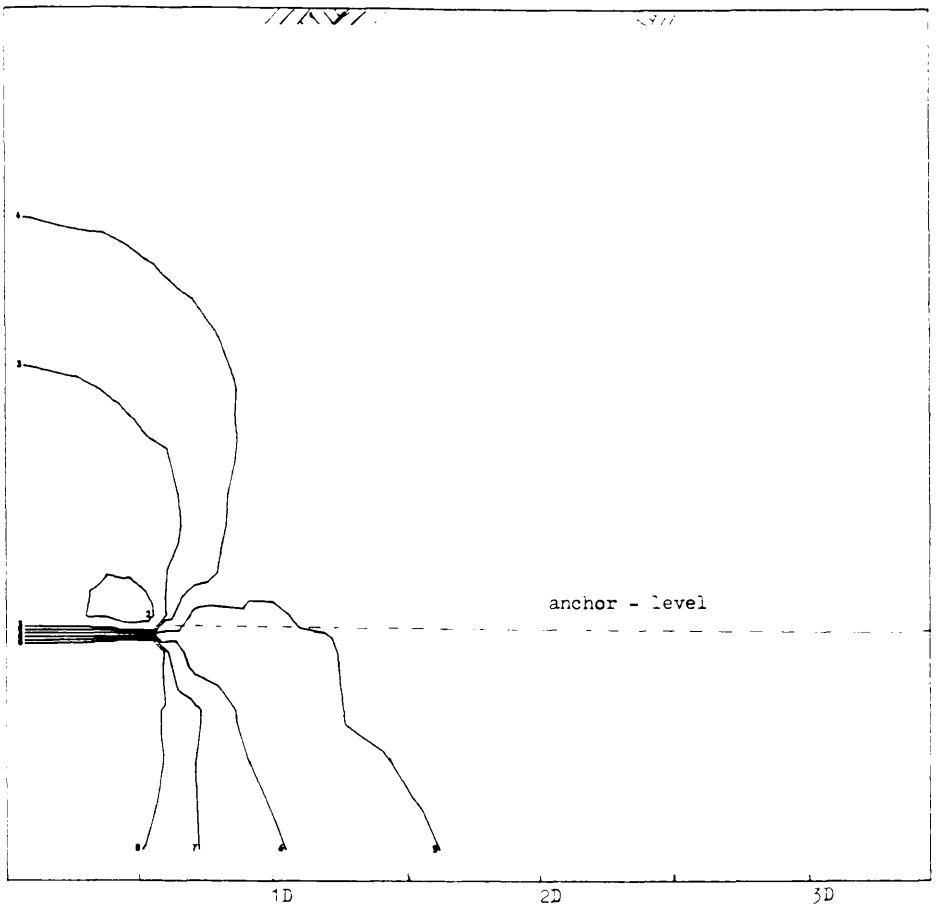

VERTICAL STRESS

FIG 4.29 STRESS DISTRIBUTION FOR SHALLOW ANCHORS IN ELASTIC STATE

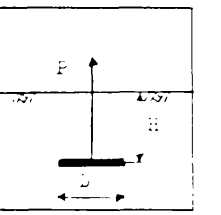

LEVELS	STRESS (Pa)
1	-0.89600E 05
2	-0.51800E 05
3	-0.14000E 05
4	-0.45500E 04
5	0.49000E 04
6	0.14350E 05
7	0.23800E 05
8	0.33250E 05

RADIAL STRESS

FIG 4.30 STRESS DISTRIBUTION FOR SHALLOW ANCHORS IN ELASTIC STATE

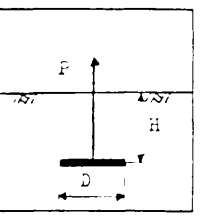

LEVELS	STRESS (Pa)
1	-0.36900E 05
2	-0.24120E 05
3	-0.11340E 05
4	-0.81450E 04
5	-0.49500E 04
6	-0.17550E 04
7	0.14400E 04
8	0.46350E 04

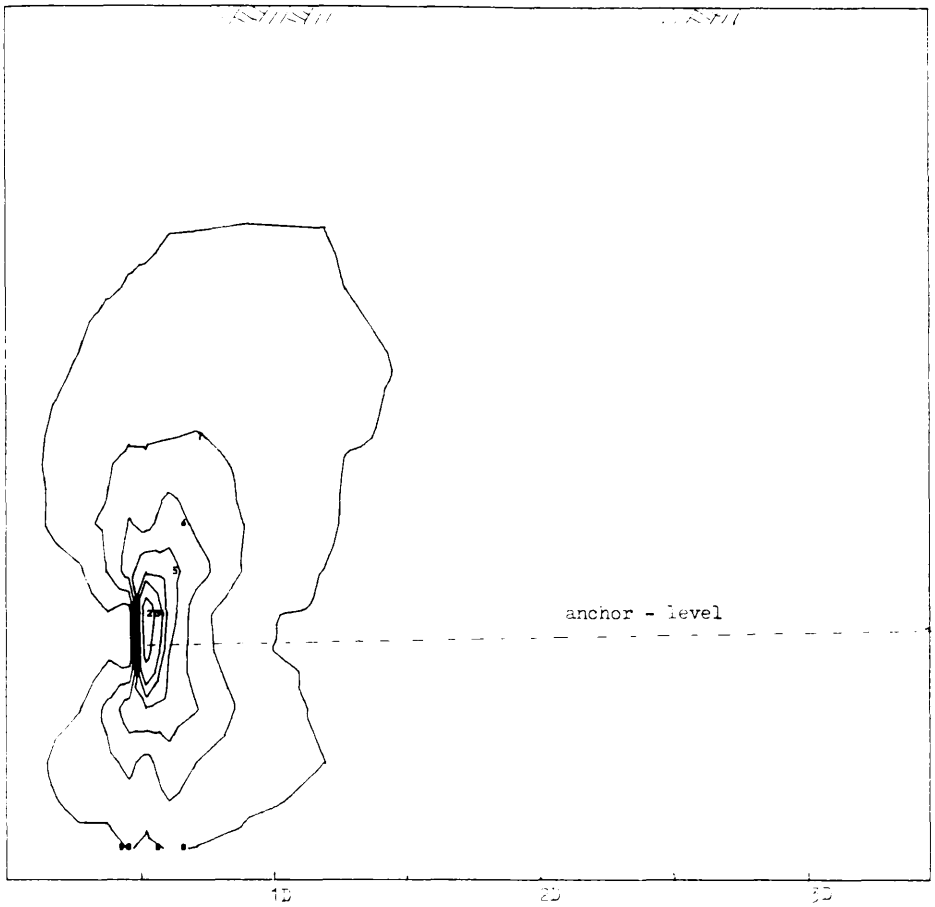

SHEAR STRESS

FIG 4.31 STRESS DISTRIBUTION FOR SHALLOW ANCHORS IN ELASTIC STATE

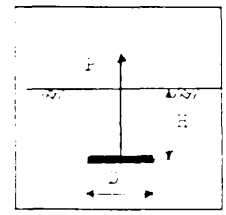

LEVELS	STRESS (Pa)
1	-0.53400E 05
2	-0.42184E 05
3	-0.30968E 05
4	-0.25360E 05
5	-0.19752E 05
6	-0.14144E 05
7	-0.85360E 04
8	-0.29280E 04

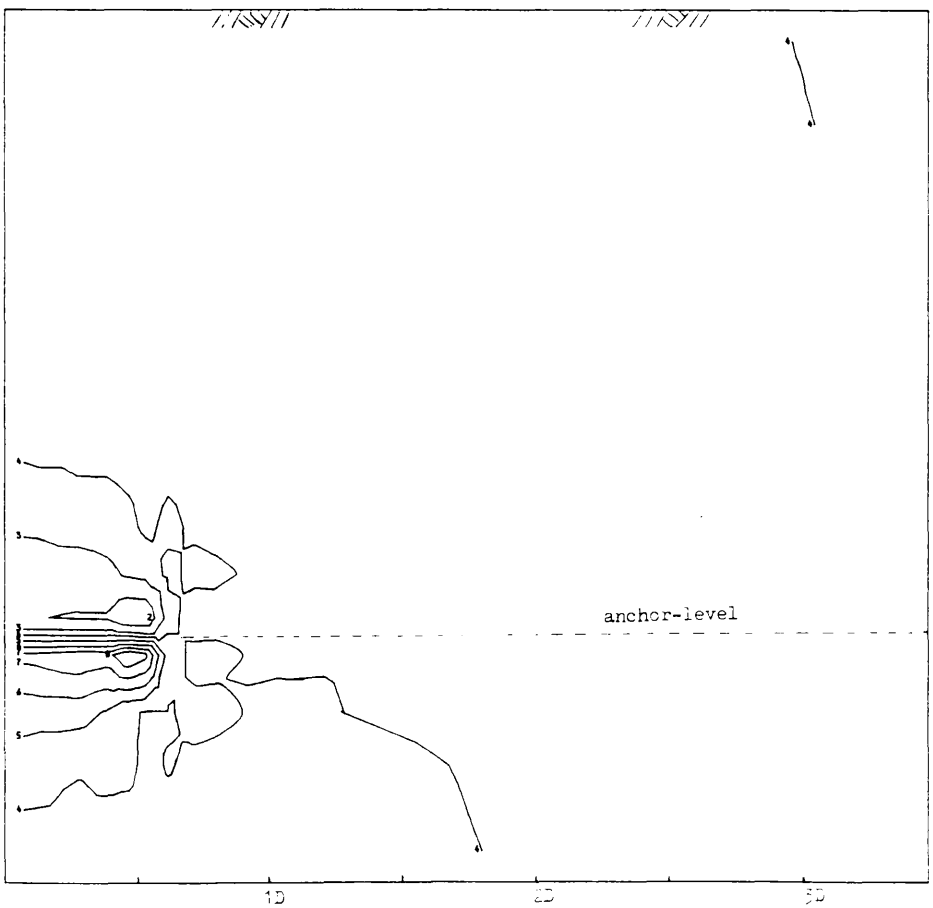

CIRCUMFERENTIAL STRESS

FIG 4.32 STRESS DISTRIBUTION FOR SHALLOW ANCHORS IN ELASTIC STATE

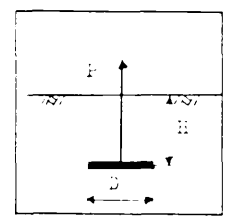

LEVELS	STRESS (Pa)
1	-0.30200E 05
2	-0.18200E 05
3	-0.62000E 04
4	-0.20000E 03
5	0.58000E 04
6	0.11800E 05
7	0.17800E 05
8	0.23800E 05

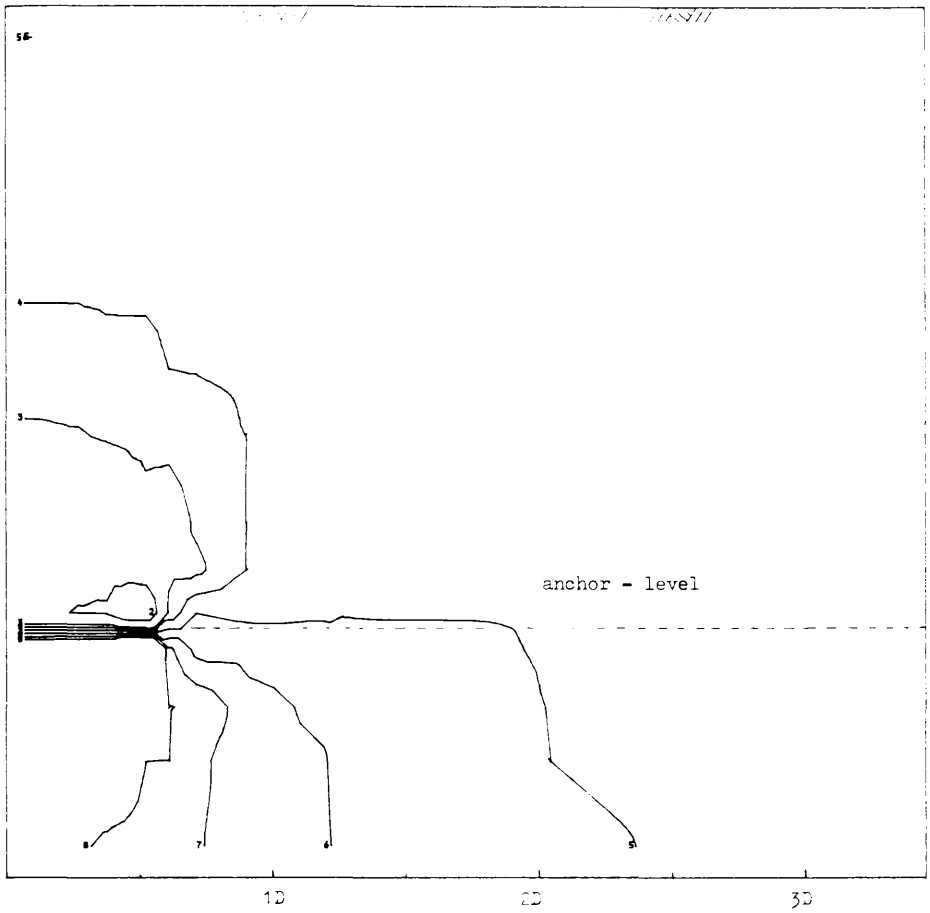

MEAN STRESS

FIG 4.33 STRESS DISTRIBUTION FOR SHALLOW ANCHORS IN ELASTIC STATE

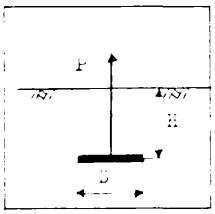

LEVELS	STRESS (Pa)
1	-0.56850E 05
2	-0.33230E 05
3	-0.96100E 04
4	-0.37050E 04
5	0.22000E 04
6	0.81050E 04
7	0.14010E 05
8	0.19915E 05

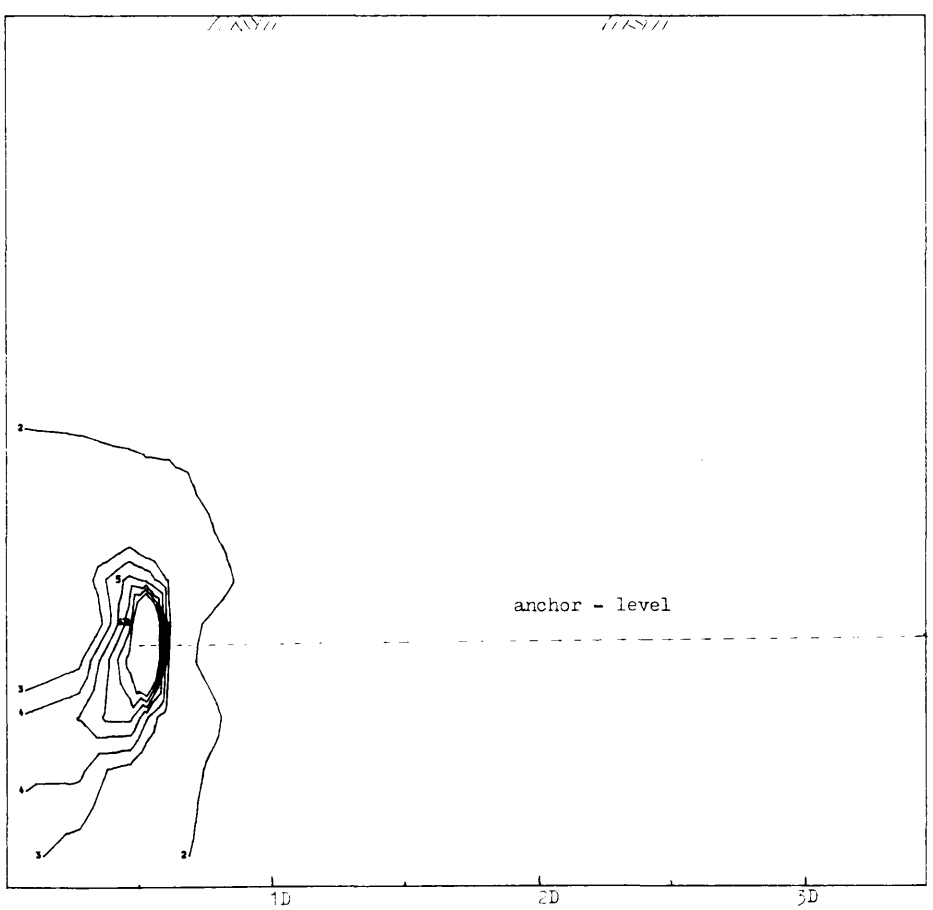

MAXIMUM SHEAR STRESS

FIG 4.34 STRESS DISTRIBUTION FOR SHALLOW ANCHORS IN ELASTIC STATE

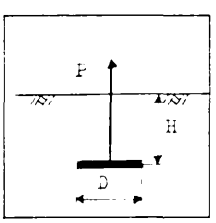

LEVELS	STRESS (Pa)
1	0.00000E 00
2	0.11346E 05
3	0.22692E 05
4	0.25528E 05
5	0.28364E 05
6	0.31201E 05
7	0.34037E 05
8	0.36874E 05

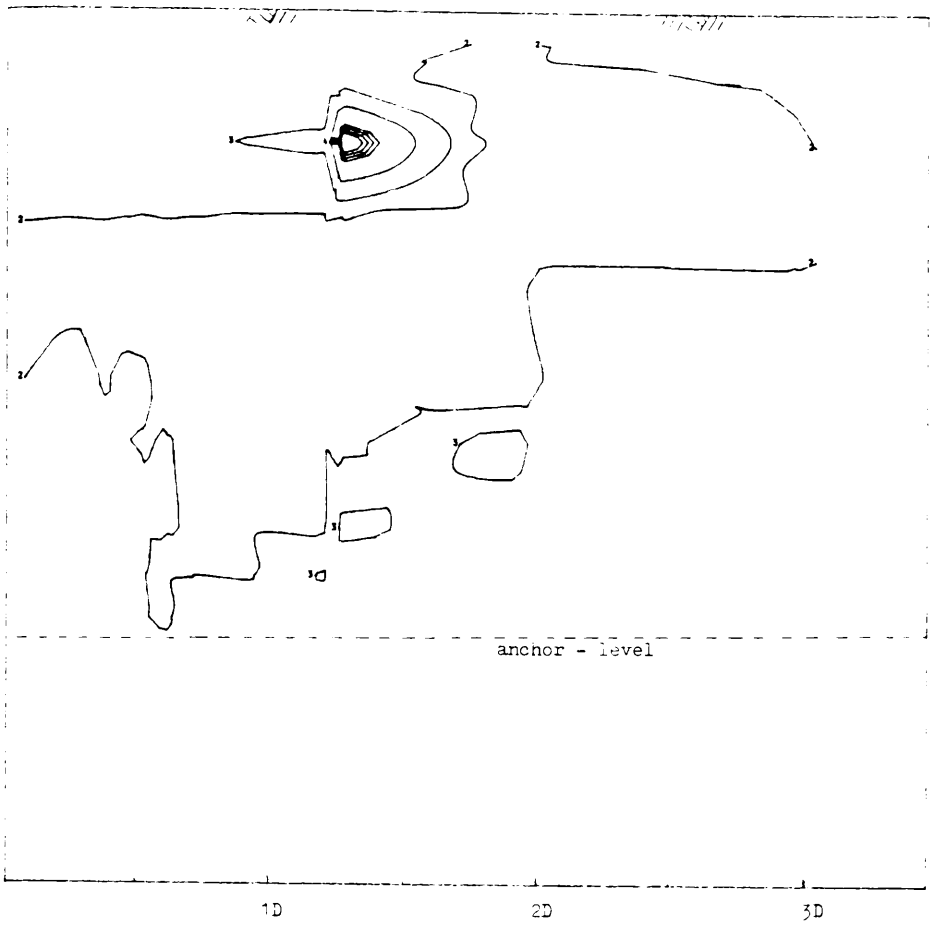

FIG 4.35 STRESS DISTRIBUTION FOR SHALLOW ANCHORS IN ELASTIC STATE

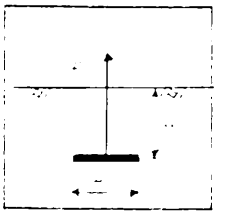

LEVELS	MAGNITUDE
1	-0.16571E 02
2	-0.13902E 01
3	0.13791E 02
4	0.28971E 02
5	0.44152E 02
6	0.46581E 02
7	0.49010E 02
8	0.51439E 02

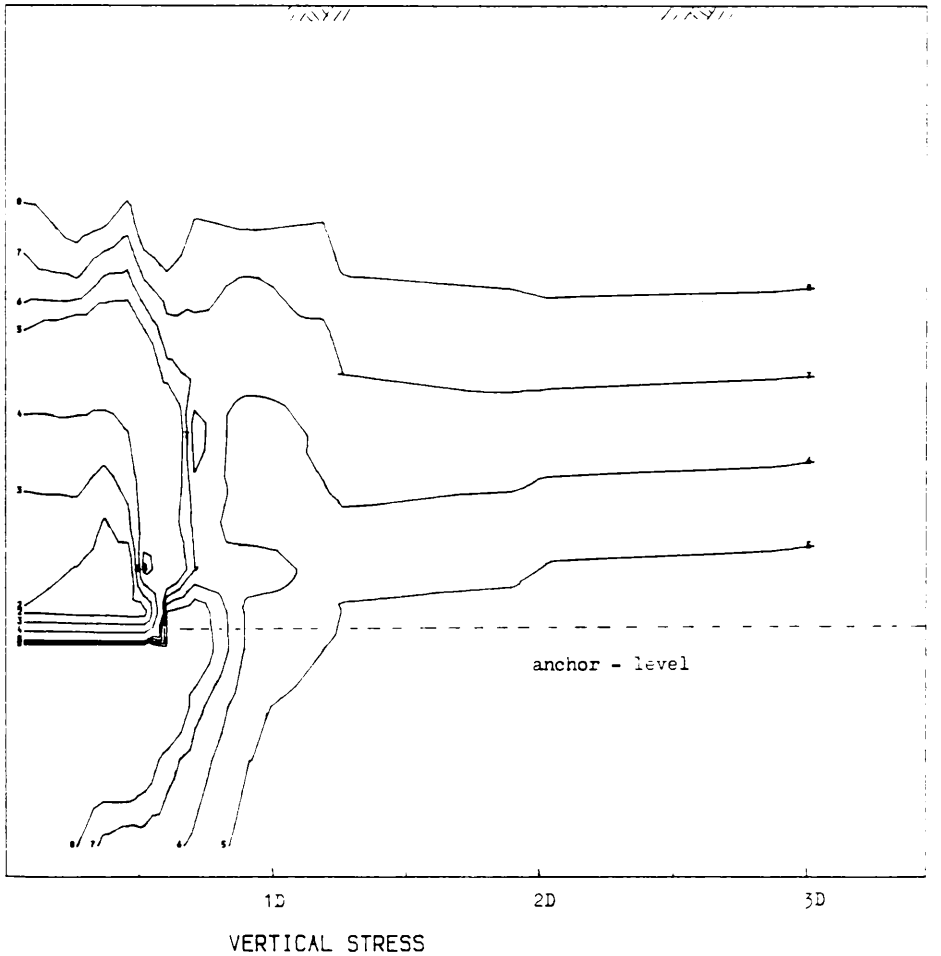

FIG 4.36 STRESS DISTRIBUTION FOR SHALLOW ANCHORS AT ULTIMATE STATE

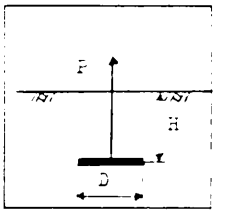

LEVELS	STRESS (Pa)
1	-0.42400E 06
2	-0.33917E 06
3	-0.25434E 06
4	-0.16952E 06
5	-0.84688E 05
6	-0.71116E 05
7	-0.57543E 05
8	-0.43971E 05

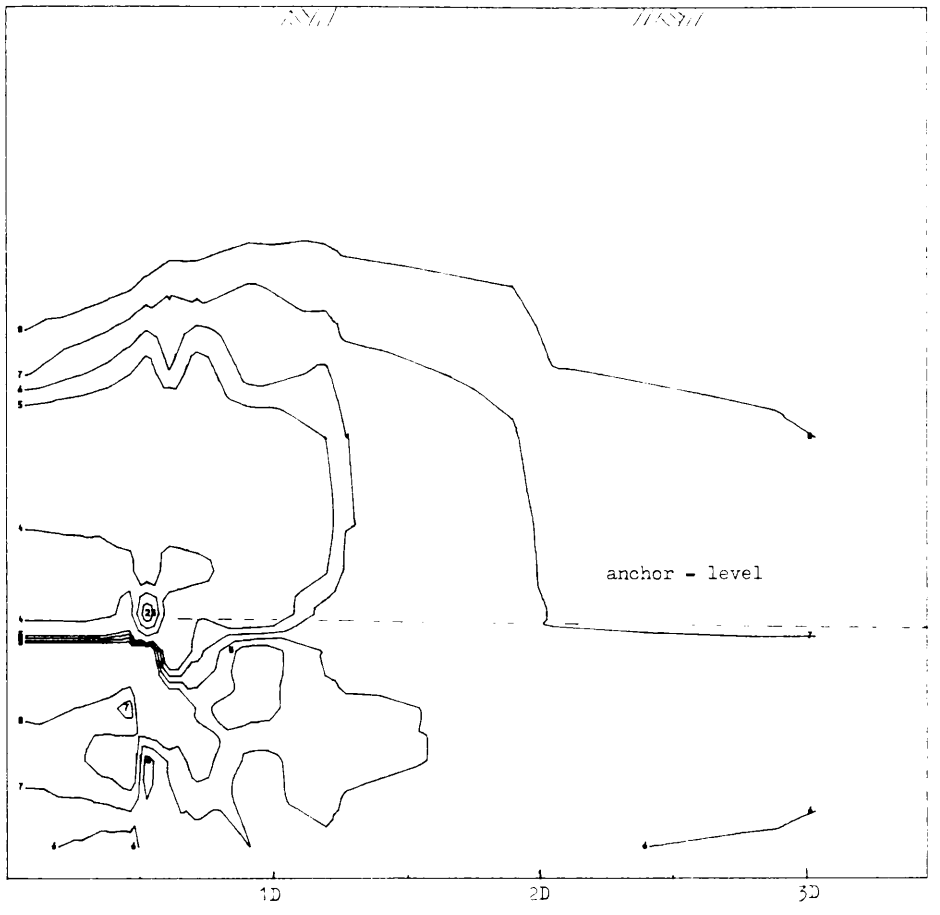

RADIAL STRESS

FIG 4.37 STRESS DISTRIBUTION FOR SHALLOW ANCHORS AT ULTIMATE STATE

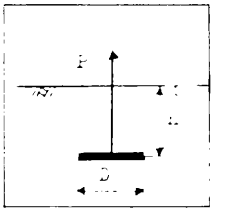

LEVELS	STRESS (Pa)
1	-0.30600E 06
2	-0.24477E 06
3	-0.18354E 06
4	-0.12231E 06
5	-0.61086E 05
6	-0.51290E 05
7	-0.41493E 05
8	-0.31697E 05

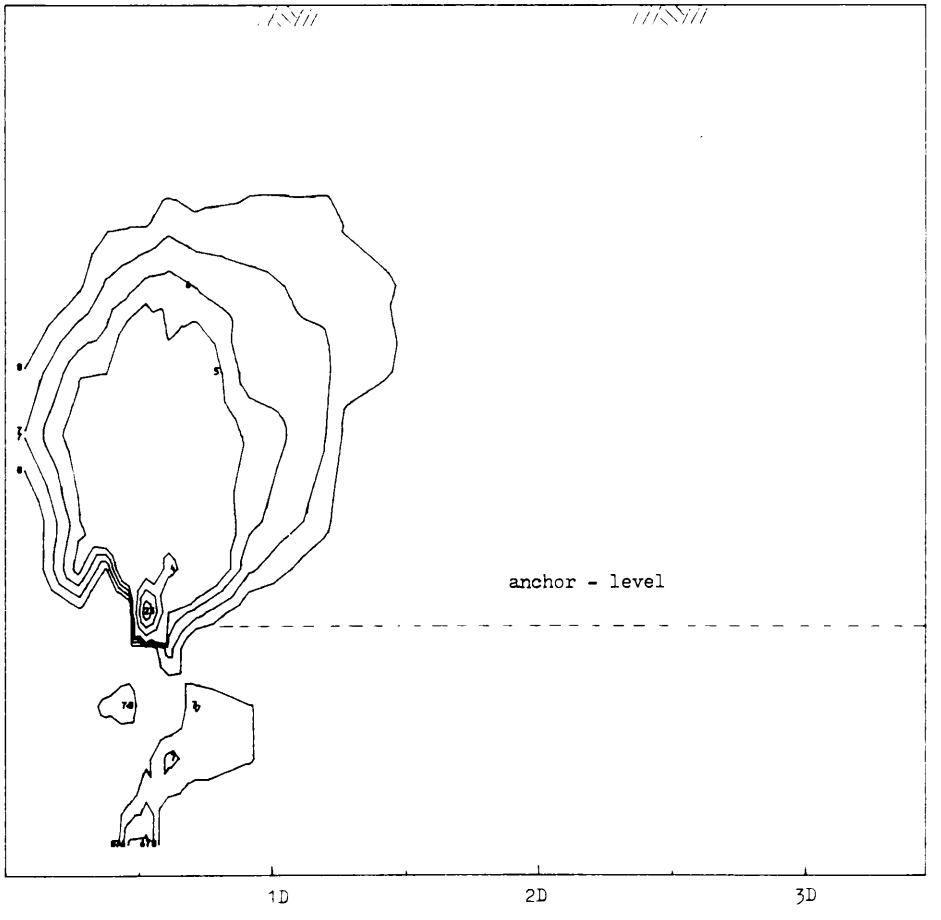

SHEAR STRESS

FIG 4.38 STRESS DISTRIBUTION FOR SHALLOW ANCHORS AT ULTIMATE STATE

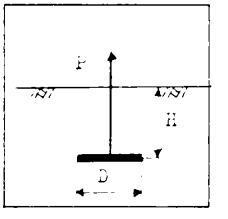

LEVELS	STRESS (Pa)
1	-0.19100E 06
2	-0.15046E 06
3	-0.10992E 06
4	-0.69380E 05
5	-0.28840E 05
6	-0.22354E 05
7	-0.15867E 05
8	-0.93808E 04

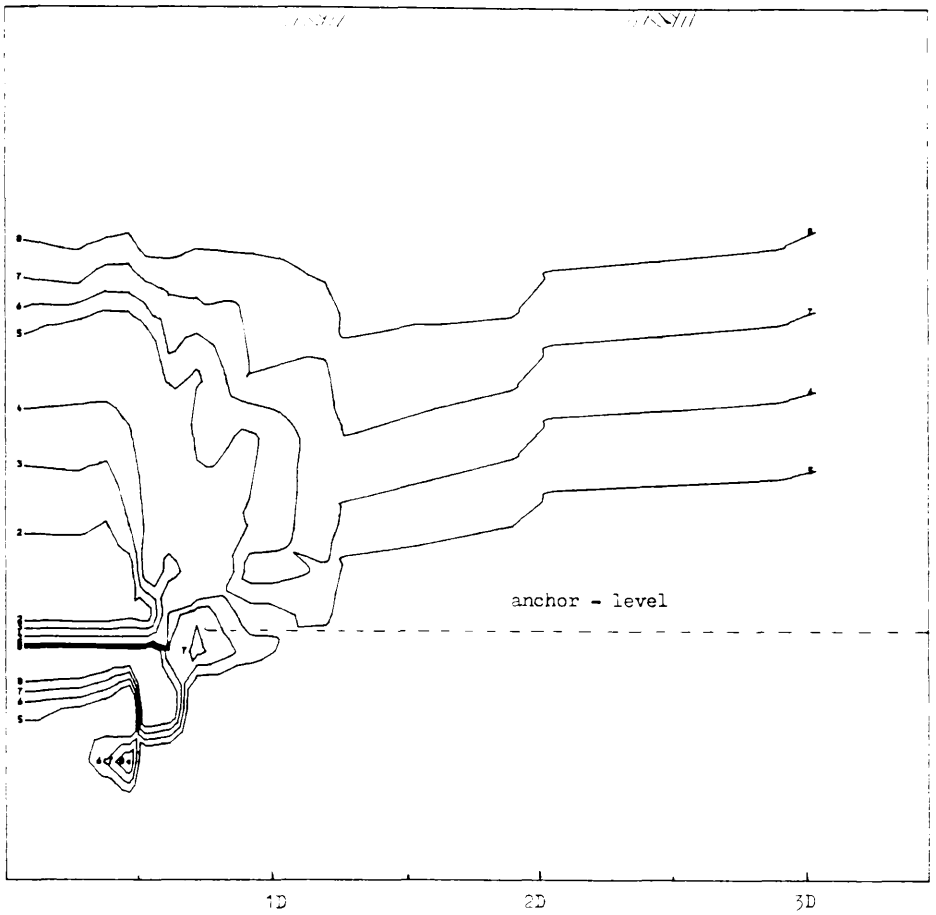

CIRCUMFERENTIAL STRESS

FIG 4.39 STRESS DISTRIBUTION FOR SHALLOW ANCHORS AT ULTIMATE STATE

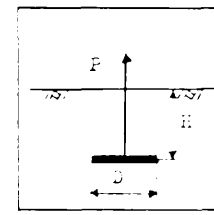

LEVELS	STRESS (Pa)
1	-0.15800E 06
2	-0.12637E 06
3	-0.94744E 05
4	-0.63115E 05
5	-0.31487E 05
6	-0.26427E 05
7	-0.21366E 05
8	-0.16306E 05

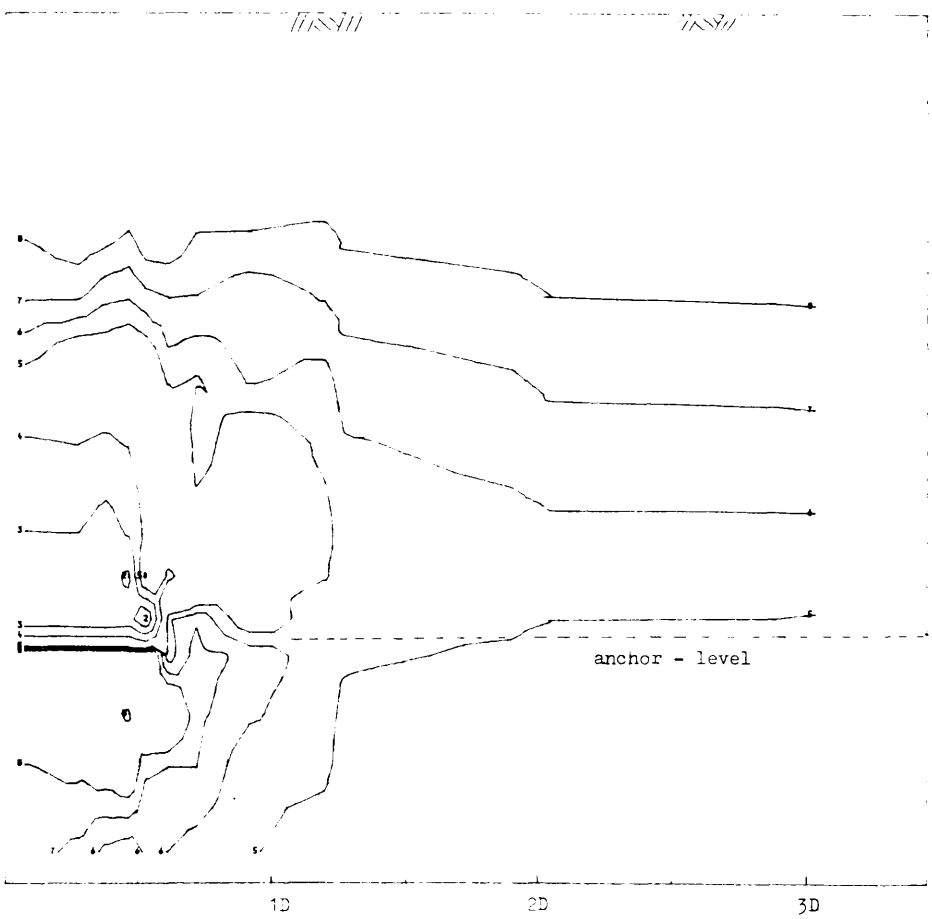

MEAN STRESS

FIG 4.40 STRESS DISTRIBUTION FOR SHALLOW ANCHORS AT ULTIMATE STATE

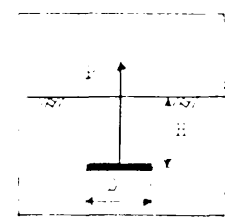

LEVELS	MAGNITUDE
1	-0.33750E 06
2	-0.26997E 06
3	-0.20244E 06
4	-0.13492E 06
5	-0.67387E 05
6	-0.56583E 05
7	-0.45778E 05
8	-0.34974E 05

FIG 4.41 STRESS DISTRIBUTION
FOR SHALLOW ANCHORS
AT ULTIMATE STATE

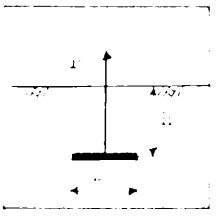

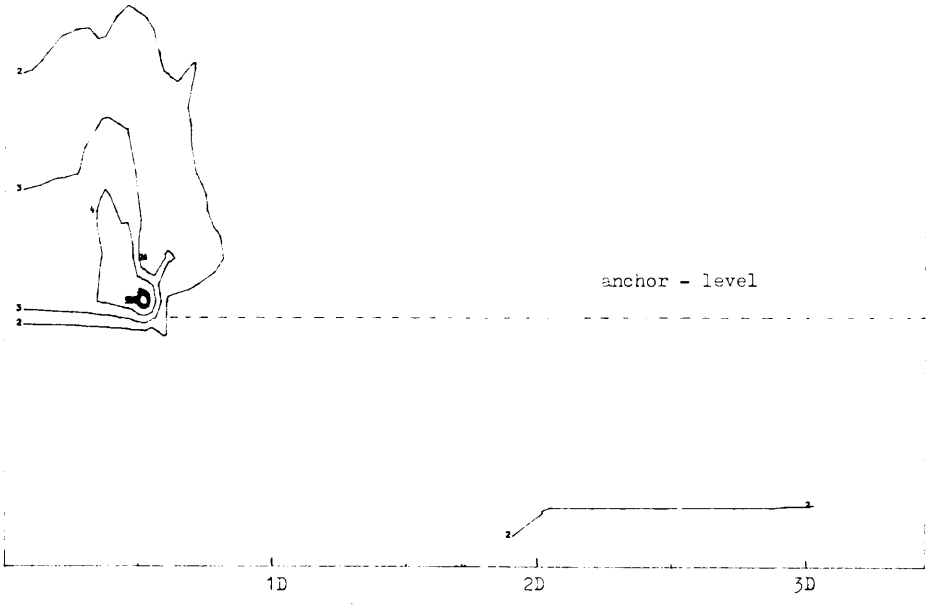

LEVELS	MAGNITUDE
1	0.00000E 00
2	0.38700E 05
3	0.77400E 05
4	0.11610E 06
5	0.15480E 06
6	0.16099E 06
7	0.16718E 06
8	0.17338E 06

MAXIMUM SHEAR STRESS

FIG 4.42 STRESS DISTRIBUTION
FOR SHALLOW ANCHORS
AT ULTIMATE STATE

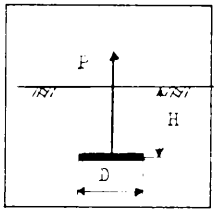

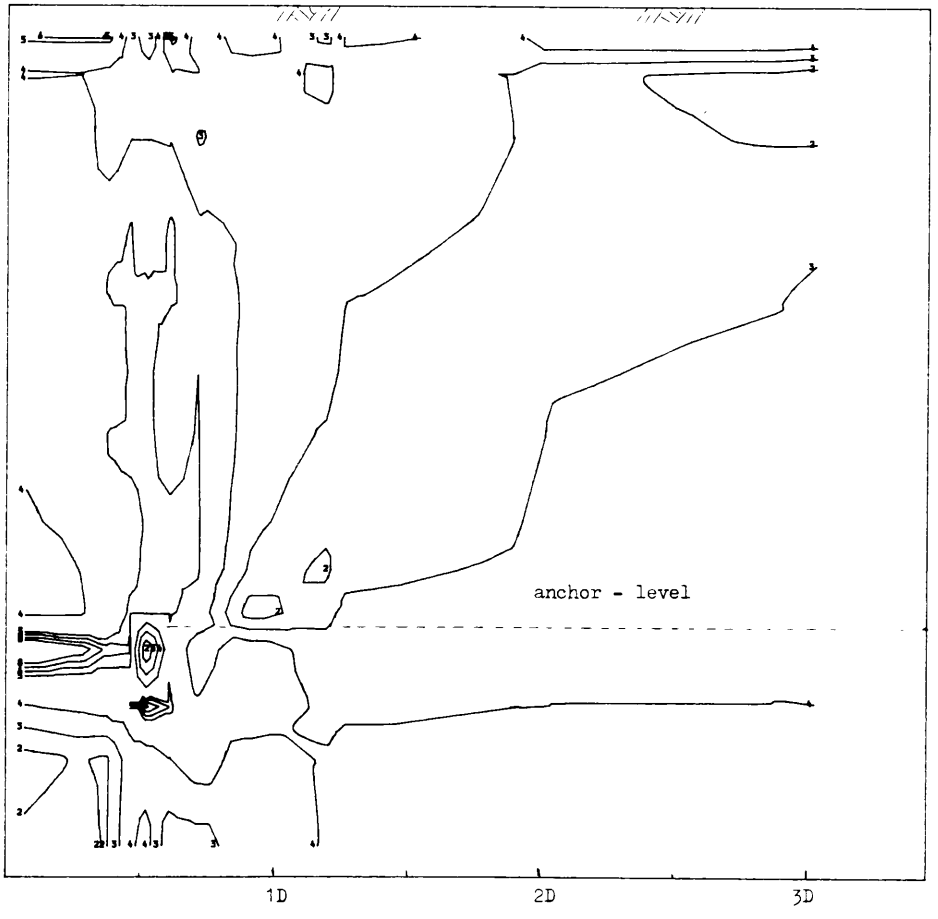

LEVELS	MAGNITUDE
1	-0.70922E-02
2	0.13551E 00
3	0.27812E 00
4	0.42072E 00
5	0.56333E 00
6	0.58614E 00
7	0.60896E 00
8	0.63178E 00

STRESS RATIO

FIG 1.43 STRESS DISTRIBUTION
FOR DEEP ANCHORS
AT ULTIMATE STATE

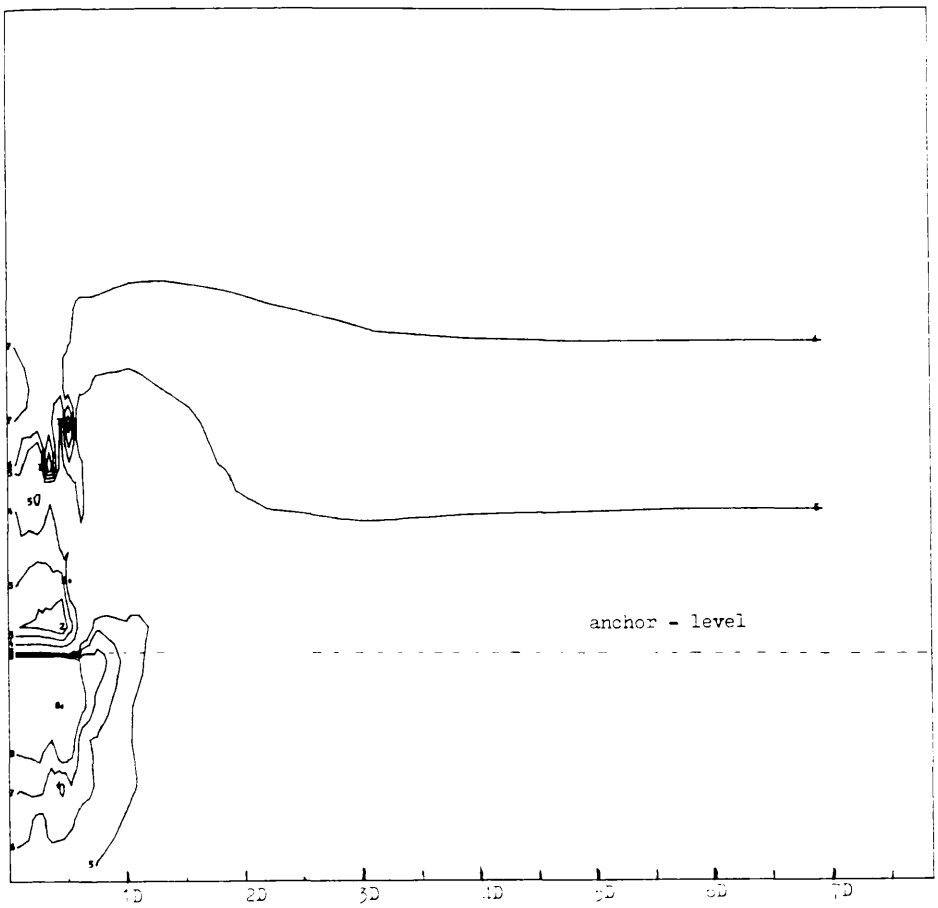

VERTICAL STRESS

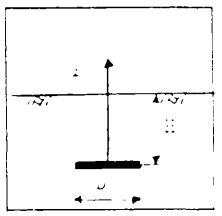

LEVELS	STRESS (Pa)
1	-0.17600E 07
2	-0.14079E 07
3	-0.10559E 07
4	-0.70384E 06
5	-0.35178E 06
6	-0.29546E 06
7	-0.23913E 06
8	-0.18280E 06

FIG 1.44 STRESS DISTRIBUTION
FOR DEEP ANCHORS
AT ULTIMATE STATE

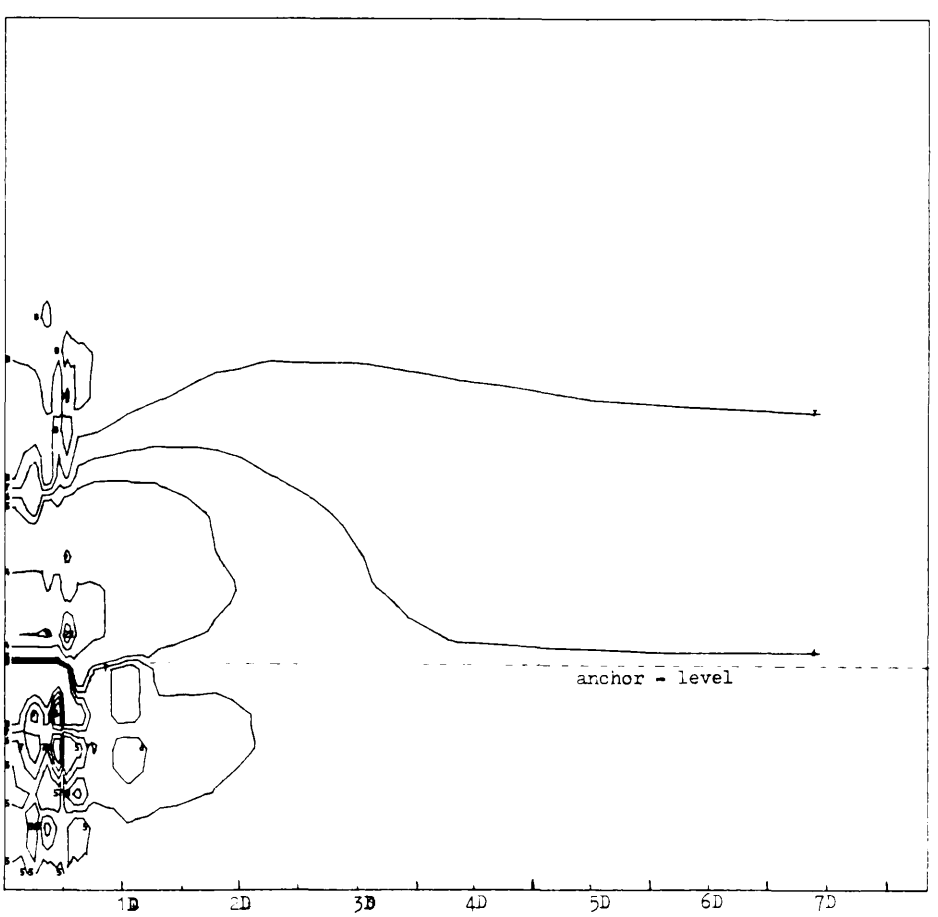

RADIAL STRESS

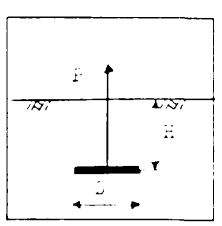

LEVELS	STRESS (Pa)
1	-0.10100E 07
2	-0.80796E 06
3	-0.60591E 06
4	-0.40387E 06
5	-0.20182E 06
6	-0.16949E 06
7	-0.13717E 06
8	-0.10484E 06

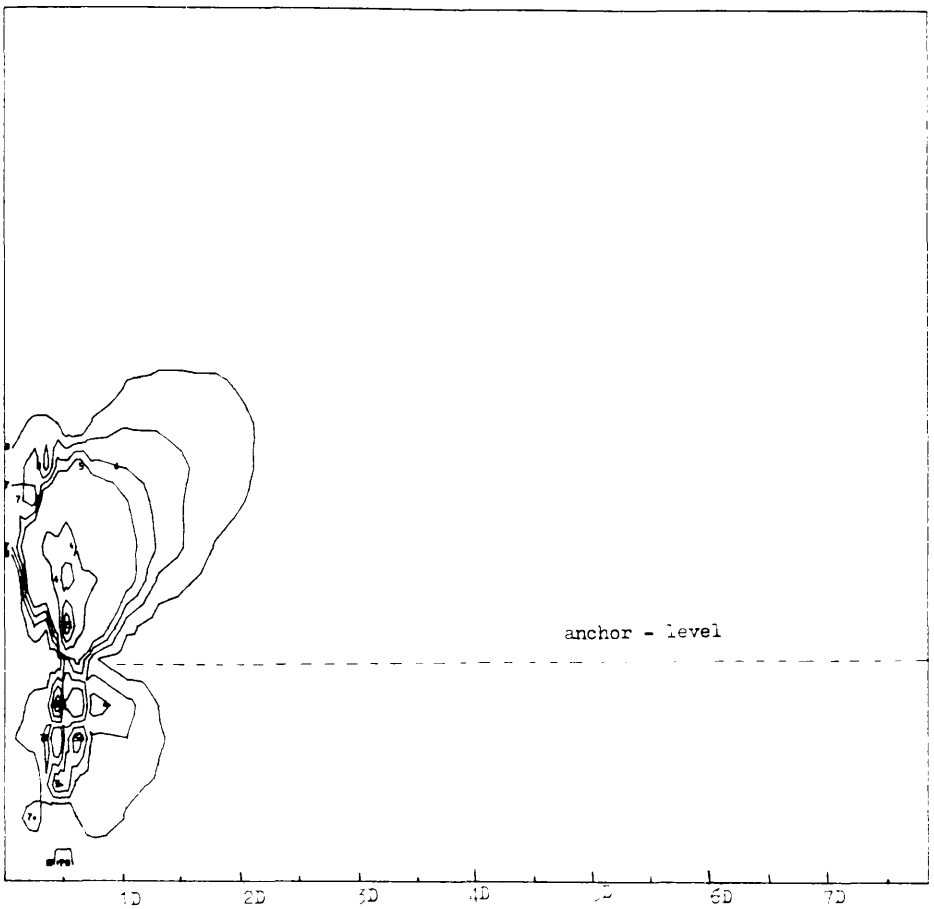

SHEAR STRESS

FIG 4.45 STRESS DISTRIBUTION
FOR DEEP ANCHORS
AT ULTIMATE STATE

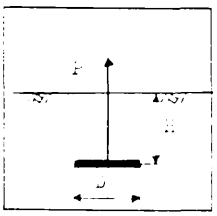

LEVELS	STRESS (Pa)
1	-0.63400E 06
2	-0.49738E 06
3	-0.36076E 06
4	-0.22414E 06
5	-0.87520E 05
6	-0.65661E 05
7	-0.43802E 05
8	-0.21942E 05

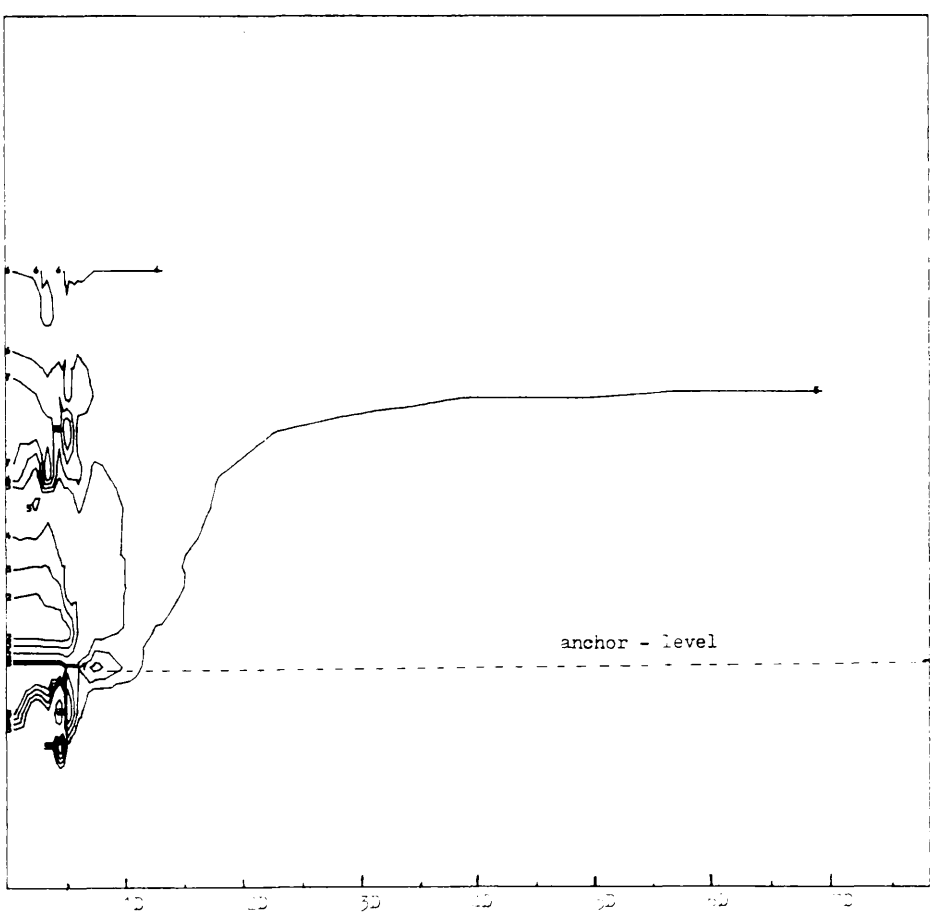

CIRCUMFERENTIAL STRESS

FIG 4.46 STRESS DISTRIBUTION
FOR DEEP ANCHORS
AT ULTIMATE STATE

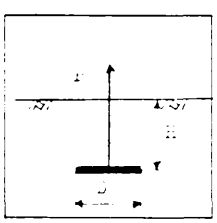

LEVELS	STRESS (Pa)
1	-0.66800E 06
2	-0.53436E 06
3	-0.40071E 06
4	-0.26707E 06
5	-0.13342E 06
6	-0.11204E 06
7	-0.90656E 05
8	-0.69273E 05

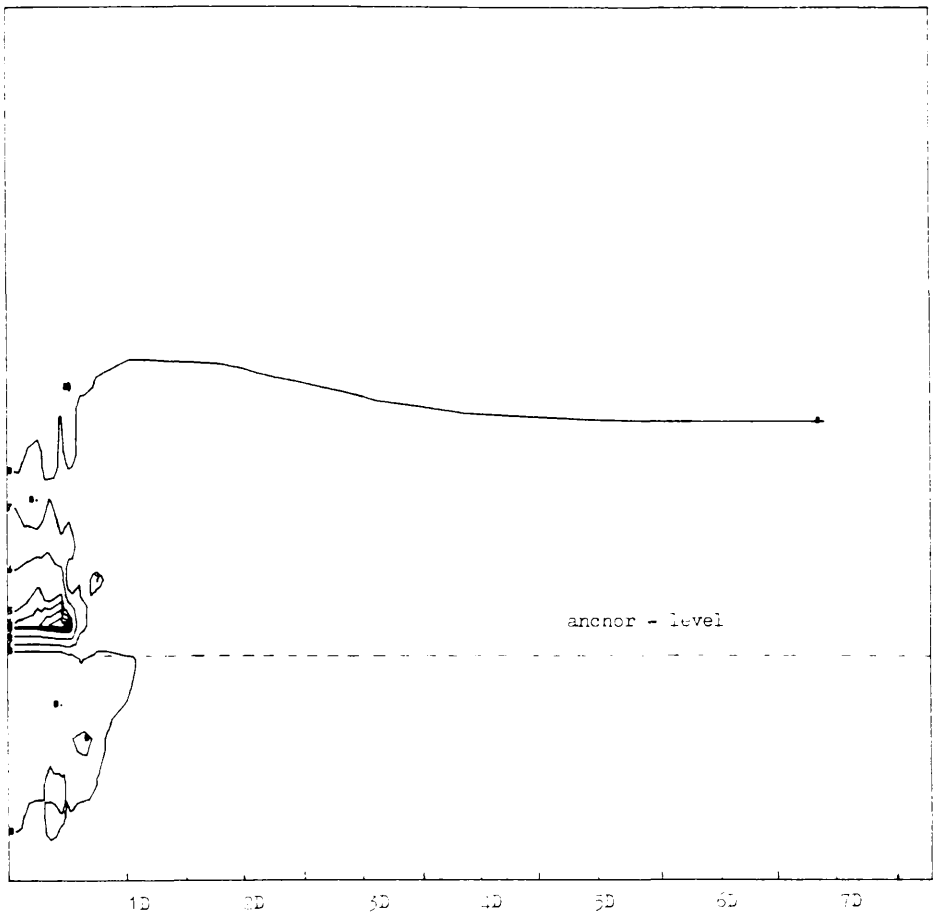

MEAN STRESS

FIG 4.47 STRESS DISTRIBUTION
FOR DEEP ANCHORS
AT ULTIMATE STATE

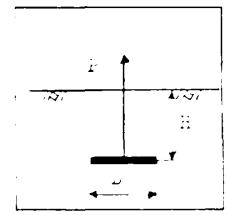

LEVELS	STRESS (Pa)
1	-0.11590E 07
2	-0.11010E 07
3	-0.10431E 07
4	-0.98511E 06
5	-0.92715E 06
6	-0.69530E 06
7	-0.46345E 06
8	-0.23160E 06

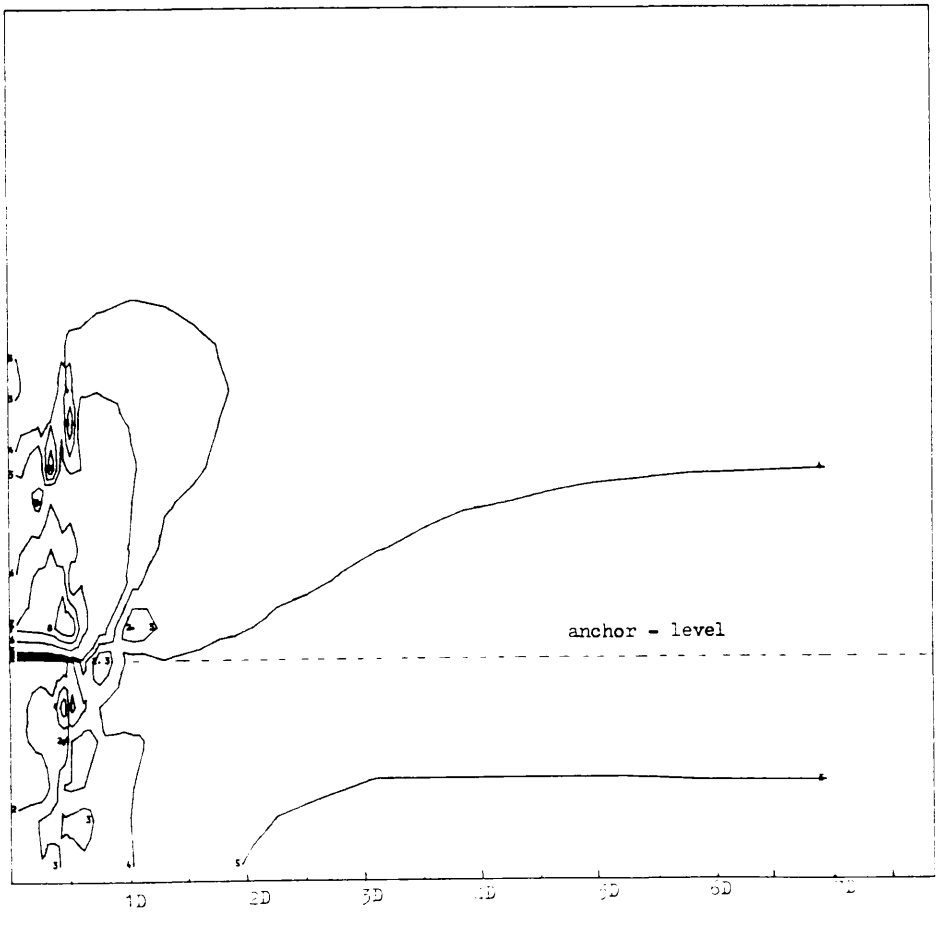

MAXIMUM SHEAR STRESS

FIG 4.48 STRESS DISTRIBUTION
FOR DEEP ANCHORS
AT ULTIMATE STATE

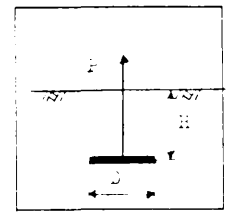

LEVELS	STRESS (Pa)
1	0.00000E 00
2	0.32050E 05
3	0.64100E 05
4	0.96150E 05
5	0.12820E 06
6	0.25640E 06
7	0.38460E 06
8	0.51280E 06

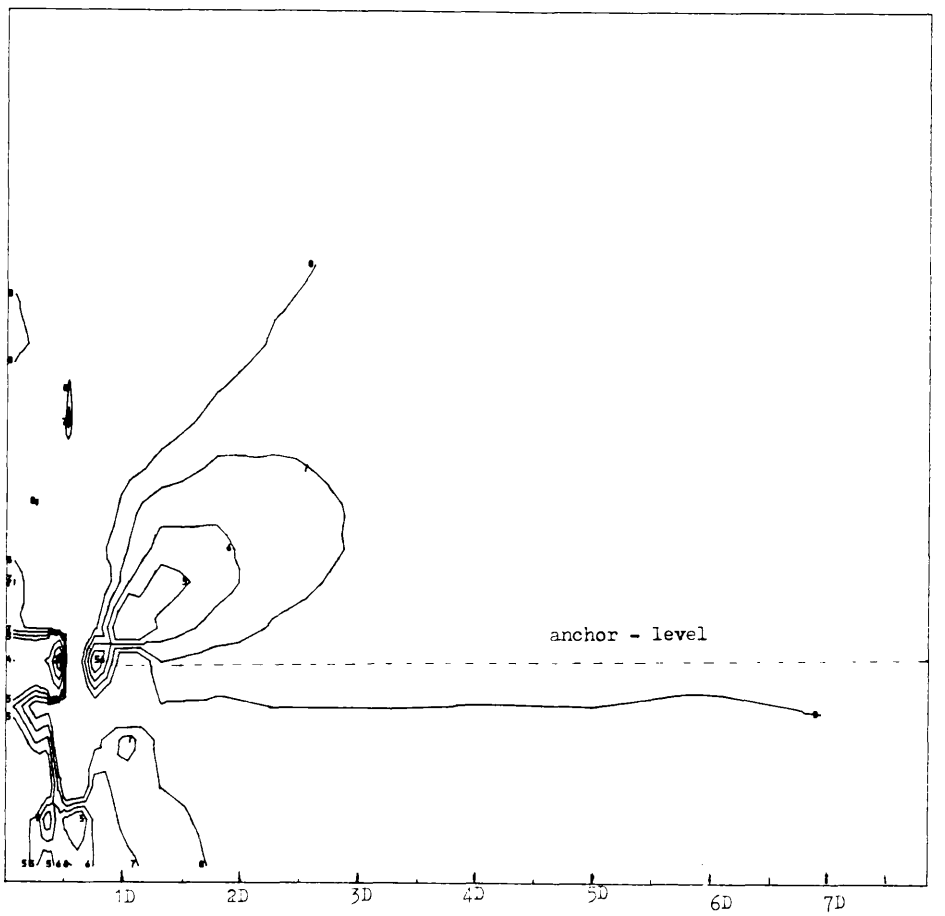

FIG 4.49 STRESS DISTRIBUTION
FOR DEEP ANCHORS
AT ULTIMATE STATE

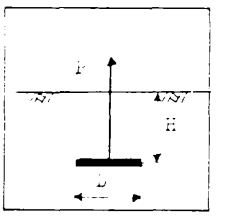

LEVELS	MAGNITUDE
1	-0.11001E 01
2	-0.76438E 00
3	-0.42865E 00
4	-0.92928E-01
5	0.24280E 00
6	0.29651E 00
7	0.35023E 00
8	0.40394E 00

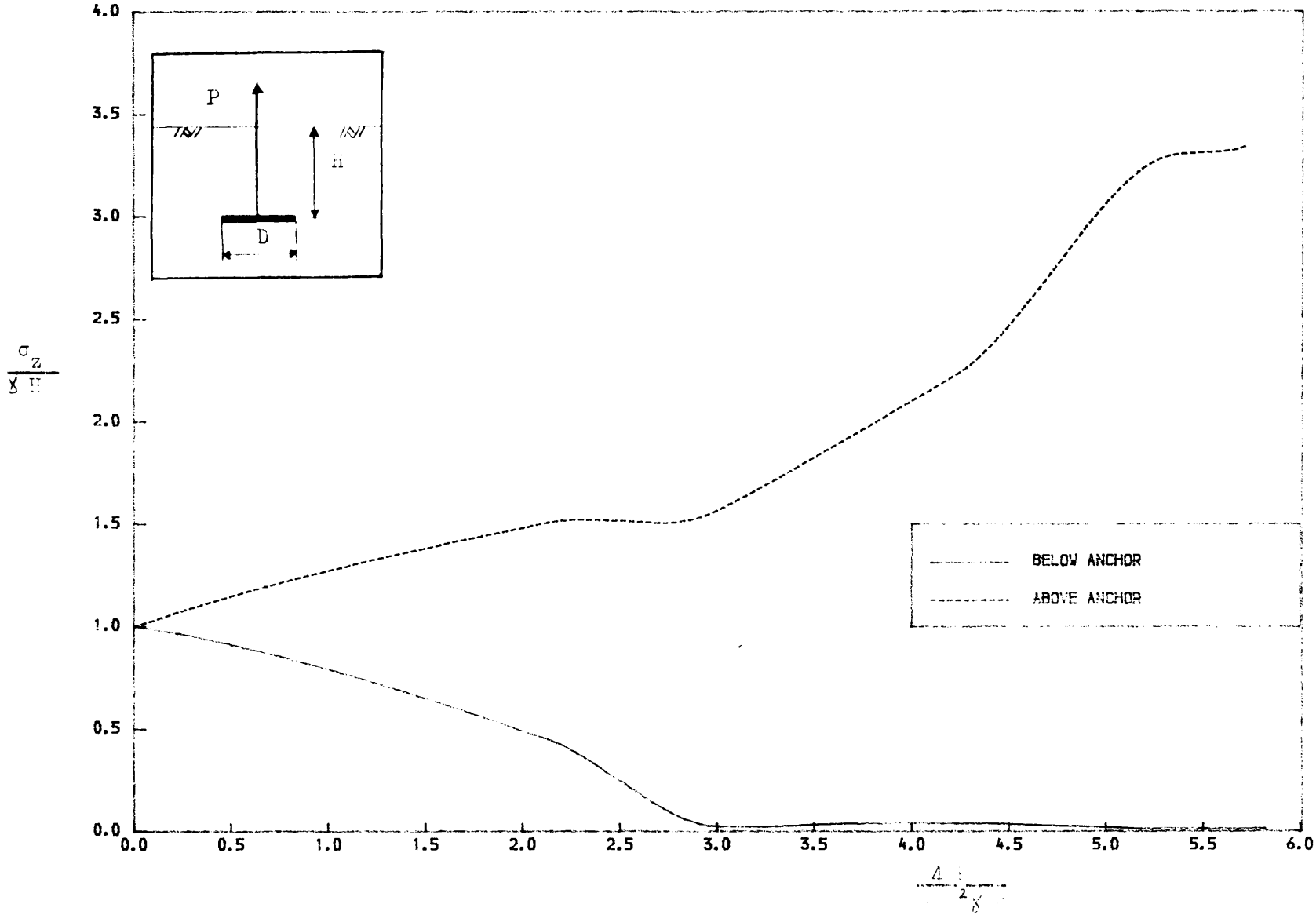

FIG 4.50 VARIATION OF VERTICAL STRESS NEAR ANCHOR PLATE

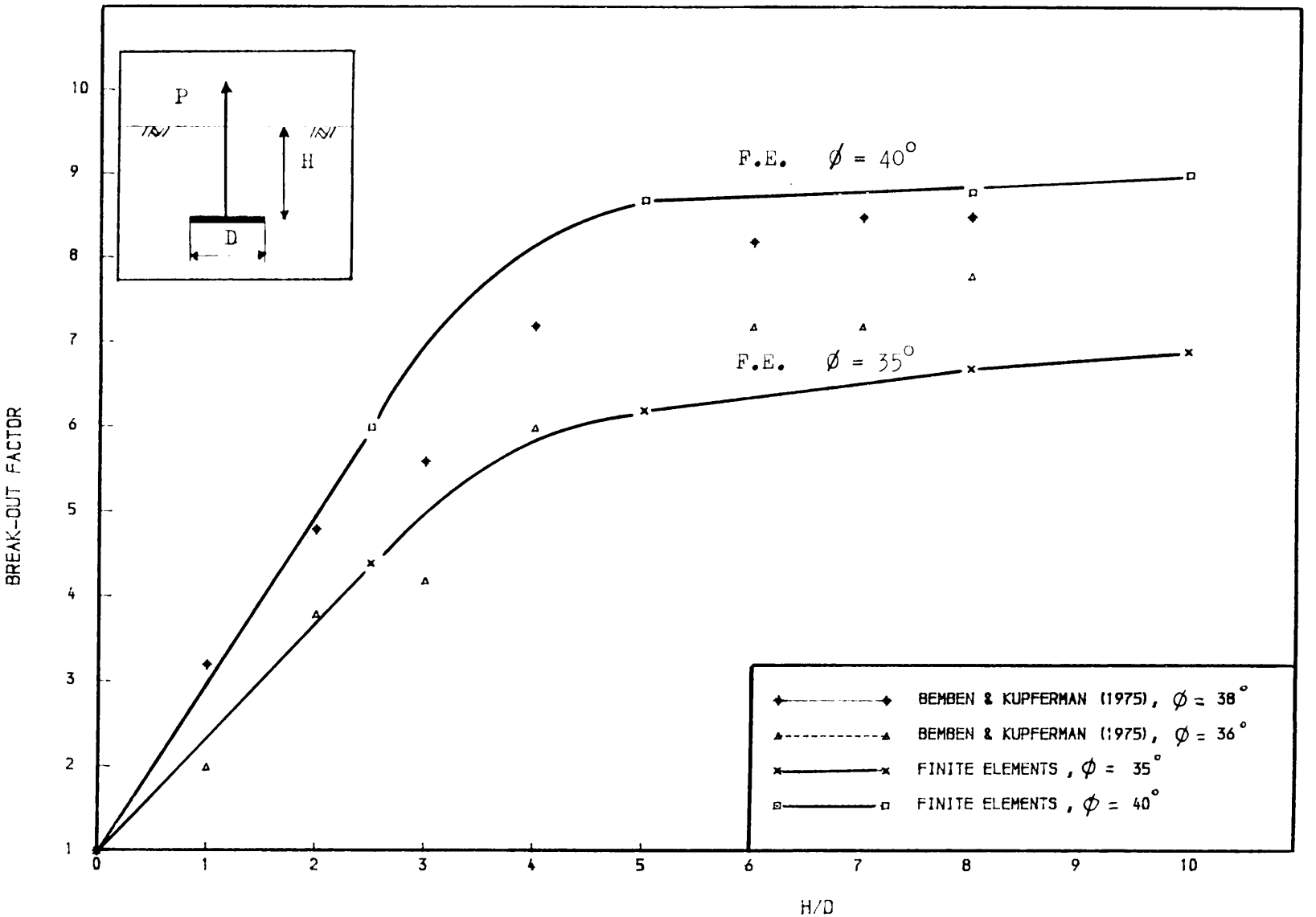

FIGURE 4.51 COMPARISON OF THEORETICAL AND EXPERIMENTAL LIMIT LOADS.

CHAPTER 5 GENERAL CONCLUSIONS AND SUGGESTIONS FOR FUTURE WORK

5.1 GENERAL CONCLUSIONS:

The work described in this thesis begins with an elastic analysis of ground anchors in which several assumptions were made. Some of these assumptions limited the applicability of the analysis but some useful insights into the stress distribution around ground anchors were obtained. However, a more realistic non–linear analysis was required before any definitive conclusion could be drawn. Finite element analysis appeared to be the most appropriate method. However, since the behaviour of sand is rather complex (dilatancy, softening,...) an appropriate stress–strain model was then necessary. After a review of several constitutive models for sands, Vermeer's model which has the merit of being relatively simple yet comprehensive, has been studied in detail. However, this model does not describe softening behaviour since this is not a material property of a continuum. For this reason among others, it was decided that little advantage would be gained by implementing the model into the finite element program. Instead, a simple linear elastic–perfectly plastic model based on the Mohr–Coulomb yield criterion was employed in the finite element analyses. The effects of soil properties, embedment depth and initial stress conditions were studied as well as the effects of sand inhomogeneity and test scale. Contours representing the stress distribution around the anchor and yield propagation during the loading history were plotted. This gave an insight into the progressive mechanism of failure occuring in the soil mass. The results from the finite element anlyses were based on the so–called k_4 failure load concept which appeared to give satisfactory results for loose sands.

5.2 SUGGESTIONS FOR FUTURE WORK:

In order to gain a better understanding of the behaviour of plate anchors embedded in sand, the following developments seem to be necessary.

1– To investigate in more detail the softening behaviour of dense sands culminating in the implementation of approach constitutive laws in a robust finite element code capable of dealing with softening behaviour.

2– An alternative technique which recognises that material discontinuities occur along shear bands would be of great utility but it is difficult to see how this could be developed in a finite element context.

3– Perhaps of lesser importance would be program enhancements to cater for finite deformations and non_ associated flow.

4– Finally, it would be useful for detailed comparison purposes with experimental data if more high quality data were available. Use of photogrammetry techniques currently under way at Glasgow University should help to fulfill this need.

REFERENCES

1- BALLA, A.

The resistance to breaking out of mushroom foundations for pylons.
Proc.5th Int.Con. Soil Mech.& Found.Eng,PARIS,1961,Vol.1,PP 569-576

2- BAKER, W.H. and KONDNER, R.L.

Pullout load capacity of a circular earth anchor buried in sand.
Highway Research Board RECORD,No. 108, Mechanics in earth masses, January 11-15,1965,PP 1-10

4- BAZANT, Z.P. ,BELYTSCHKO, T.B. and CHANG, Ta-Peng

Continuum theory for strain-softening.
Journal of Engng Mech.,Vol.110,No. 12,December 1984,PP 1666-1692

5- BEMBEN, S.M. and KUPFERMAN,M.

The vertical holding capacity of marine anchor flukes subjected to static and cyclic loading
Offshore Technology Conference,Dallas,1975,Paper No. OCT 2185

6- BOLTON, M. D.

The strength and dilatancy of sands.
Geotechnique 36,No. 1, 1986, PP 65-78

7- BOLTON, M.D.

The strength and dilatancy of sands.(Discussion)
Geotechnique 37,No. 2,1987,PP 219-226

8- BORST, R. DE and VERMEER, P.A.

Possibilities and limitations of finite elements for limit analysis
Geotechnique 34,No. 2,1984,PP 199-210

9- BOUAZZA, A.

Pull-out capacity of plate anchors in sand.
PhD thesis to be presented to Glasgow University,1988.

10- CARR, R.W. and HANNA, T.H.

Sand movement measurement near anchor plates.
Journal of soil Mech.and Found.Division,Proc.of ASCE,SM 5,1971, PP 833-840

11- CHEN, F.W.

Limit analysis and soil plasticity.

Scientific Publishing Co., Elsevier, Amsterdam, The Netherlands, 1975.

12- CLEARY, M.P.

Continuously distributed dislocation model for shear-bands in softening materials.

International Journal for Numerical Methods in Engineering,Vol. 10, 1976,PP 679-702

13- CRAGG, C.B.H. ,KIRSHNASAMY, S.G. and RADHAKRISHNA, H.S.

Uplift design of transmission tower foundations in sand A probabilistic approach.

Int. Symp. on Probabilistic Methods Appl. To Electric Power Systems Ontario Hydro Research Division,June 11-13, 1986,PP 1-7

14- DAS, B.M. and SEELEY, G.R.

Breakout resistance of shallow horizontal anchors.

Journal of the Geotechnical Engineering Division,Proc of the ASCE Vol. 101,No. GT9, September,1975, PP 999-1003

15- DAS, B.M. and SEELEY, G.R.

Uplift capacity of shallow inclined anchors.

Proc.9th Int.Conf. in Soil Mech.& Found.Eng,TOKYO,1977,Vol. 1, PP 463-466

16- DAVIE, J.R

Behaviour of cohesive soils under uplift forces.

Ph.D.Thesis presented to GLASGOW University,1973

17- DAVIE, J.R. and SUTHERLAND, H.B.

Uplift resistance of cohesive soils.

Journal of the Geotechnical Engineering Division,proc of the ASCE Vol. 103,No. GT9,September,1977, PP 935-953

18- DENAM, F.

Achsensymmetrische spannungs und verformungsfelder in strockenem sand.

Dissertation, 1975, University of Karlsruhe.

19- DAVIES,T.G. and BANERJEE,P.K.
Constitutive relationships for ocean sediments subjected to stress and temperature gradients.
Research report for Harwell, 1980, PP 1-28

20- DESAI, C.S. ,MUQTADIR, A. and SCHEELE, F.
Interactive analysis of anchor-soil systems.
Journal of Geotechnical Engrg,Vol. 112,No. 5,May,1986,PP 537-553

21- DESAI, C.S. and SIRIWARDANE, H.J.
Constitutive laws for engineering materials (with emphasis on geologic materials).
Pretice-Hall, 1984.

22- DESAI, C.S. ,SOMASUNDARAM, S. and FRANTZISKONIS, G.
A hierarchical approach for constitutive modelling of geologic materials.
Int. Jour. Num.and Anal. meth. in Geomech.,vol.10,1986,PP 225-257

23- DRESCHER, A. and VARDOULAKIS, I.
Geometric softening in triaxial tests on granular material.
Geotechnique 32,No. 4,1982, PP 291-303

24- DRUCKER,D.C., PRAGER,W. and GREENBERG, H.J.
Extended limit design theorems for continuous media
Quarterly of Applied Mathematics,Vol. 9,1952, PP 381-389

25- EL-SOHBI, M.A. and ANDRAWES, K.Z.
Experimental examination of sand anisotropy
Proc.8th Int.Conf. in Soil Mech.and Found.Eng,MOSCOW, No 1.1, 1973, PP 103-109

26- FADL, M.O.
The behaviour of plate anchors in sand.
PhD thesis presented to Glasgow University, 1981.

27- FOX, E.N.
The mean elastic settlement of a uniformly loaded area at a depth below the ground surface.
Proc.2nd Int. Conf.Soil Mechanics,Rotterdam 1, 1948,PP 129-131

28- FRANK, R. and TADJBAKHSH, S.
Finite element study of pile axial behaviour in elasto_plastic dilating media.
3rd International Conf. ,NANTES,Laboratoire Central des ponts et Chaussees.May 21-22 1986

29- HANNA, T.H.
Foundations in tension, Ground anchors.
Trans Tech Publications & Mc Graw Hill, 1982.

30- HANNA, T.H. ,SPARKS, R. and YILMAZ, M.
Anchor behaviour in sand.
Jrnl of Soil Mech. and Found. Div.,SM 11,Nov.1972,PP 1187-1208

31- HANSEN,J.B.
Some stress_strain relationships for soils.
Proc. 6th. ICSMFE,Montreal,Vol.1,1965,PP 231-234

32- HILL, R.
The mathematical theory of plasticity.
Oxford University Press, 1950.

33- HETTLER, A. and VARDOULAKIS, I.
Behaviour of dry sand tested in a large triaxial apparatus.
Geotechnique 34,No. 2,1984,PP 183-198

34- HETTLER, A., VARDOULAKIS, I., GUDEHUS, G.,
Stress-strain behaviour of sand in triaxial tests.
Prel.Proc.Int.Workshop Const.Behavior of Soils,2,1982, Grenoble.

35- HETTLER, A.,
Vershiebungen starrer under elastisher grundungsorper in sand bei monotoner und zyklisher belastung.
Dissertation, University of Karlsruhe, 1981.

36- HETTLER, A., and VARDOULAKIS, A.,
Behavior of dry sand tested in a large triaxial apparutus.
Geotechnique 34, 1984, 183.

37- ITO, H. and KITAHARA, Y.
Pulling-out resistance of electric transmission tower footing partially penetrating into the surrounding ground at its bottom slab.
Int Symp Numerical Models in Geotech/Zurich/ Sept 1982,PP 677-687

38- DE JOSSELIN DE JONG, G.
Rowe's stress_dilatancy relation based on friction.
Geotechnique 26,No. 3,1976,PP 527-534

39- HARDIN, B.O. and BLACK, M.L.
Vibration modulus of normally consolidated clay
Jou. of ASCE 94,SM2,1968,PP 353-369

40- HARDIN, B.O. and DRNEVICH, V.P.
Shear modulus and damping of soils: Design equations and curves
Jou.ASCE,SM7,1972,PP 667-692

41- KING, G.J.W. and DICKIN, E.A.
Comparison of stress_dilatancy theories.
Journal of the Soil Mechanics and Foundations Division,Proc.of the ASCE,SM5,Sep 1970,PP 1697-1714

42- KONDNER, R.L., and ZELASKO, J.S.
A hyperbolic stress-strain formulation for sands.
Proc. 2nd Pan-American CSMFE,1, 1963,p 289-324,Brasil.

43- LADE, P.V.
Elasto_plastic stress_strain theory for cohesionles soil with curved yield surfaces.
Int.J.Solids Structures,1977,Vol. 113,PP 1019-1035

44- LAMBE, T.W. and WHITMAN, R.V.
Soil mechanics, SI version
John Wiley & sons, 1979, PP 105– 108

45- LEE, I.K.
Stress-dilatancy performance of feldspar.
Journal of the Soil Mechanics and Foundations Division,Proc. of the ASCE,March,1966,SM 2,PP 79-103

46- LEE, K.L. and SEED, H.B.
Drained strength characteristics of sands.
Journal of the Soil Mechanics and Foundations Division Proc. of the ASCE,November,1967,SM 6,PP 117-141

47- MARIUPOL'SKII, L.G.
The bearing capacity of anchor foundations.
Translated from Osnovaniya,Fundamenty i Mekhanika,Gruntov,No. 1, January_February,1965,PP 14-18

48- MASE, G.E.
Theory and Problems of Continuous Mechanics.
Mc Graw Hill,1970,PP 140-159

49- MATSUO, M.
Study on the uplift resistance of footing(II)
Japanese Soc. Soil Mech. & Found. Eng. Vol. 8,No. 1,1968.

50- MATSUOKA, H. and NAKAI, T.
A new failure model for soils in three-dimensional stresses.
Proc. IUTAM Symp. on deformation and failure of granular materials, Delft, 1982, PP 253-263.

51- MEROUANI, Z. and DAVIES, T.G.
Elastic stress distribution around embedded anchors.
Research report CE/1986/3/TGD, 1986,Glasgow University.

52- MEYERHOF, G.G. and ADAMS, J.I.
The ultimate uplift capacity of foundations.
Canadian Geotechnical Journal,Vol.5,No.4,1968,PP 225-244

53- MINDLIN, R.D.
Force at a point in the interior of a semi-infinite solid
PHYSICS,a journal of general and applied physics,Vol. 7,June,1936, No.6,PP 195-202

54- MOLENKAMP, F.
Comparison of frictional material models with respect to shear band initiation.
Geotechnique, 35,No. 2,1985,PP 127-143

55- MUHLHAUS, H.B. and VARDOULAKIS, I.
The thickness of shear bands in granular materials.
Geotechnique 37,No.3,1987,PP 271-283

56- NAGTEGAAL, J.C. ,PARKS, D.M. and RICE, J.R.
On numerically accurate finite element solutions in the fully plastic range.
Computer Methods in Applied Mechanics and Engineering,4(1974), PP 153-177

57- NAYAK, G.C. and ZIENKIEWICZ, O.C.
Convenient form of stress invariants for plasticity.
Journal of the Structural Division,Proc.of the ASCE,Vol. 98,No. ST4 April,1972,PP 949-954

58- NAYAK, G. and ZIENKIEWICZ, O.C.
Elasto-plastic stress analysis. A generalisation of various constitutive relations including strain softening.
Int. J. Numer. Methods Engrg. 5, 1972, 113.

59- NAYLOR, D.J. and PANDE, G.N. et al
Finite elements in geotechnical engineering.
Pineridge Press,Swansea,U.K.,1981

60- NOVA, R. and WOOD, D.M.
A constitutive madel for sand in triaxial compression.
International Journal for Numerical and Analytical Methods in Geomechanics,Vol. 3,1979,PP 255-278

61- NOVA, R.
A model of soil behaviour in plastic and hysteretic ranges.
Part 1: Monotonic loading
Results of the International workshop on constitutive relations for Soils/Grenoble/6-8 Septembre ,1982

62- NOVA, R.
An engineering approach to shear band formation in geological media
Fifth International conference on Numrical Methods in Geomechanics/ Nagoya/1-5 April 1985,PP 509-516

63- OWEN, D.R.J. and HINTON, E.
Finite element method in plasticity, theory and practice.
Pineridge Press Ltd,Swansea,U.K.,1980

64- PIETRUSZCZAK, ST. and MROZ, Z.
Finite element analysis of deformation of strain_softening materials.
International journal for Numerical Methods in Engineering, Vol.17

1981,PP 327-334

65- POULOS, H.G. and DAVIS, E.H.
Elastic solutions for soil and rock mechanics.
John Wiley & Sons,Inc.,1973.
New_York.London.Sydney.Toronto

66- READ, H.E. and HEGEMIER, G.A.
Strain softening of rocks,soil and concrete.
A review article.
Mechanics of materials 3(1984),North_Holland,PP 271-294

67- ROSCOE, K.H.
The influence of strain in soil mechanics,10th Rankine lecture.
Geotechnique 20,No.2,1970, PP 129-170

68- ROWE, P.W.
The stress_dilatancy relation for static equilibrium of an assembly of particles in contact.
Proc.of the Royal Society,A.269,1962,PP 500-527

69- ROWE, P.W.
Theoretical meaning of observed values of deformation parameters for soil. In : Stress-strain behaviour of soils.
Proc. Roscoe Memb. Symp. ,1971,PP 143-194

70- ROWE, R.K. and BOOKER, J.R.
A method of analysis for horizontally embedded anchors in an elastic soil.
International Journal for Numerical and Analytical Methods in Geomechanics,Vol. 3,1979,PP 187-203

71- ROWE, R.K. and BOOKER, J.R.
The elastic displacements of single and multiple underream anchors in a Gibson soil.
Geotechnique 31,No. 1,1981,PP 125-141

72- ROWE, R.K. and DAVIS, E.H.
The behaviour of anchor plates in sand.
Geotechnique 32,No. 1,1982,PP 25-41

73- ROWE, R.K. and DAVIS, E.H.
The behaviour of anchor plates in clay.
Geotechnique 32,No. 1,1982,PP 9-23

74- SALENCON, J.
Theorie de la plasticite pour les applications de la mechanique des sols.
Eyrolles,Paris,1974

75- SCHOFIELD, A. and WROTH, P.
Critical state soil mechanics
Mc Graw-Hill,London,1968

76- SEED, H.B. and LEE, I.K.
Undrained strength characteristics of cohesionless soils.
Journal of the Soil Mechanics and Foundations Division. Proc. of the ASCE,November,1967,No.SM 6,PP 333-360

77- SELVADURAI, A.P.S.
Betti's reciprocal relationships for the displacements of an elastic infinite space bounded internally by a rigid inclusion.
J.Struct.Mech.,9(2),1981,PP 199-210

78- STROUD, M.A.
The behaviour of sand at low stress levels in the simple-shear apparutus.
Ph.D. Thesis, 1971, Cambridge University.

79- SUTHERLAND, H.B. ,FINLAY, T.W. and FADL, M.O.
Uplift capacity of embedded anchors in sand.
3rd Int.Conf. Behav. of off_shore Struct., Vol.1, 1983,PP 451-463

80- SUTHERLAND, H.B.
Model studies for shaft raising through cohesionless soils.
Proc.6th Int.Conf.Soil.Mech. and Fnd.Eng,Montreal,Vol.2, 1965,PP 410-413

81- TATSUOKA, F., and ISHIHARA, K.,
Yielding of sand in triaxial compression.
Soils and foundations, 1974, 14:63-76.

82- VARDOULAKIS, I.
Shear band inclination and shear modulus of sand in biaxial tests.
International Journal for Numerical and Analytical Methods in Mechanics,Vol. 4,1980,PP 103-119

83- VARDOULAKIS, I. ,GRAF, B. and HETTLER, A.
Shear band formation in a fine_grained sand
Proc.5th Int.Conf.Numer.Meth.Geomech.,Nagoya 1985,PP 517-521

84- VARDOULAKIS, I. and GUDEHUS, G.
Trap_door problem with dry sand:
A statical approach based upon model test kinematics.
Int. Jrnl Num. & Anal. Meth in Geomech.,Vol. 5,1981,PP 57-78

85- VARDOULAKIS, I.
Constitutive properties of dry sand observable in the triaxial test
Acta mechanica, 1981, 38, 219.

86- VARDOULAKIS, I.,
Rigid granular plasticity model and bifurcation in the triaxial test.
Acta mechanica, 1983, 49, 57.

87- VERMEER, P.A.
A double hardening model for sand.
Geotechnique 28,No. 4,1978,PP 413-433

88- VERMEER, P.A.

Formulation and prediction of sand behaviour.

10th Int.Conf. on Soil Mech.and Fnd.Eng,Stockholm,Vol.1,1981, PP 259-262

89- VERMEER, P.A.

A five_constant model unifying well_established concepts.

Results of the International Workshop on Constitutive Relations for Soils/Grenoble/6-8 September 1982,PP 175-197

90- VERMEER, P.A and SUTJIADI, W.

The uplift resistance of shallow embedded anchors.

Proc. of 11th Int.Conf.Soil Mech. and Fnd.Engg. ,San Francisco, August 1985,PP 1635-1638

91- VESIC, A.S.

Breakout resistance of objects embedded in ocean bottom.

Journal of the Soil Mechanics and Foundations Division. Proc. of the ASCE,Septmber,1971,No. SM 9,PP 1183-1205

92- VESIC, A.S.

Expansion of cavities in an infinite soil mass.

Jrnl of Soil Mech. Found. Div.,Proc.of ASCE,1972,No.SM 3,PP 265-291

93- WANG, M.C. and WU, A.H.

Yielding load of anchors in sand.

Proc.Symp. Appl. Plasticity on geotech. Eng.,1980,PP 291-307

94- WROTH,C.P. and HOULSBY,G.T.

Soil mechanics_Property characterization and analysis procedures

Proc. of the 11th International Conference on Soil Mechanics and Found. Engg,San Francisco/12-16 August 1985,Vol. 1, PP 1-55

95- ZAKARIA, I.B.

The effect on the uplift resistance of anchors of ground disturbance during placing.

M.Sc. Thesis presented to Glasgow University,1986

96- ZIENKIEWICZ, O.C.

The finite element method

Mc Graw Hill,1977

APPENDICES

APPENDIX-A-

The Mindlin solution for a vertical point load acting beneath the surface of the semi_infinite mass is :

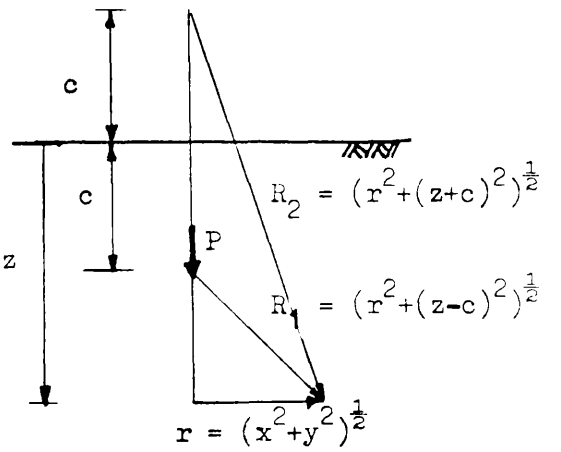

$$\sigma_x = \frac{-P}{8\,\pi(1-\nu)}\left[\frac{(1-2\nu)\,(z-c)}{R_1^3} - \frac{3x^2(z-c)}{R_1^5} + \frac{(1-2\nu)[3(z-c)-4\nu(z+c)]}{R_2^3} - \frac{3(3-4\nu)x^2(z-c)-6c(z+c)[(1-2\nu)z-2\nu c]}{R_2^5} - \frac{30\,cx^2z(z+c)}{R_2^7} - \frac{4(1-\nu)(1-2\nu)}{R_2(R_2+z+c)} \times \left[1 - \frac{x^2}{R_2(R_2+z+c)} - \frac{x^2}{R_2^2}\right]\right]$$

$$\sigma_y = \frac{-P}{8\,\pi(1-\nu)}\left[\frac{(1-2\nu)(z-c)}{R_1^3} - \frac{3y^2(z-c)}{R_1^5} + \frac{(1-2\nu)[(3(z-c)-4\nu(z+c)]}{R_2^3} - \frac{3(3-4\nu)y^2(z-c)-6c(z+c)[(1-2\nu)z-2\nu c]}{R_2^5} - \frac{30cy^2z(z+c)}{R_2^7} - \frac{4(1-\nu)(1-2\nu)}{R_2(R_2+z+c)} \times \left[1 - \frac{y^2}{R_2(R_2+z+c)} - \frac{y^2}{R_2^2}\right]\right]$$

$$\tau_{xy} = \frac{-Pxy}{8\,\pi(1-\nu)}\left[-\frac{3(z-c)}{R_1^5} - \frac{3(3-4\nu)(z-c)}{R_2^5} + \frac{4(1-\nu)(1-2\nu)}{R_2^2(R_2+z+c)}\left[\frac{1}{R_2+z+c} + \frac{1}{R_2}\right] - \frac{30\,cz(z+c)}{R_2^5}\right]$$

APPENDIX -B-

```
      PROGRAM PORES
C     ************************************************************
C     *
C     *            Pull Out RESistance of plate anchors
C     *       THIS PROGRAM COMPUTES STRESSES DUE TO THE LOAD
C     *       OF A SQUARE ANCHOR PLATE EMBEDDED IN A SOIL
C     *       WITH ELASTIC BEHAVIOUR.
C     *
C     ************************************************************
C
      COMMON /A/ D,B,ES,VS,PHI,GAMA
      COMMON /B/ NL,NLEV,NSTAT,NLSQ,NPT
      COMMON /C/ ACORD(1024,3),PSTAT(336,3),ZLEV(25),PRESSR,XSTAT(20)
      COMMON /D/ STRESS(336,8),SINIT(336,3),NLL(25)
      COMMON /I/ IBUG(10)
      CALL DATGEN
      CALL SOLV
      CALL PLOT
      STOP
      END
C
      SUBROUTINE DATGEN
C     *-------------------------------------------------------*
C     *       GENERATION OF FIELD POINTS
C     *       COMPUTE IN-SITU STRESSES
C     *-------------------------------------------------------*
      COMMON /A/ D,B,ES,VS,PHI,GAMA
      COMMON /B/ NL,NLEV,NSTAT,NLSQ,NPT
      COMMON /C/ ACORD(1024,3),PSTAT(336,3),ZLEV(25),PRESSR,XSTAT(20)
      COMMON /D/ STRESS(336,8),SINIT(336,3),NLL(25)
      COMMON /I/ IBUG(10)
      NSTATB= 7
      NSTATC= NSTATB+ 1
      READ(5,*) IBUG
      READ(5,*) D,B
      READ(5,*) ES,VS,PHI,GAMA
      READ(5,*) NLEV,NSTAT
      READ(5,*) (ZLEV(I),I= 1,NLEV)
      READ(5,*) (XSTAT(I),I= 1,NSTAT)
      READ(5,*) PRESSR
      NPT= NLEV*NSTAT
      WRITE(6,900)
      WRITE(6,910) B,D
      WRITE(6,920) ES,VS,PHI,GAMA
      WRITE(6,940) NLEV,NSTAT
      WRITE(6,980) PRESSR
C
      WRITE(6,925)
      DO 5 IZ= 2,NLEV
      IF((D- ZLEV(IZ))/B .GE. 0.05) GO TO 2
      WRITE(6,990) ZLEV(IZ)
      STOP
    2 CONTINUE
      IF((D- ZLEV(IZ))/B .GE. 0.5) GO TO 3
      ANL= 165.0*(100.0*(D- ZLEV(IZ)))**(- 1.02)+ 1.0
      NLL(IZ)= IFIX(ANL)
      GO TO 4
    3 NLL(IZ)= 4
    4 WRITE(6,930) NLL(IZ)
    5 CONTINU
```

```
C
      DO 10 K=1,1024
      ACORD(K,3)= D
   10 CONTINUE
C
      PHIR= PHI/57.3
      AKO= VS/(1.0- VS)
      K= 0
      DO 40 I=1,NLEV
      DO 30 J=1,NSTAT
      K= K+ 1
      SINIT(K,1)= AKO
      SINIT(K,2)= 0.0
      SINIT(K,3)= 1.0
      PSTAT(K,1)= XSTAT(J)
      PSTAT(K,2)= 0.0
      PSTAT(K,3)= ZLEV(I)
   30 CONTINUE
   40 CONTINUE
C        BOUNDARY CONDITION OF STRESS
      DO 44 I=1,NSTAT
      DO 42 J=1,3
      STRESS(I,J)= SINIT(I,J)
   42 CONTINUE
   44 CONTINUE
      DO 46 I=1,NSTATB
      STRESS(I,1)= STRESS(I,1)+ AKO*0.5*PRESSR
      STRESS(I,3)= STRESS(I,3)+ 0.5*PRESSR
   46 CONTINUE
      STRESS(NSTATC,3)= STRESS(NSTATC,3)+ 0.25*PRESSR
      STRESS(NSTATC,2)= STRESS(NSTATC,2)- 0.15*PRESSR
C
      IF(IBUG(2).EQ.0) GO TO 60
      WRITE(6,960)
      CALL PRINT(PSTAT,336,3,NPT,3)
   60 CONTINUE
      IF(IBUG(3).EQ.0) GO TO 70
      WRITE(6,970)
      CALL PRINT(SINIT,336,3,NPT,3)
   70 CONTINUE
  900 FORMAT(1H0,'GENERATION OF FAILURE SURFACES AROUND ANCHORS')
  910 FORMAT(1H0,'B    = ',1PE10.2,/1H ,'D    = ',E10.2)
  920 FORMAT(1H0,'ES   = ',1PE10.2,/,1H ,'VS   = ',E10.2,/,1H ,'PHI = ',
     1 E10.2,         1H ,'GAMA= ',  E10.2)
  925 FORMAT(1H0,'NUMBER OF ANCHOR ELEMENTS')
  930 FORMAT(1H0,' NL =  ',I4)
  940 FORMAT(1H0,'NUMBER OF SAMPLING POINTS (LEVELS AND
     . STATIONS)',2I6)
  960 FORMAT(1H0,'XYZ COORDS OF SAMPLING POINTS')
  970 FORMAT(1H0,'INITIAL STRESSSES (XX XZ ZZ) AT SAMPLING POINTS')
  980 FORMAT(1H0,'ANCHOR PRESSURE = ',1P10E11.2)
  990 FORMAT(1H0,'LEVEL TOO CLOSE TO ANCHOR !! Z = ',E13.4)
      RETURN
      END
C
      SUBROUTINE SOLV
C     *-----------------------------------*
C     *       COMPUTES TOTAL STRESSS IN SOIL
C     *-----------------------------------*
      COMMON /A/ D,B,ES,VS,PHI,GAMA
```

```
      COMMON /B/ NL,NLEV,NSTAT,NLSQ,NPT
      COMMON /C/ ACORD(1024,3),PSTAT(336,3),ZLEV(25),PRESSR,XSTAT(20)
      COMMON /D/ STRESS(336,8),SINIT(336,3),NLL(25)
      COMMON /I/ IBUG(10)
      DIMENSION DS(3),STR(3)
      IP= 3
      PHIR= PHI/57.3
      IF (IBUG(4).EQ.1) WRITE(6,900)
      IAA= NSTAT+ 1
      DO 50 IZ= 2,NLEV
      NL= NLL(IZ)
      NLSQ= NL*NL
      AREA= B*B/FLOAT(NLSQ)
      CALL DATA2
      DO 45 IX= 1,NSTAT
      IA= (IZ- 1)*NSTAT+ IX
      IAP= IA
      AX= PSTAT(IA,1)
      AY= PSTAT(IA,2)
      AZ= PSTAT(IA,3)
      DO 10 I= 1,3
   10 DS(I)= 0.0
      DO 30 JA= 1,NLSQ
      BX= ACORD(JA,1)
      BY= ACORD(JA,2)
      BZ= ACORD(JA,3)
      CALL PXYZ(VS,AX,AY,AZ,BX,BY,BZ,IP,STR)
      DO 20 I= 1,3
   20 DS(I)= DS(I)+ STR(I)*AREA*PRESSR
   30 CONTINUE
      DO 40 I= 1,3
   40 STRESS(IA,I)= SINIT(IA,I)+ DS(I)
      IF(IBUG(4).EQ.1) WRITE(6,910) (DS(I),I= 1,3)
   45 CONTINUE
   50 CONTINUE
  900 FORMAT(1H0,'STRESSES AT SAMPLING PTS : INCREM. STRESS XX XZ ZZ')
  910 FORMAT(1P3E10.2)
      RETURN
      END
C
      SUBROUTINE DATA2
C     *-----------------------------------*
C     *      GENERATION OF ANCHOR ELEMENTS
C     *-----------------------------------*
      COMMON /A/ D,B,ES,VS,PHI,GAMA
      COMMON /B/ NL,NLEV,NSTAT,NLSQ,NPT
      COMMON /C/ ACORD(1024,3),PSTAT(336,3),ZLEV(25),PRESSR,XSTAT(20)
      BXY= B/FLOAT(NL)
      X= - 0.5*B- 0.5*BXY
      K= 0
      DO 20 I= 1,NL
      X= X+ BXY
      Y= - 0.5*B- 0.5*BXY
      DO 10 J= 1,NL
      K= K+ 1
      Y= Y+ BXY
      ACORD(K,1)= X
      ACORD(K,2)= Y
   10 CONTINUE
   20 CONTINUE
```

```
      RETURN
      END
C
      SUBROUTINE PLOT
C     *-----------------------------------------------------------*
C     *       EVALUATE STRESS INVARIANTS
C     *       PREPARE DATA FOR CONTOURS PLOTTING
C     *-----------------------------------------------------------*
      COMMON /A/ D,B,ES,VS,PHI,GAMA
      COMMON /B/ NL,NLEV,NSTAT,NLSQ,NPT
      COMMON /C/ ACORD(1024,3),PSTAT(336,3),ZLEV(25),PRESSR,XSTAT(20)
      COMMON /D/ STRESS(336,8),SINIT(336,3),NLL(25)
      COMMON /I/ IBUG(10)
      CHARACTER*4 FLAG
      FLAG= 'PLOT'
      NMAX= 336
      PHIR= PHI/57.3
C
      EPS= 1.0E-12
      DO 20 IP= 1,NPT
      SXX= STRESS(IP,1)
      SXZ= STRESS(IP,2)
      SZZ= STRESS(IP,3)
      P= (SXX+ SZZ)/2.0
      QQ= (SXX- SZZ)**2 + 4.0*SXZ*SXZ
      Q= SQRT(QQ)/2.0
      IF(ABS(P).LT.EPS) P= EPS
      SIG1= P+ Q
      SIG3= P- Q
      STRESS(IP,4)= SIG1
      STRESS(IP,5)= SIG3
      STRESS(IP,6)= Q
      STRESS(IP,7)= P
      STRESS(IP,8)= Q/P
      IF (STRESS(IP,1).LT.0.0 .OR. STRESS(IP,3).LT.0.0) GO TO 15
      GO TO 20
   15 STRESS(IP,8)= 0.0
   20 CONTINUE
      DO 80 I= 1,NPT
      PSTAT(I,3)= D- PSTAT(I,3)
   80 CONTINUE
      IF(IBUG(6).EQ.0) GO TO 90
      WRITE(6,930)
      CALL PRINT(STRESS,NMAX,8,NPT,8)
      WRITE(6,935)
      CALL PRINT(PSTAT,NMAX,3,NPT,3)
   90 CONTINUE
C                    PLOTTING    DATA
      WRITE(6,940) FLAG
      DO 110 J= 1,8
      SMAX= 0.0
      SMIN= 0.0
      WRITE(6,950) NLEV,NSTAT
      WRITE(6,960) (XSTAT(I),I= 1,NSTAT)
      WRITE(6,960) (PSTAT(I,3),I= 1,NPT,NSTAT)
      DO 130 JJ= 1,NSTAT
      DO 120 II= 0,NLEV- 1
      KS= JJ+ II*NSTAT
      WRITE(6,960) STRESS(KS,J)
      IF(STRESS(KS,J).GT.SMAX) SMAX= STRESS(KS,J)
```

```
      IF(STRESS(KS,J).LT.SMIN) SMIN= STRESS(KS,J)
  120 CONTINUE
  130 CONTINUE
      WRITE(6,960) SMAX,SMIN
  110 CONTINUE
  910 FORMAT(1H0,'STRESSES XX XZ ZZ SIG1 SIG3 SIG1-SIG3 SIG1+SIG3')
  920 FORMAT(1P7E11.2)
  930 FORMAT(1H0,'STRESSES  XX XZ ZZ SIG1 SIG3  SIG1-SIG3  SIG1+SIG3')
  935 FORMAT(1H0,'X Y Z FIELD COORDINATES FROM ANCHOR')
  940 FORMAT(A4)
  950 FORMAT(2I4)
  960 FORMAT(1H ,1P5E13.4)
      RETURN
      END
C
      SUBROUTINE PRINT(A,L,M,LA,MA)
      DIMENSION A(L,M)
      DO 10 I=1,LA
      WRITE(6,900) (A(I,J),J=1,MA)
   10 CONTINUE
  900 FORMAT(1P8E13.4)
      RETURN
      END
C
      SUBROUTINE PXYZ(PM,AX,AY,AZ,BX,BY,BZ,IP,D)
C     *-----------------------------------------------------------*
C     *       COMPUTES STRESS INCREMENT IN SOIL
C     *-----------------------------------------------------------*
      DIMENSION D(3)
      X= AX- BX
      Y= AY- BY
      Z= AZ
      C= BZ
      ZMC= Z- C
      ZPC= Z+ C
      X2= X*X
      Y2= Y*Y
      ZMC2= ZMC*ZMC
      ZPC2= ZPC*ZPC
      R12= X2+ Y2+ ZMC2
      R22= X2+ Y2+ ZPC2
C
      R1= SQRT(R12)
      R13= R12*R1
      R15= R12*R13
      R2= SQRT(R22)
      R23= R22*R2
      R25= R22*R23
      R27= R22*R25
      R2ZC= R2+ Z+ C
C
      PM11= 1.-     PM
      PM12= 1.- 2.*PM
      PM32= 3.- 2.*PM
      PM34= 3.- 4.*PM
      PM54= 5.- 4.*PM
      W= 1.0/(25.133*PM11)
C
      GO TO (10,20,30),IP
   10 CONTINUE
```

```
   20 CONTINUE
   30 CONTINUE
      AXXAZ= W*(PM12*ZMC/R13 -  3.0*X2*ZMC/R15 +  PM12* (3.0*ZMC
     .       - 4.0*PM*ZPC)/R23 -  (3.0*PM34*X2*ZMC -  6.0*C*ZPC* (PM12*Z
     .       - 2.0*PM*C) )/R25 -  30.0*C*X2*Z*ZPC/R27
     .       -  (4.0*PM11*PM12/ (R2*R2ZC) ) * (1.0- X2/ (R2*R2ZC)
     .       -  X2/R22) )
      AZZAZ= W*(- PM12*ZMC/R13 +  PM12*ZMC/R23 - 3.0*ZMC*ZMC2/R15
     .       -  (3.0*PM34*Z*ZPC2 -  3.0*C*ZPC* (5.0*Z- C) )/R25
     .       - 30.0*C*Z*ZPC*ZPC2/R27 )
      AZXAZ= W*X*(- PM12/R13 +  PM12/R23 -  3.0*ZMC2/R15
     .       -  (3.0*PM34*Z*ZPC -  3.0*C*(3.0*Z+ C) )/R25
     .       -  30.0*Z*C*ZPC2/R27 )
C
      D(1)= AXXAZ
      D(2)= AZXAZ
      D(3)= AZZAZ
      RETURN
      END
```

```
      PROGRAM CLAYS
C     ************************************************************
C     *
C     *                        CLAYS
C     *       THIS PROGRAM SIMULATES SOIL BEHAVIOUR UNDER
C     *       DRAINED AND UNDRAINED TEST CONDITIONS.
C     *       IT GIVES THE EFFECTIVE AND TOTAL STRESS VECTORS
C     *       FOLLOWING A STRAIN PATH.
C     *       MODEL: "ASSOCIATED MODIFIED CAM CLAY"
C     *       THE YIELD SURFACE IS ELLIPTIC AND THE FLOW RULE IS
C     *       ASSOCIATED.
C     *
C     ************************************************************
C
      COMMON /PA/ AX(4),BX(4),DX(4,4),DPX(4,4),DA(4),BD(4),DABD(4,4)
      COMMON /PB/ AMDA,CAPA,PS,E0,ES,PHI,DEVP,DEDP,EE
      COMMON /PC/ ESTRS(4),STRES(4),STRAN(4),SS(4),SN(4)
      COMMON /PD/ P0,EM,PP,QQ,IYILD,NLOAD,ILOAD
      COMMON /PE/ IDRAN,NYILD(10),NLOOP,NPRINT
C
C*** READ DATA
C
      READ(5,*) IDRAN
      READ(5,*) NLOAD
      READ(5,*) (STRES(I),I=1,4)
      READ(5,*) (SN(I),I=1,4)
      READ(5,*) AMDA,CAPA,PS,E0,PHI
      READ(5,*) P0
C
C*** INITIALIZATION OF VARIABLES
C
      DO 5 I=1,4
      STRAN(I)=0.0
      ESTRS(I)=STRES(I)
    5 CONTINUE
      EPSIV=0.0
      EPSID=0.0
      DEVP=0.0
      DEDP=0.0
      QQ0=0.0
      PWP=0.0
      EE=E0
      PI23=2.0944
      EPSH=0.01
      TP=(STRES(1)+STRES(2)+STRES(3))/3.0
      P00=P0
      NLOOP=10
      NPRINT=NLOAD/NLOOP
      WRITE(6,820)
      WRITE(6,830)
      IF(IDRAN.EQ.0) THEN
      WRITE(6,840)
      ELSE
      WRITE(6,845)
      ENDIF
      WRITE(6,850) AMDA,CAPA,PS,E0,PHI
      WRITE(6,860) P0
      WRITE(6,870)
      PHI=0.01745*PHI
C
```

```
C*** LOOP OVER LOADS, COMPUTING DEVIATORIC AND MEAN STRESSES
C
      DO 810 IPRINT=1,NPRINT
      DO 800 ILOOP=1,NLOOP
      QA=(ESTRS(1)-ESTRS(2))**2
      QB=(ESTRS(2)-ESTRS(3))**2
      QC=(ESTRS(3)-ESTRS(1))**2
      QD=6.0*ESTRS(4)*ESTRS(4)
      QE=0.5*(QA+QB+QC+QD)
      QQ=SQRT(QE)
      PP=(ESTRS(1)+ESTRS(2)+ESTRS(3))/3.0
C
C*** PRINCIPAL STRESSES AND MOHR COULOMB COEFFICIENT (M)
C
      IF(SN(2).EQ.SN(3)) THETA=0.5236
      IF(SN(2).EQ.SN(1)) THETA=-0.5236
      SIGM1=PP-2.0*QQ*SIN(THETA-PI23)/3.0
      SIGM2=PP-2.0*QQ*SIN(THETA)/3.0
      SIGM3=PP-2.0*QQ*SIN(THETA+PI23)/3.0
      RATIO=(SN(2)-SN(3))/(SN(1)-SN(3))
      EM0=6.0*SIN(PHI)/(3.0+SIN(PHI))
      EM1=6.0*SIN(PHI)/(3.0-SIN(PHI))
      EM=(1.0-RATIO)*EM1+RATIO*EM0
      SLOPE=(1.0+RATIO)/3.0
      ES=3.0*PP*(1.0+EE)*(1.0-2.0*PS)/CAPA
C
C*** ELASTIC CONSTITUTIVE MATRIX
C
      DO 10 I=1,4
      DO 10 J=1,4
   10 DX(I,J)=0.0
      CA=ES/((1.0+PS)*(1.0-2.0*PS))
      CB=1.0-PS
      DX(1,1)=CB*CA
      DX(1,2)=PS*CA
      DX(1,3)=PS*CA
      DX(2,1)=PS*CA
      DX(2,2)=CB*CA
      DX(2,3)=PS*CA
      DX(3,1)=PS*CA
      DX(3,2)=PS*CA
      DX(3,3)=CB*CA
      DX(4,4)=0.5*ES/(1.0+PS)
C
C*** CHECK IF ELEMENT HAS YIELDED
C
      IYILD=1
      F=PP*PP-PP*P0+QQ*QQ/(EM*EM)
      P0C=PP+QQ*QQ/(PP*EM*EM)
      EPS=EPSH*P0*P0
      EPS=ABS(EPS)
      IF(F.GT.EPS.OR.F.LT.-EPS) THEN
      IYILD=0
      DO 300 I=1,4
      DO 300 J=1,4
  300 DPX(I,J)=DX(I,J)
      ELSE
      EPSI=ABS(P0-P0C)/P0
      IF(EPSI.GE.0.01) IYILD=2
      CALL DPMAT
```

```
      ENDIF
      NYILD(ILOOP)= IYILD
C
C*** COMPUTE NEW STRAINS AND STRESSES
C
      DO 210 I=1,4
  210 SS(I)= 0.0
      DO 220 I=1,4
      DO 220 J=1,4
      SS(I)= SS(I)+ DPX(I,J)*SN(J)
  220 CONTINUE
      DO 240 K=1,4
      STRAN(K)= STRAN(K)+ SN(K)
      ESTRS(K)= ESTRS(K)+ SS(K)
  240 CONTINUE
C
C     COMPUTE EFFECTIVE AND TOTAL STRESSES
C        "         PORE WATER PRESSURE
C
      QAD= (SS(1)- SS(2))**2
      QBD= (SS(2)- SS(3))**2
      QCD= (SS(3)- SS(1))**2
      QDD= 6.0*SS(4)*SS(4)
      QED= 0.5*(QAD+ QBD+ QCD+ QDD)
      QQDOT= SQRT(QED)
      EPDOT= (SS(1)+ SS(2)+ SS(3))/3.0
      IF(IDRAN.EQ.0) GO TO 760
      TPDOT= EPDOT
      DEVE= 3.0*EPDOT*(1.0- 2.0*PS)/ES
      DEVEP= DEVE+ DEVP
      EPSIV= EPSIV+ DEVEP
      DEDE= 2.0*(1.0+ PS)*QQDOT/(3.0*ES)
      DEDEP= DEDE+ DEDP
      EPSID= EPSID+ DEDEP
      EDOT= - (1.0+ EE)*DEVEP
      EE= EE+ EDOT
      IF(EE.LT.0.0) THEN
      WRITE(6,960)
      STOP
      ELSE
      CONTINUE
      ENDIF
      GO TO 780
  760 CONTINUE
      TPDOT= SLOPE*QQDOT
      IF(QQ0.GT.QQ) TPDOT= - TPDOT
      DEVP= - 3.0*EPDOT*(1.0- 2.0*PS)/ES
  780 CONTINUE
      UDOT= TPDOT- EPDOT
      PWP= PWP+ UDOT
      DO 790 I=1,3
  790 STRES(I)= STRES(I)+ SS(I)+ UDOT
      STRES(4)= STRES(4)+ SS(4)
      TP= TP+ TPDOT
      UDP= PWP/P00
      QDP= QQ/P00
      QQ0= QQ
      P0= P0+ (1.0+ EE)*P0*DEVP/(AMDA- CAPA)
C
  800 CONTINUE
```

```
      WRITE(6,920) STRAN(1),STRES(1),ESTRS(1),EE,TP,PP,QQ,P0,QDP,UDP
     .     ,EPSIV,EPSID
      WRITE(6,930) STRAN(2),STRES(2),ESTRS(2)
      WRITE(6,930) STRAN(3),STRES(3),ESTRS(3)
      WRITE(6,940) STRAN(4),STRES(4),ESTRS(4),(NYILD(I),I= 1,10),EM
  810 CONTINUE
  820 FORMAT(20X,36HELASTO- PLASTIC BEHAVIOUR OF CAM CLAY,///)
  830 FORMAT(10X,37HN.C. CLAY   -   Q= ELLIPSE  F= ELLIPSE,/)
  840 FORMAT(10X,19HUNDRAINED BEHAVIOUR,//)
  845 FORMAT(10X,17HDRAINED BEHAVIOUR,//)
  850 FORMAT(4X,7HLAMDA = ,1PE10.2,5X,7HKAPPA = ,1PE10.2,5X,9HPOISSON = ,
     .          1PE10.2,5X,6HVOID = ,1PE10.2,5X,5HPHI = ,1PE10.2)
  860 FORMAT(4X,21HPAST MAXIMUM STRESS = ,1PE10.2)
  870 FORMAT(//,1H0,' STRAIN     TOT.STRESS    EFF.STRESS      VOID     TOT.
     .P     EFF.P          Q            EFF.P0     Q/P0         U/P0        V- STRAIN
     .      D- STRAIN')
  920 FORMAT(/,1P12E11.2)
  930 FORMAT(1P3E11.2)
  940 FORMAT(1P3E11.2,4X,10I1,4X,3HM = ,1PE9.2)
  950 FORMAT(7HSIGMA1= ,1PE9.2,5X,7HSIGMA2= ,1PE9.2,5X,7HSIGMA3= ,1PE9.2)
  960 FORMAT(36H*** NEGATIVE VALUE OF VOID RATIO ***)
      STOP
      END
      SUBROUTINE DPMAT
C     *-----------------------------------------*
C     *       THIS SUBROUTINE COMPUTES THE ELASTO- PLASTIC
C     *       CONSTITUTIVE MATRIX
C     *-----------------------------------------*
      COMMON /PA/ AX(4),BX(4),DX(4,4),DPX(4,4),DA(4),BD(4),DABD(4,4)
      COMMON /PB/ AMDA,CAPA,PS,E0,ES,PHI,DEVP,DEDP,EE
      COMMON /PC/ ESTRS(4),STRES(4),STRAN(4),SS(4),SN(4)
      COMMON /PD/ P0,EM,PP,QQ,IYILD,NLOAD,ILOAD
      COMMON /PE/ IDRAN,NYILD(10),NLOOP,NPRINT
C
      EM2= EM*EM
C
C***            ..... DERIVATIVES .....
C
      DP= 1.0/3.0
      IF(QQ.EQ.0.0) THEN
      DQA= 1.5
      DQB= 1.5
      DQC= 1.5
      DQD= 1.5
      ELSE
      DQA= 1.5*(ESTRS(1)- PP)/QQ
      DQB= 1.5*(ESTRS(2)- PP)/QQ
      DQC= 1.5*(ESTRS(3)- PP)/QQ
      DQD= 3.0*ESTRS(4)/QQ
      ENDIF
C
      DPE= P0*(1.0+ EE)/(AMDA- CAPA)
      DQE= 0.0
C
      DFP= 2.0*PP- P0
      DFQ= 2.0*QQ/EM2
      DQP= DFP
      DQQ= DFQ
      DFP0= - PP
      DFQ0= 0.0
```

```
      DQQP= DQQ/DQP
      GAMA= DFP0*DPE*DQP+ DFQ0*DQE*DQQ
C
      AX(1)= DP*DQP+ DQA*DQQ
      AX(2)= DP*DQP+ DQB*DQQ
      AX(3)= DP*DQP+ DQC*DQQ
      AX(4)=         DQD*DQQ
      BX(1)= AX(1)
      BX(2)= AX(2)
      BX(3)= AX(3)
      BX(4)= AX(4)
C
C*** ELASTO- PLASTIC CONSTITUTIVE MATRIX
C
      DO 30 I= 1,4
      DA(I)= 0.0
      DO 20 K= 1,4
      DA(I)= DA(I)+ DX(I,K)*AX(K)
   20 CONTINUE
   30 CONTINUE
      DO 50 J= 1,4
      BD(J)= 0.0
      DO 40 K= 1,4
      BD(J)= BD(J)+ BX(K)*DX(K,J)
   40 CONTINUE
   50 CONTINUE
      DO 70 I= 1,4
      DO 60 J= 1,4
      DABD(I,J)= DA(I)*BD(J)
   60 CONTINUE
   70 CONTINUE
      BDA= 0.0
      DO 80 I= 1,4
      BDA= BDA+ BD(I)*AX(I)
   80 CONTINUE
      CONST= 1.0/(BDA- GAMA)
      DO 100 I= 1,4
      DO  90 J= 1,4
      DPX(I,J)= DX(I,J)- CONST*DABD(I,J)
   90 CONTINUE
  100 CONTINUE
      IF(IDRAN.EQ.0) RETURN
      BDSN= 0.0
      DO 110 I= 1,4
      BDSN= BDSN+ BD(I)*SN(I)
  110 CONTINUE
      DAMDA= BDSN*CONST
      DEVP= DAMDA*DQP
      DEDP= DAMDA*DQQ
      RETURN
      END
```

```
      SUBROUTINE INSITU (COORD,LNODS,MELEM,MPOIN,MTOTG,NDOFN,NEVAB,
     .                   NTYPE,NELEM,NGAUS,NNODE,NSTRE,NTOTG,WLOAD,
     .                   POSGP,WEIGP)
C*****************************************************************
C
C     THIS SUBROUTINE COMPUTES THE INITIAL STRESS IN THE SOIL
C     AND EVALUATES THE EQUIVALENT NODAL LOADS
C
C*****************************************************************
      COMMON/BLOC7/ AKO,GAMMA,HIGHT,NSITU
      DIMENSION COORD(MPOIN,2),ELCOD(2,9),GPCOD(2,9),LNODS(MELEM,9),
     .      DERIV(2,9),POSGP(4),WLOAD(MELEM,18),SHAPE(9),
     .      CARTD(2,9),WEIGP(4),BMATX(4,18),STRIS(4,1350)
C
C     READ UNIT WEIGHT, Ko AND HIGHT OF SOLID
C
      READ(5,*) GAMMA,AKO,HIGHT
      WRITE(6,900) GAMMA,AKO,HIGHT
  900 FORMAT(//,13HUNIT WEIGHT = ,E8.3,5X,5H KO = ,E8.3,5X,
     .  16HDEPTH OF LAYER = ,E8.3)
      NGAU2= NGAUS*NGAUS
      TWOPI= 6.283185
      DO 60 IELEM= 1,NELEM
      DO 60 IEVAB= 1,NEVAB
   60 WLOAD(IELEM,IEVAB)= 0.0
      KGAUS= 0
C
C     LOOP OVER EACH ELEMENT
C
      DO 110 IELEM= 1,NELEM
C
C     COMPUTE COORDINATES OF THE ELEMENT NODAL POINTS
C
      DO 80 INODE= 1,NNODE
      LNODE= IABS(LNODS(IELEM,INODE))
      DO 80 IDIME= 1,2
   80 ELCOD(IDIME,INODE)= COORD(LNODE,IDIME)
C
C     ENTER LOOPS FOR COMPUTATION OF IN SITU STRESSES
C     AND AREA NUMERICAL INTEGRATION
C
      KGASP= 0
      DO 100 IGAUS= 1,NGAUS
      DO 100 JGAUS= 1,NGAUS
      EXISP= POSGP(IGAUS)
      ETASP= POSGP(JGAUS)
      KGAUS= KGAUS+ 1
      KGASP= KGASP+ 1
C
C     COMPUTE THE SHAPE FUNCTIONS AT THE SAMPLING POINTS
C     AND ELEMENTAL VOLUME
C
      CALL SFR2(DERIV,ETASP,EXISP,NNODE,SHAPE)
      CALL JACOB2(CARTD,DERIV,DJACB,ELCOD,GPCOD,IELEM,KGASP,
     .            NNODE,SHAPE)
      DVOLU= DJACB*WEIGP(IGAUS)*WEIGP(JGAUS)
      IF(NTYPE.EQ.3) DVOLU= DVOLU*TWOPI*GPCOD(1,KGASP)
C
C     COMPUTE IN SITU STRESSES
C
```

```
      STRIS(1,KGAUS)= AKO*GAMMA*(HIGHT- GPCOD(2,KGASP))
      STRIS(2,KGAUS)= GAMMA*(HIGHT- GPCOD(2,KGASP))
      STRIS(3,KGAUS)= 0.0
      STRIS(4,KGAUS)= AKO*GAMMA*(HIGHT- GPCOD(2,KGASP))
C
C*** CALL THE B MATRIX
C
      CALL BMATPS(BMATX,CARTD,NNODE,SHAPE,GPCOD,NTYPE,KGASP)
C
C     CALCULATE LOADS AND ASSOCIATE WITH ELEMENT NODAL POINT
C
      MGASH= 0
      DO 90 INODE= 1,NNODE
      DO 90 IDOFN= 1,NDOFN
      MGASH= MGASH+ 1
      DO 90 ISTRE= 1,NSTRE
   90 WLOAD(IELEM,MGASH)= WLOAD(IELEM,MGASH)+ BMATX(ISTRE,MGASH)*
     . STRIS(ISTRE,KGAUS)*DVOLU
  100 CONTINUE
  110 CONTINUE
      WRITE(6,970)
      DO 130 IELEM= 1,NELEM
  130 WRITE(6,980) IELEM,(WLOAD(IELEM,IEVAB),IEVAB= 1,NEVAB)
  970 FORMAT(1H0,5X,35HNODAL FORCES DUE TO INSITU STRESSES)
  980 FORMAT(1X,I4,5X,8E12.3/(10X,8E12.3))
      RETURN
      END
```

N.B. The subroutines BMATPS,SFR2 and JACOB2 are listed in
"Finite Element in Plasticity, theory and practice."
by Owen, D.R.J. and Hinton, E.
Pineridge Press Ltd, Swansea, U.K., 1980.